POLITECHNIKA RZESZOWSKA
im. Ignacego Łukasiewicza
WYDZIAŁ CHEMICZNY
Katedra Chemii Nieorganicznej
i Analitycznej

PRACA DOKTORSKA

SPEKTROMETRIA MAS Z LASEROWĄ ABLACJĄ DO BADANIA ZWIĄZKÓW MAŁOCZĄSTECZKOWYCH ORAZ MATERIAŁÓW POCHODZENIA BIOLOGICZNEGO

mgr inż. Aneta Płaza-Altamer

Promotor:
prof. dr hab. inż. Tomasz Ruman

Rzeszów, 2023

Składam serdeczne podziękowania:

Panu prof. dr hab. Tomaszowi Rumanowi, prof. PRz
za nieocenione wsparcie merytoryczne, ciągłą motywację do dalszej pracy, ogromne zaufanie, poświęcony czas, wiarę w moje umiejętności, jak również za cierpliwość i życzliwość okazaną mi podczas kilkuletniej opieki naukowej w trakcie studiów magisterskich i doktoranckich.

Pani dr hab. Joannie Nizioł, prof. PRz
za możliwość udziału w realizacji projektu, wszelkie cenne wskazówki, przekazaną wiedzę i doświadczenie, a także za życzliwość oraz miłą atmosferę w pracy.

Panu mgr. inż. Arturowi Kołodziejowi
za całokształt 4-letniej współpracy, ale przede wszystkim, za nieocenione wsparcie i zrozumienie, za ciągłą gotowość do pomocy, życzliwość i miłą atmosferę w pracy.

Pracownikom Katedry Chemii Nieorganicznej i Analitycznej
za wsparcie, życzliwość oraz miłą atmosferę w pracy.

Mojemu Mężowi
za wsparcie, wiarę we mnie, dodawanie otuchy w chwilach zwątpienia, cierpliwość oraz za pomoc w zachowaniu równowagi między pracą a życiem prywatnym.

Moim Rodzicom i Braciom
za wsparcie i nieustającą wiarę we mnie.

NARODOWE CENTRUM NAUKI

Część badań została zrealizowana w ramach grantu SONATA 14
nr UMO-2018/31/D/ST4/00109 finansowanego przez Narodowe Centrum Nauki

Spis treści

I. Streszczenie w języku polskim

W niniejszej rozprawie doktorskiej przedstawiono tematykę spektrometrii mas z laserową ablacją do badania materiałów biologicznych i syntetycznych. Zaprezentowany cykl publikacji dotyczy zarówno opracowania nowych laserowych metod MS jak również ich zastosowania.

W pracy doktorskiej przedstawiono wyniki obrazowania wycinków ludzkich tkanek nerek z częścią prawidłową i nowotworową za pomocą nowatorskiej metody LARESI MSI. Związki zawarte na powierzchni badanego obiektu zidentyfikowano poprzez pomiar w trybie SRM/MRM.

Kolejne zaprezentowane wyniki stanowiły obrazy jonowe wygenerowane dla odcisków fragmentów ludzkich tkanek pęcherza moczowego uzyskane w wyniku obrazowania spektrometrią mas z laserową desorpcją/jonizacją. Do pomiaru wykorzystano napylone na badany obiekt nanocząstki srebra-109 wytworzone metodą redukcji chemicznej.

Przedstawiono rozwiązanie problemów wynikających ze stosowania nanocząstek wytwarzanych metodą chemicznej redukcji w spektrometrii mas poprzez opracowanie nowej metody generowania NPs. Omówiono metodę syntezy poprzez laserową ablację w roztworze z użyciem impulsowego lasera światłowodowego z głowicą 2D skanera galwanometrycznego do wytwarzania czystych chemicznie nanocząstek z powierzchni blaszki metalu. Przedstawiono również charakterystykę uzyskanych ^{109}AgNPs i AuNPs wraz z wynikami eksperymentów LDI MS wykonanymi dla kilku małocząsteczkowych związków. Wyniki LDI MSI odcisku palca pokrytego nanocząstkami ^{109}Ag wytworzonymi metodą LASIS, dodatkowo potwierdziły użyteczność uzyskanych nanocząstek do analizy zarówno prostych jak i złożonych obiektów.

W ostatniej części przedstawiono zastosowanie laserowo generowanych nanocząstek srebra-109 do analizy jakościowej i ilościowej związków chemicznych za pomocą manualnych pomiarów LDI jak i półautomatycznego LDI MSI. Do badań wykorzystano zarówno roztwory wodne jak i materiał biologiczny – surowicę krwi ludzkiej. Dla uzyskanych wyników przeprowadzono analizę regresji z wykorzystaniem różnego rodzaju funkcji. Na podstawie wykonanych eksperymentów wykazano przewagę metody LDI MSI nad ręcznie wykonywanymi pomiarami LDI MS.

Dodatkowo wytworzone nanocząstki złota i srebra monoizotopowego wykorzystano do identyfikacji metabolitów w surowicy krwi pacjentów z nowotworem pęcherza moczowego metodą LDI MS.

II. Streszczenie w języku angielskim

This doctoral dissertation presents the topic of mass spectrometry with laser ablation for the study of biological and synthetic materials. The presented series of publications concerns both the development of new MS laser methods and their application.

The doctoral thesis presents the results of imaging sections of human kidney tissues with normal and cancer parts using the innovative LARESI MSI method. The compounds contained on the surface of the tested object were identified by measuring in the SRM/MRM mode.

The next presented results were ion images generated for imprints of human bladder tissue fragments obtained as a result of mass spectrometry imaging with laser desorption/ionization. Silver-109 nanoparticles sputtered onto the test object, produced by chemical reduction, were used for the measurement.

A solution to the problems arising from the use of nanoparticles produced by chemical reduction in mass spectrometry by developing a new method for generating NPs is presented. The method of synthesis by laser ablation in a solution with the use of a pulsed fiber laser with a 2D galvanometric scanner head for the production of chemically pure nanoparticles from the surface of a metal plate is discussed. The characteristics of the obtained ^{109}AgNPs and AuNPs are also presented with the results of LDI MS experiments performed for several low molecular weight compounds. The LDI MSI results of the fingerprint covered with ^{109}Ag nanoparticles produced by the LASIS method additionally confirmed the usefulness of the obtained nanoparticles for the analysis of both simple and complex objects.

The last part presents the use of laser-generated silver-109 nanoparticles for the qualitative and quantitative analysis of chemical compounds using manual LDI measurements and semi-automatic LDI MSI. Both aqueous solutions and biological material - human blood serum - were used for the study. For the obtained results, a regression analysis was performed using various types of functions. Based on the performed experiments, the advantage of the LDI MSI method over the manual LDI MS measurements was demonstrated.

In addition, the gold and monoisotopic silver nanoparticles were used to identify metabolites in the blood serum of patients with bladder cancer using the LDI MS method.

III. Wykaz stosowanych skrótów

^{109}AgNPET	(ang. *^{109}Ag-nanoparticle-enhanced target*) – płytka modyfikowana nanocząstkami srebra-109
^{109}AgTFA	(ang. *^{109}Ag-trifluoroacetate*) – trifluorooctan srebra-109
2D GS	(ang. *2D galvanometer scanner*) – dwuwymiarowy skaner galwanometryczny
DESI	(ang. *desorption electrospray ionization*) – desorpcja/jonizacja przez elektrosprej
DHB	(ang. *2,5-dihydroxybenzoic* acid) – kwas 2,5-dihydroksybenzoesowy
DLS	(ang. *dynamic light scattering*) – dynamiczne rozpraszanie światła
ESI	(ang. *electrospray ionization*) – jonizacja w elektrospreju
HPLC-MS	(ang. *high-performance liquid chromatography – mass spectrometry*) - wysokosprawna chromatografia cieczowa sprzężona ze spektrometrią mas
HR SEM	(ang. *high resolution scanning electron microscopy*) – wysoko rozdzielcza skaningowa mikroskopia elektronowa
IR	(ang. *infrared*) – podczerwień
LA-remote-ESI MS	(ang. *Laser Ablation – remote – Electrospray Ionization Mass Spectrometry*) – spektrometria mas ze zdalną laserową ablacją i jonizacją przez elektrorozpylanie
LASIS	(ang. *laser ablation synthesis in solution*) – synteza poprzez ablację laserową w roztworze
LDI	(ang. *laser desorption/ionization*) – laserowa desorpcja/jonizacja
LGN	(ang. *laser generated nanomaterial*) – nanomateriał wytwarzany laserowo
MALDI	(ang. *matrix-assisted laser desorption/ionization*) – laserowa desorpcja/jonizacja wspomagana matrycą
MALDI-MSI	(ang. *matrix-assisted laser desorption/ionization mass spectrometry imaging*) – obrazowanie spektrometrią mas z laserową desorpcją/jonizacją wspomaganą matrycą
MEMS	(ang. *microelectromechanical system*) – mikroukład elektromechaniczny
MOEMS	(ang. *microoptoelectromechanical systems*) – mikroukład optoelektromechaniczny

MRM	(ang. *multiple reaction monitoring*) – monitorowanie wielu reakcji
MS	(ang. *mass spectrometry*) – spektrometria mas
MS/MS	(ang. *tandem mass spectrometry*) – tandemowa spektrometria mas
MSI	(ang. *mass spectrometry imaging*) – obrazowanie spektrometrią mas
nano-PALDI MS	(ang. *nanoparticle-assisted laser desorption/ionization mass spectrometry*) – spektrometria mas z wspomaganą nanocząstkami laserową desorpcją jonizacją
NPs	(ang. *nanoparticles*) – nanocząstki
PFL	(ang. *pulsed fiber laser*) – impulsowy laser światłowodowy
RCC	(ang. *renal cell carcinoma*) – rak nerkowokomórkowy
S/N	(ang. *signal/noise*) – stosunek sygnał/szum
SALDI	(ang. *surface-assisted laser desorption ionization*) – wspomagana powierzchnią laserowa desorpcja jonizacja
SPR	(ang. *surface plasmon resonance*) – powierzchniowy rezonans plazmonowy
ToF	(ang. *Time of Flight*) – analizator czasu przelotu
UHPLC-ESI-UHRMS	(ang. *ultra-high-resolution liquid chromatography – electrospray ionization – ultra-high-resolution mass spectrometry*) – ultra-wysokorozdzielcza chromatografia cieczowa sprzężona z ultra-wysokorozdzielczą spektrometrią mas z jonizacją elektrosprejem
UV	(ang. *ultraviolet*) – nadfiolet

IV. Wykaz publikacji wchodzących w skład osiągnięcia naukowego przedkładanego do oceny

Na rozprawę doktorską ***Spektrometria mas z laserową ablacją do badania związków małocząsteczkowych i materiałów pochodzenia biologicznego*** składa się spójnie tematyczny zbiór 9 publikacji:

PUBLIKACJA I: Joanna Nizioł, Jan Sunner, Iwona Beech, Krzysztof Ossoliński, Anna Ossolińska, Tadeusz Ossoliński, **Aneta Płaza**, Tomasz Ruman *Localization of Metabolites of Human Kidney Tissue with Infrared Laser-Based Selected Reaction Monitoring Mass Spectrometry Imaging and Silver-109 Nanoparticle-Based Surface Assisted Laser Desorption/Ionization Mass Spectrometry Imaging*, **Analytical Chemistry**, 2020, 92, 6, 4251–4258, DOI:10.1021/acs.analchem.9b04580

MEiN	140
Impact Factor (2023)	8,008
Impact Factor 5-letni	6,737
Udział w realizacji materiału naukowego	2%

PUBLIKACJA II: **Aneta Płaza**, Artur Kołodziej, Joanna Nizioł, Tomasz Ruman *Laser Ablation Synthesis in Solution and Nebulization of Silver-109 Nanoparticles for Mass Spectrometry and Mass Spectrometry Imaging*, **ACS Measurement Science Au**, 2021, DOI: 10.1021/acsmeasuresciau.1c00020

MEiN	-
Impact Factor (2023)	Nowe czasopismo ACS
Impact Factor 5-letni	-
Udział w realizacji materiału naukowego	25%

PUBLIKACJA III: **Aneta Płaza-Altamer**, Artur Kołodziej, Joanna Nizioł, Tomasz Ruman *Infrared pulsed fiber laser-produced silver-109-nanoparticles for laser desorption/ionization mass spectrometry of amino acids,* **Journal of Mass Spectrometry**, 2022, 57:e4815, DOI: https://doi.org/10.1002/jms.4815

MEiN	70
Impact Factor (2023)	2,394
Impact Factor 5-letni	1,732
Udział w realizacji materiału naukowego	25%

PUBLIKACJA IV: Artur Kołodziej, **Aneta Płaza-Altamer**, Joanna Nizioł, Tomasz Ruman *Infrared pulsed fiber laser-produced silver-109-nanoparticles for laser desorption/ionization mass spectrometry of carboxylic acids*, **International Journal of Mass Spectrometry**, 2022, 474, 116816, DOI: 10.1016/j.ijms.2022.116816

MEiN	70
Impact Factor (2023)	1,934
Impact Factor 5-letni	1,877
Udział w realizacji materiału naukowego	25%

PUBLIKACJA V: **Aneta Płaza-Altamer**, Artur Kołodziej, Joanna Nizioł, Tomasz Ruman *Laser generated gold nanoparticles for mass spectrometry of low molecular weight compounds*, **Chemical Technology and Biotechnology**, 2022, ISSN 2720-6793, DOI: 10.7862/rc.2022.1

MEiN	-
Impact Factor (2023)	-
Impact Factor 5-letni	-
Udział w realizacji materiału naukowego	25%

PUBLIKACJA VI: Joanna Nizioł, Krzysztof Ossoliński, **Aneta Płaza-Altamer**, Artur Kołodziej, Anna Ossolińska, Tadeusz Ossoliński, Tomasz Ruman *Untargeted ultra-high-resolution mass spectrometry metabolomic profiling of blood serum in bladder cancer*, **Scientific Reports**, 2022, 12, 1, DOI: 10.1038/s41598-022-19576-9

MEiN	140
Impact Factor (2023)	4,997
Impact Factor 5-letni	4,409
Udział w realizacji materiału naukowego	14%

PUBLIKACJA VII: Krzysztof Ossoliński, Tomasz Ruman, Valérie Copié, Brian P. Tripet, Leonardo B. Nogueira, Katiane O.P.C. Nogueira, Artur Kołodziej, **Aneta Płaza-Altamer**, Anna Ossolińska, Tadeusz Ossoliński, Joanna Nizioł *Metabolomic and elemental profiling of blood serum in bladder cancer* **Journal of Pharmaceutical Analysis**, 2022, DOI: 10.1016/j.jpha.2022.08.004

MEiN	140
Impact Factor (2023)	14,026
Impact Factor 5-letni	4,449
Udział w realizacji materiału naukowego	9%

PUBLIKACJA VIII: Artur Kołodziej, **Aneta Płaza-Altamer**, Joanna Nizioł, Tomasz Ruman *Infrared pulsed fiber laser-produced silver-109-nanoparticles for laser desorption/ionization mass spectrometry of 3-hydroxycarboxylic acids,* **Rapid Communication in Mass Spectrometry**, 2022, 36, 21, DOI: 10.1002/rcm.9375

MEiN	70
Impact Factor (2023)	2,586
Impact Factor 5-letni	2,149
Udział w realizacji materiału naukowego	25%

PUBLIKACJA IX: Krzysztof Ossoliński, Tomasz Ruman, Tadeusz Ossoliński, Anna Ossolińska, Adrian Arendowski, Artur Kołodziej, **Aneta Płaza-Altamer**, Joanna Nizioł *Monoisotopic silver nanoparticles-based mass spectrometry imaging of human bladder cancer tissue: Biomarker discovery* **Advances in Medical Sciences**, 2023, 68(1), 38-45, DOI: 10.1016/j.advms.2022.12.002

MEiN	70
Impact Factor (2023)	2,852
Impact Factor 5-letni	3,230
Udział w realizacji materiału naukowego	14%

Dla przedstawionych powyżej publikacji sumaryczny Impact Factor (2023) wynosi **36,797**, natomiast punktacja MEiN wynosi **700** punktów.

V. Cel i zakres pracy

Celem pracy było opracowanie metodologii pomiarowej pozwalającej na badanie rozkładu powierzchniowego małocząsteczkowych związków chemicznych na różnorodnych powierzchniach oraz możliwości jej zastosowania do analizy wybranych obiektów.

Zakres pracy obejmował następujące etapy badawcze:

1. Badania literaturowe tematyki spektrometrii mas z laserową ablacją.
2. Badania literaturowe tematyki obrazowania spektrometrią mas.
3. Opracowanie metody obrazowania wykorzystującej LARESI MSI.
4. Obrazowanie za pomocą MS materiałów biologicznych i syntetycznych:
    a. Obrazowanie wycinka tkanki nerki z obszarem nowotworowym z wykorzystaniem metody LARESI MSI.
    b. Obrazowanie tkanki nowotworowej pęcherza moczowego z wykorzystaniem nanocząstek srebra-109.
    c. Obrazowanie odcisku palca z wykorzystaniem ^{109}AgNPs wytworzonych za pomocą PFL 2D LGN.
5. Wytwarzanie nanocząstek złota i srebra monoizotopowego metodą syntezy laserowej, ich charakterystyka (UV-Vis, DLS) i zastosowanie do LDI MS oraz LDI MSI.
6. Analiza ilościowa wybranych grup związków z wykorzystaniem ^{109}AgNPs wytworzonych za pomocą PFL 2D LGN metodami LDI MS oraz LDI MSI.
7. Profilowanie metabolomiczne surowicy krwi pochodzącej od pacjentów z nowotworem pęcherza moczowego za pomocą metod LDI MS i UHPLC-ESI-UHRMS+MS/MS.

VI. Omówienie osiągnięć badawczych przedstawionych do oceny

5.1. Wstęp teoretyczny

Proces ablacji laserowej polegający na usuwaniu materiału z ciała stałego za pomocą promieniowania elektromagnetycznego emitowanego przez laser znajduje szereg zastosowań. W przemyśle jest ona wykorzystywana do wytwarzania układów mikroelektromechanicznych (MEMS, z ang. *microelectromechanical system*) czy mikrooptoelektromechanicznych (MOEMS, z ang. *microoptoelectromechanical systems*) [1], do produkcji nanomateriałów [2–4], w osadzaniu cienkich warstw metalicznych i dielektrycznych [5], w spawalnictwie do łączenia części metalowych [6], a także do oczyszczania powierzchni [7,8]. Z kolei w medycynie laserowa ablacja wykorzystywana jest w okulistyce, chirurgii ogólnej, neurochirurgii, laryngologii oraz stomatologii. Wiązka lasera o odpowiedniej długości fali promieniowania pozwala na ablację zarówno tkanek twardych jak i miękkich, dlatego wykorzystując proces ablacji laserowej możliwa jest regeneracja powierzchni skóry, korekcja wzroku czy też biopsja lub usunięcie nowotworu bądź zmiany chorobowej [9]. Ablacja laserowa wykorzystywana jest również w analizie chemicznej, gdzie w połączeniu z innymi technikami takimi jak spektrometria mas, dostarcza informacji o związkach znajdujących się z badanej próbce [10].

Pierwsze próby zastosowania lasera w spektrometrii mas (MS, z ang. *mass spectrometry*) rozpoczęły się w połowie lat 60 XX wieku [11]. Eksperymenty te potwierdziły możliwość wykorzystania laserów, jako wszechstronnych źródeł energii, oferując jednoczesną desorpcję i jonizację związków w badanej próbce, wykazujących wystarczającą zdolność absorpcji światła. Obecnie w spektrometrii mas laserowa desorpcja/jonizacja (LDI, z ang. *laser desorption/ionization*) stanowi oddzielną grupę technik wykorzystywanych do analizy związków pochodzenia naturalnego jak i syntetycznych.

Laserowa desorpcja/jonizacja laserowa posiada szereg zalet, takich jak brak konieczności stosowania skomplikowanych procedur na etapie przygotowania próbki, w związku z czym, istnieje niskie ryzyko jej zanieczyszczenia. Do badań wykorzystywane są niewielkie ilości próbki, co ma bardzo duże znaczenie w przypadku analizy materiału biologicznego, którego ilość często jest ograniczona [12]. Kolejną zaletą jest również krótki czas pomiaru liczony w sekundach, gdzie w przypadku konkurencyjnych metod wysokosprawnej chromatografii cieczowej sprzężonej ze spektrometrią mas (HPLC-MS, z ang. *high-performance liquid chromatography – mass spectrometry*) długość analizy sięga od kilku minut nawet do kilku godzin. Jedną z najpopularniejszych metod wykorzystujących LDI jest

laserowa desorpcja/jonizacja wspomagana matrycą (MALDI, z ang. *matrix assisted laser desorption/ionization*). Dzięki jej zdolności do miękkiej jonizacji jest jednym z najważniejszych narzędzi analitycznych wykorzystywanych do analizy związków o dużej masie cząsteczkowej. Metoda MALDI do laserowej ablacji wykorzystuje laser nadfioletowy (UV, z ang. *ultraviolet*), jednak nie wszystkie badane obiekty biologiczne wystarczająco skutecznie absorbują promieniowanie UV. W takich przypadkach, niezbędny jest dodatek stosunkowo dużych ilości matryc. Prowadzi to do wytwarzania licznych sygnałów tła chemicznego poniżej wartości *m/z* 1000, co znacznie ogranicza zdolność wykrywania metabolitów komórkowych [13]. Ponadto, kwasowe matryce generują wiele jonów podczas procesu desorpcji/jonizacji co znacznie komplikuje widmo masowe, utrudnia kalibrację w zakresie niskich mas i powoduje tłumienie sygnałów pochodzących od analitów. Co więcej, mogą powodować hydrolizę różnych biomolekuł. MALDI charakteryzuje się również niską wydajnością jonizacji dla niepolarnych związków oraz występowaniem efektu „sweet spot" [14–16].

Innym podejściem jest LDI z wykorzystaniem obrazowania spektrometrią mas (MSI, z ang. *mass spectrometry imaging*), które pozwala na analizę i wizualizację rozkładu powierzchniowego związków w stosunkowo szerokim zakresie mas cząsteczkowych w złożonych układach z doskonałą specyficznością molekularną. Ciągle rosnące zainteresowanie naukowców metodami MSI wynika głównie z możliwości zdobycia informacji dotyczących lokalizacji związków w badanym obiekcie, co często przyczynia się do poznania funkcji czy właściwości analitów. Jedną z najpopularniejszych metod obrazowania molekularnego wykorzystującą laserową ablację jest obrazowanie spektrometrią mas z laserową desorpcją/jonizacją wspomaganą matrycą (MALDI-MSI, z ang. *matrix-assisted laser desorption/ionization mass spectrometry imaging*) [17,18]. Tylko do końca lutego 2023 roku w bazie danych Scopus zarejestrowano 27 503 prac naukowych dotyczących MALDI-MS oraz 1311 – MALDI-MSI. Opublikowane wyniki badań potwierdzają użyteczność MALDI-MSI m.in. do wizualizacji i analizy powierzchniowego rozkładu białek [19–21] czy lipidów [22–25] w materiale biologicznym.

Liczne publikacje naukowe wskazują na prowadzenie eksperymentów obrazowania spektrometrią mas prawie wyłącznie w trybie niecelowanym [26–28]. W przypadku materiału biologicznego charakteryzującego się wysoką złożonością, czułość dla wielu analitów jest niska ze względu na tło chemiczne. Z kolei za niską selektywność odpowiadają związki izobaryczne często obecne w próbce, których identyfikacja wyłącznie na podstawie masy dokładnej monoizotopowej obarczona jest wysoką niepewnością. W związku z tym, ilość i jakość informacji uzyskanych z niecelowanego MSI materiałów biologicznych jest częściowo

ograniczona. Powyższe problemy skutecznie rozwiązuje tandemowa spektrometria mas (MS/MS, z ang. *tandem mass spectrometry*), gdzie zwiększona selektywność dla docelowego analitu wynika z monitorowania fragmentacji unikalnych jonów w trybie monitorowania wybranych reakcji (SRM, z ang. *selected reaction monitoring*) lub monitorowania wielu reakcji (MRM, z ang. *muliple reaction monitoring*). Dzięki temu, że tło chemiczne jest redukowane, wzrasta czułość pomiaru, co pozwala na znacznie pewniejszą identyfikację związków o niskiej masie cząsteczkowej. W 2012 roku zespół Elizabeth J. Clemis zastosował celowaną metodę obrazowania spektrometrią mas – MALDI do lokalizacji i ilościowego oznaczenia białek w tkankach. Eksperyment obejmował optymalizację trawienia trypsyną in situ, napylanie roztworu znakowanego izotopowo peptydu i napylanie roztworu matrycy. Pomiar wykonano w trybie monitorowania wielu reakcji, a analizę przeprowadzono na podstawie stosunku intensywności przejść MRM dla endogennych nieznakowanych peptydów proteolitycznych do odpowiednich przejść z zastosowanych peptydów znakowanych izotopowo [29]. Pomimo iż uzyskano zadowalające wyniki, opracowana metoda jest skomplikowana, wieloetapowa oraz wymaga stosowania kosztownych znaczników izotopowych.

Inną rodziną metod, wykorzystującą laserową ablację, w której nanomateriały zastąpiły powszechnie stosowane w MALDI matryce organiczne, jest laserowa desorpcja/jonizacja wspomagana powierzchnią (SALDI, z ang. *surface-assisted laser desorption ionization*) [30]. Według definicji IUPAC, SALDI to grupa metod bezmatrycowych stosowanych do analizy cząsteczek pochodzenia biologicznego za pomocą MS [17,31]. Wielu naukowców wciąż próbuje wyjaśnić mechanizm SALDI [32–34], jednak nie jest to łatwe. Przyczynia się do tego duża ilość czynników wpływających na wydajność analityczną procesów SALDI oraz brak określonego jednoznacznego wpływu każdego z nich [33]. Badania wykazują, że za poprawę sygnału pochodzącego od analitu na widmie masowym może odpowiadać: (1) gwałtowny wzrost temperatury wywołany laserem; (2) morfologia powierzchni (kształt, rozmiar, porowatość); (3) zdolność do wychwytywania cząsteczek rozpuszczalnika; (4) obecność grup funkcyjnych na powierzchni; (5) powierzchnia przewodząca prąd elektryczny; (6) desorpcja akustyczna indukowana laserem, (7) desorpcja pola indukowana laserowo, (8) topienie/restrukturyzacja powierzchni indukowana laserem [34]. Jedynym punktem, w którym społeczność naukowa dochodzi do pewnego rodzaju porozumienia, jest to, że nanostruktury odgrywają główną rolę w mechanizmach desorpcji/jonizacji, pochłaniając energię lasera, umożliwiając gwałtowny wzrost temperatury powierzchni, oraz że zarówno procesy termiczne jak i nietermiczne mogą być zaangażowane w ogólny proces SALDI-MS [32].

Lasery stosowane do ablacji tkanek najczęściej wykorzystują promieniowanie UV lub podczerwone (IR, z ang. *infrared*). Lasery średniej podczerwieni o długości fali około 2,94 µm są skuteczne w ablacji tkanek ze względu na nakładanie się długości fali lasera z absorpcją drgań rozciągających O-H cząsteczek wody, obecnej w każdym uwodnionym materiale biologicznym [35]. Wśród modeli opisujących laserową ablację wymienia się głównie model termiczny, gdzie laserowe nagrzewanie wody w tkance prowadzi do gwałtownej zmiany fazy objętościowej i ablacji naświetlanego obszaru, co skutkuje usunięciem rozerwanej tkanki [36]. Z kolei, Song i Cheng w swojej pracy opisują ablację laserową jako nietermiczny proces, w którym plazma generowana jest z powierzchni materiału za pomocą promieniowania laserowego. W opisywanym modelu ablacja laserowa towarzyszy topnieniu, dysocjacji, odparowaniu, usuwaniu i jonizacji materiału za pomocą fali uderzeniowej. Plazma indukowana laserem zawiera m.in.: elektrony, cząsteczki obojętne czy jony [33]. Liczne publikacje prezentują badania, które nie wykazały żadnej znaczącej fragmentacji biocząsteczek za pomocą lasera [37–40]. Głębokość penetracji tkanek za pomocą laserów o różnych długościach fal przedstawia poniższy rysunek 1.

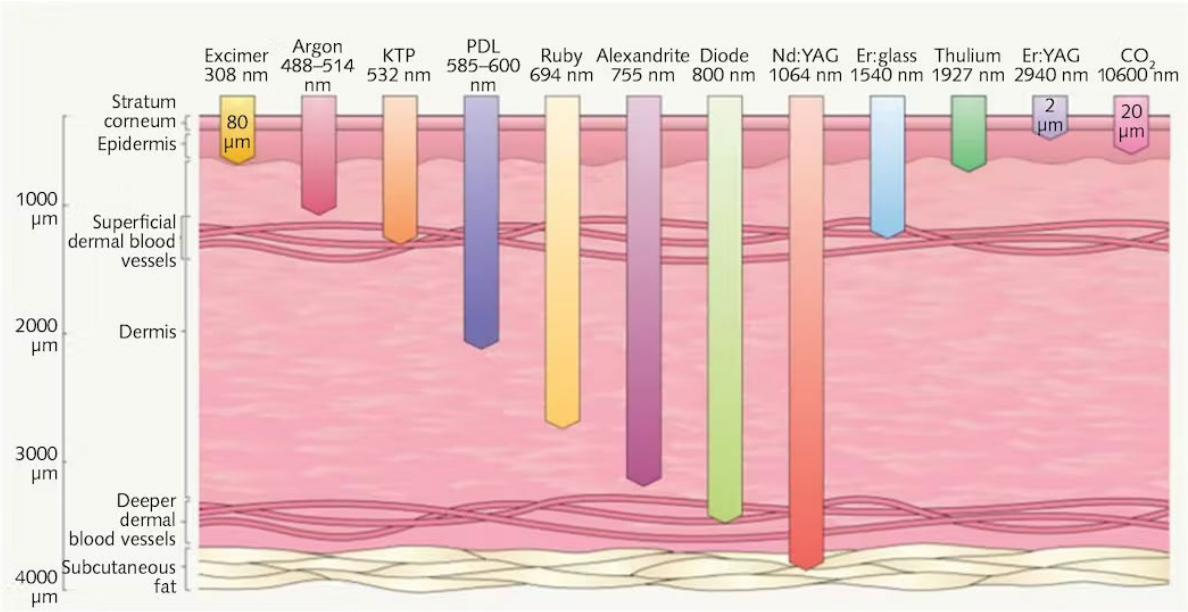

Rysunek 1. Głębokość penetracji tkanek przy różnych długościach fal lasera [41].

W przeciwieństwie do MALDI-MS, metody odpowiedniej do analizy dużych cząsteczek, takich jak białka czy peptydy, SALDI, dzięki zastosowaniu nanostruktur pełniących rolę powszechnie stosowanych matryc organicznych do procesu LDI, pozwala na analizę związków małocząsteczkowych poprzez znaczne ograniczenie występujących interferencji w niskim zakresie *m/z*. Z tego względu, wiele metod z rodziny SALDI-MS jest chętnie wykorzystywanych w metabolomice i lipidomice [17,42–45]. Nanostruktury wspomagające

powierzchnię muszą spełniać te same wymagania co matryce organiczne, tj. muszą przede wszystkim wykazywać zdolność do pochłaniania energii promieniowania laserowego, umożliwiać desorpcję i jonizację analitów. Do analizy MSI materiału pochodzenia roślinnego i zwierzęcego wykorzystywane są różnego rodzaju nanostruktury, których przykłady zestawiono w tabeli 1.

Tabela 1. Zestawienie przykładowych technik SALDI-MSI wraz z rodzajem modyfikacji powierzchni.

Skrót nazwy metody	Pełna nazwa metody	Rodzaj modyfikacji powierzchni	Ref.
AgLDI	Silver-assisted LDI	Napylone Ag	[46]
DIOS	Desorption/ionization on silicon	Porowaty krzem	[47]
GALDI	Graphite-assisted LDI	Tlenek grafenu	[48]
LDI	Laser desorption/ionization	^{109}AgNPET, AuNPET	[49,50]
NALDI	Nanostructure-assisted LDI	Au	[51]
Nano-PALDI	Nano-Particle-assisted LDI	TiO_2	[52]
NIMS	Nanostructure-initiator MS	fluorowane-AuNPs	[53]

W literaturze opisano dwa główne podejścia do syntezy nanostruktur: podejście top-down, w którym większa struktura jest rozbijana do postaci nanocząstek (NPs, z ang. *nanoparticles*) oraz podejście bottom-up, w którym nanomateriał jest syntetyzowany z poziomu molekularnego lub atomowego [54,55]. Redukcja chemiczna jest klasyfikowana jako podejście oddolne i jest jedną z najczęściej stosowanych strategii syntezy nanocząstek w eksperymencie MS [56–58]. Jednak pojawiają się problemy z czystością chemiczną uzyskanych NPs wynikające ze stosowania substancji do reakcji chemicznych, takich jak jako prekursory metali, reduktory czy stabilizatory, które są źródłem jonów związanych z odczynnikami, dającymi liczne sygnały na widmach masowych.

Wymienione problemy rozwiązuje zastosowanie jednej z fizycznych metod wytwarzania nanocząstek, czyli syntezy ablacji laserowej w roztworze (LASiS, z ang. laser *ablation synthesis in solution*). LASiS wykorzystuje impulsowe promieniowanie laserowe do ablacji obiektu stałego zanurzonego w cieczy, wyrzucając nanocząsteczki z chmury plazmy do otaczającej cieczy. Metoda ta pozwala na produkcję nanocząstek bez konieczności stosowania stabilizatorów i środków redukujących, dzięki czemu uzyskana zawiesina NPs charakteryzuje się wysoką czystością chemiczną. Nanocząstki srebra monoizotopowego i złota wytworzono za pomocą światłowodowego lasera impulsowego z dwuwymiarowym skanerem

galwanometrycznym (PFL 2D-GS, z ang. *pulsed fiber laser 2D-galvo-scanner)*. Przedstawiono również ich charakterystykę wraz z wynikami prezentującymi użyteczność w laserowej spektrometrii mas do analizy jakościowej i ilościowej dla różnych związków chemicznych. Nanocząstki ^{109}Ag i Au wykorzystano do pomiarów LDI MS materiału biologicznego w celu analizy metabolomicznej nowotworu pęcherza moczowego.

5.2. Ablacja laserowa materiału biologicznego – metoda LARESI MSI

Obrazowanie spektrometrią mas dostarcza cennych informacji dotyczących rozkładu powierzchniowego związków na badanej powierzchni. Standardowa procedura MSI obejmuje kilka etapów: przygotowanie próbki, pomiar oraz analizę wyników w formie obrazów jonowych i/lub uśrednionych widm MS lub MS/MS z wybranych obszarów. W ostatnim etapie generowane są obrazy jonowe, przedstawiające rozkład związku na badanej powierzchni.

Najbardziej złożonym i czasochłonnym, natomiast kluczowym etapem w MSI jest przygotowanie próbki. Obejmuje ono m.in. pobranie materiału do badań, przechowywanie, cięcie czy umieszczenie na płytce [59]. Próbki pochodzenia naturalnego najczęściej badane metodą MSI obejmują tkanki roślinne, zwierzęce lub ludzkie, jak również kultury komórkowe. Niezależnie od tego w jaki sposób materiał biologiczny został pobrany, w momencie oddzielenia od żywego organizmu rozpoczynają się w próbce procesy biologiczne, wpływające na skład chemiczny. Z tego powodu, konieczna jest konserwacja materiału biologicznego w celu zachowania jego integralności. W przypadku tkanek wymienia się trzy powszechnie stosowane metody konserwacji: (a) zamrażanie świeżego materiału, (b) zamrażanie materiału utrwalonego w formalinie, (c) utrwalanie próbki w formalinie i zatapianie w parafinie (FFPE, z ang. *formalin-fixed paraffin-embedded*) [60]. Fragmenty tkanek przygotowane i zakonserwowane zgodnie z protokołami FFPE są powszechnie stosowane w histologii i patologii ze względu na wysoką jakość zachowania integralności morfologicznej i niemal nieograniczoną możliwość przechowywania w warunkach otoczenia. Niestety, każdy rodzaj chemicznego utrwalania tkanek może prowadzić do modyfikacji związków, co w przypadku obrazowania molekularnego jest niedopuszczalne. Z kolei procedury przemywania obiektów stosowane w celu usunięcia parafiny, powodują delokalizację związków, przez co tracona jest większość metabolitów małocząsteczkowych o wysokiej lipofilowości [60–62].

W przypadku analizy związków małocząsteczkowych za pomocą MSI, do badań preferowane są tkanki zamrożone bezpośrednio po pobraniu. Tkanki najlepiej zamrażać w stanie swobodnym, aby zapobiec ich deformacji i przybieraniu kształtu pojemnika, a tym samym stwarzaniu komplikacji podczas cięcia na skrawki w późniejszym czasie [62].

Kolejnym aspektem jest grubość tkanki wykorzystywanej do badań. Najczęściej stosuje się wycinki o grubości 5-20 µm uzyskane z wykorzystaniem kriotomów [63–65]. Jednak niektóre tkanki czy narządy charakteryzują się wysoką kruchością, dlatego niezwykle trudne jest uzyskanie wystarczająco cienkich skrawków. Dodatkowo, łatwiej manipuluje się grubszymi fragmentami, bez ryzyka rozerwania obiektu.

W komercyjnie dostępnych spektrometrach mas desorpcja analitów prowadzona jest w warunkach wysokiej próżni, gdzie badany obiekt ulega wysuszeniu, powodując jego odkształcenie, co z kolei uniemożliwia precyzyjną lokalizację analitów. Co więcej, komora ablacyjna najczęściej znajduje się wewnątrz instrumentu, nie ma więc możliwości obserwacji obiektu podczas pomiaru. Większość aparatów MS nie posiada funkcji zamrażania badanego materiału biologicznego podczas trwania eksperymentu MSI, dlatego w obiekcie mogą zachodzić zmiany mające wpływ na skład chemiczny.

Szereg ograniczeń rozwiązano wykorzystując metodę spektrometrii mas z laserową ablacją oraz jonizacją w elektrospreju przedstawioną w **publikacji I**. Schemat wykorzystanego zestawu badawczego pokazano na Fig. 1 w dołączonej kopii publikacji I. Do komory ablacyjnej umiejscowionej poza spektrometrem mas, doprowadzono gazowy azot z niewielkim nadciśnieniem, aby wytworzyć jego przepływ w kierunku źródła jonów. Próbkę umieszczono na zestawie zmotoryzowanych stolików w geometrii poziomej ustalonej jako osie X i Y z chłodzeniem modułem Peltiera utrzymującym temperaturę -18°C. Nadmiar ciepła generowanego przez ogniwo Peltiera usuwano za pomocą zewnętrznego radiatora. Stosując moduł chłodzący rozwiązano problem degradacji metabolitów w tkance zachodzący w temperaturze pokojowej, a także migracji związków powierzchniowych. Ablację laserowa prowadzono za pomocą lasera impulsowego o długości fali 2,94 µm. Dobór odpowiedniej długości fali lasera jest bardzo istotny, ze względu na bardzo małą głębokość penetracji takiego materiału czy stopień degradacji termicznej. Podczas obrazowania ognisko lasera pozostawało nieruchome w przestrzeni, podczas gdy próbkę przesuwano przez sterowany komputerowo stolik XY. W osi pionowej zamontowano sferyczną soczewkę CaF_2 pozwalającą na zogniskowanie promieniowania lasera na powierzchni próbki. Rurkę PTFE umieszczono nad miejscem ablacji laserowej. Nadciśnienie w komorze powodując przepływ azotu przez rurkę, umożliwiło transport materiału usuniętego z powierzchni badanego materiału do źródła jonów z elektrosprejem (ESI, z ang. *electrospray ionization*) spektrometru masowego SCIEX QTRAP 5500.

W eksperymencie LARESI SRM MSI wykorzystano skrawki tkanki nerki o grubości 100 µm wycięte za pomocą kriotomu. Celem tego badania było porównanie intensywności sygnałów metabolitów w tkance nowotworowej i prawidłowej. Pomiar LARESI-MSI

przeprowadzono w trybie SRM lub MRM wybierając szesnaście związków opisanych w literaturze jako różnicujące obszar nowotworowy i nienowotworowy w tkankach ludzkich. Docelowe metabolity to aminokwasy, nukleozydy, zasady nukleotydowe, mleczan i witamina E.

Badania literaturowe dotyczące zawartości aminokwasów u pacjentów z wieloma różnymi rodzajami nowotworów wykazały zmiany stężeń tych związków w osoczu krwi, moczu jak i w tkankach. Wyniki uzyskane z obrazowania LARESI tkanki nerkowej objętej przez rak nerkowokomórkowy (RCC, z ang. *renal cel carcinoma*) ujawniły podobne zależności. Dla celów porównawczych wygenerowano obrazy jonowe uzyskane za pomocą obrazowania spektrometrią mas z laserową desorpcją/jonizacją z wykorzystaniem lasera o długości fali 355 nm i płytki stalowej modyfikowanej nanocząstkami srebra monoizotopowego 109 (^{109}AgNPET, z ang. *^{109}Ag-nanoparticle-enhanced target*). Obie metody przedstawione w **publikacji I** dały podobne wyniki, co potwierdza przydatność LARESI SRM/MRM MSI zarówno do badania, jak i odkrywania biomarkerów nowotworowych w tkance ludzkiej. Dodatkowo, metoda LARESI umożliwia bezpośrednią analizę próbek o różnej wielkości, kształcie i formie fizycznej oraz nie wymaga stosowania matryc. Brak konieczności odwadniania czy derywatyzacji przed analizą pozwala zachować anatomiczną integralność próbki, zmniejszając ryzyko delokalizacji analitów i zanieczyszczenia chemicznego próbek. Laserowa ablacja prowadzona w warunkach ciśnienia atmosferycznego eliminuje problem deformacji obiektu pojawiający się w przypadku działania wysokiej próżni w instrumentach MS. Zastosowane moduły chłodzące zapobiegają parowaniu wody z obiektów, co dodatkowo zabezpiecza je przed utratą integralności. Kolejną zaletą LARESI MSI jest proces jonizacji analitów z dominującym protonowaniem. Uzyskane w ten sposób wyniki są kompatybilne z powszechnie dostępnymi bazami danych wykorzystywanymi w analizie metabolomicznej. Możliwość wykonania pomiaru w trybie fragmentacyjnym zwiększa zarówno czułość jak i selektywność.

5.3. Obrazowanie tkanki nowotworowej pęcherza moczowego z wykorzystaniem nanocząstek srebra-109

Innym podejściem w porównaniu do obrazowania wycinków tkanek jest wykonanie ich odcisków na docelowych oczyszczonych powierzchniach, a następnie przeprowadzenie eksperymentu MSI. Taka metoda pozwala na analizę związków powierzchniowych badanego obiektu, bez ingerencji w jego strukturę. Dodatkowo taki materiał może być wykorzystany ponownie do dalszych analiz wymagających homogenizacji czy ekstrakcji. Wyniki

obrazowania odcisków ludzkich tkanek nowotworowych pęcherza moczowego przedstawiono w **publikacji IX**.

Obiektem badań były wycinki tkanek pęcherza moczowego pobrane w trakcie operacji od sześciu pacjentów. Materiał kontrolny stanowiły niewielkie fragmenty stanowiące minimalny margines tkanki zdrowej wokół nowotworu. Analiza histopatologiczna wyciętych nowotworów u wszystkich pacjentów potwierdziła nieinwazyjny urotelialny rak brodawkowaty o niskim stopniu złośliwości. Tkanki kontrolne nie zwierały komórek nowotworowych.

Odciski wszystkich wycinków wykonano na stalowej płytce modyfikowanej nanocząstkami srebra monoizotopowego, przygotowanej według określonej procedury [66]. Dodatkowo na każdy odcisk napylono zawiesinę nanocząstek ^{109}Ag, wytworzoną za pomocą metody chemicznej polegającej na redukcji trifluorooctanu srebra-109 (^{109}AgTFA) z kwasem 2,5-dihydroksybenzoesowym (DHB). Tak przygotowane obiekty umieszczono w spektrometrze masowym, gdzie wykonano eksperyment obrazowania MS.

Analizę wyników przeprowadzono porównując średnie widmo masowe uzyskane z obszaru odcisku pochodzącego z tkanki nowotworowej z obszarem tkanki prawidłowej. Zebrane dane pozwoliły na wskazanie 28 jonów, wykazujących największe zróżnicowanie między obszarem prawidłowym a nowotworowym. Obrazy jonowe wygenerowane dla dwóch adduktów prezentowały wyższe średnie intensywności w tkance nowotworowej, natomiast pozostałe 26 adduktów – w tkance prawidłowej. Kolejnym etapem było przeprowadzenie analizy statystycznej wykorzystującej informacje o średniej intensywności sygnałów pochodzących z części prawidłowej i nowotworowej dla wszystkich zidentyfikowanych związków.

Uzyskane wyniki pozwoliły na wytypowanie dziesięciu specyficznych metabolitów o wysokim potencjale diagnostycznym, z wysoką zdolnością do rozróżniania tkanek zdrowych od nowotworowych u pacjentów z rozpoznanym rakiem pęcherza moczowego. Wśród tych związków znalazły się: glicyna, glutamina, hipotauryna, 3-metylobutanal, fosforan etylu, miosmina, PI(22:0/0:0), aminopentanal, *N,N*-dimetyloprolina i metyloguanidyna. Badania literaturowe wymienionych metabolitów wykazały ich powiązanie z rozwojem nowotworów. Spadek lub wzrost stężenia analitu obserwowano u pacjentów chorujących na różnego rodzaju nowotwory prowadząc badania zarówno moczu, surowicy krwi jak i tkanek. Przykładowo, spadek stężenia aminokwasów wskazuje na zwiększone zapotrzebowanie na te związki podczas wzrostu nowotworu, a to z kolei wiąże się ze zwiększoną intensywnością glikolizy, będącej głównym źródłem energii dla komórek nowotworowych. Może się również wiązać z potrzebą zwiększonej syntezy białek w komórkach nowotworowych [67,68]. Costello i Franklin w swojej pracy przeglądowej sugerują, że glikoliza jest konieczna do prawidłowego przebiegu

lipogenezy i cholesterogenezy, które są niezbędne do wzrostu i proliferacji komórek nowotworowych [69]. Wielu autorów publikacji naukowych związanych z tematyką biomarkerów nowotworowych, jako bardzo ważną grupę związków, wykazujących ścisłe powiązanie z licznymi procesami metabolicznymi zachodzącymi w komórkach z ich udziałem wymienia lipidy. Biorą one udział m.in. w sygnalizacji komórkowej, homeostazie, apoptozie, metabolizmie, adhezji i migracji komórek, uczestniczą w transporcie pęcherzykowym, są neuroprzekaźnikami. Mnogość i różnorodność procesów, w których uczestniczą lipidy sprawia, że są ściśle związane z procesem kancerogenezy. Więcej szczegółowych informacji przedstawiono w **publikacji IX.**

Zastosowanie nanocząstek srebra-109 w eksperymencie obrazowania ludzkiej tkanki pęcherza moczowego techniką LDI MSI pozwoliło na detekcję i identyfikację związków na powierzchni obiektu badanego. Wygenerowano kilkadziesiąt obrazów jonowych dla wybranych związków, przedstawiających największe zróżnicowanie intensywności sygnałów pomiędzy obszarem nowotworowym a prawidłowym. Analiza statystyczna pozwoliła na wytypowanie dziesięciu metabolitów, zdolnych do odróżnienia tkanki prawidłowej od nowotworowej, które mogą być potencjalnymi biomarkerami.

5.4. Zastosowanie do badań nanocząstek Au i ^{109}Ag wytwarzanych za pomocą LASIS

W **publikacji II** i **publikacji V**, opisano metodę laserowego wytwarzania i aplikacji chemicznie czystych nanocząstek srebra-109 oraz złota. Opublikowane wyniki przedstawiają zastosowanie impulsowego lasera światłowodowego (PFL, z ang. *pulsed fiber laser*) 1064 nm z głowicą galwoskanera 2D (2D GS, z ang. *2D galvanometer scanner*) do generowania nanocząstek z powierzchni blaszki metalu.

Zastosowanie metod MS w oparciu o srebro monoizotopowe pozwala na uzyskanie sygnałów analitów o około 2-krotnie większej intensywności w porównaniu z naturalnym srebrem. Sygnały oparte na pojedynczym izotopie srebra-109 mają również wyższy stosunek sygnału do szumu (S/N, z ang. *signal/noise*). Nanocząstki ^{109}Ag wykazują znacznie lepszą kompatybilność z analizą złożonych mieszanin, takich jak próbki biologiczne [66]. Inne zalety zastosowania nanocząstek srebra w analizie MS to wysoka powtarzalność, wysoka tolerancja na zanieczyszczenia takie jak sole. Z kolei właściwości przeciwbakteryjne i przeciwgrzybicze Ag zapewniają ochronę badanych materiałów biologicznych. Zaletą AuNPs jest wysoka wydajność jonizacji związków polarnych i wyraźnie mniejsza intensywność sygnałów klastrów złota, ułatwiająca pomiary śladowych ilości związków. Podobnie jak w przypadku nanocząstek srebra-109 [66,70,71], istnieje możliwość wewnętrznej kalibracji widma MS w oparciu o

sygnały pochodzące od klastrów złota. Co więcej, nanocząstki Au tworzą warstwę o znacznie większej stabilności ze względu na mniejszą reaktywność złota w porównaniu ze srebrem. AuNPs nie wykazują reaktywności wobec tlenu [13].

Nanocząstki srebra i złota mogą być wytwarzane za pomocą metod chemicznych, fizycznych lub biologicznych [72,73]. W zależności od wybranej metody wytwarzania NPs, otrzymuje się nanomateriał o różnej wielkości, innym kształcie, ale również o innych właściwościach fizycznych i chemicznych. Nanocząstki uzyskane z wykorzystaniem metod fizycznych charakteryzują się przede wszystkim wysoką czystością, ponieważ nie wymagają stosowania żadnych dodatków chemicznych, takich jak substancje redukujące czy stabilizatory. Najczęściej wybieraną metodą do produkcji nanocząstek srebra wykorzystywanych w spektrometrii mas jest chemiczna redukcja Ag^+ do pierwiastkowego srebra w różnych warunkach. Do przeprowadzenia syntezy chemicznej konieczne jest użycie prekursora – soli lub kompleksu metalu oraz środka redukującego, często również dodawane są stabilizatory takie jak związki powierzchniowo czynne czy polimery [74,75].

Problemy wynikające ze składu nanocząstek wytwarzanych metodą syntezy chemicznej w MS rozwiązano, wykorzystując jedną z metod fizycznych, czyli syntezę laserową ablacją. Ablację powierzchni blaszki ^{109}Ag lub Au zanurzonej w rozpuszczalniku, przeprowadzono za pomocą światłowodowego lasera impulsowego (o długości fali 1064 nm) z głowicą skanera galwanometrycznego. Optymalne warunki wytwarzania nanocząstek w tym: dobór rozpuszczalnika, częstotliwość lasera, moc lasera, prędkość skanowania określono na podstawie szeregu wykonanych eksperymentów LDI MS. Uzyskane nanocząstki ^{109}Ag i Au scharakteryzowano za pomocą spektroskopii UV-Vis oraz dynamicznego rozpraszania światła (DLS, z ang. *dynamic light scattering*). Badania obrazujące wielkość uzyskanych nanocząstek z wykorzystaniem skaningowej mikroskopii elektronowej o wysokiej rozdzielczości (HR SEM, z ang. *high resolution scanning electron microscopy*) zostały wykonane w Centrum Mikroelektroniki i Nanotechnologii znajdującym się na Uniwersytecie Rzeszowskim.

Badanie NPs wykonano m.in. za pomocą spektrofotometrii UV-Vis. Określone długości fal światła wywołując oscylacje elektronów metalicznych, powodują efekt znany jako powierzchniowy rezonans plazmonowy (SPR, z ang. *surface plasmon resonance*), który związany jest z rozmiarem i kształtem nanocząstek oraz ich otoczeniem chemicznym. Dlatego metoda spektroskopii UV-Vis może być pomocna w określaniu wielkości i kształtu nanocząstek [76,77]. Uzyskane wyniki wraz z danymi literaturowymi pozwoliły na określenie kształtu wytworzonych nanocząstek ^{109}Ag za pomocą LASiS jako sferyczne i o średniej wielkości wynoszącej 10 nm [73,76,78]. Badanie z wykorzystaniem DLS według rozkładu cząstek po liczbie wykazało, że w zawiesinie znajduje się najwięcej nanocząstek o średnicy

około 30 nm, z rozrzutem wielkości w zakresie od 20 do 100 nm. Z kolei na obrazach uzyskanych za pomocą HR SEM widoczne są NPs w rozmiarach 25-35 nm.

Na podstawie widma UV-Vis i danych literaturowych kształt otrzymanych AuNPs określono jako sferyczny, a ich średni rozmiar wynosił około 12 nm [79,80]. Z kolei na podstawie rozkładu wielkości cząstek po intensywności uzyskanego za pomocą DLS, wykazano że w zawiesinie AuNPs LGN znajduje się najwięcej nanocząstek o średnicy 60 nm, co potwierdziły obrazy uzyskane za pomocą HR SEM. Najprawdopodobniej przyczyną różnic w wielkościach NPs oznaczonych za pomocą UV-vis i DLS jest użycie innego rozpuszczalnika do wytwarzania nanocząstek do badań DLS niż zoptymalizowany dla LASiS.

W kolejnym etapie, nanocząstki wytworzone za pomocą LASiS wykorzystano jako matrycę w analizie LDI MS. Proces ten wymagał zastosowania odpowiedniej metody aplikacji na powierzchnię zawierającą badany obiekt. Wybraną metodą była nebulizacja. Uzyskaną zawiesinę nanocząstek wprowadzono do strzykawki, którą umieszczono w pompie strzykawkowej, co zapewniło stały przepływ zawiesiny NPs do nebulizera. Jako gaz rozpylający wykorzystano argon, który równomiernie rozpylał ciecz wypływającą z nebulizera.

Do pomiarów LDI MS wykorzystano cztery związki testowe (histydynę, rybozę, tymidynę, poli(glikol propylenowy)) umieszczone na stalowej płytce, na które napylono zawiesinę ^{109}AgNPs z wykorzystaniem zestawu do nebulizacji przedstawionego na Fig. 1 **publikacji II**. W porównaniu z MALDI wyniki uzyskane dla kilku związków małocząsteczkowych z laserowo wytworzonymi nanocząstkami dają mniejsze błędy dopasowania *m/z* (obliczonych i doświadczalnych) wyrażane w ppm.

Zbadano również użyteczność nanocząstek srebra-109 uzyskanych za pomocą PFL 2D GS LASiS do obrazowania MS. Obiektem badań był odcisk palca z wyraźnymi śladami linii papilarnych. Badanie miało na celu identyfikację związków egzogennych i endogennych zawartych na ludzkim palcu. Odciski palców dostarczają bardzo wiele informacji fizycznych jak i chemicznych wykorzystywanych w analizie kryminalistycznej. Pozwalają na identyfikację osób na podstawie wzoru linii papilarnych, geometrii, rozmieszczenia i wielkości porów potowych czy również występujących indywidualnych cech tzw. minucji [13,81,82]. Z kolei informacje chemiczne znalezione w odciskach palców mogą obejmować związki endogenne w tym: lipidy, peptydy, aminokwasy, białka, mocznik, proste związki nieorganiczne czy sole organiczne, jak również związki egzogenne, do których zalicza się m.in: toksyny, trucizny, substancje psychoaktywne, składniki kosmetyków lub przyborów toaletowych [82].

Przygotowanie obiektu badanego do eksperymentu MSI wymagało jedynie dotknięcia palcem powierzchni płytki ze stali nierdzewnej. Na uzyskany odcisk napylono zawiesinę nanocząstek srebra-109 oraz wykonano pomiar LDI MSI. Uzyskane wyniki pozwoliły na

identyfikację 33 związków z różnych grup, takich jak sole nieorganiczne (NaCl, KCl), proste związki organiczne (mocznik, aminokwasy, krótkie kwasy karboksylowe), kwasy tłuszczowe, lipidy i inne. Wszystkie zidentyfikowane substancje uznawane są za związki endogenne.

W **publikacji V** przedstawiono użyteczność wytworzonych laserowo nanocząstek złota do detekcji związków małocząsteczkowych za pomocą LDI MS na przykładzie aminokwasów i poli(glikolu propylenowego). Na oczyszczoną stalową płytkę naniesiono roztwory badanych związków, a następnie napylono na nie zawiesinę AuNPs z wykorzystaniem zestawu do nebulizacji.

Nanocząstki ^{109}Ag i Au wytwarzane za pomocą impulsowego lasera światłowodowego z powodzeniem mogą być wykorzystywane w metodzie MS wspomaganej nanocząstkami laserowej desorpcji/jonizacji (nanoPALDI MS, z ang. *Nanoparticle-Assisted Laser Desorption/Ionization*). Metoda ta, w porównaniu do przygotowania ^{109}AgNPs czy AuNPs na drodze syntezy chemicznej, jest znacznie szybsza, skracając czas ich przygotowania z 24 godzin do kilku minut. Jest to również opłacalne i ekologiczne rozwiązanie, nie wymagające stosowania dodatkowych substancji chemicznych. Co więcej, metalowa blaszka srebra-109 jak również złota, może być wielokrotnie wykorzystywana.

5.5. Zastosowanie laserowo wytworzonych nanocząstek ^{109}Ag do analizy ilościowej wybranych związków metodami LDI MS i LDI MSI

Nanocząstki uzyskiwane za pomocą laserowej syntezy wykorzystano do analizy jakościowej i ilościowej aminokwasów (**publikacja III**), kwasów karboksylowych (**publikacja IV**) i kwasów 3-hydroksykarboksylowych (**publikacja VIII**).

Aminokwasy odgrywają bardzo ważną rolę w funkcjonowaniu organizmu. Są niezbędne do prawidłowego przebiegu wielu procesów życiowych, takich jak budowa białek, enzymów, komórek, synteza hormonów i neuroprzekaźników. Stężenie aminokwasów w organizmie człowieka zmienia się w zależności od spożywanego pokarmu lub stanu zdrowia [83,84]. Zarówno zbyt wysokie, jak i zbyt niskie wartości stężeń aminokwasów w organizmie mogą świadczyć o zaburzeniach metabolicznych lub rozwijających się chorobach. Stąd konieczne jest wykonywanie analiz ilościowych aminokwasów.

Powyższe aspekty przyczyniły się do wykonania oznaczeń ilościowych aminokwasów w materiale biologicznym z wykorzystaniem nanocząstek srebra-109 generowanych laserowo (LGN, z ang. *laser generated nanomaterial)* do LDI MS oraz LDI MSI, co przedstawiono w **publikacji III**. Do badań wybrano cztery związki reprezentujące grupę aminokwasów: alaninę, izoleucynę, lizynę i fenyloalaninę.

Przygotowane roztwory aminokwasów oraz 500-krotnie rozcieńczoną wodą dejonizowaną próbkę surowicy krwi ludzkiej nałożono na stalową płytkę, na którą w kolejnym etapie napylono zawiesinę nanocząstek ^{109}Ag generowanych światłowodowym laserem impulsowym (**publikacja III**). Najpierw wykonano pomiar LDI MS dla każdej plamki, a następnie dla tej samej płytki przeprowadzono eksperyment MSI. Aminokwasy badano w warunkach 1 000 000-krotnej zmiany stężenia w zakresie od 1 mg/ml do 1 ng/ml. Przeprowadzono również analizę regresji uzyskanych danych dotyczących intensywności w funkcji stężenia. Dla wszystkich badanych aminokwasów najlepsze dopasowanie wyników uzyskano z użyciem regresji wielomianowej, gdzie wartość współczynnika korelacji R^2 wynosiła powyżej 0,90. Wyjątek stanowił wynik uzyskany metodą LDI MS dla izoleucyny, gdzie wartość R^2 wynosiła 0,43. Tak duże różnice w intensywności sygnału dla kolejnych stężeń, mające wpływ na wynik korelacji są efektem ręcznego wyboru punktów pomiarowych. Efekt ten występuje powszechnie w ręcznie wykonywanych pomiarach metodą MALDI. Różnice w rozmieszczeniu aminokwasów w obrębie plamki potwierdzają również uzyskane obrazy jonowe z MSI.

Zastosowanie MSI do ilościowego oznaczenia aminokwasów pozwoliło uzyskać znacznie lepszy wynik korelacji R^2 niż za pomocą manualnych pomiarów LDI MS, co wskazuje na przydatność MSI do analizy ilościowej. Porównanie wyników uzyskanych za pomocą obu metod zdecydowanie wskazało przewagę LDI MSI nad ręcznie wykonywanym pomiarem LDI MS. Należy zaznaczyć, że analizę regresji przeprowadzono w bardzo szerokim zakresie stężeń dla wszystkich siedmiu badanych stężeń.

Analiza odtwarzalności *spot-to-spot* (miejsce-do-miejsca) polegała na porównaniu intensywności sygnału analitów w obrębie trzech plamek i *shot-to-shot* (strzał-do-strzału) – w obrębie jednej plamki. Analizę przeprowadzono dla trzech aminokwasów: izoleucyny, lizyny i fenyloalaniny. Wyniki analizy *shot-to-shot* dla wszystkich badanych związków wykazały 15% różnice w intensywności sygnału pochodzącego od analitu. Wyniki analizy typu *spot-to-spot* dla izoleucyny wykazały 4% różnice w intensywności sygnału. Z kolei dla lizyny i fenyloalaniny różnice w intensywnościach wynosiły odpowiednio 15% i 10%.

Kolejnym etapem było wykonanie analizy ilościowej wybranych aminokwasów w rozcieńczonej próbce surowicy krwi ludzkiej. W tym celu wykonano krzywe wzorcowe dla alaniny, izoleucyny, leucyny i fenyloalaniny wykorzystując dane z eksperymentu LDI MSI dla roztworów pojedynczych aminokwasów. Na wykresach przedstawiono zależność intensywności sygnału adduktu aminokwas-srebro-109 w funkcji stężenia.

Opublikowane wyniki prezentują użyteczność ^{109}AgNPs uzyskanych za pomocą metody PFL 2D GS LGN do analizy jakościowej i ilościowej aminokwasów w materiale

biologicznym. Dodatkowo wykazano przewagę analizy LDI MSI nad ręcznym pomiarem LDI MS.

Kolejną grupą związków poddanych analizie ilościowej z wykorzystaniem ^{109}Ag LGN, przedstawioną w **publikacji IV**, były kwasy karboksylowe (kwas azelainowy, kwas 3-metylohipurowy, kwas linolowy, kwas oleinowy, kwas arachidowy i kwas erukowy). Wybrane kwasy karboksylowe uczestniczą w procesach metabolicznych w organizmie człowieka lub mogą przyczyniać się do rozwoju różnych chorób [85–89]. Dla każdego związku wykonano krzywą wzorcową wykorzystując wyniki pomiarów LDI MS i LDI MSI dla przygotowanej serii rozcieńczeń. Dodatkowo analizie poddano również surowicę krwi wzbogaconą badanymi wzorcami kwasów w celu określenia efektu matrycy na oznaczaną ilość związku. Analogicznie jak w przypadku analizy aminokwasów, roztwory kwasów karboksylowych zostały nałożone na stalową płytkę, na którą napylono zawiesinę nanocząstek srebra monoizotopowego generowanych laserowo.

Dla wszystkich kwasów karboksylowych wykonano analizę regresji danych uzyskanych zarówno podczas manualnych pomiarów LDI MS jak i półautomatycznych eksperymentów MSI. Najlepsze dopasowanie wyników uzyskano z wykorzystaniem funkcji wielomianowej, gdzie najniższa wartość współczynnika korelacji R^2 wynosiła 0,96. Należy podkreślić fakt, że analiza prowadzona była w bardzo szerokim zakresie stężeń. Przykładowo zastosowana metoda pozwoliła na detekcję kwasu azaleinowego w warunkach 1 000 000-krotnej zmiany stężenia. Wykonane eksperymenty jednoznacznie wskazują na przydatność MSI do analizy ilościowej kwasów karboksylowych. Metoda obrazowania MS daje możliwość pokrycia całego badanego obiektu siatką punktów pomiarowych, dzięki czemu łatwiejsza staje się analiza próbek niejednorodnie rozmieszczonych w obrębie plamki. Dodatkowo uzyskane wyniki potwierdziły użyteczność nanocząstek ^{109}Ag wytwarzanych laserowo do analizy ilościowej kwasów karboksylowych. Wyniki pomiarów LDI MSI wzbogaconej kwasami karboksylowymi surowicy krwi, wyraźnie pokazują, że matryca biologiczna ma umiarkowany wpływ na wartość intensywności sygnałów od nich pochodzących.

Kolejną badaną grupą związków były kwasy 3-hydroksykarboksylowe, będące jednym z głównych składników lipidu A, budującego lipidową częścią endotoksyn odpowiedzialnych za toksyczność bakterii Gram-ujemnych. W literaturze odnotowano również, że lipid A bierze udział w odpowiedzi układu odpornościowego podczas zakażenia bakteriami Gram-ujemnymi [90,91]. Z tego względu, detekcja i analiza ilościowa kwasów 3-hydroksykarboksylowych może być wykorzystywana do określenia poziomu endotoksyn w różnych próbkach [92]. Wymienione aspekty przyczyniły się do zbadania możliwości detekcji

kwasów 3-hydroksykarboksylowych z wykorzystaniem nanocząstek srebra-109 generowanych laserowo za pomocą LDI MS.

Uzyskane wyniki przedstawiono w **publikacji VIII**. Po raz pierwszy zaprezentowano zastosowanie metody laserowej spektrometrii mas oraz nanocząstek do detekcji kwasów 3-hydroksykarboksylowych. Związki badano w warunkach 1 000 000-krotnej zmiany stężenia w zakresie od 1 mg/ml do 1 ng/ml. Co więcej, uzyskane wyniki wykazały użyteczność ^{109}AgNPs do oznaczania ilościowego kwasów 3-hydroksykarboksylowych za pomocą MS w bardzo szerokim zakresie stężeń, nawet do 1 ng/mL (dla kwasu 3-hydroksydodekanowego). W porównaniu do LDI MS w większości przypadków wyniki uzyskane za pomocą MSI charakteryzowały się lepszym dopasowaniem do linii trendu i dawały wartość R^2 równą 0,98 dla większości analizowanych kwasów. Dodatkowo wykonano pomiary MSI surowicy krwi wzbogaconej badanym kwasem 3-hydroksykarboksylowym w celu określenia wpływu matrycy biologicznej. Wyniki wykazały znaczny wpływ matrycy na detekcję oraz oznaczaną ilość kwasu 3-hydroksydodekanowego, 3-hydroksyheksadekanowego i 3hydroksyoktadekanowego.

5.6. Profilowanie metabolomiczne surowicy krwi w raku pęcherza moczowego za pomocą LDI MS oraz UHPLC-ESI-UHRMS+MS/MS

Po wykonaniu licznych eksperymentów potwierdzających zastosowanie wytwarzanych laserowo nanocząstek, zostały one wykorzystane w pomiarach LDI MS materiału biologicznego. Badania miały na celu identyfikację metabolitów występujących w surowicy krwi osób chorujących na nowotwór pęcherza moczowego. Uzyskane wyniki przedstawiono w **publikacji VII.**

Do analizy niecelowanej próbki surowicy krwi pobrane od pacjentów chorujących na nowotwór pęcherza moczowego jaki również od osób zdrowych (próbki kontrolne) rozcieńczono 500-krotnie metanolem. Następnie zostały naniesione na stalowe płytki, na które napylono odpowiednio nanocząstki srebra monoizotopowego lub złota. Łącznie zarejestrowano czterysta widm LDI MS z wykorzystaniem nanocząstek ^{109}Ag i Au wytwarzanych za pomocą PFL 2D GS LASiS.

Ponadto z wykorzystaniem LDI MS zaobserwowano 22 związki lipidowe wykazujące zdolność różnicowania próbek nowotworowych i kontrolnych. Dodatkowo badania pozwoliły na wytypowanie metabolitów pozwalających na rozróżnianie stadiów chorobowych.

Profilowanie metabolomiczne ekstraktów surowicy krwi, pochodzących od tych samych pacjentów, których próbki wykorzystano do badań LDI MS, NMR, ICP-OES wykonano na podstawie wyników uzyskanych z pomiarów niecelowanych, techniką ultra-

wysokosprawnej chromatografii cieczowej połączonej z ultra-wysokorozdzielczą spektrometrią mas z jonizacją elektrosprejem (UHPLC-ESI-UHRMS, z ang. *ultra-high-resolution liquid chromatography – electrospray ionization – ultra-high-resolution mass spectrometry*). W **publikacji VI** przedstawiono wyniki przeprowadzonych analiz statystycznych, które pozwoliły na wytypowanie związków różnicujących pacjentów z nowotworem pęcherza moczowego od osób zdrowych, jak również związków odróżniających stadia choroby.

Wszystkie uzyskane wyniki sugerują, że pomiar metabolitów w surowicy może zapewnić łatwiejszą i mniej inwazyjną metodologię diagnostyczną do wykrywania raka pęcherza moczowego oraz leczenia chorób.

VII. Podsumowanie i wnioski

Optymalizacja metody LARESI MSI pozwoliło na wyeliminowanie kilku problemów technicznych pojawiających się podczas eksperymentów MSI wykonywanych za pomocą komercyjnych instrumentów. Zastosowanie lasera podczerwonego oraz zewnętrznej komory ablacyjnej umożliwiło wykonanie eksperymentu obrazowania w warunkach ciśnienia atmosferycznego. Z kolei na podstawie badań literaturowych dotyczących nowotworu nerki z powodzeniem przeprowadzono analizę celowaną wycinka tkanki nerki ludzkiej objętej nowotworem, dokonując pomiaru LARESI SRM MSI. Opracowana metoda wykazuje obiecujący potencjał badawczy.

Obrazowanie spektrometrią mas odcisków wycinków tkanek pęcherza moczowego na powierzchni modyfikowanej nanocząstkami srebra-109 pozwoliło na wygenerowanie obrazów jonowych metabolitów znajdujących się na ich powierzchni. Wykazały one zróżnicowanie pomiędzy obszarem tkanki prawidłowej a nowotworowej.

Z kolei opracowanie metody wytwarzania laserowo nanocząstek pozwoliło na otrzymanie chemicznie czystych nanocząstek w prosty i szybki sposób. Co więcej, płytka metalu, która poddawana jest ablacji laserowej może być wykorzystywana wielokrotnie. Brak konieczności stosowania związków metali, związków redukujących czy stabilizatorów dodatkowo pozwolił na obniżenie poziomu tła chemicznego na widmie masowym, zwiększając czułość metod LDI oraz upraszczając jego interpretację. Po raz pierwszy do ablacji nanocząstek z metalowej płytki wykorzystano impulsowy laser światłowodowy z galwanometrem 2-osiowym. Wykonane badania UV-Vis, DLS oraz HR SEM pozwoliły określić rozmiar i kształt wytwarzanych nanocząstek. Użyteczność wytworzonych nanocząstek srebra-109 potwierdzono za pomocą pomiaru wielu związków testowych metodą LDI MS oraz eksperymentów LDI MSI. Z kolei wyniki detekcji aminokwasów i PPG z użyciem nanocząstek złota wytworzonego za pomocą PFL 2D GS LGN potwierdziły możliwość wykorzystania ich do badań za pomocą LDI MS.

Kolejne badania przeprowadzone z użyciem nanocząstek ^{109}Ag generowanych laserowo demonstrują ich użyteczność do analizy jakościowej i ilościowej aminokwasów, kwasów karboksylowych oraz kwasów 3-hydroksykarboksylowych. Wytworzone laserowo nanocząstki złota i srebra monoizotopowego z powodzeniem zastosowano do analizy metabolomicznej surowicy krwi pacjentów nowotworowych i zdrowych. Wyniki pomiarów LDI MS, NMR, ICP-OES i UHPLC-ESI-UHRMS+MS/MS 200 próbek surowic pozwoliły na wytypowanie metabolitów różnicujących pacjentów nowotworowych od zdrowych, a także na rozróżnienie stadiów choroby.

VIII. BIBLIOGRAFIA

[1] M.C. Gower, Applications of laser ablation to microengineering, in: Proceedings of SPIE, SPIE, Santa Fe, NM, USA, 2000: pp. 452–460. https://doi.org/10.1117/12.407367.

[2] C.A. Charitidis, P. Georgiou, M.A. Koklioti, A.-F. Trompeta, V. Markakis, Manufacturing nanomaterials: from research to industry, (2014).

[3] A. Balachandran, Nanoparticle production via laser ablation synthesis in solution method and printed electronic application - A brief review, (2022).

[4] N.G. Semaltianos, Nanoparticles by Laser Ablation, Critical Reviews in Solid State and Materials Sciences. 35 (2010) 105–124. https://doi.org/10.1080/10408431003788233.

[5] P. Balling, J. Schou, Femtosecond-laser ablation dynamics of dielectrics: basics and applications for thin films, Rep. Prog. Phys. 76 (2013) 036502. https://doi.org/10.1088/0034-4885/76/3/036502.

[6] D.M. D'Addona, S. Genna, A. Giordano, C. Leone, D. Matarazzo, L. Nele, Laser Ablation of Primer During the Welding Process of Iron Plate for Shipbuilding Industry, Procedia CIRP. 33 (2015) 464–469. https://doi.org/10.1016/j.procir.2015.06.055.

[7] A. Kaminska, M. Sawczak, K. Komar, Application of the laser ablation for conservation of historical paper documents, Applied Surface Science. (2007).

[8] A.J. López, J. Lamas, J.S. Pozo-Antonio, T. Rivas, A. Ramil, Development of processing strategies for 3D controlled laser ablation: Application to the cleaning of stonework surfaces, Optics and Lasers in Engineering. (2020).

[9] E. Schena, P. Saccomandi, Y. Fong, Laser Ablation for Cancer: Past, Present and Future, (2017).

[10] R.E. Russo, X. Mao, J.J. Gonzalez, V. Zorba, J. Yoo, Laser Ablation in Analytical Chemistry, Anal. Chem. 85 (2013) 6162–6177. https://doi.org/10.1021/ac4005327.

[11] V.A. Azov, L. Mueller, A.A. Makarov, LASER IONIZATION MASS SPECTROMETRY AT 55: QUO VADIS?, Mass Spec Rev. 41 (2022) 100–151. https://doi.org/10.1002/mas.21669.

[12] N. Bergman, D. Shevchenko, J. Bergquist, Approaches for the analysis of low molecular weight compounds with laser desorption/ionization techniques and mass spectrometry, Anal Bioanal Chem. 406 (2014) 49–61. https://doi.org/10.1007/s00216-013-7471-3.

[13] J. Sekuła, J. Nizioł, W. Rode, T. Ruman, Gold nanoparticle-enhanced target (AuNPET) as universal solution for laser desorption/ionization mass spectrometry analysis and imaging of low molecular weight compounds, Analytica Chimica Acta. 875 (2015) 61–72. https://doi.org/10.1016/j.aca.2015.01.046.

[14] S. Berkenkamp, Infrared MALDI Mass Spectrometry of Large Nucleic Acids, Science. 281 (1998) 260–262. https://doi.org/10.1126/science.281.5374.260.

[15] B. Domon, Mass Spectrometry and Protein Analysis, Science. 312 (2006) 212–217. https://doi.org/10.1126/science.1124619.

[16] K. Shrivas, H.-F. Wu, Single drop microextraction as a concentrating probe for rapid screening of low molecular weight drugs from human urine in atmospheric-pressure matrix-assisted laser desorption/ionization mass spectrometry, Rapid Commun. Mass Spectrom. 21 (2007) 3103–3108. https://doi.org/10.1002/rcm.3192.

[17] W.H. Müller, A. Verdin, E. De Pauw, C. Malherbe, G. Eppe, Surface-assisted laser desorption/ionization mass spectrometry imaging: A review, Mass Spectrometry Reviews. 41 (2022) 373–420. https://doi.org/10.1002/mas.21670.

[18] B.A. Dilmetz, Y. Lee, M.R. Condina, M. Briggs, C. Young, C.T. Desire, M. Klingler-Hoffmann, P. Hoffmann, Novel technical developments in mass spectrometry imaging in 2020: A mini review, Analytical Science Advances. 2 (2021) 225–237. https://doi.org/10.1002/ansa.202000176.

[19] Proteomics Clinical Apps - 2016 - Longuesp e - MALDI mass spectrometry imaging A cutting-edge tool for fundamental and.pdf, (n.d.).

[20] D.J. Ryan, J.M. Spraggins, R.M. Caprioli, Protein identification strategies in MALDI imaging mass spectrometry: a brief review, Current Opinion in Chemical Biology. 48 (2019) 64–72. https://doi.org/10.1016/j.cbpa.2018.10.023.

[21] M. Dilillo, R. Ait-Belkacem, C. Esteve, D. Pellegrini, S. Nicolardi, M. Costa, E. Vannini, E.L. de Graaf, M. Caleo, L.A. McDonnell, Ultra-High Mass Resolution MALDI Imaging Mass

Spectrometry of Proteins and Metabolites in a Mouse Model of Glioblastoma, Sci Rep. 7 (2017) 603. https://doi.org/10.1038/s41598-017-00703-w.
[22] V. Denti, A. Mahajneh, G. Capitoli, F. Clerici, I. Piga, L. Pagani, C. Chinello, M.M. Bolognesi, G. Paglia, S. Galimberti, F. Magni, A. Smith, Lipidomic Typing of Colorectal Cancer Tissue Containing Tumour-Infiltrating Lymphocytes by MALDI Mass Spectrometry Imaging, Metabolites. 11 (2021) 599. https://doi.org/10.3390/metabo11090599.
[23] H.J. Jang, K.J. Kwon, C.Y. Shin, G.S. Lee, J.H. Moon, T.G. Lee, S. Yoon, Investigation of Phospholipid Differences in Valproic Acid-Induced Autistic Mouse Model Brain Using Mass Spectrometry Imaging, Metabolites. 13 (2023) 178. https://doi.org/10.3390/metabo13020178.
[24] X. Wang, Y. Chen, Y. Liu, L. Ouyang, R. Yao, Z. Wang, Y. Kang, L. Yan, D. Huai, H. Jiang, Y. Lei, B. Liao, Visualizing the Distribution of Lipids in Peanut Seeds by MALDI Mass Spectrometric Imaging, Foods. 11 (2022) 3888. https://doi.org/10.3390/foods11233888.
[25] K.R. Wiedemann, A. Peter Ventura, S. Gerbig, M. Roderfeld, T. Quack, C.G. Grevelding, E. Roeb, B. Spengler, Changes in the lipid profile of hamster liver after Schistosoma mansoni infection, characterized by mass spectrometry imaging and LC–MS/MS analysis, Anal Bioanal Chem. 414 (2022) 3653–3665. https://doi.org/10.1007/s00216-022-04006-6.
[26] G. Sighinolfi, S. Clark, L. Blanc, D. Cota, B. Rhourri-Frih, Mass spectrometry imaging of mice brain lipid profile changes over time under high fat diet, Sci Rep. 11 (2021) 19664. https://doi.org/10.1038/s41598-021-97201-x.
[27] Y. Zou, W. Tang, B. Li, Mass spectrometry imaging and its potential in food microbiology, International Journal of Food Microbiology. 371 (2022) 109675. https://doi.org/10.1016/j.ijfoodmicro.2022.109675.
[28] B.M. Prentice, N.J. Hart, N. Phillips, R. Haliyur, A. Judd, R. Armandala, J.M. Spraggins, C.L. Lowe, K.L. Boyd, R.W. Stein, C.V. Wright, J.L. Norris, A.C. Powers, M. Brissova, R.M. Caprioli, Imaging mass spectrometry enables molecular profiling of mouse and human pancreatic tissue, Diabetologia. 62 (2019) 1036–1047. https://doi.org/10.1007/s00125-019-4855-8.
[29] E.J. Clemis, D.S. Smith, A.G. Camenzind, R.M. Danell, C.E. Parker, C.H. Borchers, Quantitation of Spatially-Localized Proteins in Tissue Samples using MALDI-MRM Imaging, Anal. Chem. 84 (2012) 3514–3522. https://doi.org/10.1021/ac202875d.
[30] C.-C. Hu, M.-F. Huang, H.-T. Chang, Quantitative surface-assisted laser desorption/ionization–MS approaches for bioanalysis, Bioanalysis. 5 (2013) 633–635. https://doi.org/10.4155/bio.13.4.
[31] K.K. Murray, R.K. Boyd, M.N. Eberlin, G.J. Langley, L. Li, Y. Naito, Definitions of terms relating to mass spectrometry (IUPAC Recommendations 2013), Pure and Applied Chemistry. 85 (2013) 1515–1609. https://doi.org/10.1351/PAC-REC-06-04-06.
[32] W.H. Müller, A. Verdin, E. De Pauw, C. Malherbe, G. Eppe, Surface-assisted laser desorption/ionization mass spectrometry imaging: A review, Mass Spec Rev. (2020) mas.21670. https://doi.org/10.1002/mas.21670.
[33] K. Song, Q. Cheng, Desorption and ionization mechanisms and signal enhancement in surface assisted laser desorption ionization mass spectrometry (SALDI-MS), (n.d.).
[34] R. Arakawa, H. Kawasaki, Functionalized Nanoparticles and Nanostructured Surfaces for Surface-Assisted Laser Desorption/Ionization Mass Spectrometry, 26 (2010).
[35] Vogel i Venugopalan - 2003 - Mechanisms of Pulsed Laser Ablation of Biological .pdf, (n.d.).
[36] A. Vogel, V. Venugopalan, Mechanisms of Pulsed Laser Ablation of Biological Tissues, Chem. Rev. 103 (2003) 577–644. https://doi.org/10.1021/cr010379n.
[37] C. Dong, L.T. Richardson, T. Solouki, K.K. Murray, Infrared Laser Ablation Microsampling with a Reflective Objective, J. Am. Soc. Mass Spectrom. 33 (2022) 463–470. https://doi.org/10.1021/jasms.1c00306.
[38] K. Wang, F. Donnarumma, M.D. Baldone, K.K. Murray, Infrared laser ablation and capture of enzymes with conserved activity, Analytica Chimica Acta. 1027 (2018) 41–46. https://doi.org/10.1016/j.aca.2018.04.058.
[39] K. Wang, F. Donnarumma, S.W. Herke, P.F. Herke, K.K. Murray, Infrared laser ablation sample transfer of tissue DNA for genomic analysis, Anal Bioanal Chem. 409 (2017) 4119–4126. https://doi.org/10.1007/s00216-017-0373-z.
[40] K. Wang, F. Donnarumma, S.W. Herke, C. Dong, P.F. Herke, K.K. Murray, RNA sampling from tissue sections using infrared laser ablation, Analytica Chimica Acta. 1063 (2019) 91–98. https://doi.org/10.1016/j.aca.2019.02.054.

[41] J.D. Slagle Rick, Laser advancements offer pain-free aesthetic treatments, Laser Focus World. (2021). https://www.laserfocusworld.com/lasers-sources/article/14208992/laser-advancements-offer-painfree-aesthetic-treatments (accessed March 7, 2023).
[42] J. Szulc, J. Karbowska-Berent, A. Drążkowska, T. Ruman, I. Beech, J.A. Sunner, B. Gutarowska, Metabolomics and metagenomics analysis of 18th century archaeological silk, International Biodeterioration & Biodegradation. 156 (2021) 105120. https://doi.org/10.1016/j.ibiod.2020.105120.
[43] J. Szulc, T. Ruman, B. Gutarowska, Metabolome profiles of moulds on carton-gypsum board and malt extract agar medium obtained using an AuNPET SALDI-ToF-MS method, International Biodeterioration & Biodegradation. 125 (2017) 13–23. https://doi.org/10.1016/j.ibiod.2017.08.002.
[44] R. Sun, W. Tang, B. Li, Gold-TiO2@gallic acid nanospheres for enhanced surface-assisted laser desorption/ionization mass spectrometry imaging, Applied Materials Today. 26 (2022) 101336. https://doi.org/10.1016/j.apmt.2021.101336.
[45] D. Chen, M. Du, Y. Huang, Y. Xu, Y. Chen, L. Ma, Q. Xie, X. Zhu, Z. Chen, H. Xu, X. Wu, Z. Yin, Plasmonic polydopamine-modified TiO2 nanotube substrates for surface-assisted laser desorption/ionization mass spectrometry imaging, Nano Res. 16 (2023) 3028–3039. https://doi.org/10.1007/s12274-022-4924-z.
[46] G. Baquer, L. Sementé, M. García-Altares, Y.J. Lee, P. Chaurand, X. Correig, P. Ràfols, rMSIcleanup: an open-source tool for matrix-related peak annotation in mass spectrometry imaging and its application to silver-assisted laser desorption/ionization, J Cheminform. 12 (2020) 45. https://doi.org/10.1186/s13321-020-00449-0.
[47] D.A. Rudd, K. Benkendorff, C. Chahal, T. Guinan, O.J.R. Gustafsson, B. Esmaeelian, H. Krysinska, L. Pogson, N.H. Voelcker, C.A. Abbott, Mapping insoluble indole metabolites in the gastrointestinal environment of a murine colorectal cancer model using desorption/ionisation on porous silicon imaging, Sci Rep. 9 (2019) 12342. https://doi.org/10.1038/s41598-019-48533-2.
[48] D. Zhou, S. Guo, M. Zhang, Y. Liu, T. Chen, Z. Li, Mass spectrometry imaging of small molecules in biological tissues using graphene oxide as a matrix, Analytica Chimica Acta. 962 (2017) 52–59. https://doi.org/10.1016/j.aca.2017.01.043.
[49] J. Nizioł, M. Misiorek, T. Ruman, Mass spectrometry imaging of low molecular weight metabolites in strawberry fruit (Fragaria x ananassa Duch.) cv. Primoris with 109Ag nanoparticle enhanced target, Phytochemistry. 159 (2019) 11–19. https://doi.org/10.1016/j.phytochem.2018.11.014.
[50] M. Misiorek, J. Sekuła, T. Ruman, Mass Spectrometry Imaging of low Molecular Weight Compounds in Garlic (*Allium sativum* L.) with Gold Nanoparticle Enhanced Target: Mass spectrometry imaging of Allium sativum L., Phytochem. Anal. 28 (2017) 479–486. https://doi.org/10.1002/pca.2696.
[51] L. Krasny, O. Benada, M. Strnadova, K. Lemr, V. Havlicek, Lateral resolution in NALDI MSI: back to the future, Anal Bioanal Chem. 407 (2015) 2141–2147. https://doi.org/10.1007/s00216-014-8294-6.
[52] L. Morosi, P. Spinelli, M. Zucchetti, F. Pretto, A. Carrà, M. D'Incalci, R. Giavazzi, E. Davoli, Determination of Paclitaxel Distribution in Solid Tumors by Nano-Particle Assisted Laser Desorption Ionization Mass Spectrometry Imaging, PLoS ONE. 8 (2013) e72532. https://doi.org/10.1371/journal.pone.0072532.
[53] A. Palermo, Charting Metabolism Heterogeneity by Nanostructure Imaging Mass Spectrometry: From Biological Systems to Subcellular Functions, J. Am. Soc. Mass Spectrom. 31 (2020) 2392–2400. https://doi.org/10.1021/jasms.0c00204.
[54] R.K. Das, V.L. Pachapur, L. Lonappan, M. Naghdi, R. Pulicharla, S. Maiti, M. Cledon, L.M.A. Dalila, S.J. Sarma, S.K. Brar, Biological synthesis of metallic nanoparticles: plants, animals and microbial aspects, Nanotechnol. Environ. Eng. 2 (2017) 18. https://doi.org/10.1007/s41204-017-0029-4.
[55] S. Bayda, M. Adeel, T. Tuccinardi, M. Cordani, F. Rizzolio, The History of Nanoscience and Nanotechnology: From Chemical–Physical Applications to Nanomedicine, Molecules. 25 (2019) 112. https://doi.org/10.3390/molecules25010112.
[56] L. Xu, Y.-Y. Wang, J. Huang, C.-Y. Chen, Z.-X. Wang, H. Xie, Silver nanoparticles: Synthesis, medical applications and biosafety, Theranostics. 10 (2020) 8996–9031. https://doi.org/10.7150/thno.45413.

[57] J. Sekuła, J. Nizioł, W. Rode, T. Ruman, Gold nanoparticle-enhanced target (AuNPET) as universal solution for laser desorption/ionization mass spectrometry analysis and imaging of low molecular weight compounds, Analytica Chimica Acta. 875 (2015) 61–72. https://doi.org/10.1016/j.aca.2015.01.046.
[58] M. Magro, M. Zaccarin, G. Miotto, L. Da Dalt, D. Baratella, P. Fariselli, G. Gabai, F. Vianello, Analysis of hard protein corona composition on selective iron oxide nanoparticles by MALDI-TOF mass spectrometry: identification and amplification of a hidden mastitis biomarker in milk proteome, Anal Bioanal Chem. 410 (2018) 2949–2959. https://doi.org/10.1007/s00216-018-0976-z.
[59] A.R. Buchberger, K. DeLaney, J. Johnson, L. Li, Mass Spectrometry Imaging: A Review of Emerging Advancements and Future Insights, Anal. Chem. 90 (2018) 240–265. https://doi.org/10.1021/acs.analchem.7b04733.
[60] R. Buchholz, S. Krossa, M.K. Andersen, M. Holtkamp, M. Sperling, U. Karst, M.-B. Tessem, A simple preparation protocol for shipping and storage of tissue sections for laser ablation-inductively coupled plasma-mass spectrometry imaging, Metallomics. 14 (2022) mfac013. https://doi.org/10.1093/mtomcs/mfac013.
[61] K. Ščupáková, B. Balluff, C. Tressler, T. Adelaja, R.M.A. Heeren, K. Glunde, G. Ertaylan, Cellular resolution in clinical MALDI mass spectrometry imaging: the latest advancements and current challenges, Clinical Chemistry and Laboratory Medicine (CCLM). 58 (2020) 914–929. https://doi.org/10.1515/cclm-2019-0858.
[62] R.J.A. Goodwin, Sample preparation for mass spectrometry imaging: Small mistakes can lead to big consequences, Journal of Proteomics. 75 (2012) 4893–4911. https://doi.org/10.1016/j.jprot.2012.04.012.
[63] Y. Dong, B. Li, S. Malitsky, I. Rogachev, A. Aharoni, F. Kaftan, A. Svatoš, P. Franceschi, Sample Preparation for Mass Spectrometry Imaging of Plant Tissues: A Review, Front. Plant Sci. 7 (2016). https://doi.org/10.3389/fpls.2016.00060.
[64] X. Wang, L. Zhang, Y. Xiang, N. Ye, K. Liu, Systematic study of tissue section thickness for MALDI MS profiling and imaging, Analyst. 148 (2023) 888–897. https://doi.org/10.1039/D2AN01739C.
[65] J.G. Swales, G. Hamm, M.R. Clench, R.J.A. Goodwin, Mass spectrometry imaging and its application in pharmaceutical research and development: A concise review, International Journal of Mass Spectrometry. 437 (2019) 99–112. https://doi.org/10.1016/j.ijms.2018.02.007.
[66] J. Nizioł, W. Rode, B. Laskowska, T. Ruman, Novel Monoisotopic ^{109} AgNPET for Laser Desorption/Ionization Mass Spectrometry, Anal. Chem. 85 (2013) 1926–1931. https://doi.org/10.1021/ac303770y.
[67] R.W. Moreadith, A.L. Lehninger, The pathways of glutamate and glutamine oxidation by tumor cell mitochondria. Role of mitochondrial NAD(P)+-dependent malic enzyme., Journal of Biological Chemistry. 259 (1984) 6215–6221. https://doi.org/10.1016/S0021-9258(20)82128-0.
[68] R. Possemato, K.M. Marks, Y.D. Shaul, M.E. Pacold, D. Kim, K. Birsoy, S. Sethumadhavan, H.-K. Woo, H.G. Jang, A.K. Jha, W.W. Chen, F.G. Barrett, N. Stransky, Z.-Y. Tsun, G.S. Cowley, J. Barretina, N.Y. Kalaany, P.P. Hsu, K. Ottina, A.M. Chan, B. Yuan, L.A. Garraway, D.E. Root, M. Mino-Kenudson, E.F. Brachtel, E.M. Driggers, D.M. Sabatini, Functional genomics reveal that the serine synthesis pathway is essential in breast cancer, Nature. 476 (2011) 346–350. https://doi.org/10.1038/nature10350.
[69] L.C. Costello, R.B. Franklin, 'Why do tumour cells glycolyse?': From glycolysis through citrate to lipogenesis, Mol Cell Biochem. 280 (2005) 1–8. https://doi.org/10.1007/s11010-005-8841-8.
[70] J. Sekuła, J. Nizioł, W. Rode, T. Ruman, Silver nanostructures in laser desorption/ionization mass spectrometry and mass spectrometry imaging, Analyst. 140 (2015) 6195–6209. https://doi.org/10.1039/C5AN00943J.
[71] J. Nizioł, T. Ruman, Silver 109 Ag Nanoparticles for Matrix-Less Mass Spectrometry of Nucleosides and Nucleic Bases, IJCEA. (2013) 46–49. https://doi.org/10.7763/IJCEA.2013.V4.259.
[72] R. Herizchi, E. Abbasi, M. Milani, A. Akbarzadeh, Current methods for synthesis of gold nanoparticles, Artificial Cells, Nanomedicine, and Biotechnology. 44 (2016) 596–602. https://doi.org/10.3109/21691401.2014.971807.

[73] L. Xu, Y.-Y. Wang, J. Huang, C.-Y. Chen, Z.-X. Wang, H. Xie, Silver nanoparticles: Synthesis, medical applications and biosafety, Theranostics. 10 (2020) 8996–9031. https://doi.org/10.7150/thno.45413.
[74] Bae, Eun-Joo, Park, Hee-Jin, Park, Junsu, Yoon, Jeyong, Kim, Younghun, Choi, Kyunghee, Effect of Chemical Stabilizers in Silver Nanoparticle Suspensions on Nanotoxicity, Bulletin of the Korean Chemical Society. 32 (2011) 613–619. https://doi.org/10.5012/BKCS.2011.32.2.613.
[75] H. Al-Khateeb, F. Alzoubi, M. Alqadi, M. Mohammed, Stability of Colloidal Silver Nonoparticle Solutions Prepared by Chemical Reduction, Acta Phys. Pol. A. 134 (2018) 217–221. https://doi.org/10.12693/APhysPolA.134.217.
[76] I. De Leersnyder, H. Rijckaert, L. De Gelder, I. Van Driessche, P. Vermeir, High Variability in Silver Particle Characteristics, Silver Concentrations, and Production Batches of Commercially Available Products Indicates the Need for a More Rigorous Approach, Nanomaterials. 10 (2020) 1394. https://doi.org/10.3390/nano10071394.
[77] R. Desai, V. Mankad, SanjeevK. Gupta, PrafullaK. Jha, Size Distribution of Silver Nanoparticles: UV-Visible Spectroscopic Assessment, Nanosci Nanotechnol Lett. 4 (2012) 30–34. https://doi.org/10.1166/nnl.2012.1278.
[78] V. Amendola, S. Polizzi, M. Meneghetti, Free Silver Nanoparticles Synthesized by Laser Ablation in Organic Solvents and Their Easy Functionalization, Langmuir. 23 (2007) 6766–6770. https://doi.org/10.1021/la0637061.
[79] V. Amendola, M. Meneghetti, Size Evaluation of Gold Nanoparticles by UV−vis Spectroscopy, J. Phys. Chem. C. 113 (2009) 4277–4285. https://doi.org/10.1021/jp8082425.
[80] W. Haiss, N.T.K. Thanh, J. Aveyard, D.G. Fernig, Determination of Size and Concentration of Gold Nanoparticles from UV−Vis Spectra, Anal. Chem. 79 (2007) 4215–4221. https://doi.org/10.1021/ac0702084.
[81] S. Francese, R. Bradshaw, L.S. Ferguson, R. Wolstenholme, M.R. Clench, S. Bleay, Beyond the ridge pattern: multi-informative analysis of latent fingermarks by MALDI mass spectrometry, Analyst. 138 (2013) 4215. https://doi.org/10.1039/c3an36896c.
[82] J. Nizio, Surface-Transfer Mass Spectrometry Imaging on a Monoisotopic Silver Nanoparticle Enhanced Target, Anal. Chem. (2013) 7.
[83] M.C. Gueli, G. Taibi, Alzheimer's disease: amino acid levels and brain metabolic status, Neurol Sci. 34 (2013) 1575–1579. https://doi.org/10.1007/s10072-013-1289-9.
[84] E. Socha, M. Koba, P. Kośliński, Amino acid profiling as a method of discovering biomarkers for diagnosis of neurodegenerative diseases, Amino Acids. 51 (2019) 367–371. https://doi.org/10.1007/s00726-019-02705-6.
[85] M. Behbahani, S. Bagheri, F. Omidi, M.M. Amini, An amino-functionalized mesoporous silica (KIT-6) as a sorbent for dispersive and ultrasonication-assisted micro solid phase extraction of hippuric acid and methylhippuric acid, two biomarkers for toluene and xylene exposure, Microchim Acta. 185 (2018) 505. https://doi.org/10.1007/s00604-018-3038-5.
[86] C.-H. Chiu, C.-T. Chen, M.-H. Cheng, L.-H. Pao, C. Wang, G.-H. Wan, Use of urinary hippuric acid and o-/p-/m-methyl hippuric acid to evaluate surgical smoke exposure in operating room healthcare personnel, Ecotoxicology and Environmental Safety. 217 (2021) 112231. https://doi.org/10.1016/j.ecoenv.2021.112231.
[87] M.F. Cury-Boaventura, R. Gorjão, T.M. de Lima, P. Newsholme, R. Curi, Comparative toxicity of oleic and linoleic acid on human lymphocytes, Life Sciences. 78 (2006) 1448–1456. https://doi.org/10.1016/j.lfs.2005.07.038.
[88] F.P. Samson, A.T. Patrick, T.E. Fabunmi, M.F. Yahaya, J. Madu, W. He, S.R. Sripathi, J. Tyndall, H. Raji, D. Jee, D.R. Gutsaeva, W.J. Jahng, Oleic Acid, Cholesterol, and Linoleic Acid as Angiogenesis Initiators, ACS Omega. 5 (2020) 20575–20585. https://doi.org/10.1021/acsomega.0c02850.
[89] M.A. Sieber, J.K.E. Hegel, Azelaic Acid: Properties and Mode of Action, Skin Pharmacol Physiol. 27 (2014) 9–17. https://doi.org/10.1159/000354888.
[90] A. Steimle, I.B. Autenrieth, J.-S. Frick, Structure and function: Lipid A modifications in commensals and pathogens, International Journal of Medical Microbiology. 306 (2016) 290–301. https://doi.org/10.1016/j.ijmm.2016.03.001.
[91] S. Uhlig, M. Negård, K.K. Heldal, A. Straumfors, L. Madsø, B. Bakke, W. Eduard, Profiling of 3-hydroxy fatty acids as environmental markers of endotoxin using liquid chromatography

coupled to tandem mass spectrometry, Journal of Chromatography A. 1434 (2016) 119–126. https://doi.org/10.1016/j.chroma.2016.01.038.
[92] S.J. Reynolds, D.K. Milton, D. Heederik, P.S. Thorne, K.J. Donham, E.A. Croteau, K.M. Kelly, J. Douwes, D. Lewis, M. Whitmer, I. Connaughton, S. Koch, P. Malmberg, B.-M. Larsson, J. Deddens, A. Saraf, L. Larsson, Interlaboratory evaluation of endotoxin analyses in agricultural dusts—comparison of LAL assay and mass spectrometry, J. Environ. Monit. 7 (2005) 1371. https://doi.org/10.1039/b509256f.

IX. Wykaz pozostałych osiągnięć naukowych

Publikacje w recenzji:

1. J. Nizioł, K. Ossoliński, **A. Płaza-Altamer**, A. Kołodziej, A. Ossolińska, T. Ossoliński, A. Nieczaj, T. Ruman*, Untargeted urinary metabolomics for bladder cancer biomarker screening with ultrahigh-resolution mass spectrometry*, Scientific Reports, 2023
2. K. Ossoliński, T. Ruman, V. Copié, B. P. Tripet, A. Kołodziej, **A. Płaza-Altamer**, A. Ossolińska, T. Ossoliński, A. Nieczaj, J. Nizioł, *Urinary metabolic profiling of bladder cancer*, 2023

Materiały pokonferencyjne:

1. J. Nizioł, **A. Płaza-Altamer**, A. Kołodziej, T. Ruman, *Obrazowanie tkanek za pomocą spektrometrii mas z laserową desorpcją/jonizacją*, Nauka i Przemysł metody spektroskopowe w praktyce nowe wyzwania i możliwości, Wydawnictwo UMCS, Lublin, 2022, ISBN 978-83-227-9602-3
2. J. Nizioł, K. Ossoliński, **A. Płaza-Altamer**, A. Kołodziej, A. Nieczaj, T. Ruman, *Analiza metabolomiczna surowicy krwi w poszukiwaniu biomarkerów raka pęcherza moczowego,* Nauka i Przemysł metody spektroskopowe w praktyce nowe wyzwania i możliwości, Wydawnictwo UMCS, Lublin, 2023

Konferencje:

1. Virtual International Students Conference ISC-Adamas 2020. Topic: Education: Creating Future Today. Going Beyond The Pandemic. **Wystąpienie: referat**, temat prezentacji: *Mass spectrometry imaging of biological materials* (05.12.2020r.)

Granty:

1. Wykonawca w projekcie grantowym finansowanym przez NCN pt. „Poszukiwanie oraz charakterystyka biomarkerów raka pęcherza" o nr umowy UMO-2018/31/D/ST4/00109

Szkolenia:

1. „Kompetencje, obowiązki i zadania kierownictwa w laboratorium zgodnie z wymaganiami normy PN-EN ISO/IEC 17025:2018-2 w drodze do akredytacji" – szkolenie online, 25-26.10.2021r.
2. „Kompetencje laboratorium w rozumieniu wymagań normy PN-EN ISO/IEC 17025:2018-02" – szkolenie online PCA, 23-25.11.2021r.
3. „Podstawowe zagadnienia z zakresu Polskich Norm i dokumentów normalizacyjnych" – szkolenie online PKN, 30.06.2022r.

Inne:

1. Udział w organizacji V Nocnego Spotkania z Nauką na Wydziale Chemicznym (18.10.2019r.)
2. Udział w organizacji VI Nocnego Spotkania z Nauką na Wydziale Chemicznym (14.10.2022r.)
3. Wyjazdy do szkół średnich w ramach promocji nowych kierunków studiów na Wydziale Chemicznym

X. Zbiór oświadczeń współautorów publikacji przedkładanych do oceny

al. Powstańców Warszawy 12, 35-959 Rzeszów
tel.: +48 17 865 1100, e-mail: kancelaria@prz.edu.pl
www.prz.edu.pl

Mgr inż. Aneta Płaza-Altamer
Wydział Chemiczny, Politechnika Rzeszowska
Katedra Chemii Nieorganicznej i Analitycznej
al. Powstańców Warszawy 6, 35-959 Rzeszów
e-mail: a.plaza@prz.edu.pl

Rzeszów, 05.04.2023r.

OŚWIADCZENIE

Oświadczam, że w niżej wymienionych pracach mój udział merytoryczny oraz procentowy był następujący:

Lp.	Tytuł publikacji oraz informacje bibliograficzne	Udział merytoryczny	Udział %
1	Joanna Nizioł, Jan Sunner, Iwona Beech, Krzysztof Ossoliński, Anna Ossolińska, Tadeusz Ossoliński, Aneta Płaza, Tomasz Ruman Localization of Metabolites of Human Kidney Tissue with Infrared Laser-Based Selected Reaction Monitoring Mass Spectrometry Imaging and Silver-109 Nanoparticle-Based Surface Assisted Laser Desorption/Ionization Mass Spectrometry Imaging, Analytical Chemistry, 2020, 92, 6, 4251–4258 DOI:10.1021/acs.analchem.9b04580	- przeprowadzenie eksperymentów (LARESI) - analiza wyników	2%
2	Aneta Płaza, Artur Kołodziej, Joanna Nizioł, Tomasz Ruman Laser Ablation Synthesis in Solution and Nebulization of Silver-109 Nanoparticles for Mass Spectrometry and Mass Spectrometry Imaging, ACS Measurement Science Au, 2021, DOI:10.1021/acsmeasuresciau.1c00020	- przeprowadzenie eksperymentów (synteza nanocząstek, badania UV-vis, DLS, obrazowanie MS) - analiza, wizualizacja i opracowanie wyników, - zredagowanie i edycja treści manuskryptu, - odniesienie się do uwag recenzentów i zredagowanie końcowej formy publikacji	25%

al. Powstańców Warszawy 6, 35-959 Rzeszów
tel.: +48 17 865 1652, e-mail: chemia@prz.edu.pl
www.wch.prz.edu.pl

al. Powstańców Warszawy 12, 35-959 Rzeszów
tel.: +48 17 865 1100, e-mail: kancelaria@prz.edu.pl
www.prz.edu.pl

3	Aneta Płaza-Altamer, Artur Kołodziej, Joanna Nizioł, Tomasz Ruman Infrared pulsed fiber laser-produced silver-109-nanoparticles for laser desorption/ionization mass spectrometry of amino acids, Journal of Mass Spectrometry, 2022, 57:e4815, DOI: https://doi.org/10.1002/jms.4815	- przeprowadzenie eksperymentów, - analiza, wizualizacja i opracowanie statystyczne wyników, - zredagowanie i edycja treści manuskryptu, - odniesienie się do uwag recenzentów i zredagowanie końcowej formy publikacji, - pełnienie funkcji autora korespondencyjnego	25%
4	Artur Kołodziej, Aneta Płaza-Altamer, Joanna Nizioł, Tomasz Ruman Infrared pulsed fiber laser-produced silver-109-nanoparticles for laser desorption/ionization mass spectrometry of carboxylic acids, International Journal of Mass Spectrometry, 2022, 474, 116816, DOI: 10.1016/j.ijms.2022.116816	- wytworzenie płytek ^{109}AgLGN do analizy związków, - współtworzenie i edycja manuskryptu	25%
5	Aneta Płaza-Altamer, Artur Kołodziej, Joanna Nizioł, Tomasz Ruman Laser generated gold nanoparticles for mass spectrometry of low molecular weight compounds, Chemical Technology and Biotechnology, 2022, ISSN 2720-6793, DOI: 10.7862/rc.2022.1	- przeprowadzenie eksperymentów (synteza nanocząstek, badania UV-vis, DLS, pomiary LDI MS), - analiza, wizualizacja i opracowanie statystyczne wyników, - zredagowanie i edycja treści manuskryptu, - odniesienie się do uwag recenzentów i zredagowanie końcowej formy publikacji, - pełnienie funkcji autora korespondencyjnego	25%
6	Joanna Nizioł, Krzysztof Ossoliński, Aneta Płaza-Altamer, Artur Kołodziej, Anna Ossolińska, Tadeusz Ossoliński, Tomasz Ruman Untargeted ultra-high-resolution mass spectrometry metabolomic profiling of blood serum in bladder cancer, Scientific Reports, 2022, 12, 1, DOI: 10.1038/s41598-022-19576-9	- przygotowanie próbek do analizy - przeprowadzenie pomiarów UHPLC-ESI-UHRMS+MS/MS	14%
7	Krzysztof Ossoliński, Tomasz Ruman, Valérie Copié, Brian P. Tripet, Leonardo	- przygotowanie próbek do analizy	9%

al. Powstańców Warszawy 6, 35-959 Rzeszów
tel.: +48 17 865 1652, e-mail: chemia@prz.edu.pl
www.wch.prz.edu.pl

	B. Nogueira, Katiane O.P.C. Nogueira, Artur Kołodziej, Aneta Płaza-Altamer, Anna Ossolińska, Tadeusz Ossoliński, Joanna Nizioł Metabolomic and elemental profiling of blood serum in bladder cancer Journal of Pharmaceutical Analysis, 2022, DOI: 10.1016/j.jpha.2022.08.004		
8	Artur Kołodziej, Aneta Płaza-Altamer, Joanna Nizioł, Tomasz Ruman Infrared pulsed fiber laser-produced silver-109-nanoparticles for laser desorption/ionization mass spectrometry of 3-hydroxycarboxylic acids. Rapid Communication in Mass Spectrometry, 2022, 36, 21, DOI: 10.1002/rcm.9375	- wytworzenie płytek ^{109}AgLGN do analizy związków.	25%
9	Krzysztof Ossoliński, Tomasz Ruman, Tadeusz Ossoliński, Anna Ossolińska, Adrian Arendowski, Artur Kołodziej, Aneta Płaza-Altamer, Joanna Nizioł Monoisotopic silver nanoparticles-based mass spectrometry imaging of human bladder cancer tissue: Biomarker discovery Advances in Medical Sciences, 2023, 68(1), 38-45, DOI: 10.1016/j.advms.2022.12.002	- analiza i wizualizacja uzyskanych wyników, - odniesienie się do uwag recenzentów i współopracowanie końcowej formy pracy	14%

Aneta Płaza-Altamer

Podpis

al. Powstańców Warszawy 12, 35-959 Rzeszów
tel.: +48 17 865 1100, e-mail: kancelaria@prz.edu.pl
www.prz.edu.pl

Prof. dr hab. inż. Tomasz Ruman
Wydział Chemiczny, Politechnika Rzeszowska
Katedra Chemii Nieorganicznej i Analitycznej
al. Powstańców Warszawy 6, 35-959 Rzeszów
tel: (17) 743 18 96, e-mail: tomruman@prz.edu.pl

Rzeszów, 05.04.2023r.

OŚWIADCZENIE

Oświadczam, że w niżej wymienionych pracach mój udział merytoryczny oraz procentowy był następujący:

Lp.	Tytuł publikacji oraz informacje bibliograficzne	Udział merytoryczny	Udział %
1	Joanna Nizioł, Jan Sunner, Iwona Beech, Krzysztof Ossoliński, Anna Ossolińska, Tadeusz Ossoliński, Aneta Płaza, Tomasz Ruman Localization of Metabolites of Human Kidney Tissue with Infrared Laser-Based Selected Reaction Monitoring Mass Spectrometry Imaging and Silver-109 Nanoparticle-Based Surface Assisted Laser Desorption/Ionization Mass Spectrometry Imaging, Analytical Chemistry, 2020, 92, 6, 4251–4258 DOI:10.1021/acs.analchem.9b04580	- tworzenie koncepcji badań, - przeprowadzenie eksperymentów LARESI MSI i LDI MSI - korekta treści manuskryptu, - odniesienie się do uwag recenzentów i współopracowanie końcowej formy pracy, - nadzór naukowy nad badaniami, - pozyskanie środków na badania - pełnienie funkcji autora korespondencyjnego	30%
2	Aneta Płaza, Artur Kołodziej, Joanna Nizioł, Tomasz Ruman Laser Ablation Synthesis in Solution and Nebulization of Silver-109 Nanoparticles for Mass Spectrometry and Mass Spectrometry Imaging, ACS Measurement Science Au, 2021, DOI: 10.1021/acsmeasuresciau.1c00020	- wybór metodologii prowadzenia badań, - korekta treści manuskryptu, - odniesienie się do uwag recenzentów i współopracowanie końcowej formy pracy, - nadzór naukowy nad badaniami	25%

al. Powstańców Warszawy 6, 35-959 Rzeszów
tel.: +48 17 865 1652, e-mail: chemia@prz.edu.pl
www.wch.prz.edu.pl

al. Powstańców Warszawy 12, 35-959 Rzeszów
tel.: +48 17 865 1100, e-mail: kancelaria@prz.edu.pl
www.prz.edu.pl

3	Aneta Płaza-Altamer, Artur Kołodziej, Joanna Nizioł, Tomasz Ruman Infrared pulsed fiber laser-produced silver-109-nanoparticles for laser desorption/ionization mass spectrometry of amino acids, Journal of Mass Spectrometry, 2022, 57:e4815, DOI: https://doi.org/10.1002/jms.4815	- wybór metodologii prowadzenia badań , - korekta treści manuskryptu, - odniesienie się do uwag recenzentów i współopracowanie końcowej formy pracy, - nadzór naukowy nad badaniami	25%
4	Artur Kołodziej, Aneta Płaza-Altamer, Joanna Nizioł, Tomasz Ruman Infrared pulsed fiber laser-produced silver-109-nanoparticles for laser desorption/ionization mass spectrometry of carboxylic acids, International Journal of Mass Spectrometry, 2022, 474, 116816, DOI: 10.1016/j.ijms.2022.116816	- wybór metodologii prowadzenia badań, - korekta treści manuskryptu, - odniesienie się do uwag recenzentów i współopracowanie końcowej formy pracy, - nadzór naukowy nad badaniami	25%
5	Aneta Płaza-Altamer, Artur Kołodziej, Joanna Nizioł, Tomasz Ruman Laser generated gold nanoparticles for mass spectrometry of low molecular weight compounds, Chemical Technology and Biotechnology, 2022, ISSN 2720-6793, DOI: 10.7862/rc.2022.1	- wybór metodologii prowadzenia badań, - korekta treści manuskryptu, - odniesienie się do uwag recenzentów i współopracowanie końcowej formy pracy, - nadzór naukowy nad badaniami	25%
6	Joanna Nizioł, Krzysztof Ossoliński, Aneta Płaza-Altamer, Artur Kołodziej, Anna Ossolińska, Tadeusz Ossoliński, Tomasz Ruman Untargeted ultra-high-resolution mass spectrometry metabolomic profiling of blood serum in bladder cancer, Scientific Reports, 2022, 12, 1, DOI: 10.1038/s41598-022-19576-9	- wybór metodologii badań, - analiza uzyskanych danych, - przygotowanie treści manuskryptu, - odniesienie się do uwag recenzentów i współopracowanie końcowej formy pracy, - nadzór naukowy nad badaniami	14%
7	Krzysztof Ossoliński, Tomasz Ruman, Valérie Copié, Brian P. Tripet, Leonardo B. Nogueira, Katiane O.P.C. Nogueira, Artur Kołodziej, Aneta Płaza-Altamer, Anna Ossolińska, Tadeusz Ossoliński,	- wybór metodologii badań, - analiza uzyskanych danych, - przygotowanie treści manuskryptu, - odniesienie się do uwag recenzentów i współopracowanie końcowej formy pracy,	9%

al. Powstańców Warszawy 6, 35-959 Rzeszów
tel.: +48 17 865 1652, e-mail: chemia@prz.edu.pl
www.wch.prz.edu.pl

al. Powstańców Warszawy 12, 35-959 Rzeszów
tel.: +48 17 865 1100, e-mail: kancelaria@prz.edu.pl
www.prz.edu.pl

	Joanna Nizioł Metabolomic and elemental profiling of blood serum in bladder cancer Journal of Pharmaceutical Analysis, 2022, DOI: 10.1016/j.jpha.2022.08.004	- nadzór naukowy nad badaniami	
8	Artur Kołodziej, Aneta Płaza-Altamer, Joanna Nizioł, Tomasz Ruman Infrared pulsed fiber laser-produced silver-109-nanoparticles for laser desorption/ionization mass spectrometry of 3-hydroxycarboxylic acids, Rapid Communication in Mass Spectrometry, 2022, 36, 21, DOI: 10.1002/rcm.9375	- wybór metodologii prowadzenia badań, - korekta treści manuskryptu, - odniesienie się do uwag recenzentów i współopracowanie końcowej formy pracy, - nadzór naukowy nad badaniami	25%
9	Krzysztof Ossoliński, Tomasz Ruman, Tadeusz Ossoliński, Anna Ossolińska, Adrian Arendowski, Artur Kołodziej, Aneta Płaza-Altamer, Joanna Nizioł Monoisotopic silver nanoparticles-based mass spectrometry imaging of human bladder cancer tissue: Biomarker discovery Advances in Medical Sciences, 2023, 68(1), 38-45, DOI: 10.1016/j.advms.2022.12.002	- tworzenie koncepcji badań, - analiza uzyskanych wyników, - korekta treści manuskryptu, - odniesienie się do uwag recenzentów i współopracowanie końcowej formy pracy, - nadzór naukowy nad badaniami	30%

KIEROWNIK
KATEDRY CHEMII
NIEORGANICZNEJ I ANALITYCZNEJ
WYDZIAŁ CHEMICZNY PRz
prof. dr hab. inż. Tomasz Ruman

.....

Podpis

al. Powstańców Warszawy 6, 35-959 Rzeszów
tel.: +48 17 865 1652, e-mail: chemia@prz.edu.pl
www.wch.prz.edu.pl

al. Powstańców Warszawy 12, 35-959 Rzeszów
tel.: +48 17 865 1100, e-mail: kancelaria@prz.edu.pl
www.prz.edu.pl

Dr hab. Joanna Nizioł, prof. PRz
Wydział Chemiczny, Politechnika Rzeszowska
Katedra Chemii Nieorganicznej i Analitycznej
al. Powstańców Warszawy 6, 35-959 Rzeszów
tel: (17) 743 13 10, e-mail: jniziol@prz.edu.pl

Rzeszów, 05.04.2023r.

OŚWIADCZENIE

Oświadczam, że w niżej wymienionych pracach mój udział merytoryczny oraz procentowy był następujący:

Lp.	Tytuł publikacji oraz informacje bibliograficzne	Udział merytoryczny	Udział %
1	Joanna Nizioł, Jan Sunner, Iwona Beech, Krzysztof Ossoliński, Anna Ossolińska, Tadeusz Ossoliński, Aneta Płaza, Tomasz Ruman Localization of Metabolites of Human Kidney Tissue with Infrared Laser-Based Selected Reaction Monitoring Mass Spectrometry Imaging and Silver-109 Nanoparticle-Based Surface Assisted Laser Desorption/Ionization Mass Spectrometry Imaging, Analytical Chemistry, 2020, 92, 6, 4251–4258 DOI:10.1021/acs.analchem.9b04580	- przygotowanie treści manuskryptu, - odniesienie się do uwag recenzentów i współopracowanie końcowej formy pracy, - przeprowadzenie eksperymentów LDI MSI	50%
2	Aneta Płaza, Artur Kołodziej, Joanna Nizioł, Tomasz Ruman Laser Ablation Synthesis in Solution and Nebulization of Silver-109 Nanoparticles for Mass Spectrometry and Mass Spectrometry Imaging, ACS Measurement Science Au, 2021, DOI: 10.1021/acsmeasuresciau.1c00020	- pozyskanie środków na badania	25%
3	Aneta Płaza-Altamer, Artur Kołodziej, Joanna Nizioł, Tomasz Ruman Infrared pulsed fiber laser-produced silver-109-nanoparticles for	- pozyskanie środków na badania	25%

al. Powstańców Warszawy 6, 35-959 Rzeszów
tel.: +48 17 865 1652, e-mail: chemia@prz.edu.pl
www.wch.prz.edu.pl

	laser desorption/ionization mass spectrometry of amino acids, Journal of Mass Spectrometry, 2022, 57:e4815, DOI: https://doi.org/10.1002/jms.4815		
4	Artur Kołodziej, Aneta Płaza-Altamer, Joanna Nizioł, Tomasz Ruman Infrared pulsed fiber laser-produced silver-109-nanoparticles for laser desorption/ionization mass spectrometry of carboxylic acids, International Journal of Mass Spectrometry, 2022, 474, 116816, DOI: 10.1016/j.ijms.2022.116816	- pozyskanie środków na badania	25%
5	Aneta Płaza-Altamer, Artur Kołodziej, Joanna Nizioł, Tomasz Ruman Laser generated gold nanoparticles for mass spectrometry of low molecular weight compounds, Chemical Technology and Biotechnology, 2022, ISSN 2720-6793, DOI: 10.7862/rc.2022.1	- pozyskanie środków na badania	25%
6	Joanna Nizioł, Krzysztof Ossoliński, Aneta Płaza-Altamer, Artur Kołodziej, Anna Ossolińska, Tadeusz Ossoliński, Tomasz Ruman Untargeted ultra-high-resolution mass spectrometry metabolomic profiling of blood serum in bladder cancer, Scientific Reports, 2022, 12, 1, DOI: 10.1038/s41598-022-19576-9	- współtworzenie koncepcji badań, - analiza statystyczna i wizualizacja uzyskanych wyników, - przygotowanie manuskryptu, - odniesienie się do uwag recenzentów i współopracowanie końcowej formy pracy, - pozyskanie środków na badania	14%
7	Krzysztof Ossoliński, Tomasz Ruman, Valérie Copié, Brian P. Tripet, Leonardo B. Nogueira, Katiane O.P.C. Nogueira, Artur Kołodziej, Aneta Płaza-Altamer, Anna Ossolińska, Tadeusz Ossoliński, Joanna Nizioł Metabolomic and elemental profiling of blood serum in bladder cancer Journal of Pharmaceutical Analysis, 2022, DOI: 10.1016/j.jpha.2022.08.004	- współtworzenie koncepcji badań, - analiza statystyczna i wizualizacja uzyskanych wyników, - przygotowanie manuskryptu, - odniesienie się do uwag recenzentów i współopracowanie końcowej formy pracy, - pozyskanie środków na badania	9%
8	Artur Kołodziej, Aneta Płaza-Altamer, Joanna Nizioł, Tomasz Ruman Infrared pulsed fiber	- pozyskanie środków na badania	25%

al. Powstańców Warszawy 12, 35-959 Rzeszów
tel.: +48 17 865 1100, e-mail: kancelaria@prz.edu.pl
www.prz.edu.pl

	laser-produced silver-109-nanoparticles for laser desorption/ionization mass spectrometry of 3-hydroxycarboxylic acids. Rapid Communication in Mass Spectrometry, 2022, 36, 21, DOI: 10.1002/rcm.9375		
9	Krzysztof Ossoliński, Tomasz Ruman, Tadeusz Ossoliński, Anna Ossolińska, Adrian Arendowski, Artur Kołodziej, Aneta Płaza-Altamer, Joanna Nizioł Monoisotopic silver nanoparticles-based mass spectrometry imaging of human bladder cancer tissue: Biomarker discovery Advances in Medical Sciences, 2023, 68(1), 38-45, DOI: 10.1016/j.advms.2022.12.002	- współtworzenie koncepcji badań, - analiza statystyczna i wizualizacja uzyskanych wyników, - przygotowanie manuskryptu, - pozyskanie środków na badania	30%

dr hab. Joanna Nizioł, prof. PRz
Wydział Chemiczny PRz

.....

Podpis

al. Powstańców Warszawy 6, 35-959 Rzeszów
tel.: +48 17 865 1652, e-mail: chemia@prz.edu.pl
www.wch.prz.edu.pl

al. Powstańców Warszawy 12, 35-959 Rzeszów
tel.: +48 17 865 1100, e-mail: kancelaria@prz.edu.pl
www.prz.edu.pl

Mgr inż. Artur Kołodziej
Wydział Chemiczny, Politechnika Rzeszowska
Katedra Chemii Nieorganicznej i Analitycznej
al. Powstańców Warszawy 6, 35-959 Rzeszów
e-mail: a.kolodziej@prz.edu.pl

Rzeszów, 05.04.2023r.

OŚWIADCZENIE

Oświadczam, że w niżej wymienionych pracach mój udział merytoryczny oraz procentowy był następujący:

Lp.	Tytuł publikacji oraz informacje bibliograficzne	Udział merytoryczny	Udział %
2	Aneta Płaza, Artur Kołodziej, Joanna Nizioł, Tomasz Ruman *Laser Ablation Synthesis in Solution and Nebulization of Silver-109 Nanoparticles for Mass Spectrometry and Mass Spectrometry Imaging*, ACS Measurement Science Au, 2021, DOI: 10.1021/acsmeasuresciau.1c00020	- prowadzenie eksperymentów (synteza nanocząstek, obrazowanie SEM, pomiar LDI MS związków testowych), - analiza i wizualizacja uzyskanych wyników, - odniesienie się do uwag recenzentów i współopracowanie końcowej formy pracy	25%
3	Aneta Płaza-Altamer, Artur Kołodziej, Joanna Nizioł, Tomasz Ruman *Infrared pulsed fiber laser-produced silver-109-nanoparticles for laser desorption/ionization mass spectrometry of amino acids*, Journal of Mass Spectrometry, 2022, 57:e4815, DOI: https://doi.org/10.1002/jms.4815	- wytworzenie płytek ^{109}AgLGN do analizy związków, - wykonanie analizy odtwarzalności - współtworzenie i edycja manuskryptu	25%
4	Artur Kołodziej, Aneta Płaza-Altamer, Joanna Nizioł, Tomasz Ruman *Infrared pulsed fiber laser-produced silver-109-nanoparticles for laser desorption/ionization mass spectrometry of carboxylic acids*, International Journal of Mass Spectrometry, 2022, 474, 116816,	- przeprowadzenie eksperymentów, - analiza, wizualizacja i opracowanie statystyczne wyników, - zredagowanie i edycja treści manuskryptu,	25%

al. Powstańców Warszawy 6, 35-959 Rzeszów
tel.: +48 17 865 1652, e-mail: chemia@prz.edu.pl
www.wch.prz.edu.pl

	DOI: 10.1016/j.ijms.2022.116816	- odniesienie się do uwag recenzentów i zredagowanie końcowej formy publikacji, - pełnienie funkcji autora korespondencyjnego	
5	Aneta Płaza-Altamer, Artur Kołodziej, Joanna Nizioł, Tomasz Ruman *Laser generated gold nanoparticles for mass spectrometry of low molecular weight compounds*, Chemical Technology and Biotechnology, 2022, ISSN 2720-6793, DOI: 10.7862/rc.2022.1	- - prowadzenie eksperymentów (synteza nanocząstek, obrazowanie SEM, pomiar LDI MS, MALDI MS związków testowych), - analiza i wizualizacja uzyskanych wyników.	25%
6	Joanna Nizioł, Krzysztof Ossoliński, Aneta Płaza-Altamer, Artur Kołodziej, Anna Ossolińska, Tadeusz Ossoliński, Tomasz Ruman *Untargeted ultra-high-resolution mass spectrometry metabolomic profiling of blood serum in bladder cancer*, Scientific Reports, 2022, 12, 1, DOI: 10.1038/s41598-022-19576-9	- przygotowanie próbek do analizy	14%
7	Krzysztof Ossoliński, Tomasz Ruman, Valérie Copié, Brian P. Tripet, Leonardo B. Nogueira, Katiane O.P.C. Nogueira, Artur Kołodziej, Aneta Płaza-Altamer, Anna Ossolińska, Tadeusz Ossoliński, Joanna Nizioł *Metabolomic and elemental profiling of blood serum in bladder cancer* Journal of Pharmaceutical Analysis, 2022, DOI: 10.1016/j.jpha.2022.08.004	- przeprowadzenie eksperymentów (analiza próbek z wykorzystaniem spektrometru mas typu MALDI), - analiza danych uzyskanych po eksperymentach	9%
8	Artur Kołodziej, Aneta Płaza-Altamer, Joanna Nizioł, Tomasz Ruman *Infrared pulsed fiber laser-produced silver-109-nanoparticles for laser desorption/ionization mass spectrometry of 3-hydroxycarboxylic acids*, Rapid Communication in Mass Spectrometry, 2022, 36, 21, DOI: 10.1002/rcm.9375	- przeprowadzenie eksperymentów, - analiza, wizualizacja i opracowanie statystyczne wyników, - zredagowanie i edycja treści manuskryptu, - odniesienie się do uwag recenzentów i zredagowanie końcowej formy publikacji, - pełnienie funkcji autora korespondencyjnego	25%

al. Powstańców Warszawy 12, 35-959 Rzeszów
tel.: +48 17 865 1100, e-mail: kancelaria@prz.edu.pl
www.prz.edu.pl

9	Krzysztof Ossoliński, Tomasz Ruman, Tadeusz Ossoliński, Anna Ossolińska, Adrian Arendowski, Artur Kołodziej, Aneta Płaza-Altamer, Joanna Nizioł *Monoisotopic silver nanoparticles-based mass spectrometry imaging of human bladder cancer tissue: Biomarker discovery* Advances in Medical Sciences, 2023, 68(1), 38-45, DOI: 10.1016/j.advms.2022.12.002	- prowadzenie eksperymentów (analiza tkanek metodą ^{109}AgNPET), - przygotowanie manuskryptu	14%

Kołodziej Artur
.....
Podpis

al. Powstańców Warszawy 6, 35-959 Rzeszów
tel.: +48 17 865 1652, e-mail: chemia@prz.edu.pl
www.wch.prz.edu.pl

al. Powstańców Warszawy 12, 35-959 Rzeszów
tel.: +48 17 865 1100, e-mail: kancelaria@prz.edu.pl
www.prz.edu.pl

Lek. Krzysztof Ossoliński, specjalista urolog FEBU
Samodzielny Publiczny Zespół Opieki Zdrowotnej w Kolbuszowej
Oddział Urologii Ogólnej i Onkologicznej
ul. Grunwaldzka 4, 36-100 Kolbuszowa

Rzeszów, 05.04.2023r.

OŚWIADCZENIE

Oświadczam, że w niżej wymienionych pracach mój udział merytoryczny oraz procentowy był następujący:

Lp.	Tytuł publikacji oraz informacje bibliograficzne	Udział merytoryczny	Udział %
1	Joanna Nizioł, Jan Sunner, Iwona Beech, Krzysztof Ossoliński, Anna Ossolińska, Tadeusz Ossoliński, Aneta Płaza, Tomasz Ruman Localization of Metabolites of Human Kidney Tissue with Infrared Laser-Based Selected Reaction Monitoring Mass Spectrometry Imaging and Silver-109 Nanoparticle-Based Surface Assisted Laser Desorption/Ionization Mass Spectrometry Imaging, Analytical Chemistry, 2020, 92, 6, 4251–4258 DOI:10.1021/acs.analchem.9b04580	- dostarczanie materiału biologicznego do badań	4%
6	Joanna Nizioł, Krzysztof Ossoliński, Aneta Płaza-Altamer, Artur Kołodziej, Anna Ossolińska, Tadeusz Ossoliński, Tomasz Ruman Untargeted ultra-high-resolution mass spectrometry metabolomic profiling of blood serum in bladder cancer, Scientific Reports, 2022, 12, 1, DOI: 10.1038/s41598-022-19576-9	- dostarczanie materiału biologicznego do badań - współtworzenie koncepcji badań, - przygotowanie manuskryptu	14%
7	Krzysztof Ossoliński, Tomasz Ruman, Valérie Copié, Brian P. Tripet, Leonardo B.	- dostarczanie materiału biologicznego do badań	9%

al. Powstańców Warszawy 6, 35-959 Rzeszów
tel.: +48 17 865 1652, e-mail: chemia@prz.edu.pl
www.wch.prz.edu.pl

al. Powstańców Warszawy 12, 35-959 Rzeszów
tel.: +48 17 865 1100, e-mail: kancelaria@prz.edu.pl
www.prz.edu.pl

	Nogueira, Katiane O.P.C. Nogueira, Artur Kołodziej, Aneta Płaza-Altamer, Anna Ossolińska, Tadeusz Ossoliński, Joanna Nizioł Metabolomic and elemental profiling of blood serum in bladder cancer Journal of Pharmaceutical Analysis, 2022, DOI: 10.1016/j.jpha.2022.08.004	- współtworzenie koncepcji badań, - przygotowanie manuskryptu	
9	Krzysztof Ossoliński, Tomasz Ruman, Tadeusz Ossoliński, Anna Ossolińska, Adrian Arendowski, Artur Kołodziej, Aneta Płaza-Altamer, Joanna Nizioł Monoisotopic silver nanoparticles-based mass spectrometry imaging of human bladder cancer tissue: Biomarker discovery Advances in Medical Sciences, 2023, 68(1), 38-45, DOI: 10.1016/j.advms.2022.12.002	- dostarczanie materiału biologicznego do badań - współtworzenie koncepcji badań, - przygotowanie manuskryptu	5%

.....

Podpis

al. Powstańców Warszawy 6, 35-959 Rzeszów
tel.: +48 17 865 1652, e-mail: chemia@prz.edu.pl
www.wch.prz.edu.pl

XI. Kopie publikacji przedkładanych do oceny

analytical chemistry

pubs.acs.org/ac Article

Localization of Metabolites of Human Kidney Tissue with Infrared Laser-Based Selected Reaction Monitoring Mass Spectrometry Imaging and Silver-109 Nanoparticle-Based Surface Assisted Laser Desorption/Ionization Mass Spectrometry Imaging

Joanna Nizioł, Jan Sunner, Iwona Beech, Krzysztof Ossoliński, Anna Ossolińska, Tadeusz Ossoliński, Aneta Płaza, and Tomasz Ruman*

Cite This: *Anal. Chem.* 2020, 92, 4251−4258 Read Online

ACCESS | Metrics & More | Article Recommendations | Supporting Information

ABSTRACT: Infrared (IR) laser ablation-remote-electrospray ionization (LARESI) platform coupled to a tandem mass spectrometer (MS/MS) operated in selected reaction monitoring (SRM) or multiple reaction monitoring (MRM) modes was developed and employed for imaging of target metabolites in human kidney cancer tissue. SRM or MRM modes were employed to avoid artifacts that are present in full scan MS mode. Four tissue samples containing both cancerous and noncancerous regions, obtained from three patients with renal cell carcinoma (RCC), were imaged. Sixteen endogenous metabolites that were reported in the literature as varying in abundance between cancerous and noncancerous areas in various human tissues were selected for analysis. Target metabolites comprised ten amino acids, four nucleosides and nucleobases, lactate, and vitamin E. For comparison purposes, images of the same metabolites were obtained with ultraviolet (UV) desorption/ionization mass spectrometry imaging (UV-LDI-MSI) using monoisotopic silver-109 nanoparticle-enhanced target (^{109}AgNPET) in full-scan MS mode. The acquired MS images revealed differences in abundances of selected metabolites between cancerous and noncancerous regions of the kidney tissue. Importantly, the two imaging methods offered similar results. This study demonstrates the applicability of the novel ambient LARESI SRM/MRM MSI method to both investigating and discovering cancer biomarkers in human tissue.

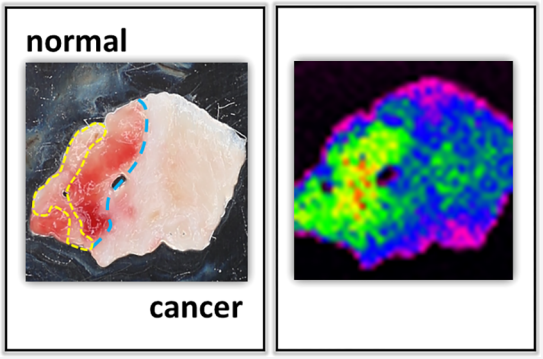

INTRODUCTION

Kidney cancer accounts for 2.2% of the total worldwide cancers and is the third most common cancer of the urinary tract after prostate and bladder cancer, whether measured by incidence or prevalence. In 2018, over 400 000 cases of kidney cancer were diagnosed and more than 170 000 deaths were due to this disease. Furthermore, its incidence is on the rise.[1] There are three main histological subtypes of renal cancer, namely chromophobe RCC (cRCC), papillary RCC (pRCC), and clear cell RCC (ccRCC). Of these, ccRCC accounts for nearly 90% of all kidney tumors.[2] Diagnosis of RCC is based on medical imaging (computed tomography, CT), magnetic resonance imaging (MRI), ultrasound). More than 50% of RCC's are diagnosed incidentally, and approximately one-third of patients have metastatic tumors beyond the kidney at the time of diagnosis.[3] Although the most effective treatment for localized RCC is radical nephrectomy with nephron-sparing surgery at an early stage, even after such optimal surgery, nearly one-third of patients experience disease recurrence after surgical resection.[4] Various RCC biomarkers, most of which are proteins, (C-reactive protein (CRP), PTEN, carbonic anhydrase IX (CAIX), hypoxia-inducible factors (HIF-1α and HIF-1β), vascular endothelial growth factor (VEGF, CD44, E-cadherin, osteopontin, antigen K_i-67, and tumor protein p53) have been proposed, and their monitoring might promote timely prognosis of metastatic RCC. However, these biomarkers suffer from low sensitivity and specificity. Thus, further research to identify new RCC biomarkers is required for early detection, diagnosis, treatment guidance and assessment, monitoring of treatments, identifying relapses, as well as elucidation of molecular processes behind the disease states.[5]

The interest in mass spectrometry imaging (MSI) has grown steadily in recent years. MSI is used for visualization and analysis of spatial distributions of molecules, within a relatively wide molecular weight range, in complex biological systems

Received: October 8, 2019
Accepted: February 18, 2020
Published: February 21, 2020

with excellent molecular specificity.[6] It is noteworthy that MSI has been employed almost exclusively in nontargeted mode, using full mass scan, MS^1-spectrum mode.[7] Matrix-assisted laser desorption/ionization (MALDI) is the chosen technique for molecular imaging of tissue samples. Indeed, MALDI MSI has been successfully employed to analyze the spatial distribution of proteins[8] and lipids[9] within kidney tissue of patients with RCC. However, in MALDI MSI, due to utilization of a near-UV laser for ablation, relatively large amounts of additional low-molecular-weight organic acids are added as an ablation matrix. This leads to the generation of numerous and abundant chemical background peaks in the low-mass region (under m/z 1000) and the ability to detect cellular metabolites is limited. Further, acidic matrices can cause acid-catalyzed hydrolysis of various biomolecules. MALDI also suffers from a highly variable sensitivity (the sweet spot effect) and low ionization efficiency for low-polarity compounds. To overcome the limitations of MALDI, a matrix-free, laser desorption−ionization method that uses a steel target covered with cationic silver or gold nanoparticles (AgNPs and AuNPs) has been developed.[10,11] The latter represents a surface-assisted laser desorption ionization method (SALDI) that, unlike MALDI, is matrix-free. When Ag-109 nanoparticles are used, the method is referred to as ^{109}AgNPET LDI.

MSI techniques that allow imaging of biological material under ambient ionization conditions have also been developed.[12] To the best of our knowledge, desorption electrospray ionization (DESI) is the only ambient ionization technique that has been applied to the imaging of lipids and other low molecular compounds in kidney cancer tissue.[13−15] With DESI, the main limitations include a relatively low spatial resolution, usually limited to 100 μm, a low ionization efficiency for some molecules, and a low desorption efficiency for molecules that are strongly bound to surfaces.[16] Moreover, the DESI sampling depth is very shallow, which greatly reduces the amount of material that is available for analyses in the mass spectrometer. As in MALDI, this increases the risk that MS signals are obtained mainly from extracellular fluids.

Among ambient environment MS methods, the ones that use a mid-IR laser for sampling are the most suitable for the analysis of metabolites within biological tissues. A laser beam with a wavelength of about 2.94 μm effectively couple its energy into the O−H stretching mode in hydrogen-bonded water, present in any hydrated biological material.[17] A main advantage of IR laser over UV laser, for ablation from tissue, is a greater depth of sampling, about 10 μm for a single laser pulse and arbitrarily deep for repeated pulses. Literature contains mentions regarding experimental setup examples that also use laser ablation and electrospray ionization, LAESI.[18] This method was recently used to perform imaging of human hepatocarcinoma tissue samples.[19] However, mentioned work differs considerably in technical design with the one presented herein and measurements were made in ToF-mode, without using ion fragmentation techniques.

In tandem mass spectrometry (MS/MS), the selectivity for a targeted analyte is enhanced by monitoring a compound-unique ion fragmentation in selected reaction monitoring (SRM), or multiple reaction monitoring (MRM), mode. As the chemical noise is effectively removed, this usually enhances sensitivity despite the lower ion detection efficiency. For these reasons, MS/MS is a powerful tool for high-sensitivity detection and near-certain identification of targeted low-molecular-weight compounds. The method is also characterized by a wide dynamic range, extremely high speed, and suitability for quantitation.[20]

The aim of this study is to report the development of new experimental MSI setup referred to as "laser ablation-remote-electrospray ionization" (LARESI) and to present unique MS imaging results of human tissue, that is, to demonstrate LARESI SRM targeted MS/MS imaging of frozen kidney tissue containing cancerous and noncancerous regions. Images depict 16 target metabolites. Importantly, each metabolite was identified based on its MS/MS fragmentation using SRM measurement mode. No additional sample preparation other than rinsing was required.. The tissue was sampled employing laser ablation and all metabolites were detected from the same ablation event in any one pixel. The ion plume-gathering interface used LARESI platform. The ESI-produced ions were analyzed on a QTRAP mass spectrometer, and this is the first report of results from this MS imaging instrument.

Images of kidney tissue with RCC were also obtained with the ^{109}AgNPET LDI" method.[21] In the latter, ablation occurs in vacuum and ions are detected in full-scan mode on a TOF-mass spectrometer. Images of RCC kidney tissue obtained with these two markedly different MSI methods are compared, and it is found that the they are comparable.

EXPERIMENTAL SECTION

1. Participants. The study protocol was approved by the Bioethics Committee at the University of Rzeszow (Poland, permission no. 2018/04/10), and the research was performed in accordance with relevant guidelines and regulations. Specimens and clinical data from patients involved in the study were collected with informed consent. All laboratory test results for the cancer patients (complete blood count, kidney function tests, CRP, urine analysis, bleeding profile) were within normal limits. Whole tumors and small fragments of adjacent healthy tissue were resected (cancer and control tissue, respectively). Control tissue was recognized as normal based on pathological analysis. Patients characteristics are provided in Section S3 of the Supporting Information (SI).

2. Materials and Equipment. Silver-109 (min. 99.75% of ^{109}Ag) isotope was purchased from BuyIsotope (Sweden) and transformed to trifluoroacetate salt using known methods (involving dissolution in HNO_3; precipitation of ^{109}AgOH; reaction with trifluoroacetic acid; and recrystallization from tetrahydrofuran/hexane mixed solvent system). 2,5-Dihydroxybenzoic acid (DHB) was purchased from Aldrich. Steel targets were machined from H17 stainless steel. All solvents were of HPLC quality, except for water (18 MΩ water produced locally) and methanol (LCMS grade, Fluka). The silver-109 nanoparticles were synthesized on the surface of steel targets[11] Optical photographs of tissue samples were obtained on an Olympus SZ10 microscope, equipped with an 8 Megapixel Olympus camera.

3. Tissue Processing. Following surgery, tissue samples were immediately frozen in dry ice to minimize sample degradation and stored at −60 °C until analysis. For the LARESI SRM MSI imaging experiments, 100-μm-thick tissue sections were cut using a microtome, and the slices were mounted on the Peltier stage set to −18 °C to minimize lateral mixing of compounds in the sample surface.

Four different kidney tissue sections (Specimen 1−4 as described in SI Section S3) recovered from three different patients were examined. Specimens 2 and 3 were obtained

from the same patient (SI Section S3). Each of the four tissue sections contained both a cancerous (RCC) and a non-cancerous (control) region.

4. Laser Ablation, Remote-Electrospray Ionization, Selected Reaction Monitoring, Mass Spectrometry Imaging: LARESI SRM MSI of Kidney Cancer Tissue.

4.1. Laser System. An Nd/YAG-pumped, tunable OPO laser (IR Opolette 2731-HE; Opotek, Carlsbad, CA) with 4 ns, mid-IR laser pulses with a maximum repetition frequency of 20 Hz, was tuned to 2.94 μm. The pulse energy was 3.5 mJ (measured using a pyroelectric energy meter PE25-SH-V2; Ophir-Spiricon, Logan, UT).

4.2. Imaging Sample Chamber and Imaging Procedure. The experiment was performed in an airtight chamber as depicted in Figure 1. The chamber is pressurized with nitrogen

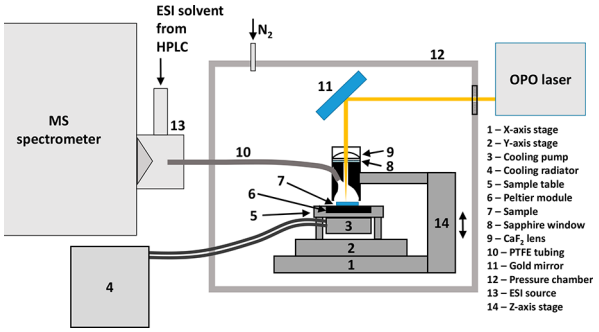

Figure 1. Schematic representation of the LARESI SRM MSI experimental setup.

gas to produce nitrogen flow of 2 L/min. The specimen is placed on a 50 × 50 mm sample stage. A Peltier cooling plate (TE-127−1.4−1.5; TE Technology, Traverse City, M) maintains the sample at of −18 °C. Excess heat generated from the Peltier element is removed using circulating water and an external radiator. The temperature-controlled sample stage is mounted on a motorized XY-stage (MTS50-Z8; Thorlabs, Newton, NJ). The pulsed beam from the OPO laser enters the sample chamber through a 1" Infrasil window (Thorlabs) and is redirected toward the sample stage by a gold-plated mirror (PF10−03-M01; Thorlabs). The beam is focused onto the sample surface by a 40 mm focal length CaF_2 spherical lens (Thorlabs), mounted on a *Z*-axis stage (Thorlabs). The incidence angle on the sample is 90°; the size of the laser focus is 60 ± 10 μm and the pulse energy measured at the sample surface is 2.5 mJ. During imaging, the laser focal point remains fixed in space, while the sample is moved by the computer-controlled XY-stage. A funnel, connected to a 4 mm I.D. PTFE tube, is positioned over the laser ablation site. The overpressure in the chamber drives a 2 L × atm/min nitrogen gas flow through the tube. The laser ablation plumes are entrained into the gas and transported to the electrospray ionization (ESI) source of the SCIEX QTRAP 5500 mass spectrometer. The outlet end of the Teflon tube is mounted axially with the MS sampling cone inside the ESI source, and the distance between the butt end of the tube and the tip of the cone is 20 mm. A binary HPLC pump (Agilent G1312A) provides a steady flow of a binary solvent mixture (2:1 IPA:water with 0.5% acetic acid; 20 μL/min) to the electrospray needle.

Samples were maintained at −18 °C during analysis by the Peltier module. Imaging of tissue sections was performed over a square or rectangular area of about 1 cm^2. The spatial resolution was in a range from 175 to 300 μm. Each of 1.5 × 10^3 pixels was exposed to the laser for 2 s, at a laser pulse repetition rate of 15 Hz. Between pixels, the sample stage moved with a speed of 2 mm/s. The time delay between pixels, during which the stage was moving along a straight line (the

Table 1. Mass Spectrometry Parameters of LARESI SRM MSI Experiments (Q1, Q3, Scan Time, DP, EP, CE, CXP) and Observed Abundance Ratios of Selected Metabolites between Cancer and Cancer-Free Human Kidney Tissue Regions both for LARESI SRM MSI ("ESI") and ^{109}AgNPET LDI MSI ("LDI")

				abundance ratio							
compound name	polarity[a]	Q1 [*m*/*z*]	Q3 [*m*/*z*]	ESI[b]	LDI[c]	scantime [ms]	DP [V]	EP [V]	CE [V]	CXP [V]	image
alanine	+	90.1	44.0	0.6	0.7	30	6	4	17	6	Figure 2C
serine	+	106.1	60.0	0.5	0.7	30	6	10	16	7	Figure 2D
threonine	+	120.1	103.2	0.8	0.8	30	20	14	27	10	Figure 2E
lysine	+	147.1	84.0	0.7	0.8	30	15	14	23	10	Figure 2F
glutamic acid	+	148.1	84.0	0.4	0.6	30	21	14	21	10	Figure 2G
methionine	+	150.2	104.0	0.7	0.6	30	6	12	15	12	Figure 2H
histidine	+	156.1	110.0	0.6	0.7	30	16	13	19	12	Figure 2I
phenylalanine	+	166.1	103.0	0.6	0.8	30	11	14	37	12	Figure 2J
arginine	+	175.2	70.0	1.2	1.1	30	40	11	27	8	Figure 2K
tryptophan	+	205.1	146.0	1.1	0.8	30	20	14	16	10	Figure 2L
guanine	−	150.0	108.0	1.2	0.7	50	−80	−10	−18	−13	Figure 3C
uridine	−	243.0	110.2	0.4	0.9	50	−80	−10	−18	−13	Figure 3D
thymine	−	125.0	42.0	1.8	1.3	50	−80	−10	−14	−13	Figure 3E
inosine	−	267.0	135.2	2.9	1.7	30	−80	−10	−23	−13	Figure 3F
lactate	−	89.0	43.1	2.3	1.0	30	−80	−10	−15	−13	Figure 3G
vitamin E	+	431.4	165.1	2.0	1.1	30	120	9	40	15	Figure 4C
			137.1			30	120	9	68	19	Figure 3D

[a]"−" = negative ion mode; "+" = positive ion mode. [b]Averaged cancer-to-normal signal intensity ratio in LARESI SRM MSI (calculated by dividing averaged signal intensity from cancer region by value from normal region), [c]Averaged cancer-to-normal signal intensity ratio in ^{109}AgNPET LDI MS imaging; DP = declustering potential; EP = entrance potential; CE = collision energy; CXP = cell exit potential.

https://dx.doi.org/10.1021/acs.analchem.9b04580
Anal. Chem. 2020, 92, 4251−4258

horizontal direction in Figures 3−5), was 4 s, and the time delay between lines was 5 s. Control and analysis software was described recently.[22]

4.3. Mass Spectrometer Parameters. A SCIEX QTRAP 5500 mass spectrometer was used in positive ion mode with selected reaction monitoring (SRM) measurement mode with Q1/Q3/DP/EP/CE and CXP settings as stated in Table 1. In MRM mode, each compound-specific fragmentation was monitored for specific time (Table 1) with a 5 ms delay to the next fragmentation. The settings of the ESI source were as follows: source temperature 500 °C, curtain gas 20 psi, ion source gas 1−30 psi, ion source gas 2−20 psi, ion-spray voltage −4500 V (for negative mode) and +5500 V (for positive mode), collision gas (nitrogen): medium. Images of extracted ion chromatograms for compounds studied with LARESI are provided in SI Section S4.

4.4. LARESI Method Test in Enhanced Product Ion (EPI) MS/MS Mode. Volume of 10 μL of serine and aqueous lysine solution (0.1 mg/mL) was poured onto filter paper (2 × 2 cm) of 0.2 mm thickness. After drying, paper was attached to stainless steel plate (2 × 3 cm; 0.8 mm thickness) with sticky tape and inserted into LARESI chamber. Mass spectrometer was working in EPI mode set on protonated lysine (m/z 147) and deprotonated serine (m/z 104). Line resolution was 300 μm. Other parameters were as stated in Sections 4.2 and 4.3.

5. Monoisotopic Silver-109 Nanoparticles-Enhanced Target Laser Desorption/Ionization Mass Spectrometry Imaging: ^{109}AgNPET LDI MSI of the Kidney Cancer Tissue. Silver-109 nanoparticle-enhanced target (^{109}AgNPET) preparation and imaging of human kidney tissue with the use of nanoparticle-based methods were described in our recent works.[10,11,23] For more details see SI Section S1. Studied specimen contained both normal and cancer regions and was 23 × 26 × 20 mm in size, and the MS imaging was made for imprint of tissue with 250 × 250 μm resolution.

RESULTS AND DISCUSSION

LARESI Method Test in Enhanced Product Ion (EPI) MS/MS Mode. LARESI experimental setup was tested in order to provide data on variability of pixel-to-pixel MS/MS signal intensity. The ideal test object should have homogeneous distribution of a studied compound, but this alone does not provide perfect results as instrumental components of the setup, generate signal variability. As LARESI is capable of analysis of various biological and nonbiological objects due to application of relatively powerful pulsed laser, low-water content object—0.2 mm thick filter paper—was used as a matrix for test compounds. Data shown inSI Section S5 figure provide pixel intensity variation visualization for two test compounds,lysine and serine and their fragments in positive and negative MS/MS modes, respectively. Variabilities calculated as standard deviation of pixel maximum intensities were found to be 12% and 16% for protonated lysine and lysine fragment and 14% and 15% for deprotonated serine and serine fragment, respectively. The observed variabilities are very low when compared to the ones reported for MALDI MSI.[24]

LARESI SRM MS Imaging of Kidney Cancer Tissue. MS images for 16 selected metabolites in cancerous kidney tissue samples were obtained with two different MSI methods. IR-laser-ablation-based LARESI targeted MSI experiments utilizes tandem mass spectrometry (MS/MS) in fragmentation-based SRM or MRM modes, whereas ^{109}AgNPET LDI[11] employs a ToF/MS operating in the standard full scan MS[1] mode. One of the study aims was to compare these two methods. It is recognized that both amino acid and nucleic acid metabolism are often upregulated in cancerous, relative to noncancerous tissue.[25] Therefore, compounds representing the above pathways, namely 10 amino acids and 4 nucleosides or nucleobases were selected for imaging. Lactate, which is a key cancer metabolite,[26] and vitamin E, were also included.

In this first reported application of the LARESI SRM MSI method, images for 16 selected metabolites (Table 1) in frozen human kidney tissue sections are presented. Three different sections were used, and they were obtained from Specimens 1, 2, and 3, respectively. Each section contains both cancerous and noncancerous regions. The images obtained for the Specimen 1, 2, and 3 sections are shown in Figures 2, 3, and 4, respectively. For each metabolite, the m/z values of the precursor/parent ion (Q1) and the product/daughter ion (Q3) are listed in Table 1, together with their optimized values for declustering potential (DP), entrance potential (EP), collision energy (CE), and cell exit potential (CXP).

Images of the 10 selected amino acids were obtained from the Specimen 1 tissue section. A photograph of the tissue prior to imaging, with outlined cancerous and noncancerous regions is presented in Figure 2A. SRM ion images, (Figure 2C−L),

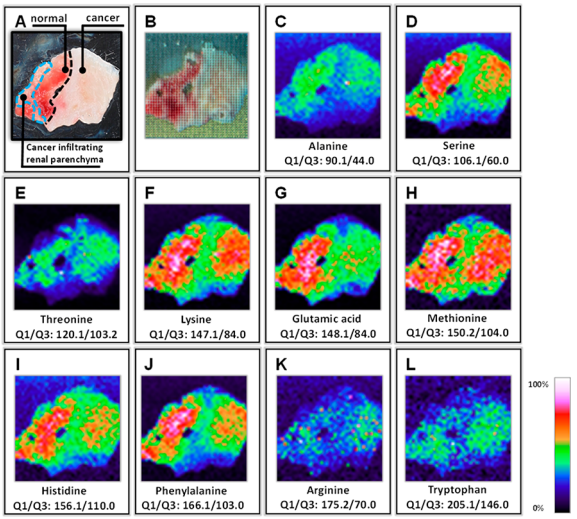

Figure 2. Photographs and LARESI SRM MSI ion images of selected amino acids in kidney tissue section from Specimen 1 (SI Section S3). Optical photographs of the imaged kidney tissue (A) prior to and (B) following imaging. LARESI SRM MSI ion images of the kidney tissue (C−L). The imaged area is 12 × 12 mm obtained with 40 × 40 pixels and at 300 × 300 μm resolution.

reveal that several of the amino acids are detected with a lower abundance in the RCC than in the control. The cancer-to-control SRM signal abundances, averaged over the respective regions are listed in Table 1. In noncancerous tissue eight of the 10 amino acids (alanine, serine, threonine, lysine, glutamic acid, methionine, histidine, and phenylalanine) had a higher abundance than in cancerous tissue. Two of 10 amino acids (arginine, tryptophan) were detected with a slightly higher abundance in the RCC area. The largest differences between noncancerous and cancerous tissue was observed for serine, glutamic acid, histidine and phenylalanine.

The results obtained using LARESI imaging platform are consistent with the ones reported in several previous renal

cancer studies. It has been demonstrated that serum levels of alanine, serine, lysine, glutamic acid, methionine, histidine, and phenylalanine were significantly decreased in patients with RCC while arginine levels were increased.[27] A similar pattern of amino acid abundances within the kidney tissue is revealed with LARESI system (Figure 2). It should be noted that the phenomenon of amino acid up- and downregulation is not unique for renal cancers. Significant changes in the abundances of amino acids in plasma and tissue have indeed been observed for patients with many different types of cancers (lung, breast, gastric, colorectal, prostate, pancreatic, and colon).[28−31] Owing its simplicity in sample preparation, LARESI imaging platform is, therefore, ideally suited for rapid investigation of other types of malignant tumors.

Nucleosides and their metabolites play an important role in the metabolism and growth of tumors, as rapidly proliferating tumor cells have a large need for nucleotides.[32] Hsu et al. reported the increased levels of nucleosides, in particular of inosine, in urine from breast cancer patients compared to healthy persons,[33] while the suppression of uridine in urine of patients with colorectal cancer has been observed.[34] The authors proposed that nucleoside might serve as potential human tumor markers.

To demonstrate whether similar trends can be noted in tissues of kidney cancer patients, the spatial distributions of selected nucleosides (uridine, inosine), nucleobases (guanine, thymine), and organic metabolite, namely lactate, were studied in Specimen 2 (Figure 3). The SRM images for guanine,

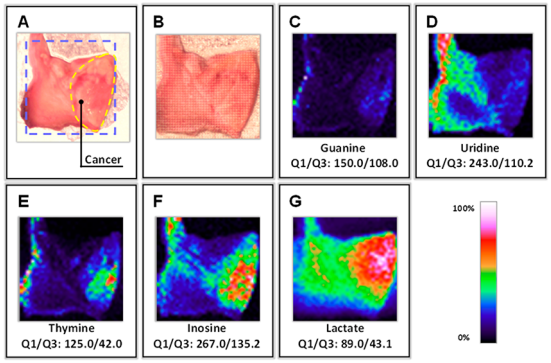

Figure 3. Photographs and LARESI SRM MS ion images of nucleobases, nucleosides, and lactate in RCC Specimen 2 (SI Section S3). Optical photographs of the kidney cancer tissue prior to (A) and after imaging (B). Corresponding LARESI SRM images (C−G). The imaged area is 8 × 8 mm obtained with 40 × 40 pixels and at 200 × 200 μm resolution.

thymine, inosine, and lactate all showed higher abundances in the cancer region. In contrast, uridine abundances were lower in the cancer tissue. A decline of uridine concentrations in kidney cancer tissue is consistent with an earlier report.[35] Apart from the differences between the cancer and cancer-free tissue regions, it is noteworthy that the images also demonstrate significant SRM abundance variations within each of the two regions. The MSI of guanine, uridine, thymine, and inosine with LARESI platform is the first report on the distribution of these metabolites within human kidney tissue.

The SRM image of lactate (Figure 3G) shows that the RCC cancer tissue contains approximately 2-fold higher level of lactate than does noncancerous tissue. Lactate is recognized as a key metabolite related to cancer progression and metastasis. It has long been known that cancer cells exhibit different metabolism than cancer-free cells. In 1920s Warburg found that cancer cells prefer aerobic glycolysis rather than oxidative respiration. In this process, tumor cells produce large amounts of lactate from glucose even in the presence of sufficient levels of cellular oxygen.[36] In cervical cancer, accumulation of lactate within tumors was inversely correlated to patient survival.[37] Similar correlations were observed in patients with neck and head squamous cell carcinoma, as the cancers in patients with short-term survivals had a significantly higher content of lactate than those in patients with long-term survival.[38] Increased level of lactate were found also in RCC tissue,[39,40] particularly for higher-grades of cancer.[41] Hence, here is good evidence that tumor lactate metabolism and lactate levels are directly correlated with the aggressiveness of cancer. Conceivably, detection of high lactate levels would be a supportive tool for tumor diagnosis, prognosis, and for predicting probability of drug effectiveness.

Ion images in Figure 4 were obtained using LARESI SRM MSI of tissue from Specimen 3. Elevated levels of vitamin E

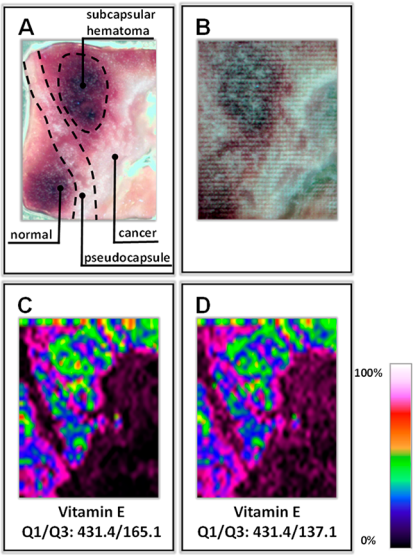

Figure 4. Photographs and LARESI SRM ion images of kidney tissue representing specimen 3 (SI Section S3). Optical photographs of the sample (A) prior to and (B) after imaging; Images of vitamin E distributions (C, D) from two different SRM fragmentation reactions. The imaged area is 7 × 9 mm using 40 × 40 pixels with 175 × 225 μm resolution.

(α-tocopherol) are observed in the cancer zone. The uptake of lipids and fatty acids is increased in cancer cells and the high concentration of vitamin E that is an antioxidant, may be explained by the need of cells to resist oxidative stress.[42] Increased level of vitamin E in RCC tissue compared with a noncancer tissue has previously been reported.[40,43]

^{109}AgNPET LDI MS Imaging of Kidney Cancer Tissue. All MSI methods are associated with matrix effects that influence the ratio of measured abundance to actual concentration of compounds. These effects are not trivial to quantify. The reliability of an abundance measurement in imaging as a predictor of relative concentrations will require substantial future work. In this study, a first step is taken by comparing MSI results from two very different MSI methods: LARESI SRM MSI, which uses an IR laser, and ^{109}AgNPET

LDI MSI, which employs a UV laser for ablation and/or desorption. The ^{109}AgNPET LDI MSI experiment was performed by recording high-resolution TOF/MS spectra at 32 × 44 pixel-locations over an 8 × 11 mm size area, that is, with 250 × 250 μm resolution. Specimen 4 was used to make a tissue imprint on the ^{109}Ag nanoparticle-covered target plate. The ion images are shown in Figure 5. The averaged ion

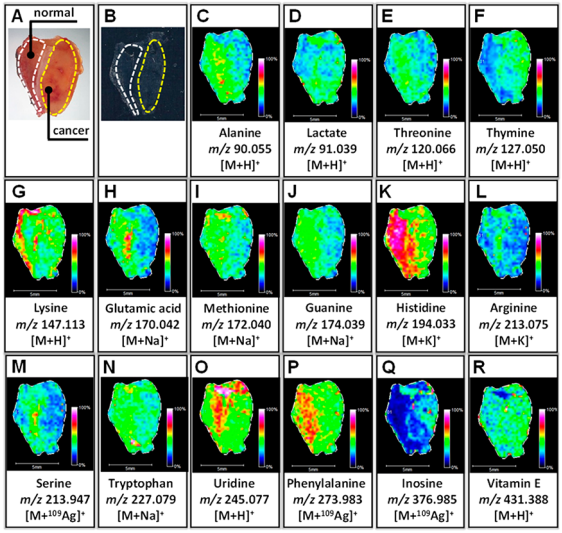

Figure 5. Photographs and LDI-MSI analysis with ^{109}AgNPET of the surface of the RCC Specimen 4 (SI Section S3). (A) An optical photograph of the imaged surface of the kidney cancer sample. (B) An optical image of the ^{109}AgNPET surface with RCC tissue imprint. Dashed lines represent cancer-free and cancer regions. (C−R) Ion images (TIC normalization) for ions of m/z as specified below each image. All images are within ±0.05 m/z and spatial resolution of 250 × 250 μm.

intensities for both cancerous and noncancerous regions and normal regions presented in the sixth column of Table 1. The identity of some of compounds was confirmed with LIFT MS/MS experiments (SI Section S2).

Ion images of adduct-type ions of 10 amino acids presented in Figure 5 were obtained for the same selected metabolites as the ones investigated with LARESI SRM MSI system. The abundances of alanine, serine, threonine, lysine, methionine, histidine, phenylalanine, and glutamic acid ions are at slightly higher levels in the noncancer tissue region versus tumor tissue. Ions assigned to potassium adduct of arginine were present in higher abundance in cancer tissue compared to a noncancer tissue. A different result from that of LARESI SRM MS imaging, was obtained for sodiated tryptophan ion that was found to be in a higher abundance in noncancer tissue. The greatest difference in abundance within the examined tissue was observed for proton adduct of thymidine (Figure 5F) and silver-109 isotope adduct of inosine (Figure 5Q), which show higher intensity in the area of cancer tissue versus cancer-free region. Large variations can also be seen for ion putatively assigned to proton adduct of vitamin E. The latter were found dominating cancer-free tissue region compared to cancer one (Figure 5R). A number of recent scientific reports have suggested that potential biomarkers should have cancer to control fold change of at least 1.2 or under 0.8.[44−46] Using this criteria for both tested MSI methods, the downregulated compounds, namely alanine, serine, glutamic acid, methionine, histidine, and upregulated ones such as thymine and inosine could be considered as kidney cancer biomarkers.

METHODS COMPARISON

Imaging of tissue with the ^{109}AgNPET LDI MSI method is an excellent alternative to the MALDI MSI method. The absence of an organic matrix and the option of performing internal mass calibration are two of the many advantages of this method. Important advantage of AgNPET-based family of methods is ease of use and also higher imaging speed (ca. 2−3-times), the latter providing images of much higher resolution in the same experiment time. Additional advantage is a smaller UV laser focal point diameter, compared to that of 2.9 μm IR laser. However, a drawback of the method is that intercellular fluid is preferentially transferred to the plate during imprinting, which may cause the loss of information from intracellular metabolism. In MALDI or similar LDI methods, for example, AgNPET, significant variations in sodium and potassium ion concentrations and in pH over the imaged tissue region may lead to quantitative problems. In this case, it is likely that analyte intensity may change more due to sodium/potassium local concentration than of metabolite itself. Moreover, in most MALDI instruments, the sample stage is at room temperature, which promotes tissue degradation and allows warping and cracking of high vacuum-dried tissue samples. These problems are virtually nonexistent when employing the LARESI SRM MSI method. It is an atmospheric pressure method that uses ablation of frozen sample material from a surface to the gas phase with a 2.9 μm IR laser, followed ionization by electrically charged solvent clusters generated through electrospray. In order to maximize the collection and ionization efficiencies in LARESI SRM MSI, a funnel-type device coupled with optics was positioned above the sample to confine the ablation plume and to guide the material through the PTFE tube and into the ESI source. The method has several advantages. LARESI SRM MSI enables direct analysis of samples of varying sizes, shape and physical form. There is no need for sample pretreatment steps such as application of a matrix or solvent, dehydration, or derivatization prior to analysis. Thus, it allows preserving the anatomical integrity of the sample, reducing the risk of delocalization of analytes and chemical contamination of the samples. The samples are not exposed to vacuum and this reduces the possibility of deformation. The latter would produce mass shifts of detected ions, a significant problem with vacuum, TOF-analyzer-based MS instruments. The cooling stage holds the specimen in a frozen state, which prevents water loss thus preserving sample integrity. In LARESI SRM MSI analytes are ionized by protonation, which greatly facilitates qualitative and quantitative analysis and makes the spectral results readily compatible with databases commonly used for metabolomics analyses. Finally, the ability of using SRM in MS/MS mode boosts both analytical sensitivity and selectivity. It is anticipated that here described LARESI setup will facilitate not only MS^3 or higher order fragmentation MSI, but also direct ambient 3D imaging of tissues.

CONCLUSIONS

A novel MSI platform termed LARESI SRM has been developed that allows direct, pretreatment-free, ambient chemical imaging of complex biological samples, such as heterogeneous human tissues. The potential of the LARESI SRM MSI method for rapid and accurate detection of

https://dx.doi.org/10.1021/acs.analchem.9b04580
Anal. Chem. 2020, 92, 4251−4258

metabolites that could serve as tumor markers in human tissues was demonstrated in kidney samples from cancer patients. For comparison purposes, a markedly different MSI method, namely ^{109}AgNPET LDI in full scan mode, was employed for untargeted analysis of the same tissue. The study is the first one to offer the comparison of molecular images from two different methods that depict spatial distribution of metabolites that included 10 amino acids, two nucleosides, and four nucleobases, as well as lactate and vitamin E, relevant to cancer diagnostics within human tissue from patients with RCC. Ion images of cancerous kidney tissue obtained for 16 selected metabolites revealed striking abundance differences and patterns versus cancer-free tissue regions. In almost every case, the abundance patterns observed with the two MSI methods were similar, thus, mutually supportive and clearly differed between cancerous and noncancerous tissues.

Employing LARESI SRM/MRM MSI platform, biomarkers discussed in this work, together with other low molecular weight compounds described in literature can aid identification of cancerous tissues. Conceivably, LARESI method can become an integral part of cancer diagnostic methods that are based on analyses of biopsy samples.

■ ASSOCIATED CONTENT

Supporting Information

The Supporting Information is available free of charge at https://pubs.acs.org/doi/10.1021/acs.analchem.9b04580.

S1 Monoisotopic silver-109 nanoparticles-enhanced target laser desorption/ionization mass spectrometry imaging: ^{109}AgNPET LDI MSI of the kidney cancer tissue. S2 LIFT MSMS analysis results. S3 Clinical characteristics of study group, and controls. S4 Extracted chromatograms (EICs) for LARESI experiments. S5 Test data of LARESI MS/MS pixel-to-pixel intensity variability (PDF)

■ AUTHOR INFORMATION

Corresponding Author

Tomasz Ruman − *Rzeszów University of Technology, Faculty of Chemistry, Rzeszów 35-959, Poland;* orcid.org/0000-0002-9899-8627; Phone: (+48 17) 865-1896; Email: tomruman@prz.edu.pl

Authors

Joanna Nizioł − *Rzeszów University of Technology, Faculty of Chemistry, Rzeszów 35-959, Poland;* orcid.org/0000-0002-4783-8615

Jan Sunner − *Center for Biofilm Engineering, Montana State University, Bozeman, Montana 59717-3980, United States*

Iwona Beech − *Center for Biofilm Engineering, Montana State University, Bozeman, Montana 59717-3980, United States*

Krzysztof Ossoliński − *Department of Urology, John Paul II Hospital, Kolbuszowa 36-100, Poland*

Anna Ossolińska − *Department of Urology, John Paul II Hospital, Kolbuszowa 36-100, Poland*

Tadeusz Ossoliński − *Department of Urology, John Paul II Hospital, Kolbuszowa 36-100, Poland*

Aneta Płaza − *Doctoral School of Engineering and Technical Sciences at the Rzeszów University of Technology, Rzeszów 35-959, Poland*

Complete contact information is available at: https://pubs.acs.org/10.1021/acs.analchem.9b04580

Notes

The authors declare no competing financial interest.

■ ACKNOWLEDGMENTS

The study was supported by National Science Centre (Poland) research project OPUS Number 2016/23/B/ST4/00062.

■ REFERENCES

(1) Bray, F.; Ferlay, J.; Soerjomataram, I.; Siegel, R. L.; Torre, L. A.; Jemal, A. *Ca-Cancer J. Clin.* **2018**, *68* (6), 394−424.

(2) Linehan, W. M.; Walther, M. M.; Zbar, B. *J. Urol.* **2003**, *170* (6), 2163−2172.

(3) Janzen, N.; Kim, H.; Figlin, R.; Belldegrun, A. *Urol. Clin. North Am.* **2003**, *30* (4), 843−852.

(4) Kuijpers, Y. A. M.; Meijer, R. P.; Jonges, G. N.; de Jong, J.; Bosch, J. L. H. R.; Horenblas, S.; Bex, A. *World J. Urol.* **2016**, *34* (8), 1073−1079.

(5) Sanganeria, B. S.; Misra, R.; Shukla, K. K. Molecular Diagnostics in Renal Cancer. In *Molecular Diagnostics in Cancer Patients*; Springer Singapore: Singapore, 2019; pp 199−218. DOI: 10.1007/978-981-13-5877-7_13.

(6) Richard, M.; Caprioli; Farmer, T. B.; Gile, J. Molecular Imaging of Biological Samples: Localization of Peptides and Proteins Using MALDI-TOF MS. *Anal. Chem.***1997**. 694751.

(7) Lippincott-Schwartz, J.; Snapp, E.; Kenworthy, A. *Nat. Rev. Mol. Cell Biol.* **2001**, *2* (6), 444−456.

(8) Seeley, E. H.; Oppenheimer, S. R.; Mi, D.; Chaurand, P.; Caprioli, R. M. *J. Am. Soc. Mass Spectrom.* **2008**, *19* (8), 1069−1077.

(9) Hájek, R.; Lísa, M.; Khalikova, M.; Jirásko, R.; Cífková, E.; Študent, V.; Vrána, D.; Opálka, L.; Vávrová, K.; Matzenauer, M.; et al. *Anal. Bioanal. Chem.* **2018**, *410* (25), 6585−6594.

(10) Nizioł, J.; Ossoliński, K.; Ossoliński, T.; Ossolińska, A.; Bonifay, V.; Sekuła, J.; Dobrowolski, Z.; Sunner, J.; Beech, I.; Ruman, T. Surface-Transfer Mass Spectrometry Imaging of Renal Tissue on Gold Nanoparticle Enhanced Target. *Anal. Chem.* **2016**, *88* (14). 7365.

(11) Nizioł, J.; Rode, W.; Laskowska, B.; Ruman, T. Novel Monoisotopic ^{109}AgNPET for Laser Desorption/Ionization Mass Spectrometry. *Anal. Chem.* **2013**, *85* (3). 1926.

(12) Perez, C. J.; Bagga, A. K.; Prova, S. S.; Yousefi Taemeh, M.; Ifa, D. R. *Rapid Commun. Mass Spectrom.* **2019**, *33* (S3), 27−53.

(13) Alfaro, C. M.; Jarmusch, A. K.; Pirro, V.; Kerian, K. S.; Masterson, T. A.; Cheng, L.; Cooks, R. G. *Anal. Bioanal. Chem.* **2016**, *408* (20), 5407−5414.

(14) Dill, A. L.; Eberlin, L. S.; Zheng, C.; Costa, A. B.; Ifa, D. R.; Cheng, L.; Masterson, T. A.; Koch, M. O.; Vitek, O.; Cooks, R. G. *Anal. Bioanal. Chem.* **2010**, *398* (7−8), 2969−2978.

(15) Tamura, K.; Horikawa, M.; Sato, S.; Miyake, H.; Setou, M. Discovery of Lipid Biomarkers Correlated with Disease Progression in Clear Cell Renal Cell Carcinoma Using Desorption Electrospray Ionization Imaging Mass Spectrometry. *Oncotarget* **2019**; Vol. *10*. DOI: 10.18632/oncotarget.26706

(16) Takáts, Z.; Wiseman, J. M.; Gologan, B.; Cooks, R. G. *Science* **2004**, *306* (5695), 471−473.

(17) Dreisewerd, K.; Draude, F.; Kruppe, S.; Rohlfing, A.; Berkenkamp, S.; Pohlentz, G.; Molecular Analysis of Native Tissue and Whole Oils by Infrared Laser Mass Spectrometry. *Anal. Chem.***2007**. DOI: 10.1021/AC070191P.

(18) Nemes, P. N.; Vertes, A. Laser ablation electrospray ionization for atmospheric pressure, in vivo, and imaging mass spectrometry. *Anal. Chem.***2007**. 798098.

(19) Zhou, W.; Hong, Y.; Huang, C.; Shen, C.; Chu, Y. Laser ablation electrospray ionization time-of-flight mass spectrometry for direct analysis of biological tissue. *J. Anal. Methods Chem.* **2019**, *2019*. 1.

(20) Kovarik, P.; Grivet, C.; Bourgogne, E.; Hopfgartner, G. *Rapid Commun. Mass Spectrom.* **2007**, *21* (6), 911−919.

(21) Nizioł, J.; Misiorek, M.; Ruman, T. *Phytochemistry* **2019**, *159*, 11−19.

(22) Brauer, J. I.; Beech, I. B.; Sunner, J. *J. Am. Soc. Mass Spectrom.* **2015**, *26* (9), 1538−1547.
(23) Nizioł, J.; Misiorek, M.; Ruman, T. *Phytochemistry* **2019**, *159*, 11−19.
(24) Porta, T.; Lesur, A.; Varesio, E.; Hopfgartner, G. *Anal. Bioanal. Chem.* **2015**, *407* (8), 2177−2187.
(25) Phan, L. M.; Yeung, S. C. J.; Lee, M. H. Cancer metabolic reprogramming: Importance, main features, and potentials for precise targeted anti-cancer therapies. *Cancer Biol. Med.* 2014, 1−19. DOI: 10.7497/j.issn.2095-3941.2014.01.001.
(26) Hirschhaeuser, F.; Sattler, U. G. A.; Mueller-Klieser, W. *Cancer Res.* **2011**, *71* (22), 6921−6925.
(27) Mustafa, A.; Gupta, S.; Hudes, G. R.; Egleston, B. L.; Uzzo, R. G.; Kruger, W. D. *J. Urol.* **2011**, *186* (4), 1206−1212.
(28) Leichtle, A. B.; Nuoffer, J. M.; Ceglarek, U.; Kase, J.; Conrad, T.; Witzigmann, H.; Thiery, J.; Fiedler, G. M. *Metabolomics* **2012**, *8* (4), 643−653.
(29) Miyagi, Y.; Higashiyama, M.; Gochi, A.; Akaike, M.; Ishikawa, T.; Miura, T.; Saruki, N.; Bando, E.; Kimura, H.; Imamura, F.; et al. Plasma free amino acid profiling of five types of cancer patients and its application for early detection. *PLoS One* **2011**, *6* (9). e24143.
(30) Dereziński, P.; Klupczynska, A.; Sawicki, W.; Pałka, J. A.; Kokot, Z. J. *Int. J. Med. Sci.* **2017**, *14* (1), 1−12.
(31) Simińska, E.; Koba, M. *Amino Acids* **2016**, *48* (6), 1339−1345.
(32) Romero-Garcia, S.; Lopez-Gonzalez, J. S.; Báez-Viveros, J. L.; Aguilar-Cazares, D.; Prado-Garcia, H. *Cancer Biol. Ther.* **2011**, *12* (11), 939−948.
(33) Hsu, W. Y.; Lin, W. De; Tsai, Y.; Lin, C. T.; Wang, H. C.; Jeng, L. Bin; Lee, C. C.; Lin, Y. C.; Lai, C. C.; Tsai, F. J. *Clin. Chim. Acta* **2011**, *412* (19−20), 1861−1866.
(34) Zheng, Y. F.; Yang, J.; Zhao, X. J.; Feng, B.; Kong, H. W.; Chen, Y. J.; Lv, S.; Zheng, M. H.; Xu, G. W. *World J. Gastroenterol.* **2005**, *11* (25), 3871−3876.
(35) Koshida, K.; Harmenberg, J.; Borgström, E.; Wahren, B.; Andersson, L. *Urol. Res.* **1985**, *13* (5), 219−221.
(36) Warburg, O.; Wind, F.; Negelein, E. *J. Gen. Physiol.* **1927**, *8* (6), 519−530.
(37) Walenta, S.; Wetterling, M.; Lehrke, M.; Schwickert, G.; Sundfør, K.; Rofstad, E. K.; Mueller-Klieser, W. High Lactate Levels Predict Likelihood of Metastases, Tumor Recurrence, and Restricted Patient Survival in Human Cervical Cancers. *Cancer Res.* **2000**, *60* (4).
(38) Ziebart, T.; Walenta, S.; Kunkel, M.; Reichert, T. E.; Wagner, W.; Mueller-Klieser, W. *J. Cancer Res. Clin. Oncol.* **2011**, *137* (2), 193−199.
(39) Gao, H.; Dong, B.; Jia, J.; Zhu, H.; Diao, C.; Yan, Z.; Huang, Y.; Li, X. *J. Cancer Res. Clin. Oncol.* **2012**, *138* (5), 753−761.
(40) Hakimi, A. A.; Reznik, E.; Lee, C.-H.; Creighton, C. J.; Brannon, A. R.; Luna, A.; Aksoy, B. A.; Liu, E. M.; Shen, R.; Lee, W.; et al. *Cancer Cell* **2016**, *29* (1), 104−116.
(41) Wettersten, H. I.; Hakimi, A. A.; Morin, D.; Bianchi, C.; Johnstone, M. E.; Donohoe, D. R.; Trott, J. F.; Aboud, O. A.; Stirdivant, S.; Neri, B.; et al. *Cancer Res.* **2015**, *75* (12), 2541−2552.
(42) Rodrigues, D.; Monteiro, M.; Jerónimo, C.; Henrique, R.; Belo, L.; Bastos, M. de L.; Guedes de Pinho, P.; Carvalho, M. Renal Cell Carcinoma: A Critical Analysis of Metabolomic Biomarkers Emerging from Current Model Systems. *Translational Research*; ‚Mosby Inc., February 1, 2017; pp 1−11. DOI: 10.1016/j.trsl.2016.07.018.
(43) Catchpole, G.; Platzer, A.; Weikert, C.; Kempkensteffen, C.; Johannsen, M.; Krause, H.; Jung, K.; Miller, K.; Willmitzer, L.; Selbig, J.; et al. *J. Cell. Mol. Med.* **2011**, *15* (1), 109−118.
(44) Tsai, C. K.; Yeh, T. Sen; Wu, R. C.; Lai, Y. C.; Chiang, M. H.; Lu, K. Y.; Hung, C. Y.; Ho, H. Y.; Cheng, M. L.; Lin, G. *World J. Gastroenterol.* **2018**, *24* (33), 3760−3769.
(45) Kalantari, S.; Nafar, M.; Samavat, S.; Parvin, M. *Magn. Reson. Chem.* **2017**, *55* (8), 693−699.
(46) Xiao, H.; Langerman, A.; Zhang, Y.; Khalid, O.; Hu, S.; Cao, C. X.; Lingen, M. W.; Wong, D. T. W. *Oral Oncol.* **2015**, *51* (11), 1011−1019.

ACS MEASUREMENT SCIENCE Au
AN OPEN ACCESS JOURNAL OF THE AMERICAN CHEMICAL SOCIETY

pubs.acs.org/measureau

Article

Laser Ablation Synthesis in Solution and Nebulization of Silver-109 Nanoparticles for Mass Spectrometry and Mass Spectrometry Imaging

Aneta Płaza, Artur Kołodziej, Joanna Nizioł, and Tomasz Ruman*

Cite This: *ACS Meas. Sci. Au* 2022, 2, 14–22

Read Online

ACCESS | Metrics & More | Article Recommendations | Supporting Information

ABSTRACT: Preparation of monoisotopic silver-109 nanoparticles (^{109}AgNPs) by pulsed fiber laser (PFL) ablation synthesis in solution (LASiS) with the use of a 2D galvoscanner (2D GS) is described. The procedure of covering of custom-made stainless-steel MALDI targets containing studied objects via nebulization is also presented. Examples of application of the new method (PFL-2D GS LASiS and nebulization) in mass spectrometry (MS) analyses and MS imaging (MSI) are shown. These include tests with a nonionic nucleoside and saccharide, ionic amino acids, and also a low-molecular-weight polymer. Fingerprint MS imaging is shown as an example of a fast and simple MSI procedure.

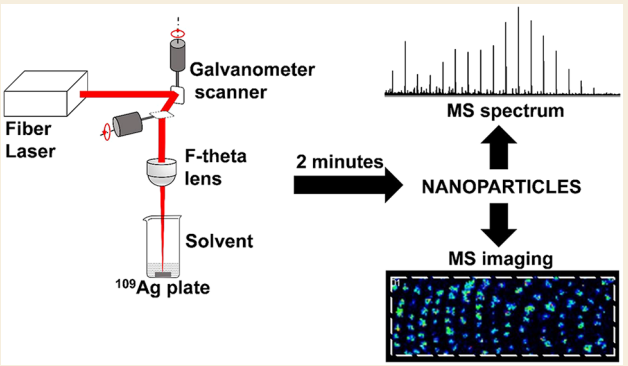

KEYWORDS: *silver-109 monoisotopic nanoparticles, laser ablation synthesis in solution, low molecular weight compounds, mass spectrometry, matrix-free laser desorption/ionization, surface-assisted desorption/ionization*

INTRODUCTION

One of the most utilized laser mass spectrometry methods is matrix-assisted laser desorption/ionization mass spectrometry (MALDI MS), which was developed by Tanaka et al. in 1988.[1] It offers soft ionization potential, being therefore a powerful analytical tool for the analysis of ionic high-molecular-weight molecules, such as peptides, proteins, and DNA/RNA,[2−4] but also, it is useful for detection of some nonionic classes of chemical compounds such as lipids, etc.[5−7] However, MALDI has not been too often applied to detect low-molecular-weight (LMW) compounds (MW < 1000 Da), because MALDI matrices are low-molecular-weight organic acids and produce a variety of matrix-related ions during the desorption/ionization process, which complicates the spectrum and causes suppression of analyte peaks.[8−10]

Discussed problems have been partly solved by the development of surface-assisted desorption/ionization (SALDI) mass spectrometry techniques, where target plates are coated with various nanostructures.[7,11−17] Applications of nanoparticles not only allow reduction of spectral interference but also simplify the mass spectrum. The sample preparation step is also much simpler; usually only application of sample is required.[16,17] What is more, methods based on nanostructures produce very good spot-to-spot reproducibility and greatly reduce the "sweet-spot" problem.[13]

The literature describes two main approaches for the synthesis of nanostructures: the top-down approach, where a larger structure is broken down into NPs, and the bottom-up approach, in which material is synthesized from the molecular or atomic level.[18,19] Chemical reduction is classified as a bottom-up approach and is one of the most common strategies in use for the synthesis of nanoparticles for experiment MS.[17,20,21] However, chemical purity problems arise due to the use of substances for chemical reactions such as metal precursors, reducing agents, stabilizers, and oxidized products, which are the source of reagent-related ions and yield numerous interfering signals.[22−25]

The above-mentioned problem was solved with the application of laser ablation synthesis in solution (LASiS) for the production of nanoparticles.[26] LASiS employs pulsed laser irradiation to ablate a solid material target submerged in liquid, ejecting NPs from the plasma plume into the surrounding solution.[27] This method allows for stabilizer- and reducing-agent-free NP production.[26−29] LASiS produces nanoparticle suspensions of a relatively high chemical purity compared to chemical methods.[30]

Received: July 3, 2021
Published: August 25, 2021

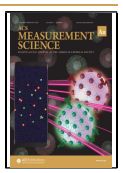

https://doi.org/10.1021/acsmeasuresciau.1c00020
ACS Meas. Sci. Au 2022, 2, 14–22

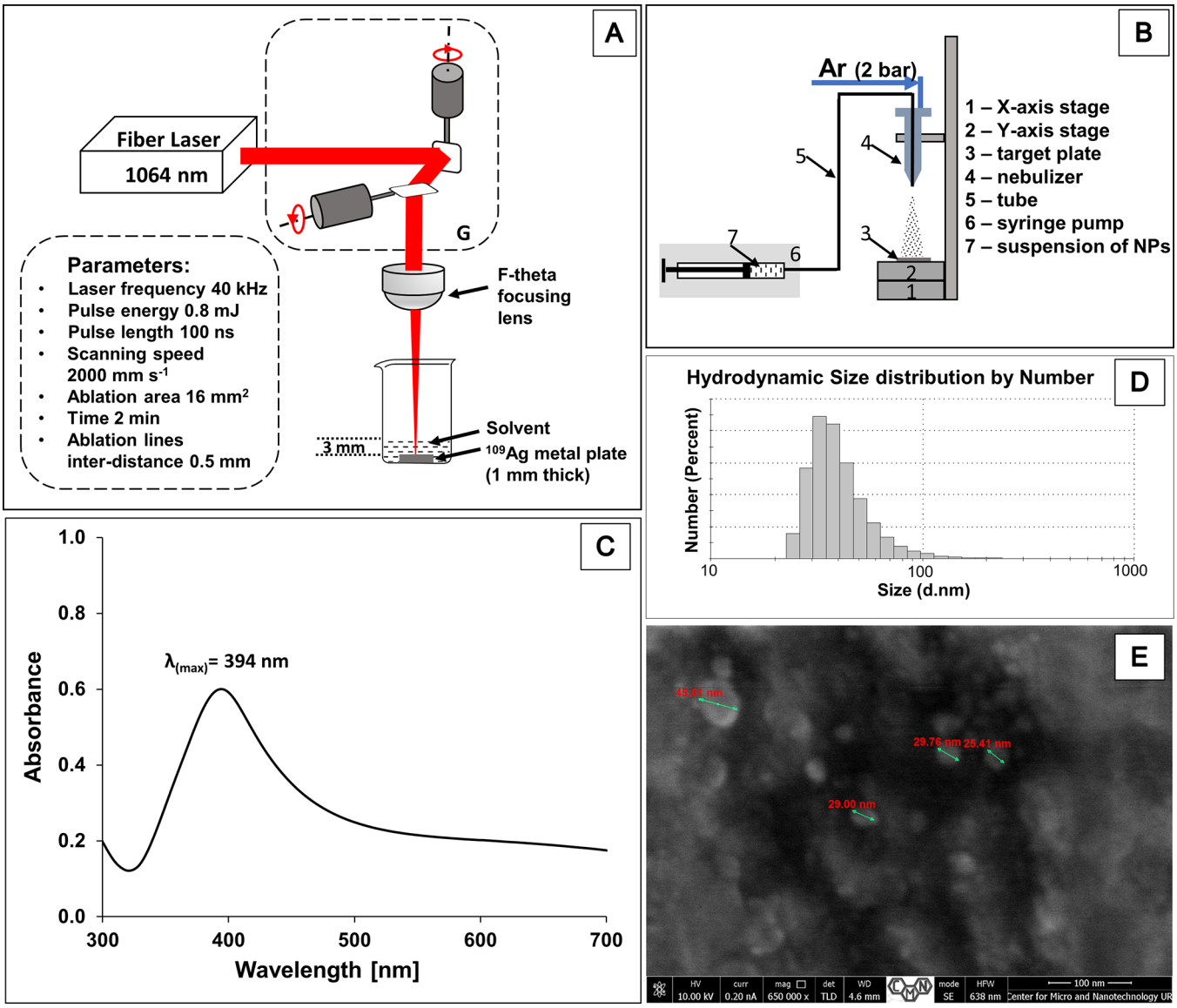

Figure 1. (A) Laser ablation setup for the preparation of ^{109}AgNPs; G – 2D galvanometer laser scanner. Right panel (B) presents setup for nebulization of nanoparticles. Panel (C) presents UV–vis spectrum of ^{109}AgNP suspension in acetonitrile. Panel (D) shows results of DLS measurement of ^{109}Ag nanoparticles' hydrodynamic size distribution by number. (E) High-resolution SEM image of target modified with ^{109}AgNPs generated by PFL 2D GS (three sizes in the center are 29.00, 29.76, and 25.41 nm).

This study describes a new method of production of chemically pure silver-109 nanoparticles in suspension with an application method for covering of studied objects or surfaces. For the first time, 1064 nm pulsed fiber laser (PFL) with 2D galvanometer scanner (2D GS) is shown as a very good source of nanoparticles. The GS module allows very precise and fast scanning of a focused laser beam on the sample surface, virtually removing any heat buildup or local melting of the ablation target. It allows very efficient and fast production of relatively big amounts of nanoparticles compared to systems without it. Moreover, the GS module allowed us to use a 20 W pulsed fiber laser directly on the ablation target with a full laser frequency of 80 kHz. Generated silver-109 nanoparticles are shown to be highly useful for LDI mass spectrometry and also mass spectrometry imaging (MSI). This work presents LDI MS results for test compounds belonging to groups such as amino acids, saccharides, nucleosides, and polymers as well as MSI results for the fingerprint.

EXPERIMENTAL SECTION

Materials

A silver-109 isotope of 99.7% isotopic purity was bought from Trace Sciences International (USA). L-Histidine and D-ribose were purchased from Sigma-Aldrich (99% purity). Thymidine was purchased from Alfa Aesar (99% purity). Poly(propylene glycol) (PPG, average Mn 1000 Da) was purchased from Sigma-Aldrich. All solvents were of HPLC quality, except for water (18 MΩ cm water produced locally). Steel targets were machined from H17 stainless steel. Before the LDI MS and MS imaging experiments, steel targets were cleaned through soaking in boiling solvents: toluene (3 × 100 mL, each plate for 30 s), chloroform (3 × 100 mL, each plate for 30 s), acetonitrile (3 × 100 mL, each plate for 30 s), and deionized water (3 × 100 mL, each plate for 30 s). Every plate was dried in high vacuum (ca. 0.01 mbar, 24 h). Optical photographs were made with the use of an Olympus SZ10 microscope equipped with an 8 MPix Olympus digital camera and also a Canon 6D camera with a macro-type 90 mm focal length lens.

https://doi.org/10.1021/acsmeasuresciau.1c00020
ACS Meas. Sci. Au 2022, 2, 14–22

PFL 2D GS Laser Ablation Synthesis in Solution (LASiS) of Silver-109 Nanoparticles

The experimental arrangement for the ^{109}AgNP preparation by laser ablation is shown in Figure 1A. The silver-109 foil (~1 mm thick) was placed at the bottom of a glass vessel containing solvent (acetonitrile or isopropanol). The ^{109}Ag foil was covered by an approximately 3 mm thick layer of solvent (total solvent volume was 3 mL). The laser ablation was carried out with a 1064 nm pulsed fiber laser (Raycus RFL-P20QE/A3). A suspension was obtained after 2 min of irradiation with a pulse energy of 0.8 mJ (100 ns pulse length) at a 40 kHz repetition rate. Laser ablation was accomplished at a scanning speed of 2000 mm/s; the ablation area was 4 × 4 mm. The suspension was immediately transferred into a syringe and used in the nebulization step.

Nebulization of ^{109}AgNP Suspension

The experimental setup for the nebulization of ^{109}AgNP suspension is shown in Figure 1B. The entire nanoparticle nebulization process was controlled by a computer. The H17 steel plate (laser mass spectrometry target plate) was placed on the table of a translation system consisting of a motorized XY table (EzM-42XL-A powered by closed-loop Ezi-SERVO motors). A glass syringe (1 mL) was filled with a previously prepared suspension of silver-109 nanoparticles and placed in a syringe pump (pumping speed 250 μL/min). The custom-made software directed the 2D system table with 10 mm/s speed using a sequence of movement designed to uniformly cover a target plate. The nebulizer was obtained from a Bruker Amazon ETD ESI ion source. Argon at a pressure of 2 bar was used as the nebulizing gas. Generally, all studied objects—for MS and MSI—were placed on the target plate before nebulization.

^{109}AgNP Characterization

The ^{109}AgNP suspension was characterized by UV−vis spectroscopy (Jasco V-670 spectrophotometer). The spectrum was registered in quartz cuvettes within a 200−800 nm spectral range. The blank sample contained acetonitrile. The suspension of ^{109}AgNPs was also characterized by dynamic light scattering (DLS) using a Zetasizer-Nano ZS from Malvern Instruments. DLS measurements were performed by backscattering at a fixed detector angle of 173°. Isopropanol was used as a dispersant.

LDI MS Experiments

LDI-ToF mass spectrometry experiments were performed using a Bruker Autoflex Speed ToF mass spectrometer equipped with a SmartBeam II laser (355 nm). The laser pulse energy was approximately 90−140 μJ, and the laser repetition rate was 1 kHz. Compounds were measured within 80−1500 or 80−2000 m/z windows, and ion deflection was turned on for ions lighter than m/z 79. The first accelerating voltage was held at 19 kV, and the second ion source voltage was held at 16.7 kV. The reflector voltages used were 21 and 9.55 kV. The spectra for histidine, thymidine, and ribose were acquired by integrating approximately 4000 shots, for which the PPG 5000 shots package was used. Spectra were internally calibrated and analyzed with FlexAnalysis (version 3.3). Mass calibration (typically enhanced cubic calibration based on 5−10 points) was performed using internal standards (silver ions and clusters from $^{109}Ag^+$ to $^{109}Ag_{10}^+$).

LDI MS Imaging Experiments

Measurements were performed using a Bruker Autoflex Speed time-of-flight mass spectrometer in reflectron mode. The apparatus was equipped with a SmartBeam II 1000 Hz, 355 nm laser. The laser impulse energy was approximately 90−140 μJ, the laser repetition rate was 1 kHz, and deflection was used for m/z lower than 80 Da. The m/z range was 80−1500 for the fingerprint experiment (40 × 40 μm spatial resolution). The first accelerating voltage was held at 19 kV, and the second ion source voltage was held at 16.7 kV. Reflector voltages used were 21 kV (the first) and 9.55 kV (the second). The experiments were made with 1000 laser shots per individual spot with random walk applied (FlexImaging 4.0). A random spot measurement pattern was used for all MSI experiments. All spectra were calibrated with the use of silver ions ($^{109}Ag^+$ to $^{109}Ag_{10}^+$). All of the generated ion images were within the ±0.05% m/z range. TIC normalization was used for all results shown.

LDI Sample Preparation

Stock solution (0.1 mg/mL) of each analyte was prepared by dissolving it in water (histidine, ribose, thymidine). In order to prepare analyte solutions of lower concentrations, the stock solution was diluted with ultrapure water. A solution of poly(propylene glycol) in isopropanol of a 10 μg/mL concentration was prepared. A 0.5 μL volume of each of the final solutions was applied to the steel target and air-dried followed by nebulization with the ^{109}AgNP suspension.

MALDI Sample Preparation

MALDI experiments were performed using a DHB matrix solution (saturated matrix in acetonitrile with 0.5% of trifluoroacetic acid) by the drying droplet method (1:1 v/v matrix:sample solution). A volume of 1 μL of sample mixed with matrix solution was placed directly on steel plate and air-dried, and the target was inserted into an MS apparatus for measurement. Calibration was performed on matrix signals.

Imaging Sample

Preparation of the ungroomed fingerprint for mass spectrometry imaging was obtained by touching the clean steel target for approximately 1 s. Then, the object was covered with a layer of nanoparticles by nebulization, as described in paragraph 2.3.

High-Resolution Scanning Electron Microscopy (HR SEM)

A target modified with ^{109}AgNPs generated by a PFL 2D GS method was inserted into the Helios Nanolab 650 electron microscope. The voltage was set at 10 and 30 kV, and the current was set as 0.2 nA. Images were made in nonimmersive mode.

RESULTS AND DISCUSSION

PFL 2D GS LASiS of ^{109}AgNPs

The laser mass spectrometry usually is realized via MALDI methodology. It employs organic low-molecular-weight matrices, such as α-cyano-4-hydroxycinnamic acid (CHCA) and 2,5-dihydroxybenzoic acid (DHB). This methodology is preferred only for ionic substances, such as peptides and proteins of molecular weights higher than 1000 Da due to (i) numerous matrix signals in the region of m/z < 1000, (ii) unreliable calibration, (iii) low mass accuracy, (iv) low ionization potential for neutral organic compounds, and (v) the sweet-spot effect. Moreover, due to the acidity of the standard matrix solutions, the analysis of various substances may be problematic.[31]

Most of above-mentioned MALDI problems may be solved by using metal nanoparticles, for example, silver ones, as desorption/ionization agents.[16,21,32] Silver nanoparticles were produced by different means including chemical, physical, and biological methods. Chemical synthesis is most commonly used to obtain AgNPs. The reaction involves the reduction of Ag^+ to elemental silver by electron transfer under various conditions. The chemical reduction method requires two substances: a metal salt precursor and a reducing agent. However, almost all procedures contain also a stabilizer. Among the many silver precursors, we can distinguish silver nitrate, silver ammonia complexes, and silver sulfate. In turn, the role of the reducing agent is often assumed by sodium borohydride or sodium citrate. Both the type of precursor and reductant used can influence the properties of the AgNPs obtained.[21] Preparation of silver nanoparticles by a chemical reduction method for laser mass spectrometry was presented by Hua and co-workers. Authors used silver nitrate as the metal precursor and sodium cyanoborohydride as the reducing agent.

https://doi.org/10.1021/acsmeasuresciau.1c00020
ACS Meas. Sci. Au 2022, 2, 14−22

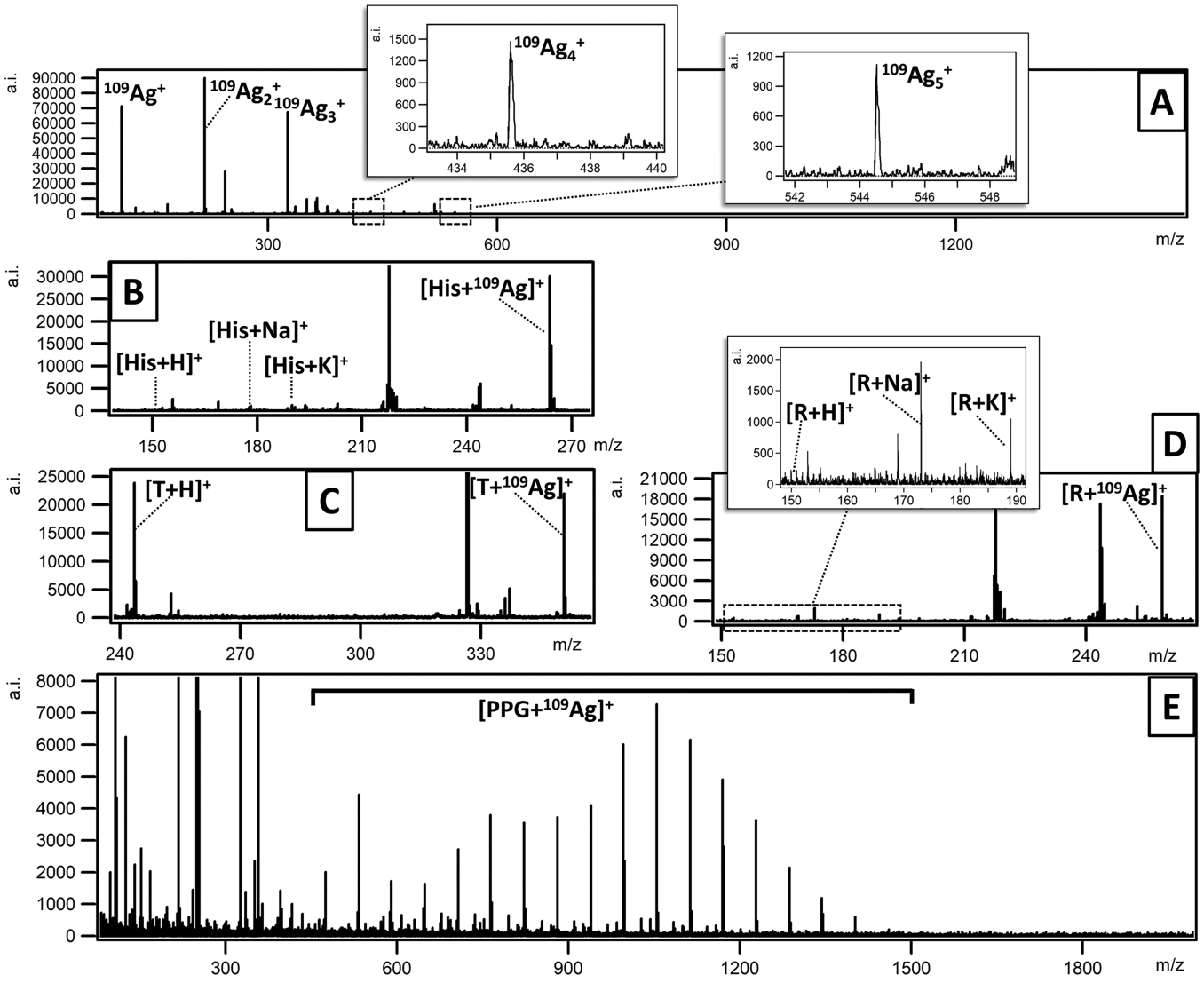

Figure 2. LDI MS positive reflectron mode spectrum of target plate covered with ^{109}AgNPs generated by PFL 2D GS (A). Others panels present LDI MS spectra fragments for histidine (B), thymidine (C), and ribose (D) of 0.1 mg/mL concentrations deposited on the target plate and covered with silver-109 nanoparticles obtained with PFL 2D GS LASiS. The last panel (E) presents an LDI MS spectrum of poly(propylene glycol) of a 10.0 μg/mL concentration spot at the same target as the above-mentioned compounds.

AgNPs were used as matrices for studying the MALDI MS of peptides such as bradykinin and angiotensin I. The obtained results present only proton adducts of the mentioned compounds along with a relatively high noise level.[33] In contrast, Sherrod et al. used commercially available 20 and 60 nm silver nanoparticles to ionize peptides and observed no signals on the MS spectrum.[34] Ding and co-workers used a chemical reduction method to obtain silver nanoparticles of different sizes. Silver nitrate or silver perchlorate was used as the metal precursor, while sodium citrate and/or sodium borohydride was used as the reducing agent. The AgNPs obtained were used as a matrix for amyloid-beta peptide MALDI-ToF-MS measurements. However, the processes of purifying the suspension from reaction byproducts or unreacted substrates make this method of producing silver nanoparticles very time-consuming and complicated.[35]

The above-mentioned problems were partly solved by Yonezawa and co-workers, who were the first to demonstrate a method for producing nanoparticles by laser ablation in an aqueous medium and their applicability as a matrix for laser MS.[24] Compared to chemical synthesis, laser ablation synthesis in solution has some very unique properties including: (i) cost-effectiveness, (ii) simplicity, (iii) time-efficiency, (iv) spectrum simplicity and low chemical background, (v) the ability to prepare NPs from a variety of metals or alloys, and (vi) in situ dispersion of the nanoparticles in a variety of liquids. In general, LASiS produces suspensions of a relatively high chemical purity as compared to chemical methods.

In this work, LASiS has been used to obtain chemically pure monoisotopic silver-109 nanoparticles. Natural silver contains two isotopes: ^{107}Ag (ca., 51.8%) and ^{109}Ag (ca., 48.2%). It is logical to state that the use of monoisotopic silver-based MS methods provide analyte peaks that are roughly 2-fold higher in intensity compared to normal silver. Signals based on a single silver-109 isotope have also a higher signal-to-noise (S/N) ratio. What is more, internal calibration with the use of silver-109 signals is greatly improved due to many times higher intensity and S/N of complex Ag_x^+ (x = 2−30) ions compared to normal silver.

https://doi.org/10.1021/acsmeasuresciau.1c00020
ACS Meas. Sci. Au 2022, 2, 14−22

Nanoparticles were generated by a pulsed 1064 nm fiber laser with galvoscanner head scanning of an ablated surface. The experimental setup for the ^{109}AgNP preparation is shown in Figure 1A. For fast synthesis of nanoparticles, a high-frequency (60−80 kHz), high-pulse-energy (up to 1 mJ/pulse) laser was used. However, in order to avoid unwanted thermal effects such as melting, solvent boiling, and oxidation of solvent and also of nanoparticles, a two-dimensional (2D) galvoscanner (GS) was used. A galvoscanner head with an f-theta lens attached to a fiber laser allowed for precise and very fast shifting of a focused laser beam on the surface of an ablated metal foil.

Prepared nanoparticles were first studied by UV−vis spectroscopy. Particular wavelengths of light can induce the metallic electrons to oscillate, which causes an effect known as surface plasmon resonance (SPR). It is associated with a specific size and shape of the silver nanoparticles as well as chemical surroundings. Therefore, the UV−vis spectroscopy method can be of some aid in determining the size and shape of nanoparticles. The literature describes that as the diameter of AgNPs increases, the absorbance band shifts toward longer wavelengths and also broadens.[36,37] The UV−vis spectrum obtained for PFL 2D GS LASiS of ^{109}AgNPs is shown in Figure 1C. The ^{109}AgNP postreaction suspension UV−vis spectrum recorded after 3 min of synthesis contains a local maximum at 394 nm, which suggests that the size of most of nanoparticles is approximately 10 nm. However, one can observe an asymmetric broadening of the SPR toward longer wavelengths, which is characteristic for a fraction of spheroidal particles. The occurrence of spheroids may indicate particle aggregation processes taking place in the suspension.[29] Similar results were reported by several authors.[21,29,36]

Figure 1D presents the results of dynamic light scattering (DLS) measurement of ^{109}AgNP size distribution by number after a few minutes after preparation of a suspension. The DLS chart of the size distribution by number indicates the highest content of nanoparticles being around 30 nm in diameter, with a distribution ranging from 20 to 100 nm. A high-resolution scanning electron microscope image of a modified target (Figure 1E) also confirms that individual nanoparticles are in roughly round/spherical shape and are of 25−35 nm size. A number of HRTEM and DLS results on size measurements of silver nanoparticles obtained with LASiS in different organic solvents indicate that NPs with a size of ∼10 nm are the most common group.[21,29] DLS results suggest bigger nanoparticles as judged from a UV−vis spectrum. Most probably, this is due the fact that the nanoparticle suspension used for the DLS measurement was prepared in a different solvent than the one optimized for LASiS. Many studies show the effect of solvent on the size of nanoparticles obtained.[29]

Application of nanoparticles in laser mass spectrometry requires a suitable method of application on the surface containing a studied object, which may be, for example, a sample spot or tissue slice. One approach of using AgNPs as a matrix is dry metal sputtering, which allows for preparation of a homogeneous layer with minimal or no lateral migration of the analyte on the laser beam size scale.[38] Silver deposition by sputtering has been applied to various types of samples, including fingerprints,[39] but also to a human carotid[40] or samples of colorectal cancer metastases to the liver.[41] However, the prevalence of this method is low, probably due to the need for a specialized sputtering system. Moreover, sputtering requires that a sample is treated in very high vacuum, which can be problematic for some of tissues due to warping and cracking. Yang, Fournelle, and Chaurand presented silver-assisted laser desorption ionization (AgLDI) MSI, where a silver salt solution was sprayed to obtain a homogeneous layer on thin tissue sections. However, the method did not achieve the same high spatial resolution as Dufresne et al. or other researchers.[38,42]

For our LDI MS measurements, 0.5 μL of each of solution of histidine, ribose, thymidine, and PPG polymer was applied to a stainless-steel plate and air-dried. The plate with all test objects was placed on the table of the translation system as shown in Figure 2B. Aliquots of colloidal silver-109 (1 mL) were sprayed three times onto the sample. Each portion was injected into the nebulizer at a constant rate of 250 μL/min. The entire nanoparticle nebulization process was controlled by a computer using a sequence of movements aimed at evenly covering the target plate.

The LDI MS spectrum of ^{109}AgNPs produced by PFL 2D GS LASiS and deposited on the surface of stainless steel of target plate by nebulization is shown in Figure 2A. The mass spectrum made in the 80−1500 m/z range contains virtually only silver-109 ion peaks of $^{109}Ag^+$ to $^{109}Ag_{10}^+$ composition. Various low-molecular-weight compounds such as ionic amino acid histidine and nonionic ribose and thymidine were tested to verify the potential of ionization of organic compounds with the silver-109 nanoparticles obtained with PFL 2D GS LASiS.

The first analyzed compound histidine (Figure 2B) was found mainly as a ^{109}Ag adduct but sodium, potassium, and protonated adducts signals were also found. Histidine was recently analyzed on diamond nanowires acting as an LDI active surface, presenting a spectrum with a number of unknown signals in the m/z 50−250 region.[43] Our previous attempt to analyze histidine was made using a ^{109}AgNPET target. The S/N ratio of the histidine−^{109}Ag adduct for ^{109}AgNPET was 214,[44] while for PFL 2D GS LASiS, ^{109}AgNPs is higher at 280. What is more, the target covered by PFL 2D GS LASiS ^{109}AgNPs that is ready for mass spectrometry can be made within 10 min of time, which is in contrast to our previous method ^{109}AgNPET, where target preparation took 48 h.

Thymidine was also tested as a very good example of a biologically important, medium-polarity nonionic compound. The LDI MS spectrum of thymidine (T; 0.1 mg/mL) with PFL 2D GS LASiS ^{109}AgNPs in reflectron positive mode is shown in Figure 2C. The thymidine MS spectrum obtained with the use of PFL 2D GS LASiS ^{109}AgNPs shows two highest peaks, assigned to a thymidine−silver adduct with an S/N ratio of 138 and protonated with an S/N ratio of 175. Measuring nucleosides using modified graphene as a matrix was shown by Wang et al.; however, the results presented a low S/N ratio.[45]

Another compound tested was ribose, a nonionic medium-polarity saccharide. The LDI MS spectrum within m/z 80−1500 in reflectron positive mode of ribose on a target covered by PFL 2D GS LASiS ^{109}AgNPs is shown in Figure 2D. The highest peak visible in the spectrum belongs to the ribose−$^{109}Ag^+$ adduct. Protonated, potassium, and sodium adducts were also visible, and the S/N ratios for protonated, sodium, potassium, and ribose−^{109}Ag adducts were 3, 23, 12, and 150, respectively. Bibi and Ju utilized quantum dots (QDs) with some modifications as a matrix for LDI-TOF MS to small monosaccharides including ribose.[46] In contrast, Zhang and colleagues showed that the use of traditional MALDI matrices such as DHB or CHCA is not suitable for the analysis of small

https://doi.org/10.1021/acsmeasuresciau.1c00020
ACS Meas. Sci. Au 2022, 2, 14−22

oligosaccharides such as ribose. The matrix-derived peaks were dominant on the spectrum and were the cause of ribose signal suppression.[47]

Poly(propylene glycol) is a compound belonging to the polymer group, consisting of propylene oxide-mers. The repeating monomer unit mass of approximately 57.9 is of the $CH_2CH(CH_3)O$ chemical formula. The LDI mass spectrum of PPG is shown in Figure 3E. As can be seen, the spectrum

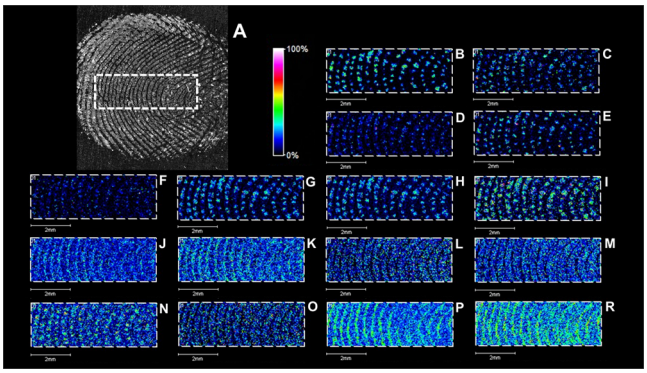

Figure 3. Results of LDI MS imaging of a fingerprint with PFL 2D GS LASiS ^{109}AgNPs. Optical microscope images of a fingerprint (A). Images (B–R) (TIC-normalized) represent spatial distribution of ions of m/z 96.922 (B), 98.996 (C), 106.050 (D), 148.061 (E), 178.0592 (F), 183.078 (G), 183.175 (H), 185.069 (I), 240.947 (J), 241.942 (K), 283.264 (L), 311.295 (M), 333.119 (N), 334.283 (O), 363.324 (P), and 391.355 (R). Spatial resolution 40 × 40 μm.

contains a typical polymer structure with a dominating mass of approximately m/z 1000, which positively corroborates with the polymer used. For example, the highest polymer signal at m/z 1055 revealed is the $^{109}Ag^+$ ion adduct of a PPG with 16-mer units. Comparison of polypropylene glycol spectra between MALDI and SALDI were made by Okuno et al. The authors identified a problem with the reproducibility of MALDI mass spectra for PPG, which showed a strong dependence on the analyte/matrix ratio and on the type of solvent and/or chemical matrix.[48]

Comparison of the new method with previously published ones is shown in Table 1. The upper part of table presents comparison of m/z matching errors (calculated and experimental) of a few test low-molecular-weight compounds shown as ppm values. Very big, unacceptable m/z errors of MALDI are surely an effect of calibration performance. The silver-method-based spectrum was calibrated with the use of nine signals, while the MALDI one was calibrated with only two matrix signals. It should be noted that the ribose signal is marked as "not found" as a big m/z difference and low intensity did not allow it to be assigned. The lower part of Table 1 contains comparison of previously published method ^{109}AgNPET that is based on the chemical synthesis of nanoparticles with the one based on PFL 2D GS LASiS. It is clearly seen that PFL 2D GS LASiS ^{109}AgNPs produce much higher signals under laser irradiation, which in turn allows better calibration, especially in the higher m/z region.

Table 1. Comparison of Mass Spectrometry Data of PFL GS LASiS Nanoparticles with Chemically Synthesized Ones (AgNPET) and Also with MALDI

	calculated−experimental m/z errors in ppms Δ m/z [ppm]	
compound	MALDI	PFL 2D GS LASiS
histidine	184	8
thymidyne	314	12
ribose	not found	7
3-methylhippuric acid	1207	21
alternariol	77	8
	comparison of signal intensity	
	^{109}AgNPET [16]	PFL 2D GS LASiS ^{109}AgNPs
$^{109}Ag^+$	14 453	59 969
$^{109}Ag_2^+$	21 351	89 591
$^{109}Ag_3^+$	19 818	77 933
$^{109}Ag_4^+$	386	1810
$^{109}Ag_5^+$	785	10 579

MS Imaging with PFL 2D GS LASiS ^{109}AgNPs

The fingerprint was chosen as a test subject to determine the applicability of PFL 2D GS LASiS ^{109}AgNPs for imaging exogenous and endogenous compounds on a human finger. Francese and co-workers[49] were the first to demonstrate the applicability of MALDI MSI for fingerprint trace analysis. The fingerprint is one of the most important means of biometric identification, as it is a source of both physical and chemical information. The physical information provided by a fingerprint is the geometry, distribution, and size of sweat pores and also local shapes such as terminations, bifurcations, islands, spurs, etc. Chemical information found on fingerprints includes exogenous and endogenous substances, including drugs, explosives, toxins, poisons, cosmetics, toiletries, etc. Endogenous compounds found on the skin include lipids, peptides, amino acids, proteins, urea, simple inorganic compounds, as well as organic salts.

The LDI MS imaging experiment involved a fingerprint left on the stainless-steel surface. Preparation of the fingerprint is extremely simple, and only requires a finger to touch the target surface. A suspension of monoisotopic silver-109 nanoparticles was sprayed onto the obtained fingerprint. Table 2 contains names and ion data for some of the compounds found in the imaging experiment. Ion images for some of the ions from Table 2 are shown in Figure 3 and the Supporting Information (S1).

The compounds that were identified in the studied fingerprint belong to different groups such as inorganic salts (e.g., NaCl, KCl), simple organic compounds (e.g., urea, amino acids, short carboxylic acids), fatty acids, lipids, and others. Most of these compounds are considered endogenous, secreted through the skin or sweat pores.

Ion images for ions presented in Table 2 are shown in Figure 3. In the fingerprint, six amino acids such as serine, cysteine, glutamic acid, asparagine, histidine, and lysine were detected. Figure 3 contains four images showing the spatial distribution of amino acids with the following m/z values of 106.050 (D), 148.061 (E), 178. 0592 (F), and 185.0692 (I), which were assigned to protonated serine, protonated glutamic acid, a histidine−sodium adduct, and a lysine−potassium adduct, respectively. As judged from the ion image, these amino acid ions are found in close proximity to sweat pores, which produce round structures rich in the mentioned ions. Numerous studies show that amino acids/proteins are one of the most numerous groups of compounds present in a fingerprint.[50] Figure 3 also contains images showing ions with relatively low m/z, such as 96.922 (B) and 98.996 (C) assigned to adduct $[KClNa]^+$ and a urea−potassium adduct.

https://doi.org/10.1021/acsmeasuresciau.1c00020
ACS Meas. Sci. Au 2022, 2, 14−22

Table 2. Compounds and Their Ions Found in MSI Experiment

	compound[a]	ion formula	$m/z_{calc.}$[b]	
1.	KCl	$[KCl + Na]^+$	96.9223	Figure 3B
2.	urea	$[CH_4N_2O + K]^+$	98.9961	Figure 3C
3.	1-hexanoic acid	$[C_6H_{12}O_2 - H_2O + H]^+$	99.0810	S1.A
4.	serine	$[C_3H_7NO_3 + H]^+$	106.0504	Figure 3D
5.	1-hexanoic acid	$[C_6H_{12}O_2 + H]^+$	117.0916	S1.B
6.	L-cysteine	$[C_3H_7NO_2S + H]^+$	122.0276	S1.C
7.	L-glutamic acid	$[C_5H_9NO_4 + H]^+$	148.0610	Figure 3E
8.	2-aminoadipic acid	$[C_6H_{10}O_4 + Na]^+$	169.0477	S1.D
9.	asparagine	$[C_4H_8N_2O_3 + K]^+$	171.0172	S1.E
10.	histidine	$[C_6H_9N_3O_2 + Na]^+$	178.0592	Figure 3F
11.	octanoic acid	$[C_8H_{16}O_2 + K]^+$	183.0787	Figure 3G
12.	dodecanoic acid	$[C_{12}H_{24}O_2 - H_2O + H]^+$	183.1749	Figure 3H
13.	2-aminoadipic acid	$[C_6H_{10}O_4 + K]^+$	185.0216	S1.F
14.	L-lysine	$[C_6H_{14}N_2O_2 + K]^+$	185.0692	Figure 3I
15.	pyruvic acid	$[C_3H_4O_3 + {}^{109}Ag]^+$	196.9208	S1.G
16.	glyceric acid	$[C_3H_6O_4 + {}^{109}Ag]^+$	214.9313	S1.H
17.	pentyl 2-hydroxybenzoate	$[C_{12}H_{16}O_2 + Na]^+$	215.1048	S1.I
18.	glutaric acid	$[C_5H_8O_4 + {}^{109}Ag]^+$	240.9470	Figure 3J
19.	asparagine	$[C_4H_8N_2O_3 + {}^{109}Ag]^+$	240.9582	S1.J
20	aspartic acid	$[C_4H_7NO_4 + {}^{109}Ag]^+$	241.9422	Figure 3K
21.	phenylacetic acid	$[C_8H_8O_2 + {}^{109}Ag]^+$	244.9572	S1.K
22.	3-oxoglutaric acid	$[C_5H_6O_5 + {}^{109}Ag]^+$	254.9262	S1.L
23.	mevalonic acid	$[C_6H_{12}O_4 + {}^{109}Ag]^+$	256.9783	S1.M
24.	ribose	$[C_5H_{10}O_5 + {}^{109}Ag]^+$	258.9575	S1.N
25.	9-octadecenoic acid	$[C_{18}H_{34}O_2 + H]^+$	283.2637	Figure 3L
26.	*cis*-13-eicosenoic acid	$[C_{20}H_{38}O_2 + H]^+$	311.2950	Figure 3M
27.	pentadecenoic acid	$[C_{15}H_{28}O + {}^{109}Ag]^+$	333.1187	Figure 3N
28.	methyl linoleate	$[C_{19}H_{34}O_2 + K]^+$	333.2196	S1.O
29.	*cis*-13-eicosenoic acid	$[C_{20}H_{38}O_2 + Na]^+$	333.2770	S1.P
30.	*N*-dodecyl-4-methyl-1-piperazine carboxamide	$[C_{18}H_{37}N_3O + Na]^+$	334.2834	Figure 3O
31.	tricosanoic acid	$[C_{23}H_{46}O_2 - H_2O + H]^+$	337.3470	S1.R
32.	butyl octadecanoate	$[C_{22}H_{44}O_2 + Na]^+$	363.3239	Figure 3P
33.	tetracosanoic acid	$[C_{24}H_{48}O_2 + Na]^+$	391.3552	Figure 3R

[a]Putative identification. [b]$m/z_{calc.}$ – calculated monoisotopic m/z value.

These ions correspond to compounds secreted directly by sweat pores (KCl/NaCl and urea) that can be used to localize sweat pores as well as dorsal patterns.

Another group of compounds that were detected in the fingerprint were free fatty acids such as octanoic, dodecanoic, octadecenoic acid, eicosenoic, pentadecenoic, and tetracosanoic acids. Figure 3 presents ion images showing the spatial distribution of mentioned fatty acids with the following m/z values of 183.0787 (G), 183.1749 (H), 283.2637 (L), 311.2950 (M), 333.1187 (N), and 391.3552 (R), which are attributed to an octanoic acid–potassium adduct, protonated dodecanoic acid with water molecule loss, protonated 9-octadecenoic acid and protonated *cis*-13-eicosanoic acid, a pentadecenoic acid–silver-109 adduct, and a tetracosanoic acid–sodium adduct, respectively. The mentioned ions are presenting very clearly representations of fingerprint ridges. Free fatty acids were previously identified in a fingerprint using different analytical techniques such as MALDI or SALDI MS.[50]

CONCLUSIONS

A novel method for synthesis and application of monoisotopic silver-109 nanoparticles onto a studied surface for LDI MS and MSI is presented. The methodology was proven to be very useful for analysis and MS imaging of low-molecular-weight (LMW) compounds and polymers as well as for mass spectrometry imaging. LASiS with the use of 1064 nm pulsed nanosecond fiber laser on galvomotors allowed highly efficient synthesis of nanoparticles of extremely high chemical purity. LASiS of ^{109}AgNPs coupled with nebulization was used for surface-transfer mass spectrometry imaging of a fingerprint, allowing investigation of ridge patterns and sweat pores as well as determination of spatial distribution of compounds.

ASSOCIATED CONTENT

Supporting Information

The Supporting Information is available free of charge at https://pubs.acs.org/doi/10.1021/acsmeasuresciau.1c00020.

Ion images of fingerprint (PDF)

AUTHOR INFORMATION

Corresponding Author

Tomasz Ruman – *Rzeszów University of Technology, Faculty of Chemistry, Inorganic and Analytical Chemistry Department, 35-959 Rzeszów, Poland;* orcid.org/0000-0002-9899-8627; Phone: (+48 17) 865-1896; Email: tomruman@prz.edu.pl

Authors

Aneta Płaza – *Doctoral School of Engineering and Technical Sciences at the Rzeszów University of Technology, Rzeszów 35-959, Poland;* orcid.org/0000-0003-1719-8730

Artur Kołodziej – *Doctoral School of Engineering and Technical Sciences at the Rzeszów University of Technology,*

https://doi.org/10.1021/acsmeasuresciau.1c00020
ACS Meas. Sci. Au 2022, 2, 14–22

Rzeszów 35-959, Poland; orcid.org/0000-0002-9222-0937

Joanna Nizioł − *Rzeszów University of Technology, Faculty of Chemistry, Inorganic and Analytical Chemistry Department, 35-959 Rzeszów, Poland*

Complete contact information is available at: https://pubs.acs.org/10.1021/acsmeasuresciau.1c00020

Author Contributions

The manuscript was written through equal contributions of all authors. All authors have given approval to the final version of the manuscript.

Notes

The authors declare no competing financial interest.

■ ACKNOWLEDGMENTS

Mrs. Małgorzata Walczak is acknowledged for DLS measurements. Zuzanna Krupa is acknowledged for providing a fingerprint. This work was supported by the National Science Centre (NCN), SONATA grant no. UMO-2018/31/D/ST4/00109.

■ REFERENCES

(1) Tanaka, K.; Waki, H.; Ido, Y.; Akita, S.; Yoshida, Y.; Yoshida, T.; Matsuo, T. Protein and polymer analyses up to m/z 100,000 by laser ionization time-of-flight mass spectrometry. *Rapid Commun. Mass Spectrom.* **1988**, *2*, 151−153.

(2) Karas, M.; Hillenkamp, F. Laser Desorption Ionization of Proteins with Molecular Masses Exceeding 10 000 Da. *Anal. Chem.* **1988**, *60*, 2299−2301.

(3) Albrethsen, J. Reproducibility in protein profiling by MALDI-TOF mass spectrometry. *Clin. Chem.* **2007**, *53*, 852−858.

(4) Tost, J.; Gut, I. G. DNA analysis by mass spectrometry—past, present and future. *J. Mass Spectrom.* **2006**, *41*, 981−995.

(5) Estrada, R.; Yappert, M. C. Alternative approaches for the detection of various phospholipid classes by matrix-assisted laser desorption/ionization time-of-flight mass spectrometry. *J. Mass Spectrom.* **2004**, *39*, 412−422.

(6) Leopold, J.; Popkova, Y.; Engel, K. M.; Schiller, J. Recent developments of useful MALDI matrices for the mass spectrometric characterization of lipids. *Biomolecules* **2018**, *8* (4), 173.

(7) Kołodziej, A.; Ruman, T.; Nizioł, J. Gold and silver nanoparticles-based laser desorption/ionization mass spectrometry method for detection and quantification of carboxylic acids. *J. Mass Spectrom.* **2020**, *55*, e4604.

(8) Domon, B.; Aebersold, R. Mass spectrometry and protein analysis. *Science* **2006**, *312* (5771), 212−217.

(9) Berkenkamp, S.; Kirpekar, F.; Hillenkamp, F. Infrared MALDI mass spectrometry of large nucleic acids. *Science* **1998**, *281* (5374), 260−262.

(10) Shrivas, K.; Wu, H. F. Single drop microextraction as a concentrating probe for rapid screening of low molecular weight drugs from human urine in atmospheric-pressure matrix-assisted laser desorption/ionization mass spectrometry. *Rapid Commun. Mass Spectrom.* **2007**, *21*, 3103−3108.

(11) Ha, M. S.; Seo, H.; Bae, D. H.; Yeo, W. S. Detection of enrofloxacin and its metabolite ciprofloxacin using gold nanoparticles and laser desorption/ionization time-of-flight mass spectrometry. *Anal. Sci.* **2014**, *30* (4), 451−455.

(12) López de Laorden, C.; Beloqui, A.; Yate, L.; Calvo, J.; Puigivila, M.; Llop, J.; Reichardt, N. C. Nanostructured indium tin oxide slides for small-molecule profiling and imaging mass spectrometry of metabolites by surface-assisted laser desorption ionization MS. *Anal. Chem.* **2015**, *87* (1), 431−440.

(13) Chiang, C. K.; Chen, W. T.; Chang, H. T. Nanoparticle-based mass spectrometry for the analysis of biomolecules. *Chem. Soc. Rev.* **2011**, *40* (3), 1269−1281.

(14) Abdelhamid, H. N. Nanoparticle assisted laser desorption/ionization mass spectrometry for small molecule analytes. *Microchim. Acta* **2018**, *185*, 200.

(15) Chu, H. W.; Unnikrishnan, B.; Anand, A.; Mao, J. Y.; Huang, C. C. Nanoparticle-based laser desorption/ionization mass spectrometric analysis of drugs and metabolites. *J. Food Drug Anal.* **2018**, *26*, 1215−1228.

(16) Nizioł, J.; Rode, W.; Laskowska, B.; Ruman, T. Novel monoisotopic ^{109}AgNPET for laser desorption/ionization mass spectrometry. *Anal. Chem.* **2013**, *85*, 1926−1931.

(17) Sekuła, J.; Nizioł, J.; Rode, W.; Ruman, T. Gold nanoparticle-enhanced target (AuNPET) as universal solution for laser desorption/ionization mass spectrometry analysis and imaging of low molecular weight compounds. *Anal. Chim. Acta* **2015**, *875*, 61−72.

(18) Das, R. K.; Pachapur, V. L.; Lonappan, L.; Naghdi, M.; Pulicharla, R.; Maiti, S.; Cledon, M.; Dalila, L. M. A.; Sarma, S. J.; Brar, S. K. Biological synthesis of metallic nanoparticles: plants, animals and microbial aspects. *Nanotechnol. Environ. Eng.* **2017**, *2*, 18.

(19) Bayda, S.; Adeel, M.; Tuccinardi, T.; Cordani, M.; Rizzolio, F. The History of Nanoscience and Nanotechnology: From Chemical−Physical Applications to Nanomedicine. *Molecules* **2020**, *25*, 112.

(20) Magro, M.; Zaccarin, M.; Miotto, G.; Da Dalt, L.; Baratella, D.; Fariselli, P.; Gabai, G.; Vianello, F. Analysis of hard protein corona composition on selective iron oxide nanoparticles by MALDI-TOF mass spectrometry: identification and amplification of a hidden mastitis biomarker in milk proteome. *Anal. Bioanal. Chem.* **2018**, *410*, 2949−2959.

(21) Xu, L.; Wang, Y.-Y.; Huang, J.; Chen, C.-Y.; Wang, Z.-X.; Xie, H. Silver nanoparticles: Synthesis, medical applications and biosafety. *Theranostics* **2020**, *10*, 8996−9031.

(22) McLean, J. A.; Stumpo, K. A.; Russell, D. H. Size-selected (2−10 nm) gold nanoparticles for matrix assisted laser desorption/ionization of peptides. *J. Am. Chem. Soc.* **2005**, *127*, 5304−5305.

(23) Pilolli, R.; Palmisano, F.; Cioffi, N. Gold nanomaterials as a new tool for bioanalytical applications of laser desorption ionization mass spectrometry. *Anal. Bioanal. Chem.* **2012**, *402*, 601−623.

(24) Yonezawa, T.; Kawasaki, H.; Tarui, A.; Watanabe, T.; Arakawa, R.; Shimada, T.; Mafune, F. Detailed investigation on the possibility of nanoparticles of various metal elements for surface assisted laser desorption/ionization mass spectrometry. *Anal. Sci.* **2009**, *25*, 339−346.

(25) Amendola, V.; Litti, L.; Meneghetti, M. LDI-MS assisted by chemical-free gold nanoparticles: enhanced sensitivity and reduced background in the low-mass region. *Anal. Chem.* **2013**, *85*, 11747−11754.

(26) Rafique, M.; Rafique, M. S.; Kalsoom, U.; Afzal, A.; Butt, S. H.; Usman, A. Laser ablation synthesis of silver nanoparticles in water and dependence on laser nature. *Opt. Quantum Electron.* **2019**, *51*, 179.

(27) Sadrolhosseini, A. R.; Mahdi, M. A.; Alizadeh, F.; Rashid, S. A. Laser Ablation Technique for Synthesis of Metal Nanoparticle in Liquid. In *Laser Technology and its Applications*; Ma, Y., Ed.; IntechOpen, 2018; pp 63−81.

(28) Freeland, B.; McCann, R.; Alkan, G.; Friedrich, B.; Foley, G.; Brabazon, D. Stable nano-silver colloid production via Laser Ablation Synthesis in Solution (LASiS) under laminar recirculatory flow. *Advances in Materials and Processing Technologies* **2020**, *6*, 677−685.

(29) Amendola, V.; Polizzi, S.; Meneghetti, M. Free silver nanoparticles synthesized by laser ablation in organic solvents and their easy functionalization. *Langmuir* **2007**, *23*, 6766−6770.

(30) Sportelli, M. C.; Izzi, M.; Volpe, A.; Clemente, M.; Picca, R. A.; Ancona, A.; Lugarà, P. M.; Palazzo, G.; Cioffi, N. The Pros and Cons of the Use of Laser Ablation Synthesis for the Production of Silver Nano-Antimicrobials. *Antibiotics* **2018**, *7*, 67.

(31) Ruman, T.; Długopolska, K.; Jurkiewicz, A.; Rut, D.; Frączyk, T.; Ciesla, J.; Leś, A.; Szewczuk, Z.; Rode, W. Thiophosphorylation of

free amino acids and enzyme protein by thiophosphoramidate ions. *Bioorg. Chem.* **2010**, *38*, 74−80.
(32) Nizioł, J.; Ruman, T. Surface-transfer mass spectrometry imaging on monoisotopic silver nanoparticle enhanced target. *Anal. Chem.* **2013**, *85*, 12070−12076.
(33) Hua, L.; Chen, J.; Ge, L.; Tan, S. N. Silver nanoparticles as matrix for laser desorption/ionization mass spectrometry of peptides. *J. Nanopart. Res.* **2007**, *9*, 1133−1138.
(34) Sherrod, S. D.; Diaz, A. J.; Russell, W. K.; Cremer, P. S.; Russell, D. H. Silver Nanoparticles as Selective Ionization Probes for Analysis of Olefins by Mass Spectrometry. *Anal. Chem.* **2008**, *80*, 6796−6799.
(35) Jamkhande, P. G.; Ghule, N. W.; Bamer, A. H.; Kalaskar, M. G. Metal nanoparticles synthesis: An overview on methods of preparation, advantages and disadvantages, and applications. *J. Drug Delivery Sci. Technol.* **2019**, *53*, 101174.
(36) De Leersnyder, I.; Rijckaert, H.; De Gelder, L.; Van Driessche, I.; Vermeir, P. High Variability in Silver Particle Characteristics, Silver Concentrations, and Production Batches of Commercially Available Products Indicates the Need for a More Rigorous Approach. *Nanomaterials* **2020**, *10*, 1394.
(37) Desai, R.; Mankad, V.; Gupta, S.; Jha, P. Size Distribution of Silver Nanoparticles: UV-Visible Spectroscopic Assessment. *Nanosci. Nanotechnol. Lett.* **2012**, *4* (1), 30−34.
(38) Dufresne, M.; Thomas, A.; Breault-Turcot, J.; Masson, J.-F.; Chaurand, P. Silver-Assisted Laser Desorption Ionization for High Spatial Resolution Imaging Mass Spectrometry of Olefins from Thin Tissue Sections. *Anal. Chem.* **2013**, *85* (6), 3318−3324.
(39) Gustafsson, O. J. R.; Guinan, T. M.; Rudd, D.; Kobus, H.; Benkendorff, K.; Voelcker, N. H. Metabolite mapping by consecutive nanostructure and silver-assisted mass spectrometry imaging on tissue sections. *Rapid Commun. Mass Spectrom.* **2017**, *31* (12), 991−1000.
(40) Patterson, N. H.; Doonan, R. J.; Daskalopoulou, S. S.; Dufresne, M.; Lenglet, S.; Montecucco, F.; Thomas, A.; Chaurand, P. Three-dimensional imaging MS of lipids in atherosclerotic plaques: Open-source methods for reconstruction and analysis. *Proteomics* **2016**, *16*, 1642−1651.
(41) Patterson, N. H.; Yang, E.; Kranjec, E. A.; Chaurand, P. Co-registration and analysis of multiple imaging mass spectrometry datasets targeting different analytes. *Bioinformatics* **2019**, *35* (7), 1261−1262.
(42) Perdian, D. C.; Cha, S.; Oh, J.; Sakaguchi, D. S.; Yeung, E. S.; Lee, Y. J. In situ probing of cholesterol in astrocytes at the single-cell level using laser desorption ionization mass spectrometric imaging with colloidal silver. *Rapid Commun. Mass Spectrom.* **2010**, *24* (8), 1147−1154.
(43) Coffinier, Y.; Szunerits, S.; Drobecq, H.; Melnyk, O.; Boukherroub, R. Diamond nanowires for highly sensitive matrix-free mass spectrometry analysis of small molecules. *Nanoscale* **2012**, *4*, 231−238.
(44) Arendowski, A.; Nizioł, J.; Ruman, T. Silver-109-based laser desorption/ionization mass spectrometry method for detection and quantification of amino acids. *J. Mass Spectrom.* **2018**, *53*, 369−378.
(45) Dong, X.; Cheng, J.; Li, J.; Wang, Y. Graphene as a Novel Matrix for the Analysis of Small Molecules by MALDI-TOF MS. *Anal. Chem.* **2010**, *82*, 6208−6214.
(46) Bibi, A.; Ju, H. Quantum dots assisted laser desorption/ionization mass spectrometric detection of carbohydrates: qualitative and quantitative analysis. *J. Mass Spectrom.* **2016**, *51*, 291−297.
(47) Zhang, H.; Cha, S.; Yeung, E. S. Colloidal graphite-assisted laser desorption/ionization MS and MS(n) of small molecules. 2. Direct profiling and MS imaging of small metabolites from fruits. *Anal. Chem.* **2007**, *79* (17), 6575−84.
(48) Okuno, S.; Wada, Y.; Arakawa, R. Quantitative analysis of polypropyleneglycol mixtures by desorption/ionization on porous silicon mass spectrometry. *Int. J. Mass Spectrom.* **2005**, *241* (1), 43−48.
(49) Francese, S.; Bradshaw, R.; Ferguson, L. S.; Wolstenholme, R.; Clench, M. R.; Bleay, S. Beyond the ridge pattern: multi-informative analysis of latent fingermarks by MALDI mass spectrometry. *Analyst* **2013**, *138*, 4215−4228.
(50) Girod, A.; Ramotowski, R.; Weyermann, C. Composition of fingermark residue: A qualitative and quantitative review. *Forensic Sci. Int.* **2012**, *223* (1), 10−24.

https://doi.org/10.1021/acsmeasuresciau.1c00020
ACS Meas. Sci. Au 2022, 2, 14−22

Received: 9 August 2021 | Revised: 28 December 2021 | Accepted: 2 February 2022

DOI: 10.1002/jms.4815

RESEARCH ARTICLE

Journal of MASS SPECTROMETRY WILEY

Infrared pulsed fiber laser-produced silver-109-nanoparticles for laser desorption/ionization mass spectrometry of amino acids

Aneta Płaza-Altamer[1] | Artur Kołodziej[1] | Joanna Nizioł[2] | Tomasz Ruman[2]

[1]Doctoral School of Engineering and Technical Sciences, Rzeszów University of Technology, Rzeszów, Poland

[2]Faculty of Chemistry, Rzeszów University of Technology, Rzeszów, Poland

Correspondence
Aneta Płaza-Altamer, Doctoral School of Engineering and Technical Sciences at the Rzeszów University of Technology, 8 Powstańców Warszawy Ave., 35-959 Rzeszów, Poland.
Email: a.plaza@prz.edu.pl

Funding information
National Science Centre (NCN), Grant/Award Number: UMO-2018/31/D/ST4/00109

Abstract

Application of monoisotopic cationic ^{109}Ag nanoparticles (^{109}AgNPs) obtained by pulsed fiber laser (PFL) 2D galvo-scanner (GS) laser generated nanomaterial (LGN) for both high resolution laser desorption/ionization mass spectrometry and mass spectrometry imaging of amino acids is presented. Four amino acids, alanine, isoleucine, lysine, and phenylalanine were used as test compounds for quantification with matrix-assisted laser desorption/ionization mas (MALDI)-type mass spectrometer. Comparison of commonly made manual measurements with semiautomatic mass spectrometry imaging (MSI) was performed providing very interesting findings. Amino acids were directly tested in 1 000 000-fold concentration change conditions ranging from 1 mg/ml to 1 ng/ml, which equates to 500 ng to 500 fg of amino acid per measurement spot. Methods were also tested on samples of human blood plasma for quantification of endogenous amino acids.

KEYWORDS
amino acids, low molecular weight compounds, monoisotopic silver-109 nanoparticles, MSI, quantification

1 | INTRODUCTION

Amino acids are organic compounds that play an important role in the functioning of the body. They are necessary for the proper course of life processes, such as the structure of proteins, enzymes, cells, and the synthesis of hormones and neurotransmitters. The concentration of amino acids in the human body varies depending on the food consumed or the health state. Both high and low values of amino acid concentrations in the body can be indicators of metabolic disorders or developing disease. Amino acids can be found in quite wide concentration range in different biological objects, for example, different amino acids are in approximately 4- to 1500-μM concentration range in human urine.[1] In blood plasma, amino acids are typically found in 7- to 721-μM concentration range.[2] However, amino acids measured in tissue such as liver can be in wide concentration range from 0.01 to 7.5 mmol per kilogram of tissue.[3] Taking into the consideration that measured samples are often extracted and concentrated, the final concentration range in measurement-ready samples can be much wider. Hence, methods of quantification of amino acids working in wide concentration range are needed.

Matrix-assisted laser desorption ionization mass spectrometry (MALDI-MS) is one of the most common soft ionization methods used in modern mass spectrometry (MS) instruments. This method has been applied in various type of analyses e.g. proteomics, microorganism identification or cancer drug analysis.[4,5] Despite all its advantages (high sensitivity, rapidness and efficiency), the MALDI method is rarely used for detection and quantification of low molecular weight (LMW) compounds. The main problem is the need for application of matrices, which are usually low molecular weight acids and during analysis produce variety of ions which may interfere with signals of analyzed sample in low mass range.[6] This problem can be solved with application of nanoparticles instead of traditional organic matrices; many articles have been published showing the use of nanoparticles in LMW analysis.[7–10]

Monoisotopic silver-109 nanoparticles (^{109}AgNPs) were found to be very efficient for cationization of various type of compounds, for example, amino acids, fatty acids, saccharides, or mould toxins.[11–14] In this article, we present quantification result of amino acids on steel plate covered with chemically pure silver-109 nanoparticles produced by a new method with the use of 1064-nm pulsed fiber laser with 2D galvanometer scanner. We also compare manual laser desorption/ionization mass spectrometry (LDI MS) and semiautomatic laser desorption/ionization mass spectrometry imaging (LDI MSI) in quantification of amino acids along with discussion of results and comparison with various surface-assisted laser desorption ionization (SALDI) and MALDI methods previously used in amino acids analysis.

2 | EXPERIMENTAL SECTION

2.1 | Materials

All amino acid standards were purchased from Sigma-Aldrich. Steel targets were machined from H17 stainless steel. Before the LDI MS and MS imaging experiments steel targets were cleaned through soaking in boiling solvents: toluene (3 × 100 ml, each plate for 30 s), chloroform (3 × 100 ml, each plate for 30 s), acetonitrile (3 × 100 ml, each plate for 30 s) and deionized water (3 × 100 ml, each plate for 30 s). Every plate was dried in high vacuum (ca. 0.01 mbar, 24 h). All solvents were of HPLC quality, except for water (18 MΩ · cm water produced locally).

2.2 | Pulsed fiber laser (PFL) 2D galvo-scanner (2D GS) laser generated nanomaterial (LGN) of silver-109 nanoparticles

The silver-109 foil (∼1 mm thick, 99.7% isotopic purity) was bought from Trace Sciences International (USA) was placed at the bottom of a glass vessel containing solvent (acetonitrile). The ^{109}Ag foil was covered by an approximately 3-mm thick layer of acetonitrile (total solvent volume was 3 ml). The laser ablation was carried out with a 1064-nm pulsed fiber laser (Raycus RFL-P20QE/A3). Suspension was obtained after 2 min. Irradiation with pulse energy of 0.8 mJ (100-ns pulse length) at a 40-kHz repetition rate. Laser ablation was accomplished at a scanning speed of 2000 mm/s; the ablation area was 4 × 4 mm. Suspension was immediately transferred into a syringe and used in the nebulization step.

2.3 | Nebulization of ^{109}AgNPs suspension

The entire nanoparticle nebulization process was controlled by a computer. The H17 steel plate (laser mass spectrometry target plate) was placed on the table of a translation system consisting of a motorized XY table (powered by closed-loop servomotors). Glass syringe (1 ml) was filled with a previously prepared suspension of silver-109 nanoparticles and placed in a syringe pump (pumping speed 250 μl/min). The custom-made software directed the 2D system table with 10 mm/s translation speed using a sequence of movements prepared to uniformly cover a target plate. Nebulizer was typical, standard flow Bruker ion source 'needle' or nebulizer. Argon at a pressure of 2 bar was used as the nebulizing gas. Studied objects—for MS and MSI—were placed on the target plate before nebulization.

2.4 | Sample preparation and handling

All amino acids standards (alanine, isoleucine, lysine, and phenylalanine) were dissolved in water to give a final concentration of 1 mg/ml. Lower concentrations were prepared by diluting of ten-times higher concentration ones. Volume of 0.5 μl of plasma was dissolved in 249.5 μl of ultrapure water. Volumes of 0.5 μl of amino acid and plasma solutions were placed directly on target plate, air dried, and then target was nebulized with ^{109}AgNPs suspension as stated in previous subchapter.

2.5 | LDI mass spectrometry

Laser desorption/ionization–time-of-flight (LDI-ToF) mass spectrometry experiments were performed in reflectron mode using Bruker Autoflex Speed time-of-flight mass spectrometer equipped with a SmartBeam II laser (355 nm). Laser impulse energy was approximately 90–140 μJ, laser repetition rate 1000 Hz. The total number of laser shots was 4000 for each spot. This amount of laser shots was divided into four, symmetrically positioned points laying in distance of approximately 1/3 of spot radius from its center. At each point, 1000 laser shots were made with default random walk applied (random points with 50 laser shots). Measurement range was *m/z* 80–1500. Suppression was turned on typically for ions of *m/z* lower than 80. Reflector voltages used were 21 kV (the first) and 9.55 kV (the second). The data were calibrated and analyzed with FlexAnalysis (version 3.3) using centroid calibration model. Mass calibration (enhanced cubic calibration based on 8–9 calibration points) was performed using internal standards (silver-109 ions and clusters from $^{109}Ag^+$ to $^{109}Ag_9^+$).

2.6 | LDI mass spectrometry imaging

Measurements were performed using a Bruker Autoflex Speed time-of-flight mass spectrometer in reflectron positive mode. The apparatus was equipped with a SmartBeam II 1000 Hz 352 nm laser. Laser impulse energy was approximately 100–120 μJ, laser repetition rate was 1000 Hz, and deflection was set on *m/z* lower than 80 Da. The *m/z* range was 80–1500 and spatial resolution 500 × 500 μm. The imaging experiments were made with 2000 laser shots per individual spot with a default random walk applied (FlexImaging 4.0). All spectra were precalibrated (cubic calibration function) with the use of silver-109 ions ($^{109}Ag^+$ to $^{109}Ag_9^+$) as internal standard. The first

accelerating voltage was held at 19 kV, and the second ion source voltage was held at 16.7 kV. Reflector voltages used were 21 kV (the first) and 9.55 kV (the second). All of the shown imaging pictures are for ±0.05% *m/z* window. MSI experiments were performed on all spots of amino acid standards and blood plasma solution.

3 | RESULTS AND DISCUSSION

Monoisotopic silver-109 nanoparticles (^{109}AgNPs) were prepared by PFL laser generated nanomaterial with the use of 2D galvo-scanner and nebulization. This method, compared to the preparation of ^{109}AgNPs by chemical synthesis, is much faster reducing the target preparation time from 24 h to few minutes. It is also cost-effective, as no other chemicals are required and the silver-109 metal foil can be reused.[15]

3.1 | Quantification results

The LDI MS and MSI LDI MS measurements using monoisotopic silver-109 PFL 2D GS LGN were performed for four amino acids such as: alanine, isoleucine, phenylalanine and lysine. Amino acids were directly measured in concentrations ranging from 1 mg/ml to 1 ng/ml which equates to 1 000 000-fold concentration change. Limit of detection (LOD) values were calculated with the use of signal/noise (S/N) ratio values obtained from spectrum of lowest concentration samples that contained signal of interest. Every sample was placed on target plate in 0.5-μl volume equating to 500 ng to 500 fg of amino acid per measurement spot which is approximately 3.03 nmol to 3 fmol, respectively, calculated for example for phenylalanine (Phe) molar mass. A regression analysis of the obtained intensity data against the concentration was also performed. The use of mass spectrometry imaging for the quantification of amino acids allowed to obtain a very good result of the correlation with the R^2 above 0.99, which indicates the usefulness of MSI for quantitative analysis. It should be noted that the regressions were performed over a very wide concentration range for all seven tested concentrations.

Alanine (Ala) is one of α-amino acids used for the ribosome-mediated biosynthesis of proteins.[16] In mammals, alanine plays a key role in the glucose-alanine cycle. This cycle allows pyruvate and glutamate to be removed from muscle and transported to the liver. There pyruvate is used to regenerate glucose, which is returned to the muscles where it is metabolized for energy. In this way, the energy burden of gluconeogenesis is transferred to the liver instead of to the muscles, and all available ATP in the muscles can be allocated to muscle contraction. Alterations in the alanine cycle that increase the levels of serum alanine aminotransferase (ALT) are linked to the development of type II diabetes.[17]

Figure 1 presents results LDI MS and MSI analysis for alanine with ^{109}AgNPs PFL 2D GS laser generated nanomaterial. Manually made measurements were taken at four random locations, which is presented in Figure 1A. Alanine was found in spectra mainly as silver-109 adduct of [Ala + ^{109}Ag]$^+$ ion formula in amounts of 500 ng to 50 pg per sample spot. Intensities of alanine-silver-109 adduct peaks were of $3.8{\cdot}10^4$ for the highest concentration, $1.5{\cdot}10^5$ for 100 μg/ml, $1.1{\cdot}10^5$ for 10 μg/ml, $1.5{\cdot}10^4$ for 1 μg/ml and $4.5{\cdot}10^3$ for 100 ng/ml. What is interesting, in manual measurement mode, the intensity for the alanine signal for the first concentration is lower than the intensity for 10- and 100-times lower concentrations (Figure 1B). This is an effect of manual placement of measurement regions, an effect existing in commonly made manual measurements of MALDI method. Comparison of results of matching the regression function to experimental results for manual MS and semiautomatic MSI measurements is presented in Table 1. Regression analysis of this data provided trendline with R^2 value 0.937 (disregarding the highest concentration). However, the best fit obtained using polynomial trendline with R^2 equals 0.962.

Mass spectrometry imaging uses a grid or raster of measurement points with specified resolution, as shown in Figure 1C. Application of MSI for analysis the same samples allowed detection of signals alanine-silver-109 adduct in all concentrations (Figure 1D). Linear regression function for LDI MS and MSI LDI MS gives similar values R^2, which was equal 0.937 and 0.936 respectively. Significantly lower R^2 values were obtained by using the power and exponential trendlines. The best results were obtained again using polynomial trendline ($R^2 = 0.975$), which is superior to manual measurements.

As can be seen on Figure 1D, ion images prove that studied amino acid is deposited nonuniformly throughout of all studied sample spots. The best fit for analysis of alanine by MSI was obtained for data set for 1 mg/ml to 10 μg/ml concentrations (Figure S1). Limit of detection based on S/N ratio of 3 was found to be 178 pg (1.99 pmol) of alanine per measured spot for LDI MS. In contrast, LOD for MSI LDI MS was found to be 1094 pg (12.28 pmol) per measured spot.

Amino acids were detected by Alterman et al. with using of MALDI. Limit of quantitation for alanine of 0.14 μM which is approximately 12 ng/ml.[18] Also, another researcher—Soga et al.—used capillary electrophoresis-electrospray ionization-tandem mass spectrometry (CE-ESI-MS/MS) for quantification amino acids i.a. alanine, obtaining limit of detection of 8.8 μM.[19]

The next analyzed amino acid was isoleucine (Ile). It is one of the branched-chain amino acids (BCAAs) for protein synthesis in human body for example hemoglobin, regulation of blood sugar and energy levels. It has also been observed that an increase in isoleucine, like other BCAAs, occurs in people with diabetes, indicating a relationship between isoleucine and insulin resistance.[20] Results of LDI MS and MSI analysis for isoleucine with PFL 2D GS LGN-produced ^{109}AgNPs were presented in Figure 1. Similarly as alanine, measurements of Ile were taken at four random locations, which is presented in Figure 1A. Isoleucine was found in spectra mainly as silver-109 adduct of [Ile + ^{109}Ag]$^+$ ion formula in 1 mg/ml to 1 μg/ml samples. Isoleucine reported similar problem as in case alanine for random measurement points chose in LDI MS. Chart of logarithm of intensity vs. logarithm of concentration (Figure 1B) presents relatively high intensity for 10 μg/ml ($8.3{\cdot}10^4$) concentration and much lower for the other ones. LODs were 5890 ng/ml (2945 pg/spot). Data analysis with the use of

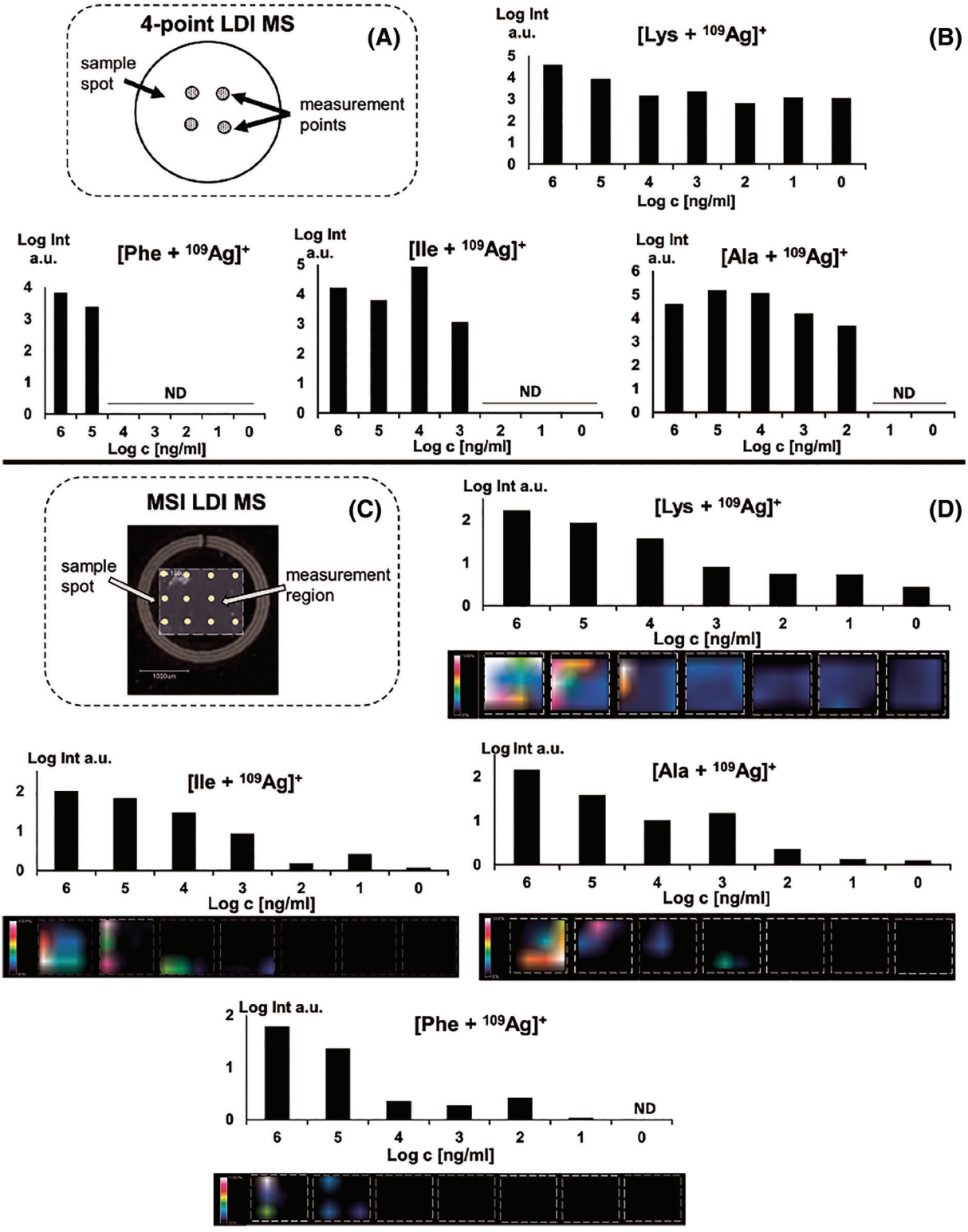

FIGURE 1 Panel A shows scheme of manual LDI MS measurement with 4 random measure points. Column charts (B and D for MS and MSI, respectively) present quantitative results for [amino acid + $^{109}Ag]^+$ ion as logarithm of the intensity versus logarithm of the concentration for four different amino acids. Panel C presents photograph of sample spot on target plate and measurement region for MSI LDI MS with grid of measurement points. ND—not detected

different types of regression functions for LDI MS allowed to obtain the highest value for a polynomial trend line with an R^2 value of 0.434. This problem was again solved by using mass spectrometry imaging with a raster of measurement points with specified resolution, as shown in Figure 1C. The value of the regression coefficient for the linear trendline is 0.153 for the LDI MS, and for MSI is 0.926.

TABLE 1 Comparison of regression function and R^2 values for manual MS and semiautomatic MSI measurements

Amino acid	Regression function	LDI MS		LDI MSI	
		Regression equation	R^2	Regression equation	R^2
Ala	Exponential	Log Int = $-6.0819e^{-0.12 \log c}$	0.918	Log Int = $5.6953e^{-0.687 \log c}$	0.891
	Linear	Log Int = $-0.5444 \log c + 5.8709$	0.937	Log Int = $-0.4406 \log c + 2.4565$	0.936
	Power	Log Int = $5.439 \log c^{-0.248}$	0.795	Log Int = $3.7367 \log c^{-1.809}$	0.722
	Polynomial	Log Int = $-0.0975 \log c^2 - 0.0568 \log c + 5.3833$	0.962	**Log Int = $0.0613 \log c^2 - 0.8699 \log c + 3.0289$**	**0.975**
Ile	Exponential	log Int = $4.7044e^{-0.071\log c}$	0.140	log Int = $4.958e^{-0.525\log c}$	0.818
	Linear	Log Int = $-0.2374 \log c + 4.5907$	0.153	log Int = $-0.3517\log c + 2.3914$	0.926
	Power	log Int = $4.345\log c^{-0.124}$	0.089	log Int = $3.7771\log c^{-1.501}$	0.596
	Polynomial	log Int = $-0.3601\log c^2 + 1.563 \log c + 2.7903$	0.434	**log Int = $0.0207\log c^2 - 0.5169\log c + 2.6393$**	**0.936**
Lys	Exponential	log Int = $4.3923e^{-0.066\log c}$	0.737	log Int = $3.1124e^{-0.271\log c}$	0.961
	Linear	log Int = $-0.2385\log c + 4.3752$	0.693	log Int = $-0.3074\log c + 2.4488$	0.935
	Power	log Int = $4.4655\log c^{-0.229}$	0.890	log Int = $2.8418\log c^{-0.815}$	0.826
	Polynomial	log Int = $0.0795\log c^2 - 0.8743 \log c + 5.3289$	0.924	**log Int = $0.0332\log c^2 - 0.5729\log c + 2.8471$**	**0.968**
Phe	Exponential	NA	NA	log Int = $3.9933e^{-0.661\log c}$	0.906
	Linear	NA	NA	log Int = $-0.3329\log c + 1.8712$	0.800
	Power	NA	NA	log Int = $2.7232\log c^{-1.761}$	0.787
	Polynomial	NA	NA	**log Int = $0.0853\log c^2 - 0.93\log c + 2.6674$**	**0.912**

Note: The best results are marked in bold.
Abbreviation: NA, not applicable.

Moreover, the best fit was obtained for the polynomial trendline with R^2 equals 0.936 in MSI measurement mode. The best linear fit for analysis isoleucine by MSI was obtained for set of concentrations from 1 mg/ml to 1 μg/ml with R^2 value of 0.955 (Figure S2). This amino acid was previously studied by Soga et al. that used capillary electrophoresis-electrospray ionization-tandem mass spectrometry (CE-ESI-MS/MS) for isoleucine with limit of detection was 1.0 μM.[19]

Another studied amino acid was lysine (Lys) which is classified as basic and aliphatic amino acid. It has been implicated to play a key role in biosynthesis of proteins, for example, structural proteins of connective tissues. The importance of lysine in many biological processes means that both underexpression and overexpression of lysine can have an adverse effect on the human body, resulting in disease.[21] Figure 1 presents results analysis LDI MS and MSI for lysine with ^{109}AgNPs produced PFL 2D GS LGN. The method of measurement of Lys with results is presented in Figure 1A. Lysine was found in spectra mainly as silver-109 adduct of [Lys + ^{109}Ag]$^+$ with adduct monoisotopic *m/z* value of 255.0095. Bar chart of logarithm of intensity vs. logarithm of concentration (Figure 1B) presents the highest intensities for the two first concentrations and much lower for the others. Limit of detection was found to be 3.06 ng (20.89 pmol) of lysine per measured spot. Signals of lysine were found in spectra of all concentrations. For both the LDI MS and the MSI LDI MS, the best fit was obtained using a polynomial trendline, with R^2 0.924. However, application of MSI allowed much better fit of R^2 being 0.968. Moreover, the best linear fit for analysis of lysine by MSI was for 1 mg/ml to 1 μg/ml sample set with R^2 value of 0.972 (Figure S3). Again, MSI ion images (Figure 1D) proved nonuniform compound localization that is the reason of much better MSI results compared to manual measurements.

The last studied amino acid was phenylalanine which contains neutral and nonpolar benzyl side chain. Phe is precursor of tyrosine and some neurotransmitters as dopamine, epinephrine and norepinephrine. The concentration of phenylalanine in the blood is of great importance for people with a genetic condition called phenylketonuria. Patients must regulate their intake of phenylalanine due to their body's inability to metabolize it.[21] Figure 1 presents results of manual measurements (LDI MS) and semiautomatic MSI for phenylalanine with ^{109}AgNPs PFL 2D GS LGN (Figure 1A). Phenylalanine was found in spectra mainly as silver-109 adduct of [Phe + ^{109}Ag]$^+$ at *m/z* value of 273.9830. The results of manual measurements for phenylalanine are shown in the bar graph in Figure 1B. Signals were found for only two highest concentrations. LOD was found to be 37 437 pg (226.3 pmol) of phenylalanine per measured spot. The bar chart of logarithm of signal intensity correlated with logarithm of compound concentration obtained by MSI with a series of ion images for the adduct [Phe + ^{109}Ag]$^+$ adduct is shown in Figure 1D. Application of MSI allowed finding signals Phe-silver-109 in all concentrations. Data analysis with the use of different types of regression functions for MSI LDI MS allowed to obtain the highest value for a polynomial

	LDI MS		LDI MSI	
Amino acid	LOD (ng/ml) µM	LLOQ (ng/ml)	LOD (ng/ml) µM	LLOQ (ng/ml)
Alanine	360 ± 360 4	590 ± 600	2190 ± 2190 30	3650 ± 3640
Isoleucine	5890 ± 7820 50	9820 ± 13 040	3250 ± 2380 30	5420 ± 3970
Lysine	6110 ± 4800 40	10 180 ± 8000	1250 ± 1330 10	2080 ± 2220
Phenylalanine	74 870 ± 68 120 450	124 790 ± 113 530	5390 ± 3090 30	8980 ± 5150

TABLE 2 Comparison of LOD and LLOQ values for manual and LDI MSI measurements

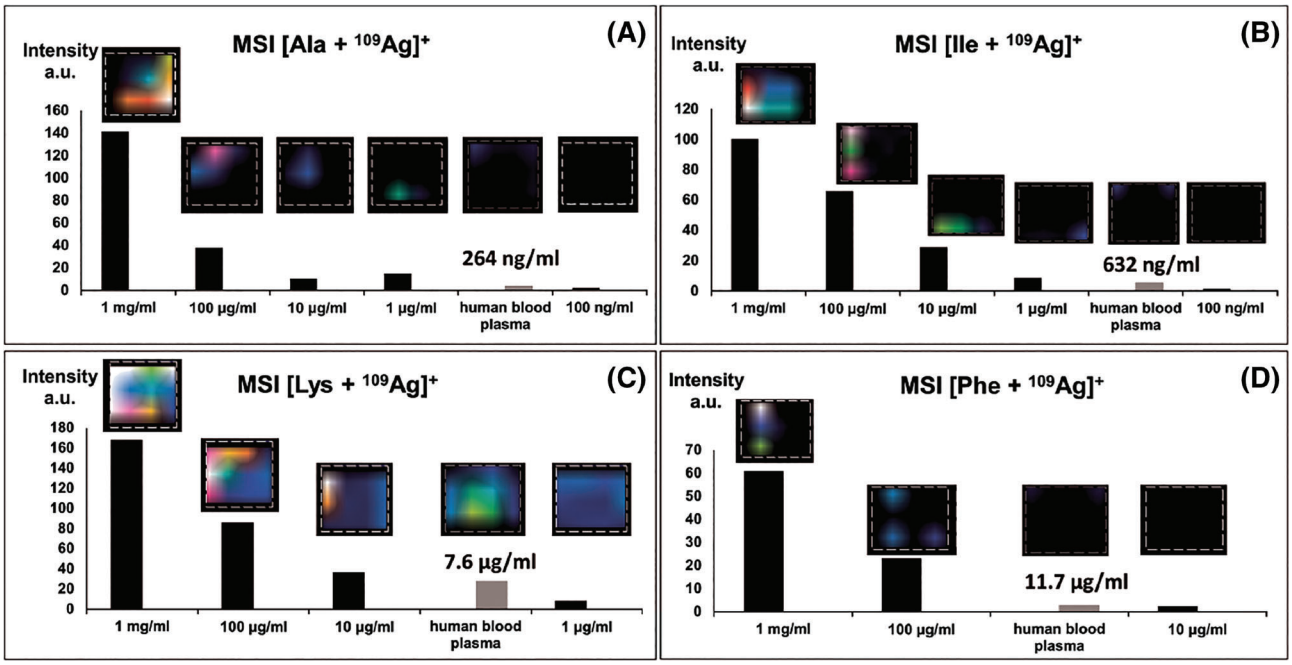

FIGURE 2 Results of quantitative analysis of selected amino acids in human blood plasma by LDI MSI with monoisotopic silver-109 nanoparticles PFL 2D GS LGN. For each identified amino acid, its labelled concentration in 0.5-µl 500-fold diluted blood plasma is given

trend line with an R^2 value of 0.912. The best linear fit for analysis phenylalanine by MSI was for 1 mg/ml to 10 µg/ml samples with R^2 value is 0.948 (Figure S4).

Table 2 shows the LOD and LLOQ values obtained for the amino acids tested by manual measurements and LDI MSI methods, respectively. Using the mass spectrometry imaging, a lower limit of detection value was achieved. In the case of lysine obtained LOD value was about 4.5 times lower. The results obtained with LDI MSI lower the randomness of the measurements, thereby providing a much more reliable quantitative analysis.

Considering the use of ^{109}AgNPs PFL 2D GS LGN in MSI to determine plasma free amino acid concentrations, the obtained LOD values of amino acids were compared with literature data. Duran[2] presented reference plasma amino acid concentration values for different age groups. For subjects over 18 years of age, the concentrations for Ala, Ile, Lys, and Phe were 182–552, 34–84, 111–248, and 39–74 µM, respectively. The reported values are much higher than the obtained LOD values in MSI experiments, so it can be concluded that the amino acids shown should be detectable in plasma.

A spot-to-spot and shot-to-shot reproducibility analysis was also performed. The obtained results are presented in bar charts in Figure S5. The results of the shot-to-shot analysis for all tested amino acids show 15% differences of intensity of the signal from the analyte. The results of the spot-to-spot analysis of isoleucine show 4% differences in signal intensities. In turn, for lysine and phenylalanine, the differences in intensities are equal 15% and 10%.

3.2 | Detection of amino acids in human blood plasma

Results obtained for water solutions of amino acids were compared to the ones based on human blood plasma in order to estimate suppression effect of biological matrix. Plasma sample had been 500-fold diluted in deionized water. The highest intensity signals for the tested amino acids in plasma were found on the MS spectrum as adducts with monoisotopic silver-109.

Figure 2 summarizes the ion images obtained from the LDI MSI experiment for single amino acid solutions and a diluted blood sample, including a plot of the amino acid-silver-109 adduct signal intensity versus concentration. The determined concentrations of alanine, isoleucine, lysine and phenylalanine identified in 0.5 μl of sample were 3.8 μg/ml, 632 ng/ml, 7.6 μg/ml, and 11.7 μg/ml respectively. Considering a 500-fold dilution of the sample, the calculated plasma amino acid concentrations are 168 μM for Ala, 41 μM for Ile, 558 μM for Lys, and 969 μM for Phe, respectively. Of the values obtained, only the concentration of Ile falls within the range given by Duran.[2] Alanine is just below normal, while lysine and phenylalanine are significantly above the ranges presented. The reason for such discrepancies in amino acid concentrations may be due to the diet, as shown by Schmidt et al.[22]They presented analysis showed that plasma concentrations of i.a. lysine and alanine differed by habitual diet group. Moreover, many studies indicate that changes in amino acid concentrations are associated with disease occurrence or progression.[17,20,21] Additionally, it is important to remember that higher concentration of Ile also originates from Leu which is of the same molecular formula. Moreover, in case of laser methods usually biological mixture separation by chromatography is omitted due to low technical compatibility, and that may introduce interferences from other compounds of complex sample.

4 | CONCLUSION

Application of monoisotopic silver-109 nanoparticles generated by new method PFL 2D GS LGN for manual LDI MS and semiautomatic LDI MSI allowed detection and quantification of amino acids in a wide range of concentration. LOD and R^2 values obtained for both types of experiments indicate that mass spectrometry imaging method allows much better quantification than for commonly used MALDI manual measurements. Ion images obtained in MSI experiments proved highly nonuniform analyte deposition that makes semiautomatic, multipixel MSI a modern requirement rather than improvement.

ACKNOWLEDGMENT

This work was supported by the National Science Centre (NCN), SONATA grant no. UMO-2018/31/D/ST4/00109.

CONFLICT OF INTEREST

The authors declare no competing and financial interest.

DATA AVAILABILITY STATEMENT

The data that support the findings of this study are available from the corresponding author upon reasonable request.

ORCID

Aneta Płaza-Altamer https://orcid.org/0000-0003-1719-8730
Artur Kołodziej https://orcid.org/0000-0002-9222-0937
Joanna Nizioł https://orcid.org/0000-0002-4783-8615
Tomasz Ruman https://orcid.org/0000-0002-9899-8627

REFERENCES

1. Harada M, Karakawa S, Miyano H, Shimbo K. Simultaneous analysis of d,l-amino acids in human urine using a chirality-switchable biaryl axial tag and liquid chromatography electrospray ionization tandem mass spectrometry. *Symmetry*. 2020;12(6):913. doi:10.3390/sym12060913
2. Duran M. Amino acids. In: Blau N, Duran M, Gibson KM, eds, *Laboratory Guide to the Methods in Biochemical Genetics*. Springer; 2008:53-89. doi:10.1007/978-3-540-76698-8_5
3. Barle H, Ahlman B, Nyberg B, Andersson K, Essén P, Wernerman J. The concentrations of free amino acids in human liver tissue obtained during laparoscopic surgery. *Clin Physiol*. 1996;16(3):217-227. doi:10.1111/j.1475-097X.1996.tb00570.x
4. Oviaño M, Rodríguez-Sánchez B. MALDI-TOF mass spectrometry in the 21st century clinical microbiology laboratory. *Enfermedades Infecc Microbiol Clin Engl Ed*. 2021;39(4):192-200. doi:10.1016/j.eimc.2020.02.027
5. He Q, Sun C, Liu J, Pan Y. MALDI-MSI analysis of cancer drugs: Significance, advances, and applications. *TrAC Trends Analyt Chem*. 2021;136:116183. doi:10.1016/j.trac.2021.116183
6. Qiao Z, Lissel F. MALDI matrices for the analysis of low molecular weight compounds: rational design, challenges and perspectives. *Chem Asian J*. 2021;16(8):868-878. doi:10.1002/asia.202100044
7. Sekuła J, Nizioł J, Rode W, Ruman T. Gold nanoparticle-enhanced target (AuNPET) as universal solution for laser desorption/ionization mass spectrometry analysis and imaging of low molecular weight compounds. *Anal Chim Acta*. 2015;875:61-72. doi:10.1016/j.aca.2015.01.046
8. Gamez RC, Castellana ET, Russell DH. Sol–gel-derived silver-nanoparticle-embedded thin film for mass spectrometry-based biosensing. *Langmuir*. 2013;29(21):6502-6507. doi:10.1021/la4008526
9. Jackson SN, Baldwin K, Muller L, et al. Imaging of lipids in rat heart by MALDI-MS with silver nanoparticles. *Anal Bioanal Chem*. 2014;406(5):1377-1386. doi:10.1007/s00216-013-7525-6
10. Zhao Y-Z, Xu Y, Gong C, Ju Y-R, Liu Z-X, Xu X. Analysis of small molecule compounds by matrix-assisted laser desorption ionization mass spectrometry with Fe_3O_4 nanoparticles as matrix. *Chinese J Anal Chem*. 2021;49(1):103-112. doi:10.1016/s1872-2040(20)60074-3
11. Arendowski A, Nizioł J, Ruman T. Silver-109-based laser desorption/ionization mass spectrometry method for detection and quantification of amino acids. *J Mass Spectrom*. 2018;53(4):369-378. doi:10.1002/jms.4068
12. Szulc J, Kołodziej A, Ruman T. Silver-109/silver/gold nanoparticle-enhanced target surface-assisted laser desorption/ionisation mass spectrometry—the new methods for an assessment of mycotoxin concentration on building materials. *Toxins*. 2021;13(1):45. doi:10.3390/toxins13010045
13. Kołodziej A, Ruman T, Nizioł J. Gold and silver nanoparticles-based laser desorption/ionization mass spectrometry method for detection and quantification of carboxylic acids. *J Mass Spectrom*. 2020;55(10):e4604. doi:10.1002/jms.4604
14. Nizioł J, Rode W, Laskowska B, Ruman T. Novel monoisotopic 109AgNPET for laser desorption/ionization mass spectrometry. *Anal Chem*. 2013;85(3):1926-1931. doi:10.1021/ac303770y
15. Płaza A, Kołodziej A, Nizioł J, Ruman T. Laser ablation synthesis in solution and nebulization of silver-109 nanoparticles for mass spectrometry and mass spectrometry imaging. *ACS Meas Sci Au*. 2021. doi:10.1021/acsmeasuresciau.1c00020
16. Nelson DL, Cox MM, Lehninger AL. *Principles of Biochemistry*. 4th ed. New York: W. H. Freeman; 2005.
17. Popović I, Nešić M, Vranješ M, Šaponjić Z, Petković M. TiO_2 nanocrystals – assisted laser desorption and ionization time-of-flight mass spectrometric analysis of steroid hormones, amino acids and

saccharides. Validation and comparison of methods. *RSC Adv*. 2016; 6(2):1027-1036. doi:10.1039/c5ra20042c
18. Alterman MA, Gogichayeva NV, Kornilayev BA. Matrix-assisted laser desorption/ionization time-of-flight mass spectrometry-based amino acid analysis. *Anal Biochem*. 2004;335(2):184-191. doi:10.1016/j.ab.2004.06.031
19. Soga T, Kakazu Y, Robert M, Tomita M, Nishioka T. Qualitative and quantitative analysis of amino acids by capillary electrophoresis-electrospray ionization-tandem mass spectrometry. *Electrophoresis*. 2004;25(13):1964-1972. doi:10.1002/elps.200305791
20. Cole JT. Metabolism of BCAAs. In: Rajendram R, Preedy VR, Patel VB, eds. *Branched Chain Amino Acids in Clinical Nutrition*. *Nutrition and Health*. Humana Press; 2015;1(1):13-24. doi:10.1007/978-1-4939-1923-9_2
21. Sprenger AG. Aromatic amino acids. In: Wendisch VF, ed. *Amino Acid Biosynthesis: Pathways*, *Regulation and Metabolic Engineering*. 1st ed. Springer; 2007. doi:10.1007/7171_2006_067
22. Schmidt JA, Rinaldi S, Scalbert A, et al. Plasma concentrations and intakes of amino acids in male meat-eaters, fish-eaters, vegetarians and vegans: a cross-sectional analysis in the EPIC-Oxford cohort. *Eur J Clin Nutr*. 2016;70(3):306-312. doi:10.1038/ejcn.2015.144

SUPPORTING INFORMATION

Additional supporting information may be found in the online version of the article at the publisher's website.

How to cite this article: Płaza-Altamer A, Kołodziej A, Nizioł J, Ruman T. Infrared pulsed fiber laser-produced silver-109-nanoparticles for laser desorption/ionization mass spectrometry of amino acids. *J Mass Spectrom*. 2022;57(3): e4815. doi:10.1002/jms.4815

International Journal of Mass Spectrometry 474 (2022) 116816

Contents lists available at ScienceDirect

International Journal of Mass Spectrometry

journal homepage: www.elsevier.com/locate/ijms

Infrared pulsed fiber laser-produced silver-109-nanoparticles for laser desorption/ionization mass spectrometry of carboxylic acids

Artur Kołodziej [a, *], Aneta Płaza-Altamer [a], Joanna Nizioł [b], Tomasz Ruman [b]

[a] Doctoral School of Engineering and Technical Sciences at the Rzeszów University of Technology, 8 Powstańców Warszawy Ave., 35-959, Rzeszów, Poland
[b] Rzeszów University of Technology, Faculty of Chemistry, 6 Powstańców Warszawy Ave., 35-959, Rzeszów, Poland

ARTICLE INFO

Article history:
Received 15 October 2021
Received in revised form
31 January 2022
Accepted 8 February 2022
Available online xxx

Keywords:
Carboxylic acids
Fatty acids
Silver
Nanoparticles
Mass spectrometry imaging
Quantification

ABSTRACT

Application of monoisotopic cationic ^{109}Ag nanoparticles (^{109}AgNPs) obtained by PFL (pulsed fiber laser) 2D GS (galvo-scanner) LASiS (laser ablation synthesis in solution) for high resolution laser desorption/ionization mass spectrometry and mass spectrometry imaging of carboxylic acids is presented. Six acids, azelaic, 3-methylhippuric, linoleic, oleic, arachidic and erucic acid were used as test compounds for quantification with a MALDI-type mass spectrometer. Comparison of commonly made manual measurements with semi-automatic MSI was performed providing very interesting findings. Carboxylic acids were directly tested in 1 000 000-fold concentration change conditions ranging from 1 mg/mL to 1 ng/mL, which equates to 300 ng to 300 fg of carboxylic acid per measurement spot. Methods were also tested on samples of spiked human blood serum for quantification of carboxylic acids and verification of the influence of biological matrix on the measurement.

1. Introduction

One of the most utilized soft ionization methods was developed by Tanaka et al., in 1988: matrix assisted laser desorption ionization mass spectrometry (MALDI-MS) [1]. This method is widely used in proteomics for protein analysis [2], in microbiology [3] for the identification of microorganisms and in pharmacy for the analysis of anticancer drugs [4]. Although it has many advantages such as high sensitivity and efficiency, the MALDI method is rarely used for the detection and quantification of low molecular weight compounds. The main problem is the necessity to use organic matrices, which include acids of low molecular weight, and during the analysis they produce various types of ions that interfere with the signals of the analyzed sample in the range of low masses [5]. This problem can be avoided by using nanoparticles instead of traditional matrices. Many published articles showing the use of nanoparticles in LMW analysis confirm their usefulness [6–9].

Monoisotopic nanoparticles of silver-109 were used to analyze various types of compounds, including amino acids, fatty acids, sugars or mycotoxins [10–13], where they have proved to be very effective in cationization. In this publication we present quantification result of carboxylic acids (including fatty acids) with chemically pure silver-109 nanoparticles produced by a 1064 nm pulsed fiber laser with 2D galvanometer scanner.

Significant advantage of nanoparticles-based method compared to MALDI is the replacement of organic matrix. This allows easy sample preparation, low chemical background, easier data analysis and fast data collection [6]. Silver nanoparticles provides unique advantages such as providing the possibility of internal calibration due to silver-related ion peaks and producing highly reproducible signals. Additionally, antibacterial and antifungal properties of silver nanoparticles help with the preservation of analyzed sample [14]. What is more, silver-109 nanoparticles (^{109}AgNPs) have a number of additional advantages: (i) simple isotopic pattern; (ii) higher intensity of analyte signal, (iii) higher detection sensitivity, (iv) much better compatibility with the analysis of complex mixtures, such as biological samples [13]. Chemically pure ^{109}AgNPs are of critical importance for mass spectrometry. They can be produced by pulsed fiber laser (PFL) 2D GS (galvo-scanner) laser ablation synthesis in solution (LASiS) that generates nanoparticle suspensions of a relatively high chemical purity compared to chemical methods as stabilizer- and reducing-agent-free NPs are obtained [15].

In this work we compare manual nanoparticle-based laser desorption/ionization mass spectrometry (LDI MS) and semi-

* Corresponding author.
E-mail address: a.kolodziej@prz.edu.pl (A. Kołodziej).

https://doi.org/10.1016/j.ijms.2022.116816
1387-3806/

automatically-performed mass spectrometry imaging (MSI) in quantification of carboxylic acids along with discussion of results and comparison with various matrix-assisted laser desorption/ionization (MALDI) and high-performance liquid chromatography coupled with mass spectrometry (HPLC-MS) methods previously used in carboxylic acids analysis.

2. Materials and methods

2.1. Materials

All carboxylic acid standards were purchased from Sigma-Aldrich. Steel targets were machined from H17 stainless steel (1.4016 steel). Before the LDI MS and MS imaging experiments steel targets were cleaned through soaking in boiling solvents: toluene (3 × 100 ml, each plate for 30 s), chloroform (3 × 100 ml, each plate for 30 s), acetonitrile (3 × 100 ml, each plate for 30 s) and deionized water (3 × 100 ml, each plate for 30 s). Every plate was dried in high vacuum (ca. 0.01 mbar, 24 h). All solvents were of HPLC quality, except for water (18 MΩ cm water produced locally).

2.2. Pulsed fiber laser 2-axis galvanometer scanner (PFL 2D GS) LASiS of silver-109 nanoparticles

The silver-109 foil (~1 mm thick, 99.7%+ isotopic purity) was bought from Trace Sciences International (USA) was placed at the bottom of a glass vessel containing solvent (acetonitrile). The ^{109}Ag foil was covered by an approximately 3 mm thick layer of acetonitrile (total solvent volume was 3 mL). The laser ablation was carried out with a 1064 nm pulsed fiber laser (Raycus RFL-P20QE/A3). Suspension was obtained after 2 min Irradiation with pulse energy of 0.8 mJ (100 ns pulse length) at a 40 kHz repetition rate. Laser ablation was accomplished at a scanning speed of 2000 mm/s, the ablation area was 4 × 4 mm [15]. Suspension was immediately transferred into a syringe and used in the nebulization step.

2.3. Sample preparation and handling

All carboxylic acids standards (azelaic, 3-methylhippuric, linoleic, oleic, arachidic and erucic acids) were dissolved in water to give a final concentration of 1 mg/mL. Lower concentrations were prepared by diluting of ten-times higher concentration ones. Volume of 1 μL of blood plasma was dissolved in 249 μL of ultrapure water, then 250 μL of 100 μg/mL acid solution were added. Volumes of 0.3 μL of carboxylic acid and blood plasma spiked with carboxylic acid solutions were placed directly on the target plate, air dried, and then the target was nebulized with ^{109}AgNPs suspension, as stated in section 2.4.

2.4. Nebulization of ^{109}AgNPs suspension

The entire nanoparticle nebulization process was controlled by a computer. The H17 steel plate (laser mass spectrometry target plate) was placed on the table of a translation system consisting of a motorized XY table (powered by closed-loop servomotors). Glass syringe (1 mL) was filled with a previously prepared suspension of silver-109 nanoparticles and placed in a syringe pump (pumping speed 250 μL/min). The custom-made software directed the 2D system table with 10 mm/s translation speed using a sequence of movements prepared to uniformly cover a target plate. Nebulizer was a standard flow Bruker ion source 'needle' or nebulizer. Argon at a pressure of 2 bar was used as the nebulizing gas.

2.5. LDI mass spectrometry

LDI-ToF mass spectrometry experiments were performed in reflectron mode using a Bruker Autoflex Speed time-of-flight mass spectrometer equipped with a SmartBeam II laser (355 nm). Laser impulse energy was approx. 90–140 μJ, laser repetition rate was 1000 Hz. The total number of laser shots was 4000 for each spot. These laser shots were divided into four, symmetrically positioned points laying in distance of *ca.* 1/3 of spot radius from its center. At each point, 1000 laser shots were made with default random walk applied (random points with 50 laser shots). The measurement range of interest was *m/z* 80–1500. Suppression was turned on typically for ions of *m/z* lower than 80. Reflector voltages used were 21 kV (first) and 9.55 kV (second). The data was calibrated and analyzed with FlexAnalysis (version 3.3) using centroid calibration model. Mass calibration (enhanced cubic calibration based on 8–9 calibration points) was performed using internal standards (silver-109 ions and clusters from $^{109}Ag^+$ to $^{109}Ag_9^+$).

2.6. LDI mass spectrometry imaging

Measurements were performed using a Bruker Autoflex Speed time-of-flight mass spectrometer in reflectron positive mode. The apparatus was equipped with a SmartBeam II 1000 Hz 355 nm laser. Laser impulse energy was approximately 100–120 μJ, laser repetition rate was 1000 Hz, and deflection was set on *m/z* lower than 80 Da. The *m/z* range was 80–1500 and spatial resolution 500 × 500 μm. The imaging experiments were made with 2000 laser shots per individual spot with a default random walk applied (FlexImaging 4.0). All spectra were pre-calibrated (cubic calibration function) with the use of silver-109 ions ($^{109}Ag^+$ to $^{109}Ag_9^+$) as internal standard. The first accelerating voltage was held at 19 kV, and the second ion source voltage was held at 16.7 kV. Reflector voltages used were 21 kV (first) and 9.55 kV (second). All of the shown imaging pictures are for ±0.05% *m/z* window. MSI experiments were performed on all spots of carboxylic acid standards and blood plasma solution.

3. Results and discussion

Synthesis, properties and application of silver-109 nanoparticles obtained in PFL 2D GS LASiS method were shown in our recent publication [15]. In that article, advantages of laser-assisted generation of nanoparticles over chemical synthesis were presented. There are many literature positions proving that silver nanoparticles are very efficient in ionization of compounds allowing detection of various low molecular weight compounds also in complex biological mixtures e.g. blood plasma or urine samples [8,13,16–18].

We selected various carboxylic acids important for human metabolism or that may contribute to various diseases. Azelaic acid has anti-inflammatory, antibacterial and anti-keratizing actions. Due to these properties, azelaic acid is used in acne treatment [19]. 3-Methylhippuric acid is one of main metabolite of toluene and xylene, and can be used as indicator of exposure to these neurotoxic compounds [20,21]. Linoleic and oleic acids may induce apoptosis of human lymphocytes, on the other hand both of these acids are angiogenesis initiators [22,23]. Arachidic acid was used in preparation of anticancer drug delivery nanoparticles, erucic acid can be accumulated in human organism which can lead to some heart disorder e.g. myocardial lipidosis that cause decrease in the contractile performance of heart muscles [24,25].

3.1. Quantification results

Standards of all listed acids were directly measured in

concentrations ranging from 1 mg/mL to 1 ng/mL which equates to 1 000 000-fold concentration change. Limit of detection (LOD) values were calculated with the use of signal/noise (S/N) value of 3 for lowest concentration samples. Every sample was placed on target plate in 0.3 μL volume equating to 0.3 μg to 0.3 pg of acid per measurement spot which is approx. 159 pmol to 1.59 fmol respectively calculated for example for azelaic acid molar mass. Shot-to-shot and spot-to-spot analyses were conducted for three exemplary carboxylic acids. Result of this analysis is presented in Supporting file (S1). This analysis proves high reproducibility of the results, for the shot-to-shot analysis, the spread of the results around the mean value was 11, 10 and 10% for 3-methylhippuric, oleic and arachidic acids respectively. For spot-to-spot analysis, spread of the results was 17, 27 and 10% for 3-methylhippuric, oleic and arachidic acids respectively. LOD and lower limits of quantification (LLOQ) values were calculated for manual LDI MS experiment and semi-automatic MSI and they are presented in Table 1.

For 3-methylhippuric acid, mass spectrometry imaging allowed to obtain lower limit of detection value than manual LDI MS. For the remaining analyzed carboxylic acids, due to the very high values of the standard deviation, it is difficult to clearly show which method allows to obtain better results. It is worth noting that application of LASiS silver-109 nanoparticles allowed to obtain 3 to 5 times lower LOD and LLOQ values for studied acids compared to previously described ^{109}AgNPET method that employs chemically produced nanoparticles [12].

Fig. 1 presents results LDI MS and MSI analyses for azelaic acid with ^{109}AgNPs PFL 2D GS laser generated nanomaterial. Manual measurements were performed at four random locations inside sample spot for each analyzed acid, the measurement scheme is presented in Fig. 1A. Azelaic acid was found in spectra mainly as silver-109 adduct of $[M+^{109}Ag]^+$ formula in amounts of 300 ng to 300 fg per sample spot. Intensities of azelaic acid-silver-109 adduct peaks were of $1.53{\cdot}10^5$ for the highest concentration, $5.18{\cdot}10^4$ for 100 μg/mL, $1.5{\cdot}10^4$ for 10 μg/mL, $5.32{\cdot}10^3$ for 1 μg/mL, $1.64{\cdot}10^3$ for 100 ng/mL, $1.2{\cdot}10^3$ for 10 ng/mL and 850 for 1 ng/mL. All of data is presented in as logInt (intensity) *vs* logc (concentration) plot (Fig. 1B). Regression analysis results of collected data is presented in Fig. 2B chart. Within this work, a preliminary calculations were conducted by fitting different trendline functions (polynomial, power, linear) to experimental data. Polynomial trendline was selected as best fitting and therefore applied to all studied compounds. For azelaic acid, results were obtained in the widest concentration range with a very good fit of trendline, the R^2 value is 0.993 for trendline.

After manual LDI MS measurement of sample the same spots with carboxylic acids were analyzed by semi-automatic MSI method. Fig. 1C presents scheme of semi-automatic MSI method which was used in the measurement of all carboxylic acids. Fig. 1D shows results of this analysis. During this measurement whole sample spot is covered by a grid of measurement points with specified resolution. Similarly, to LDI MS polynomial trendline gives very good fit (R^2 0.982). In Fig. 1D ion images of sample distribution proves that the sample is distributed non-homogeneously on the plate.

Limit of detection based on S/N ratio of 3 was found to be 434 pg (3.23 pmol) of azelaic acid per measured spot for LDI MS. In contrast, LOD for MSI was found to be 754 pg (5.62 pmol) per measured spot.

Literature provides information on LOD value for LDI MS method for this carboxylic acid that was provided by our team in previous publication. The LOD value was 31.4 μM [12], which is approx. 3-Times higher than LOD value obtained by using LASiS method. However, Garelnabi et al. presented results of GC analysis of azelaic acid with LOD value of 1 nM and LLOQ value 50 nM [26].

The next analyzed acid was 3-methylhippuric acid (3-MHA). Fig. 2A and C presents results of LDI MS and MSI analyses for this carboxylic acid with PFL 2D GS LASiS-produced ^{109}AgNPs. Similarly, as azelaic acid, measurements of 3-MHA were taken at four random locations, which is presented in Fig. 1A. 3-MHA was found in spectra mainly as silver-109 adduct of $[M+^{109}Ag]^+$ ion formula in 1 mg/mL to 1 μg/mL concentration samples. Intensities for 3-MHA were $1.9{\cdot}10^5$ for 1 mg/mL, $1.32{\cdot}10^5$ for 100 μg/mL, $2.57{\cdot}10^4$ for 10 μg/mL and $8.76{\cdot}10^3$ for 1 μg/mL. Similarly to azelaic acid analysis, charts with trendline are shown in Fig. 2A and C. The best fit for both analyses is polynomial trendline with R^2 value 0.977 and 0.967 for LDI MS and MSI respectively.

LOD value for 3-methylhippuric acid was found to be 215 pg (1.14 pmol) per spot for LDI MS and 190 pg (1.01 pmol) per measurement spot for MSI. In our publication LOD value was found 7.4 μM [12] which is over 2-times higher than LOD during this analysis. Hollow-fiber liquid-phase microextraction method provided LOD value of 2 μg/mL [27]. However, Behbahani et al. used high performance liquid chromatography with ultraviolet detector (HPLC-UV) method that provided better results (LOD = 0.2 ng/mL), but do not allows compound identification by *m/z* ratio [20].

Fig. 2B and D presents results of quantification by LDI MS and MSI for linoleic acid with ^{109}AgNPs produced by PFL 2D GS LASiS. This acid was found in spectra mainly as a silver-109 adduct of $[M+^{109}Ag]^+$ ion formula at *m/z* 389.1444. Plots of log intensity vs. log concentration (Fig. 2B) for polynomial trendline gave R-square value of 0.997. On the other hand, application of MSI allowed to obtain fit of R^2 being equal to 0.993. Limit of detection was found to be 237 pg (1.23 pmol) of linoleic acid per measured spot. MALDI-

Table 1
Limits of detection and lower limit of quantification for studied carboxylic acids.

Carboxylic acid	Manual LDI MS		Semi-automatic MSI	
	LOD[a] (ng/ml) μM	LLOQ[b] (ng/ml)	LOD[a] (ng/ml) μM	LLOQ[b](ng/ml)
Azelaic acid	1445 ± 1682 11	3211 ± 2803	2513 ± 2907 19	5585 ± 4846
3-Methylhippuric acid	716 ± 474 3.8	1590 ± 790	633 ± 194 3.3	1407 ± 324
Linoleic acid	791 ± 1122 4.1	1757 ± 1869	1075 ± 1647 5.5	2390 ± 2745
Oleic acid	201 ± 283 0.78	448 ± 472	317 ± 440 1.2	705 ± 734
Arachidic acid	1110 ± 415 3.9	2468 ± 692	2835 ± 1613 10	6299 ± 2689
Erucic acid	269 ± 386 0.94	598 ± 643	547 ± 775 1.9	1216 ± 1292

[a] Based-on S/N ratio of 3.
[b] Based on S/N ratio of 5; LLOQ – lower limit of quantification.

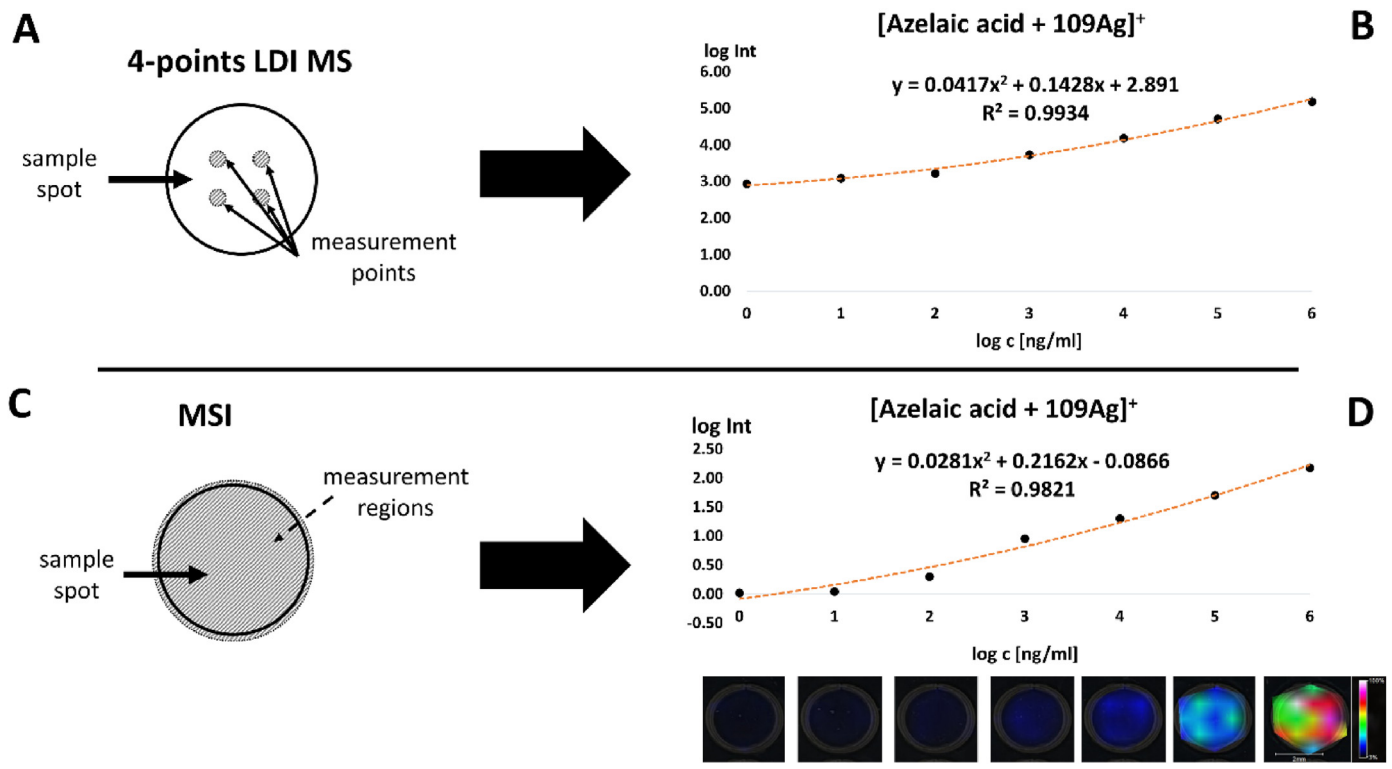

Fig. 1. Panel A shows the scheme of manual LDI MS measurement with 4 random measurement points. Panel C presents scheme of semi-automatic MSI measurements. Graphs B and D present results of quantification based on silver-109 adduct of azelaic acid signal for different concentrations obtained in LDI MS and MSI experiments. Both panels (B, D) contain the equation and the R^2 value for polynomial trendline. Panel D also contain [azelaic acid+^{109}Ag]$^+$ ion images for each concentration.

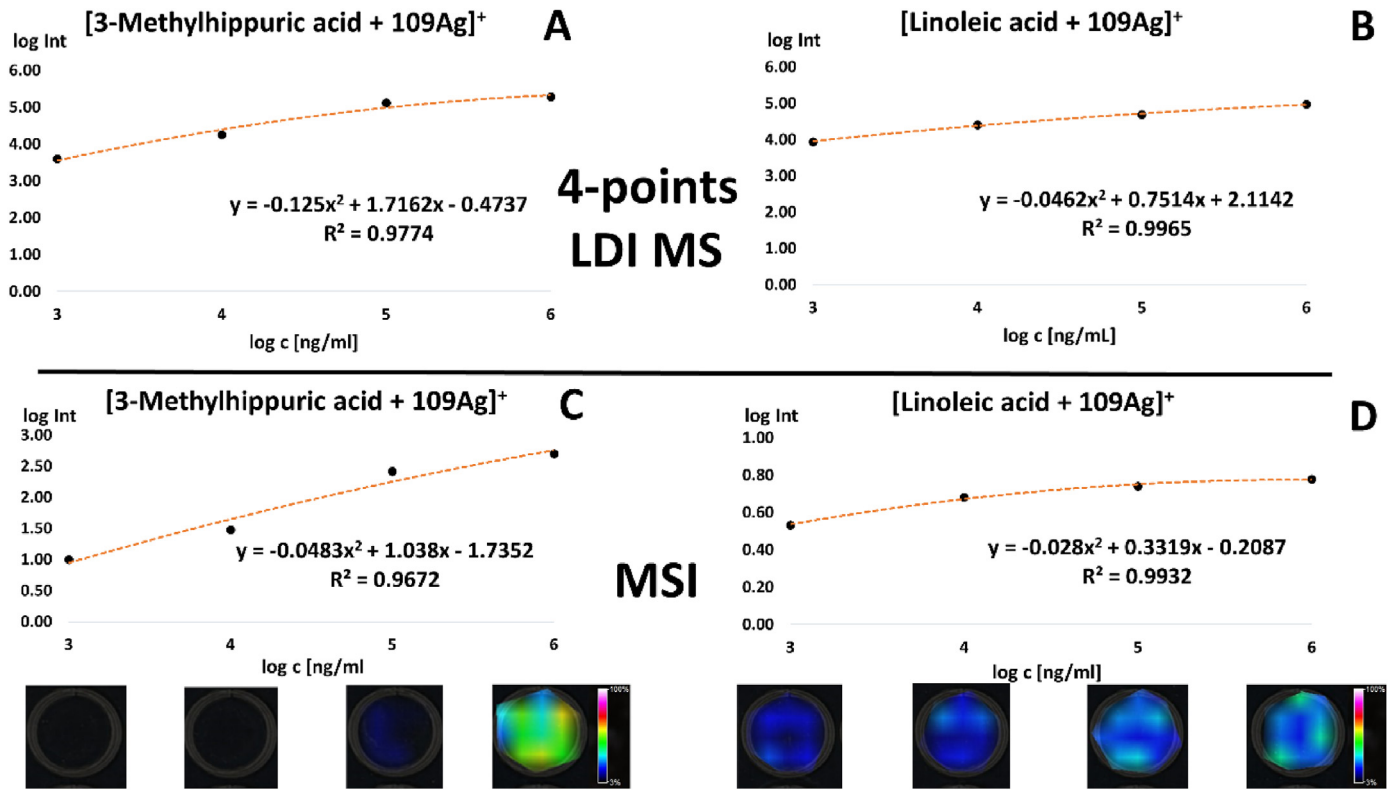

Fig. 2. Column charts A and C present results of quantification based on silver-109 adduct of 3-methylhippuric acid signal for different concentrations obtained in LDI MS and MSI experiments. Charts B and D present the same results for linoleic acid. All charts show decimal logarithm of intensity value *vs* decimal logarithm of concentration of acids. All panels contain the equation and the R^2 value for polynomial trendline. Panels C and D also contain [3-methylhippuric acid+^{109}Ag]$^+$ and [linoleic acid+^{109}Ag]$^+$ ions images for each concentration.

FTICR MS (matrix-assisted laser/desorption ionization-Fourier transform ion cyclotron resonance mass spectrometry) method provides LOD value of 1.9 μM and high-performance liquid chromatography coupled with charged aerosol detector (HPLC-CAD) and ion trap/time of flight mass spectrometry (MS-IT-TOF) provided limit of detection value 1.1 ng/mL [28,29]. Again, ion images proved nonuniform compound localization that is the reason of much better MSI results compared to manual measurements.

Fig. 3A and C shows the results of oleic acid analysis. As with previously tested acids, it was analyzed in two measurement modes: manual LDI MS and semi-automatic MSI. The measurement method is shown in Fig. 1A and C. Oleic acid was found in spectra mainly as silver-109 adduct of $[M+^{109}Ag]^+$ at *m/z* value of 391.1601. The results of manual measurements for this acid are shown in the graph in Fig. 3A. Signals were found for five concentrations with intensities $1.88{\cdot}10^5$ for 1 mg/mL, $1.68{\cdot}10^5$ for 100 μg/mL, $9.33{\cdot}10^4$ for 10 μg/mL, $4.12{\cdot}10^4$ for 1 μg/mL and $1.63{\cdot}10^4$ for 100 ng/mL. Plot in Fig. 3C present results of semi-automatic MSI method. Polynomial trendline is the best fit for both LDI MS (R^2 value 0.997) and MSI (R^2 value 0.981) for this carboxylic acid. LOD was found to be 60 pg (0.24 pmol) of oleic acid per measured spot. Methods such as HPLC-CAD/MS-IT-TOF provided LOD as low as 0.014 μg/mL [29]. On the other hand, high performance liquid chromatography-evaporative light scattering detection method provide LOD value of 13.7 ng [31].

Next analyzed acid was arachidic acid, results is presented in Fig. 3B and D. Arachidic acid was found in spectra mainly as silver-109 adduct of $[M+^{109}Ag]^+$ at *m/z* value of 421.2070. The results of manual measurements for are shown in Fig. 4B. Signals were found for four concentrations with intensities of $1.36{\cdot}10^5$ for 1 mg/mL, $6.05{\cdot}10^4$ for 100 μg/mL, $7.38{\cdot}10^3$ for 10 μg/mL and $9.32{\cdot}10^2$ for 1 μg/mL. As in the previous analyses, polynomial trendline is best fitted for LDI MS (R^2 0.994). For MSI R^2 value of polynomial trendline

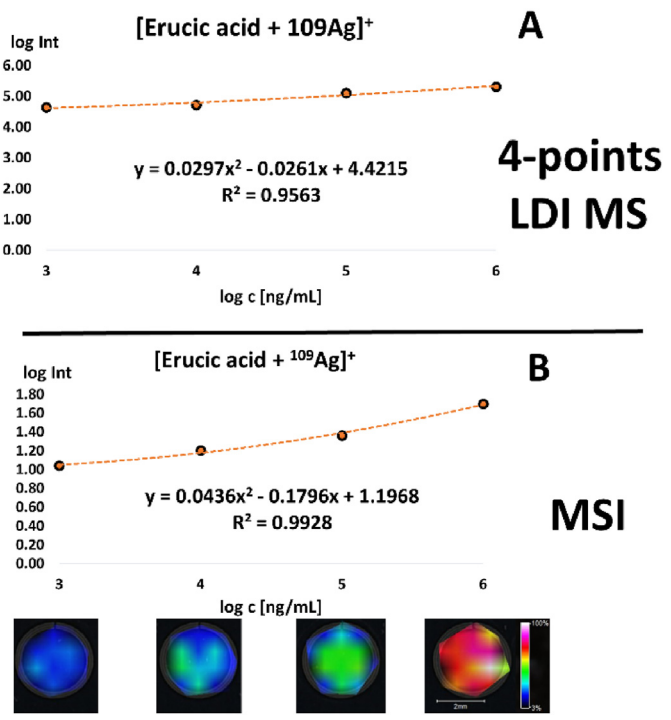

Fig. 4. Charts A and B present results of quantification based on silver-109 adduct signal of erucic acid for different concentrations obtained in LDI MS and MSI experiments. Both panels (A, B) contain the equation and the R^2 value for polynomial trendline. Panel B also contain ion [erucic acid$+^{109}Ag]^+$ images for each concentration.

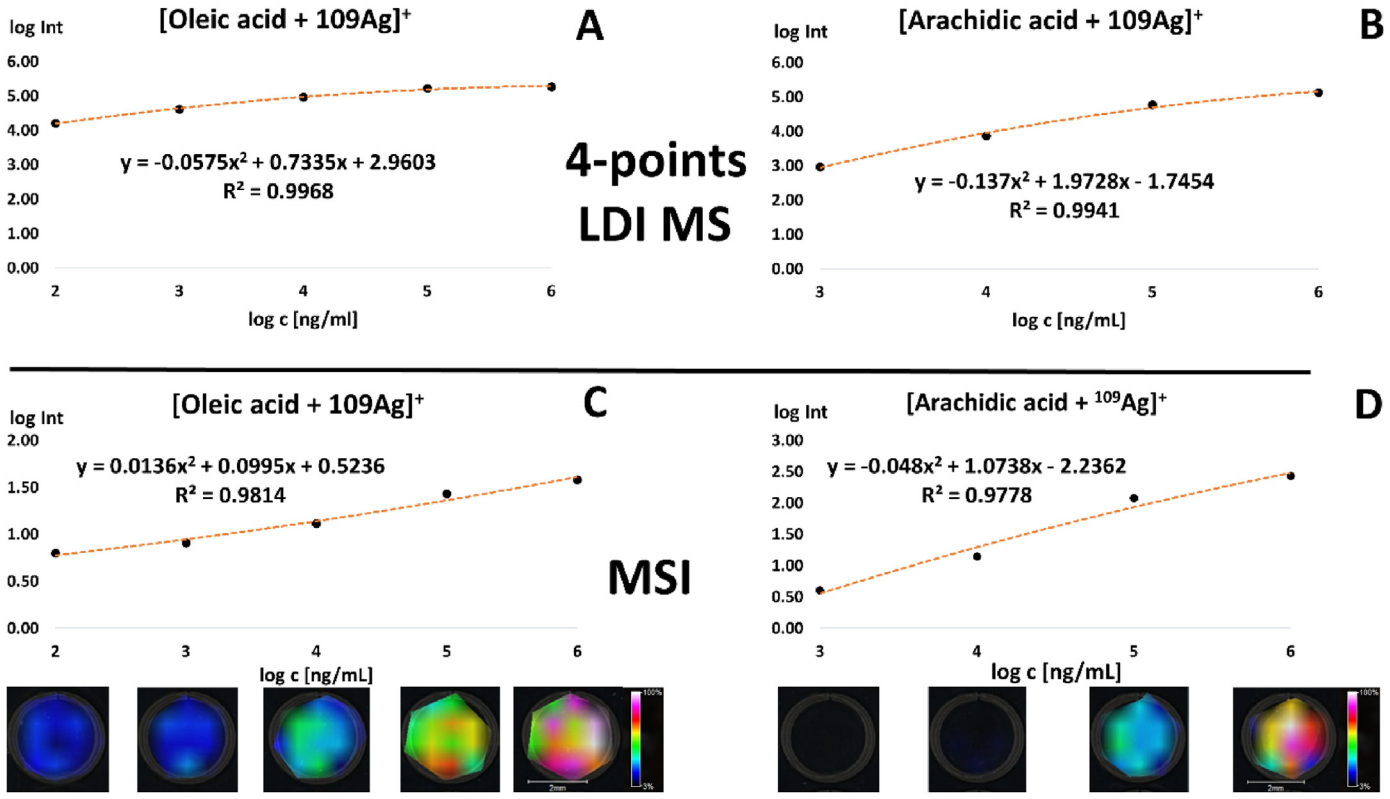

Fig. 3. Charts A and C present results of quantification based on silver-109 adduct of oleic acid signal for different concentrations obtained in LDI MS and MSI experiments. Charts B and D present the same results for arachidic acid. All charts show decimal logarithm of intensity value *vs* decimal logarithm of concentration of acids. All panels contain the equation and the R^2 value of polynomial trendline. Panels C and D also contain ions [oleic acid$+^{109}Ag]^+$ and [arachidic acid$+^{109}Ag]^+$ images for each concentration.

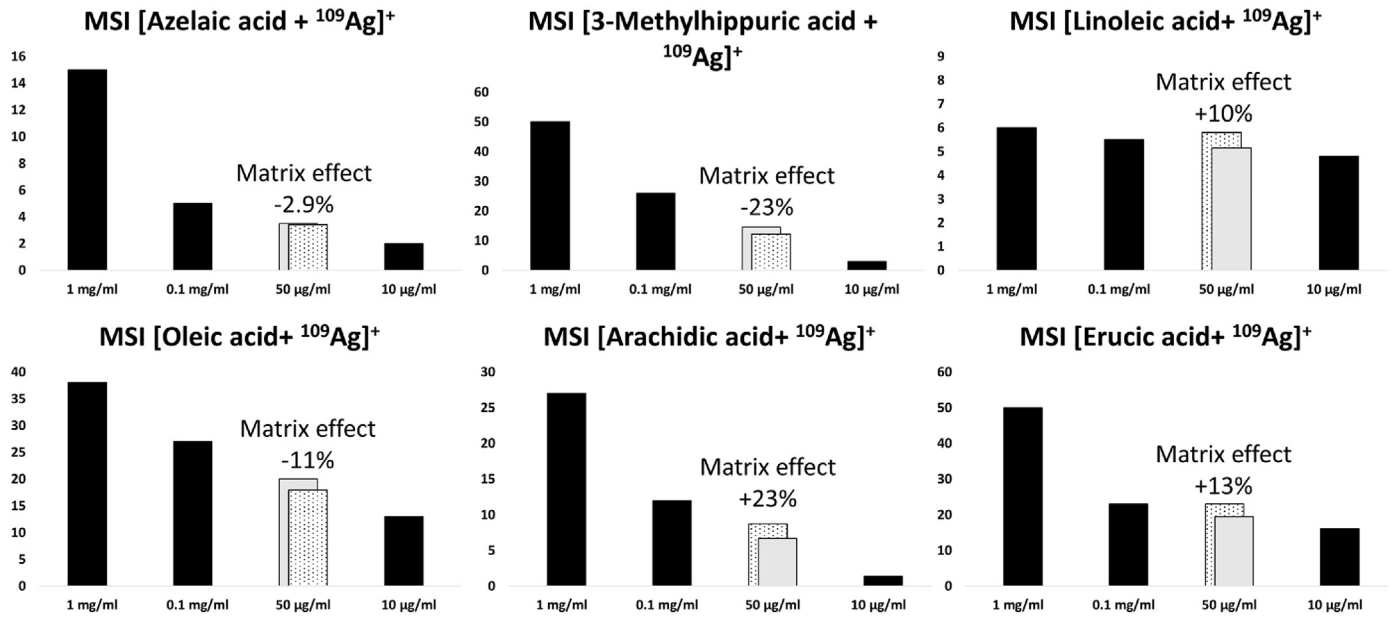

Fig. 5. Results of quantitative analysis of selected carboxylic acids in human blood serum by MSI with silver-109 nanoparticles produced by LASiS. For concentration 50 µg/mL theoretical intensity of signal was calculated (grey bar) and compared with experimental intensity of signal of analyzed acid in human blood serum spiked with carboxylic acid (white bar with dots). Intensities of signals for water solutions of carboxylic acid standards are also presented (black bars).

exceed 0.978. LOD value was found to be 333 pg (1.19 pmol) per measurement spot. In HPLC-CAD/MS-IT-TOF limit of detection value was 0.006 µg/mL and in HPLC-evaporative light scattering detection was 21.7 ng [29,30].

The last analyzed carboxylic acid was erucic acid, results of this analysis is presented in Fig. 4. Arachidic acid was found in spectra mainly as silver-109 adduct of $[M+^{109}Ag]^+$ at *m/z* value of 447.2227. The results of manual measurements for are shown in Fig. 4A. Signals were found for four concentrations with intensities $2.03{\cdot}10^5$ for 1 mg/mL, $1.29{\cdot}10^5$ for 100 µg/mL, $5.17{\cdot}10^4$ for 10 µg/mL and $4.33{\cdot}10^4$ for 1 µg/mL. As in the case of the previous analyzes, Fig. 4 shows the quantification results along with the equation and R^2 for the polynomial trendline. The trendline has very good fit with an R^2 of 0.956 for LDI MS and 0.993 for MSI. LOD value for LDI MS was 81 pg (0.29 pmol) per spot and in MSI LDI MS method 164 pg (0.58 pmol) per measurement spot. For erucic acid LOD value obtained by LC-MS method was 0.0025 µM and LLOQ value was 0.05 µM [31].

A regression analysis of the data obtained during semi-automatic MSI experiments was performed for all carboxylic acids. The use of mass spectrometry imaging for the quantification of carboxylic acids allowed to obtain good results for the polynomial function in all cases with R^2 ranging from 0.96 to 0.99. It should be noted that the regressions were performed over a very wide concentration range, from 1000-fold for 3-methylhippuric, linoleic, arachidic and erucic acids to 1 000 000-fold concentration change for azelaic acid.

These analyses indicate the usefulness of MSI for quantitative analysis of carboxylic acids and most probably other compounds. The measurement region allows coverage of the whole sample spot by using a grid or raster of measurement points with specified resolution. Application of MSI for analysis of all samples allows detecting signals of carboxylic acid-silver-109 adducts in various concentrations. As can be seen on Figs. 1D, 2C and 2D, 3C, 3D and 4B ion images prove that studied sample is deposited non-uniformly throughout of all studied sample spots. Limit of detection values obtained in both methods are worse than the values obtained during HPLC-MS analysis, however, the advantages of methods presented here are: (i) much shorter analysis time, (ii) the possibility of obtaining ion images and (iii) very fast and easy sample preparation.

3.2. Detection of carboxylic acids in human blood serum

Results obtained for 2-propanol solutions of carboxylic acids were compared to the ones based on human blood plasma in order to estimate suppression effect of biological matrix. The serum sample had been 500-fold diluted in deionized water, then the same volume of 100 µg/mL of carboxylic acid solution was added. The final concentration of analyzed acids in serum was approx. 50 µg/mL. The highest intensity signals for the tested carboxylic acids in serum were cationic adducts with silver-109.

Fig. 5 summarizes results of this analysis, theoretical intensities for 50 µg/mL of carboxylic acid solutions were calculated based on intensity value of 0.1 mg/mL sample. These values were compared with experimental data obtained for human blood serum spiked with carboxylic acids. For azelaic, 3-methylhippuric, linoleic and oleic acids, the calculated intensity is higher than experimental, for arachidic and erucic intensities of signals in blood serum were higher. The matrix effect was the lowest for azelaic acid −2.9% and the highest value was for 3-methylhippuric and arachidic acids (−23% and +23%). For rest of the result matrix effect was approx. In range of ±10%. The presented results clearly show that the biological matrix (in this example, blood serum) has moderate impact on the intensity value of the carboxylic acid during the MSI experiment, especially for azelaic acid where estimated value was nearly identical to data acquired during MALDI-ToF MSI experiment.

4. Conclusion

The application of ^{109}AgNPs generated by new method PFL 2D GS LASiS for manual LDI MS and semi-automatic MSI allowed detection and quantification of carboxylic acids in wide concentration range. Results of obtained data for both types of experiments indicate that mass spectrometry imaging method allows better quantification than for commonly used MALDI manual

measurements. Ion images obtained in MSI experiments proved highly non-uniform analyte deposition that makes semi-automatic, multi-pixel MSI a modern requirement rather than improvement. The biological matrix has little effect on the intensity value of the analyzed carboxylic acids in MSI. It is shown that polynomial function allows for very good fit of experimental quantification results for wide concentration range. The potential application of this methodology is forensic or metabolomic analysis of human body fluids, also for quantification of synthetic and biological samples.

Notes

The authors declare no competing and financial interest.

Author statement

A. Kołodziej: Formal analysis, Investigation, Writing - Original Draft, Writing - Review & Editing, Visualization.

A. Płaza: Investigation, Writing - Original Draft, Writing - Review & Editing.

J. Nizioł: Data Curation, Funding acquisition.

T. Ruman: Conceptualization, Methodology, Resources, Writing - Original Draft, Writing - Review & Editing, Supervision.

Declaration of competing interest

The authors declare that they have no known competing financial interests or personal relationships that could have appeared to influence the work reported in this paper.

Acknowledgments

This work was supported by the National Science Centre (NCN, Poland), SONATA grant no. UMO-2018/31/D/ST4/00109.

References

[1] K. Tanaka, H. Waki, Y. Ido, S. Akita, Y. Yoshida, T. Yoshida, T. Matsuo, Protein and polymer analyses up to m/z 100 000 by laser ionization time-of-flight mass spectrometry, Rapid Commun. Mass Spectrom. 2 (1988) 151–153, https://doi.org/10.1002/rcm.1290020802.

[2] N. Fasih Ramandi, M. Faranoush, A. Ghassempour, H.Y. Aboul-Enein, Mass spectrometry: a powerful method for monitoring various type of leukemia, especially MALDI-TOF in leukemia's proteomics studies Review, Crit. Rev. Anal. Chem. (2021) 1–28, https://doi.org/10.1080/10408347.2021.1871844.

[3] E. Torres-Sangiao, C. Leal Rodriguez, C. García-Riestra, Application and perspectives of MALDI–TOF mass spectrometry in clinical microbiology laboratories, Microorganisms 9 (2021) 1539, https://doi.org/10.3390/microorganisms9071539.

[4] Q. He, C. Sun, J. Liu, Y. Pan, MALDI-MSI analysis of cancer drugs: significance, advances, and applications, Trac. Trends Anal. Chem. 136 (2021) 116183, https://doi.org/10.1016/j.trac.2021.116183.

[5] C.D. Calvano, A. Monopoli, T.R.I. Cataldi, F. Palmisano, MALDI matrices for low molecular weight compounds: an endless story? Anal. Bioanal. Chem. 410 (2018) 4015–4038, https://doi.org/10.1007/s00216-018-1014-x.

[6] J. Sekuła, J. Nizioł, W. Rode, T. Ruman, Gold nanoparticle-enhanced target (AuNPET) as universal solution for laser desorption/ionization mass spectrometry analysis and imaging of low molecular weight compounds, Anal. Chim. Acta 875 (2015) 61–72, https://doi.org/10.1016/j.aca.2015.01.046.

[7] R.C. Gamez, E.T. Castellana, D.H. Russell, Sol–gel-derived silver-nanoparticle-embedded thin film for mass spectrometry-based biosensing, Langmuir 29 (2013) 6502–6507, https://doi.org/10.1021/la4008526.

[8] S.N. Jackson, K. Baldwin, L. Muller, V.M. Womack, J.A. Schultz, C. Balaban, A.S. Woods, Imaging of lipids in rat heart by MALDI-MS with silver nanoparticles, Anal. Bioanal. Chem. 406 (2014) 1377–1386, https://doi.org/10.1007/s00216-013-7525-6.

[9] Y.-Z. Zhao, Y. Xu, C. Gong, Y.-R. Ju, Z.-X. Liu, X. Xu, Analysis of small molecule compounds by matrix-assisted laser desorption ionization mass spectrometry with Fe3O4 nanoparticles as matrix, Chin. J. Anal. Chem. 49 (2021) 103–112, https://doi.org/10.1016/S1872-2040(20)60074-3.

[10] A. Arendowski, J. Nizioł, T. Ruman, Silver-109-based laser desorption/ionization mass spectrometry method for detection and quantification of amino acids, J. Mass Spectrom. 53 (2018) 369–378, https://doi.org/10.1002/jms.4068.

[11] J. Szulc, A. Kołodziej, T. Ruman, Silver-109/Silver/Gold nanoparticle-enhanced target surface-assisted laser desorption/ionisation mass spectrometry—the new methods for an assessment of mycotoxin concentration on building materials, Toxins 13 (2021) 45, https://doi.org/10.3390/toxins13010045.

[12] A. Kołodziej, T. Ruman, J. Nizioł, Gold and silver nanoparticles-based laser desorption/ionization mass spectrometry method for detection and quantification of carboxylic acids, J. Mass Spectrom. 55 (2020), e4604, https://doi.org/10.1002/jms.4604.

[13] J. Nizioł, W. Rode, B. Laskowska, T. Ruman, Novel monoisotopic ^{109} AgNPET for laser desorption/ionization mass spectrometry, Anal. Chem. 85 (2013) 1926–1931, https://doi.org/10.1021/ac303770y.

[14] J. Sekuła, J. Nizioł, W. Rode, T. Ruman, Silver nanostructures in laser desorption/ionization mass spectrometry and mass spectrometry imaging, Analyst 140 (2015) 6195–6209, https://doi.org/10.1039/C5AN00943J.

[15] A. Płaza, A. Kołodziej, J. Nizioł, T. Ruman, Laser ablation synthesis in solution and nebulization of silver-109 nanoparticles for mass spectrometry and mass spectrometry imaging, ACS Meas. Sci. Au (2021), https://doi.org/10.1021/acsmeasuresciau.1c00020.

[16] J. Nizioł, T. Ruman, Silver 109 Ag nanoparticles for matrix-less mass spectrometry of nucleosides and nucleic bases, IJCEA (2013) 46–49, https://doi.org/10.7763/IJCEA.2013.V4.259.

[17] J. Nizioł, W. Rode, Z. Zieliński, T. Ruman, Matrix-free laser desorption–ionization with silver nanoparticle-enhanced steel targets, Int. J. Mass Spectrom. 335 (2013) 22–32, https://doi.org/10.1016/j.ijms.2012.10.009.

[18] M. Yang, T. Fujino, Silver nanoparticles on zeolite surface for laser desorption/ionization mass spectrometry of low molecular weight compounds, Chem. Phys. Lett. 576 (2013) 61–64, https://doi.org/10.1016/j.cplett.2013.05.030.

[19] M.A. Sieber, J.K.E. Hegel, Azelaic acid: properties and mode of action, SPP 27 (2014) 9–17, https://doi.org/10.1159/000354888.

[20] M. Behbahani, S. Bagheri, F. Omidi, M.M. Amini, An amino-functionalized mesoporous silica (KIT-6) as a sorbent for dispersive and ultrasonication-assisted micro solid phase extraction of hippuric acid and methylhippuric acid, two biomarkers for toluene and xylene exposure, Microchim. Acta 185 (2018) 505, https://doi.org/10.1007/s00604-018-3038-5.

[21] C.-H. Chiu, C.-T. Chen, M.-H. Cheng, L.-H. Pao, C. Wang, G.-H. Wan, Use of urinary hippuric acid and o-/p-/m-methyl hippuric acid to evaluate surgical smoke exposure in operating room healthcare personnel, Ecotoxicol. Environ. Saf. 217 (2021) 112231, https://doi.org/10.1016/j.ecoenv.2021.112231.

[22] M.F. Cury-Boaventura, R. Gorjão, T.M. de Lima, P. Newsholme, R. Curi, Comparative toxicity of oleic and linoleic acid on human lymphocytes, Life Sci. 78 (2006) 1448–1456, https://doi.org/10.1016/j.lfs.2005.07.038.

[23] F.P. Samson, A.T. Patrick, T.E. Fabunmi, M.F. Yahaya, J. Madu, W. He, S.R. Sripathi, J. Tyndall, H. Raji, D. Jee, D.R. Gutsaeva, W.J. Jahng, Oleic acid, cholesterol, and linoleic acid as angiogenesis initiators, ACS Omega 5 (2020) 20575–20585, https://doi.org/10.1021/acsomega.0c02850.

[24] U. Termsarasab, H.-J. Cho, D.H. Kim, S. Chong, S.-J. Chung, C.-K. Shim, H.T. Moon, D.-D. Kim, Chitosan oligosaccharide–arachidic acid-based nanoparticles for anti-cancer drug delivery, Int. J. Pharm. 441 (2013) 373–380, https://doi.org/10.1016/j.ijpharm.2012.11.018.

[25] G. Rabbani, M.H. Baig, A.T. Jan, E. Ju Lee, M.V. Khan, M. Zaman, A.-E. Farouk, R.H. Khan, I. Choi, Binding of erucic acid with human serum albumin using a spectroscopic and molecular docking study, Int. J. Biol. Macromol. 105 (2017) 1572–1580, https://doi.org/10.1016/j.ijbiomac.2017.04.051.

[26] M. Garelnabi, D. Litvinov, S. Parthasarathy, Evaluation of a gas chromatography method for azelaic acid determination in selected biological samples, N. Am. J. Med. Sci. 2 (2010) 397–402, https://doi.org/10.4297/najms.2010.2397.

[27] F. Ghamari, A. Bahrami, Y. Yamini, F.G. Shahna, A. Moghimbeigi, Hollow-fiber liquid-phase microextraction based on carrier-mediated transport for determination of urinary methyl hippuric acids, Null 99 (2017) 760–771, https://doi.org/10.1080/02772248.2017.1280038.

[28] J. Ren, D. Zhang, Y. Liu, R. Zhang, H. Fang, S. Guo, D. Zhou, M. Zhang, Y. Xu, L. Qiu, Z. Li, Simultaneous quantification of serum nonesterified and esterified fatty acids as potential biomarkers to differentiate benign lung diseases from lung cancer, Sci. Rep. 6 (2016) 34201, https://doi.org/10.1038/srep34201.

[29] X. Zhao, Y. He, J. Chen, J. Zhang, L. Chen, B. Wang, C. Wu, Y. Yuan, Identification and direct determination of fatty acids profile in oleic acid by HPLC-CAD and MS-IT-TOF, J. Pharmaceut. Biomed. Anal. 204 (2021) 114238, https://doi.org/10.1016/j.jpba.2021.114238.

[30] J. Zhao, S.P. Li, F.Q. Yang, P. Li, Y.T. Wang, Simultaneous determination of saponins and fatty acids in Ziziphus jujuba (Suanzaoren) by high performance liquid chromatography-evaporative light scattering detection and pressurized liquid extraction, J. Chromatogr. A 1108 (2006) 188–194, https://doi.org/10.1016/j.chroma.2005.12.104.

[31] E. Koch, M. Wiebel, C. Hopmann, N. Kampschulte, N.H. Schebb, Rapid quantification of fatty acids in plant oils and biological samples by LC-MS, Anal. Bioanal. Chem. 413 (2021) 5439–5451, https://doi.org/10.1007/s00216-021-03525-y.

LASER GENERATED GOLD NANOPARTICLES FOR MASS SPECTROMETRY OF LOW MOLECULAR WEIGHT COMPOUNDS

Aneta PŁAZA-ALTAMER[1*], Artur KOŁODZIEJ[1], Joanna NIZIOŁ[2] and Tomasz RUMAN[2]

[1] Doctoral School of Engineering and Technical Sciences at the Rzeszów University of Technology, 8 Powstańców Warszawy Ave., 35-959 Rzeszów, Poland

[2] Rzeszów University of Technology, Faculty of Chemistry, 6 Powstańców Warszawy Ave., 35-959 Rzeszów, Poland

[*]Corresponding author: a.plaza@prz.edu.pl, 178651310

Abstract: Preparation of gold nanoparticles (AuNPs) by pulsed fiber laser (PFL) laser generated nanomaterial (LGN) with the use of 2D galvo-scanner (2D GS) is described. The procedure of covering of custom-made stainless steel MALDI targets containing studied objects via nebulization is also presented. Examples of application of new method (PFL-2D GS LGN and nebulization) in laser desorption/ionization mass spectrometry (LDI MS) analyses are shown. These include tests with amino acids and also low molecular weight polymer.

Keywords: gold nanoparticles; laser generated nanomaterial; low molecular weight compounds; mass spectrometry; matrix-free laser desorption/ionization; surface-assisted desorption/ionization.

1. Introduction

The development of matrix assisted laser desorption/ionization in mass spectrometry (MALDI-MS) is attributed to Tanaka et. al [1]. Due to its soft ionization potential, MALDI is one of the most selective, sensitive and efficient mass spectrometry methods. This allows it to be widely used for the analysis of ionic high-molecular weight compounds such as peptides, proteins [2], synthetic polymers [3] or polysaccharides [4], but it is also possible to detect low molecular weight (LMW) compounds such as lipids [5,6]. However, a disadvantage of MALDI which prevents it from being used too frequently for the detection of LMW compounds (MW <1000 Da) is the need to use MALDI matrices, which are low molecular weight organic acids that generate a variety of matrix-bound ions during the desorption/ionization process. The suppression of the analyte peaks then occurs, which complicates the spectra and significantly hinders the analysis of the tested compounds [7–9].

In part, the problems outlined have been resolved by developing the surface ionization assisted mass spectrometry (SALDI) technique. SALDI uses target plates coated with various nanostructures [6,10,11]. The nanoparticles used simplify the mass spectrum by reducing spectral interferences. Sample preparation is also the much simpler step demanding only applying the sample to the target plate [12]. What is more, advantage of using nanoparticles (NPs) is the reduction of the "sweet-spot" effect and very good point-to-point reproducibility [11].

Nanoparticles can be made by chemical, physical or biological methods [13,14]. The most commonly used methods for obtaining nanoparticles for MS is chemical reduction [12,15,16]. However, this approach raises a number of problems. One of them is the chemical purity of the obtained suspension. The necessity to use substances for chemical reactions, such as metal precursors, reducing agents, stabilizers, and oxidized products, make them a source of reagent-related ions and generate numerous interfering signals [17–19]. Another way NPs can also be obtained by breaking up a larger structure, for example with a laser, which is classified as physical method [13,14]. The method of generating nano-

particles by means of a laser (LGN) has many advantages, owing to which the obtained NPs are successfully used in mass spectrometry [20–22]. LGN uses pulsed laser irradiation to ablate a target from a solid material immersed in a liquid, ejecting NPs from the plasma cloud into the surrounding solution. This method allows for the production of a nanoparticle suspension of relatively high chemical purity, due to the lack of necessity to use stabilizers and reducing agents required in the chemical reduction method [20,23–25].

The most popular method of laser mass spectrometry is MALDI, which uses low molecular weight organic matrices such as 2,5-dihydroxybenzoic acid (DHB), sinapic acid (SA) or α-cyano-4-hydroxycinnamic acid (CHCA). Unfortunately, the acidic nature of the matrix solutions can make the analysis of various compounds difficult. Moreover, MALDI is the most useful for ionic compounds, and due to numerous matrix signals in the *m/z* <1000 range, low mass accuracy, unreliable calibration and the "sweet spot" effect, it is rarely used for testing low-molecular compounds [26].

Most of above-mentioned MALDI problems may be solved by using metal nanoparticles, for example gold ones, as a desorption/ionization agents [6,12,27,28]. Since the publication of Russell's work on a method for obtaining controlled-size gold nanostructures, they have become increasingly used [29], which is confirmed by an extensive review of Abdelhamid and Wu [30]. So far, various techniques have been introduced to synthesize AuNP, including chemical, physical and biological. However, the most commonly used method is the chemical reduction, which requires two substances: a metal salt precursor and a reducing agent. In addition, almost all treatments also contain a stabilizer such as capping agent preventing NPs aggregation. The reaction involves the reduction of Au_3^+ to elemental gold by electron transfer under various conditions. Among the many gold precursors, we can distinguish chloroauric acid [31] or chloro(trimethylphosphite)gold(I) [12]. In turn, the role of the reducing agent is often assumed by sodium borohydride ($NaBH_4$), sodium citrate, hydrogen peroxide or ascorbic acid [13,32]. The type of the used precursor and reducer affects the properties and size of the AuNPs obtained [31].

Preparation and application of gold nanoparticles by chemical reduction method for laser mass spectrometry was presented by Tseng and Su [33]. Authors used $HAuCl_4$ as the metal precursor and sodium borohydride as the reducing agent. The obtained nanoparticles were used as templates in LDI MS for the detection of low molecular weight neutral carbohydrates such as glucose, ribose, maltose, and cellobiose. The mass spectra present mainly sodium and potassium adducts of the mentioned compounds. However, mass spectrum of mixture glucose, maltose and ribose shows a lot of interfering signals.

The above-mentioned problems were partly solved by Amendola and co-workers, who were the first to demonstrate a method for producing nanoparticles by laser ablation synthesis in solution (LASiS) and their applicability as a matrix for LDI MS [19]. Due to the simplicity of the method, the synthesis of nanoparticles with the use of laser ablation in a solution allows to save time while providing suspensions of relatively high chemical purity compared to chemical methods. The mass spectra with nanoparticles generated by the LASiS method have a low chemical background, which simplifies the analysis of the tested compounds. In addition, LASiS enables the production of NPs from a wide variety of metal alloys.

In last year publication, for the first time, 1064 nm pulsed fiber laser (PFL) with 2D galvanometer scanner (2D GS) is shown as a very good source of silver-109 nanoparticles [20]. This study describes a new method of production of chemically pure gold nanoparticles in suspension with an application method for covering of studied objects or surfaces. Laser generated gold nanoparticles are shown to be highly useful for LDI mass spectrometry. This work presents LDI MS results for test compounds such as amino acids and polymers.

2. Results and discussion

2.1. PFL 2D GS LGN of AuNPs

In this work, LGN has been used to obtain chemically pure gold nanoparticles. Nanoparticles were generated by pulsed 1064 nm fiber laser with galvoscanner head scanning of ablated surface. The experimental setup for the AuNPs preparation is shown in Fig. 1A. For fast synthesis of nanoparticles, high-frequency (60 kHz), high pulse energy (up to 1 mJ/pulse) laser was used. However, in order to

avoid unwanted thermal effects such as melting, solvent boiling and oxidation of solvent and also of nanoparticles, two-dimensional (2D) galvo-scanner (GS) was used. Galvo-scanner head with f-theta lens attached to fiber laser allowed for precise and very fast shifting of focused laser beam on the surface of ablated gold plate.

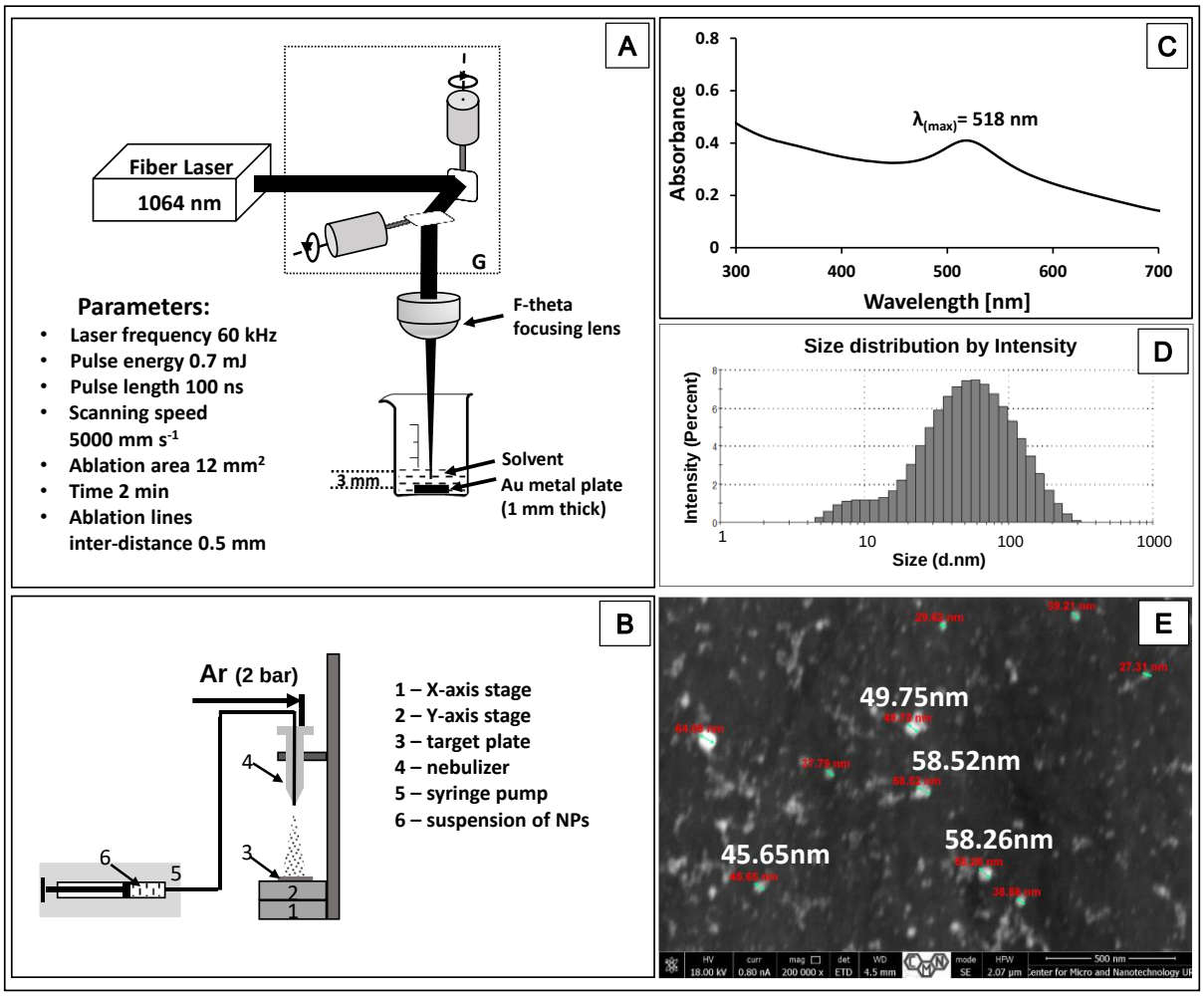

Fig 1**.** Laser ablation setup for the preparation of AuNPs (A); G – 2D galvanometer laser scanner. Down panel (B) presents setup for nebulization of nanoparticles. Panel C presents UV-VIS spectrum of AuNPs suspension in mixture solvents isopropanol and water (1:1 v/v). Panel D shows results of DLS measurement of Au nanoparticles hydrodynamic size distribution by intensity. E – High resolution SEM image of target modified with AuNPs generated by PFL 2D GS LGN.

First, the prepared nanoparticles were examined using UV-VIS spectroscopy, which allows determination of the size and shape of NPs. The vibrations of metallic electrons caused by particular wavelengths of light produce an effect known as surface plasmon resonance (SPR). It is related to the given size and shape of gold nanoparticles, as well as to their chemical environment. The literature describes that as the AuNPs diameter increases, the absorbance band shifts towards longer wavelengths and also widens [34]. The UV-VIS spectrum obtained for PFL 2D GS LGN AuNPs is presented in Fig. 1C. The UV-VIS spectrum of the post-reaction AuNP suspension recorded after 3 minutes of synthesis shows a local maximum at 518 nm, which suggests that the size of most nanoparticles is approx. 12 nm. However, an asymmetrical broadening of the SPR towards longer wavelengths, characteristic of the spheroidal particle fraction, can be observed. The presence of spheroids may indicate particle aggregation processes taking place in the suspension [34,35].

Figure 1D presents results of dynamic light scattering (DLS) measurement result of AuNPs size distribution by intensity after few minutes after preparation of suspension. DLS chart of the size distribution by intensity indicates the highest content of nanoparticles around 60 nm in diameter, with a distribution ranging from 5 to 120 nm. High resolution scanning electron microscope image of modified target (Fig. 1E) also confirms that individual nanoparticles are in roughly round/spherical shape and are

of 37-64 nm size. A number of HRTEM and DLS results on size measurements of gold nanoparticles obtained with LGN present similarly size. DLS results suggest bigger nanoparticles as judged from UV-vis spectrum. Most probably, this is due the fact that the nanoparticle suspension used for the DLS measurement was prepared in a different solvent than the one optimized for LGN. Many studies show the effect of solvent on the size of nanoparticles obtained [34,35].

The use of nanoparticles in LDI MS requires an appropriate method of application to the surface containing the tested object. One of the approaches using AuNPs as a matrix is dry metal sputtering to obtain a homogeneous layer with minimal or no lateral migration of the analyte. However, this method requires an appropriate spraying system and is therefore rarely used [36]. For our LDI MS measurements, 0.5 µl of each of solution of alanine, arginine, histidine, lysine, methionine, phenylalanine, serine and tyrosine and PPG polymer was applied to a stainless-steel plate and air-dried. The plate with all test objects was placed on the table of the translation system as shown in Figure 1B. Aliquots of colloidal gold (1 mL) were sprayed three times onto the sample. Each portion was injected into the nebulizer at a constant rate of 250 µl/min. The entire nanoparticle nebulization process was controlled by a computer using a sequence of movements aimed at evenly covering the target plate. The LDI MS spectrum of AuNPs produced by PFL 2D GS LGN and deposited on the surface of stainless steel of target plate by nebulization is shown in Figure 2A. Mass spectrum made in 80-1500 *m/z* range contains virtually only gold ion peaks of Au^+ to Au_5^+ composition. Various amino acids as low molecular weight compounds were tested to verify the potential of ionization of organic compounds with the gold nanoparticles obtained with PFL 2D GS LGN.

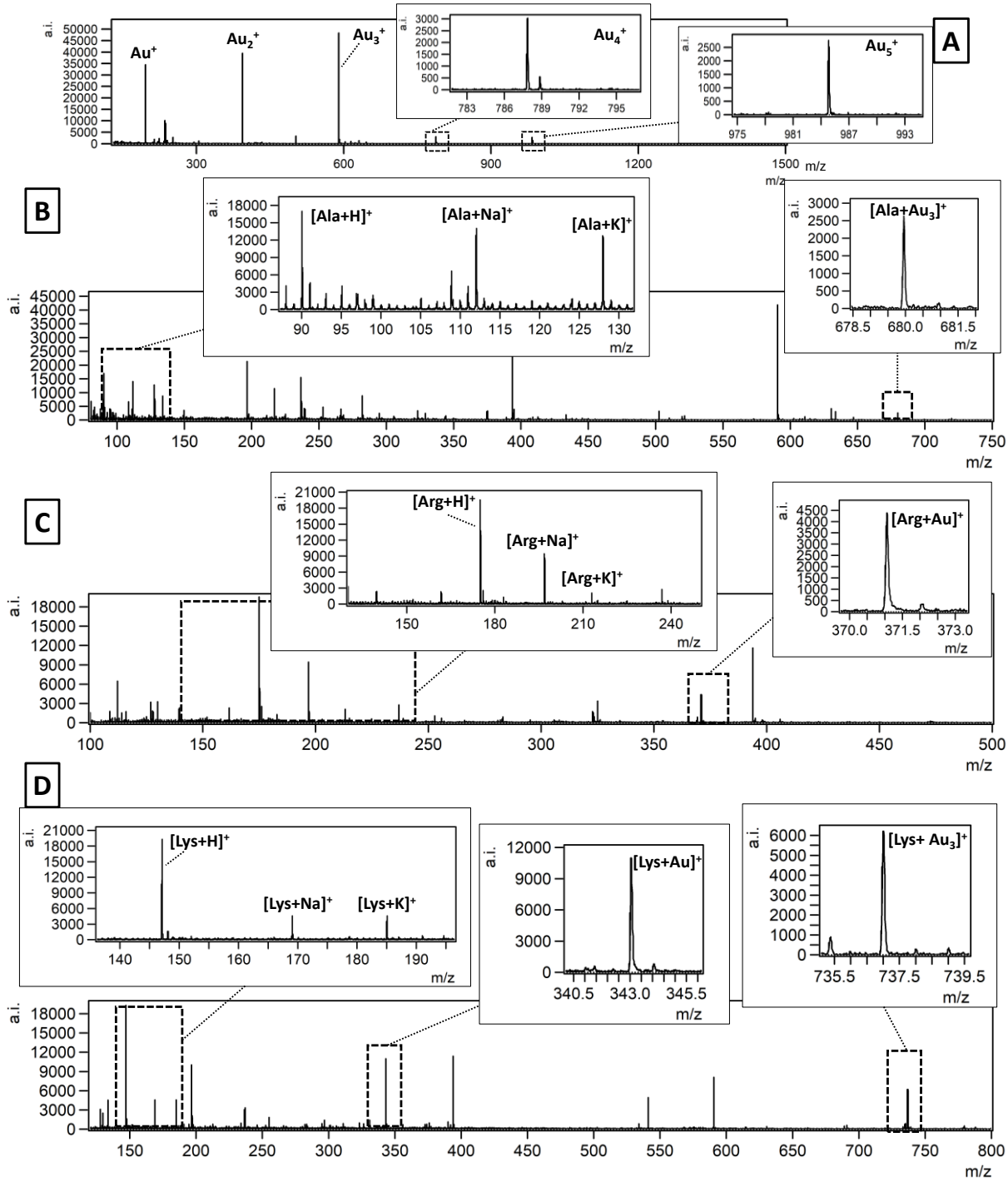

Fig 2. LDI MS positive reflectron mode spectrum of target plate covered with AuNPs generated by PFL 2D GS LGN (A). Others panels present LDI MS spectra fragments for alanine (B), arginine (C) and lysine (D) of 1 mg/mL concentrations deposited on target plate and covered with gold nanoparticles obtained with PFL 2D GS LGN.

The first analyzed compounds were alanine, arginine and lysine (Fig. 2). All listed compounds were found mainly as protonated adduct. Other adducts such as sodium, potassium as well as with Au^+ or Au_3^+ ions were also observed, but their intensities were significantly lower. For alanine (Fig. 2B), the highest S/N ratio equals 124 was observed for $[C_3H_7NO_2+H]^+$ adduct with *m/z* 90.0847. Ion of formula $[C_3H_7NO_2+Au_3]^+$ was also observed with signal intensity $2.5 \cdot 10^3$. Arginine (Fig. 2C), had the highest S/N ratio (294) for $[C_6H_{14}N_4O_2+H]^+$ adduct with *m/z* 175.1179. Lysine (Fig. 2D) was found on the mass spectrum in the form of five types of adducts: protonated, sodium and potassium as well as with Au^+ and Au_3^+ of which the protonated adduct had the highest signal intensity of $1.7 \cdot 10^5$. On the other hand,

lysine-gold adduct with chemical formula $[C_6H_{14}N_2O_2 + Au]^+$ with *m/z* 343.0651 had signal intensity of $1.1 \cdot 10^4$ and also trigold adduct $[C_6H_{14}N_2O_2 + Au_3]^+$ with *m/z* 737.0090 was found with signal intensity $6.1 \cdot 10^3$.

Alanine was analyzed on ^{109}AgNPET target for LDI MS, presenting a spectrum with the higher intensity $1.2 \cdot 10^5$ for alanine-silver 109 adduct for concentration 50 ng per spot [37]. Nitta and coworkers detected arginine with the use of laser-based mass spectrometer at amount of 100 pmol with the use of PtNPs [38]. Lysine was analyzed on AuNPET target for LDI MS, presenting a spectrum with the intensity of $7.6 \cdot 10^4$ for protonated adduct for concentration 0.1 mg/mL. The mass spectrum also showed a gold adduct $[C_6H_{14}N_2O_2 + Au]^+$ with signal intensity of $3.0 \cdot 10^4$ [39].

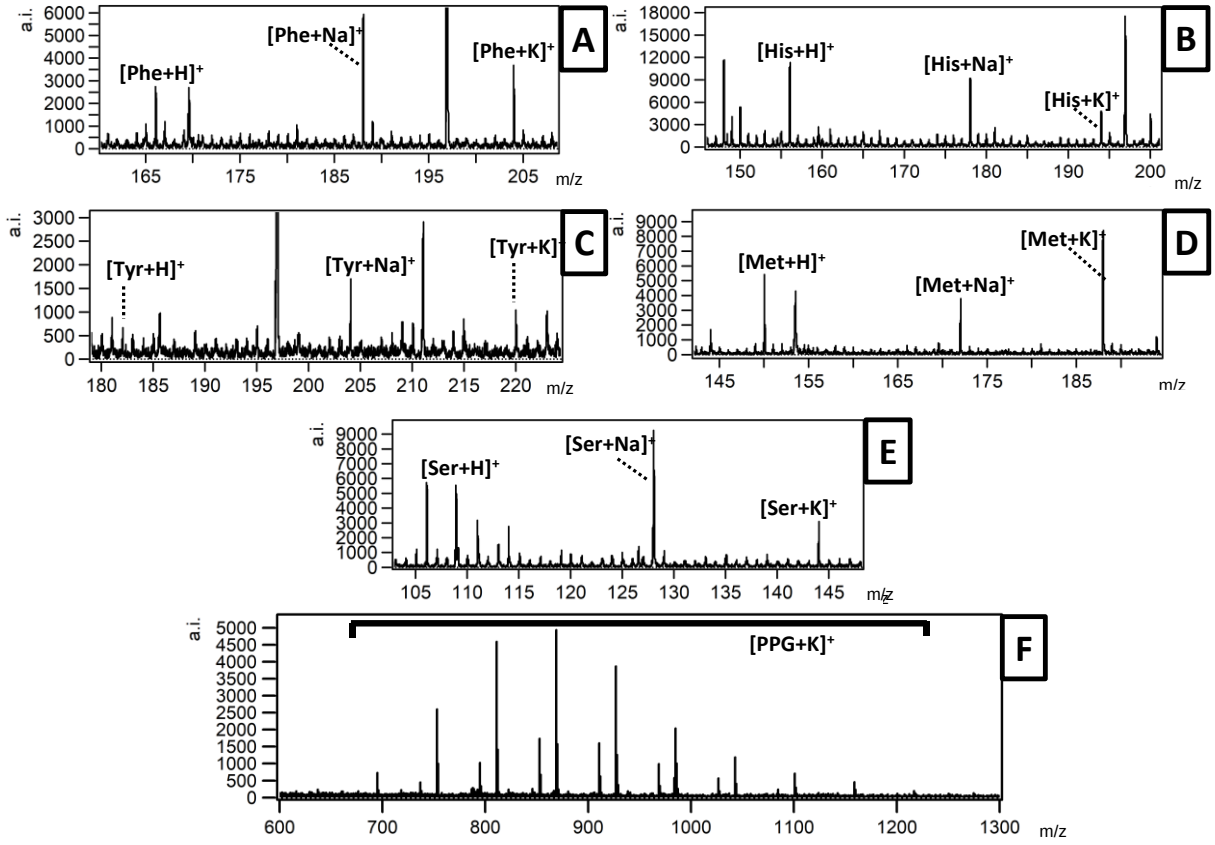

Fig 3. LDI MS positive reflectron mode mass spectra. Individual panels show fragment mass spectrum for A-phenylalanine, B-histidine, C-tyrosine, D-methionine, E-serine, respectively. The last panel (F) presents LDI MS spectrum of poly(propylene glycol) at 10.0 μg/mL concentration.

Figure 3 shows the fragments of the mass spectra obtained for phenylalanine, histidine, tyrosine, methionine, serine and poly(propylene glycol) using AuNPs LDI MS. No adducts of the tested compounds with gold ions were observed in any of the spectra in Fig. 3. For phenylalanine (Fig. 3A), tyrosine (Fig.3C) and serine (Fig. 3E) the highest signals were observed for $[C_9H_{11}NO_2+Na]^+$ adduct at *m/z* 188.0793 with signal intensity $4.5 \cdot 10^3$, $[C_9H_{11}NO_3+Na]^+$ adduct at *m/z* 204.0693 with signal intensity $1.0 \cdot 10^3$ and $[C_3H_7NO_3+Na]^+$ adduct at *m/z* 128.0789 with signal intensity $8.1 \cdot 10^3$. Sodium and potassium adducts were also present but with lower intensities. Histidine MS spectrum obtained with the use of PFL 2D GS LGN AuNPs is shown in Figure 3B. This compound was found mainly as protonated adduct $[C_6H_9N_3O_2 +H]^+$ with signal intensity of $8.9 \cdot 10^3$. On the other hand, on methionine (Fig. 3E) mass spectrum was dominated by potassium adduct $[C_5H_{11}NO_2S +K]^+$ at *m/z* 188.0242 with signal intensity $6.5 \cdot 10^3$.

Poly(propylene glycol) has repeating monomer unit of chemical formula $CH_2CH(CH_3)O$ with mass of approx. 57.9 Da. The LDI mass spectrum of PPG is shown in Fig. 3F. The spectrum show a typical

polymer structure where the dominant mass is approximately at *m/z* 1000. For example, the highest polymer signal at *m/z* 869 revealed is the K^+ ion adduct of a PPG with 14 mer units. Shoji Okuno et al. compared the PPG spectra obtained with MALDI and SALDI. The authors identified a problem with the reproducibility of the MALDI mass spectra for PPG, which showed a strong dependence on the type of solvent and/or chemical matrix and the analyte/matrix ratio [40].

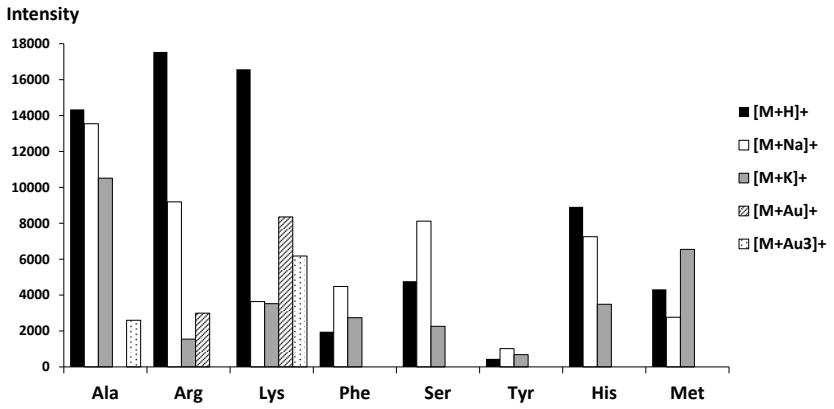

Fig 4. Signal intensity diagram for protonated, sodium, potassium, Au^+ and Au_3^+ adducts for individual amino acids.

Figure 4 contains bar chart of signal intensities for H^+, Na^+, K^+, Au^+ and Au_3^+ adducts for individual amino acids. Adducts with gold ions have been identified for only three amino acids: alanine, arginine and lysine. Proton, sodium and potassium adducts were detected on all mass spectra. For alanine, arginine, lysine and histidine, the proton adduct was the dominant adduct on the spectrum. On the other hand, the Na^+ adduct dominated in the LDI MS spectra of phenylalanine, serine and threonine.

2.2. Conclusions

Methods of synthesis and application of chemically pure monoisotopic gold nanoparticles onto studied surface for LDI MS was presented. Methodology was proven to be very useful for analysis of amino acids and also for characterization of low-mass polymers. Procedures shown are cost-effective, fast, efficient and instrument-limited.

3. Experimental

3.1. Materials

The gold foil (~ 1 mm thick) of 99.9% purity was bought from Polish Mint (Poland). Alanine, arginine, histidine, methionine, phenylalanine and serine were purchased from Sigma-Aldrich (99% purity). Lysine and tyrosine were purchased from Fluka Analytical Standards (98% purity). Poly(propylene glycol) (PPG, average Mn 1000 Da) was purchased from Sigma-Aldrich. All solvents were of HPLC grade, except for water (18 MΩ·cm water produced locally). Steel targets were machined from H17 (1.4016) stainless steel. Before the LDI MS experiments steel targets were cleaned through soaking in boiling solvents: toluene (3x100 mL, each plate for 30 s), chloroform (3x100 mL, each plate for 30 s), acetonitrile (3x100 mL, each plate for 30 s) and deionized water (3x100 mL, each plate for 30 s). Every plate was dried in high vacuum (ca. 0.01 mbar, 24h).

3.2. Methods

3.2.1 PFL 2D GS Laser Generated Nanomaterial (LGN) of gold nanoparticles

The experimental arrangement for the AuNPs preparation by laser ablation is shown in Fig.1A. The gold foil was placed at the bottom of a glass vessel containing mixture solvents isopropanol and water (1:1 v/v). The Au foil was covered by an approximately 3 mm thick layer of mixture solvents (total solvent volume was 4 mL). The laser ablation was carried out with a 1064 nm pulsed fiber laser (Raycus RFL-P20QE/A3). Suspension was obtained after 2 min. irradiation with pulse energy of 0.7 mJ (100 ns

pulse length) at a 60 kHz repetition rate. Laser ablation was accomplished at a scanning speed of 5000 mm/s, the ablation area was 4x4 mm. Suspension was immediately transferred into a syringe and used in the nebulization step.

3.2.2 Nebulization of AuNPs suspension

The experimental setup for the nebulization of AuNPs suspension is shown in Fig.1B. The entire nanoparticle nebulization process was controlled by a computer. The H17 steel plate (laser mass spectrometry target plate) was placed on the table of a translation system consisting of a motorized XY table (EzM-42XL-A powered by closed-loop Ezi-SERVO motors). Glass syringe (1 mL) was filled with a previously prepared suspension of gold nanoparticles and placed in a syringe pump (pumping speed 250 μL/min). The custom-made software directed the 2D system table with 10 mm/s speed using a sequence of movement designed to uniformly cover a target plate. Nebulizer was obtained from Bruker Amazon ETD ESI ion source. Argon at a pressure of 2 bar was used as the nebulizing gas. Generally, all studied samples for MS were placed on the target plate before nebulization.

3.2.3 AuNPs characterization

AuNPs suspension was characterized by UV–VIS spectroscopy (Jasco V-670 spectrophotometer). Spectrum was registered in quartz cuvettes within 200–800 nm spectral range. The blank sample contained mixture solvents isopropanol and water (1:1 v/v). The suspension of AuNPs was also characterized by dynamic light scattering (DLS) using a Zetasizer-Nano ZS from Malvern Instruments. DLS measurements were performed by backscattering at a fixed detector angle of 173°. Isopropanol was used as dispersant.

3.2.4 LDI MS Experiments

Laser desorption/ionization – Time-of-Flight (LDI-ToF) mass spectrometry experiments were performed in reflectron mode using Bruker Autoflex Speed time-of-flight mass spectrometer equipped with a SmartBeam II laser (352 nm). Laser impulse energy was approx. 90-140 μJ, laser repetition rate 1000 Hz. The total number of laser shots was 4000 for each spot. This amount of laser shots was divided into four, symmetrically positioned points laying in distance of ca. 1/3 of spot radius from its center. At each point, 1000 laser shots were made with default random walk applied (random points with 50 laser shots). Measurement range was *m/z* 80-1500. Suppression was turned on typically for ions of *m/z* lower than 80. Reflector voltages used were 21 kV (the first) and 9.55 kV (the second). The data was calibrated and analyzed with FlexAnalysis (version 3.3) using centroid calibration model. Mass calibration (enhanced cubic calibration based on 7-8 calibration points) was performed using internal standards (gold ions Au^+ to Au_5^+).

3.2.5 LDI Sample Preparation

Solution (1 mg/mL) of each analyte was prepared by dissolving it in water (alanine, arginine, histidine, lysine, methionine, phenylalanine, serine and tyrosine). A solution of poly(propylene glycol) in isopropanol of 10 μg/mL concentration was prepared. A 0.5 μL volume of each of the final solution was applied to the steel target and air-dried followed by nebulization with AuNPs suspension.

3.2.6 High resolution scanning electron microscopy (HR SEM)

Target modified with AuNPs generated by PFL 2D GS method was inserted into the Helios Nanolab 650 electron microscope. Voltage was set at 10 and 30 kV, current was 0.2 nA. Images were made in nonimmersive mode.

Acknowledgements
Mrs. Małgorzata Walczak is acknowledged for DLS measurements. This work was supported by the National Science Centre (NCN), SONATA grant no. UMO-2018/31/D/ST4/00109.

References

[1] Tanaka, K., Waki, H., Ido, Y., Akita, S., Yoshida,Y., Yoshida, T., Matsuo, T., *Rapid Commun. Mass Spectrom.* 1988, 2, 151–153.
[2] Egelhofer, V., Gobom, J., Seitz, H., Giavalisco, P., Lehrach, H., Nordhoff, E., *Anal. Chem.* 2002, 74, 1760–1771.
[3] Montaudo, G., Samperi, F., Montaudo, M.S., *Prog. Polym. Sci.* 2006, 31, 277-357.
[4] Wang, J., Zhao, J., Nie, S., Xie, M., Li, S., *Food Hydrocolloids* 2022, 124, 107237.
[5] Leopold, J., Popkova, Y., Engel, K., Schiller, J., *Biomolecules* 2018, 8, 173.
[6] Kołodziej, A., Płaza-Altamer, A., Nizioł, J., Ruman, T., *Int. J. Mass Spectrom.* 2022, 474, 116816.
[7] Domon, B., *Science* 2006, 312, 212–217.
[8] Berkenkamp, S., *Science* 1998, 281, 260–262.
[9] Shrivas, K., Wu, H-F., *Rapid Commun. Mass Spectrom*. 2007, 21, 3103–3108.
[10] Kołodziej A, Ruman, T., Nizioł, J., *J Mass Spectrom.* 2020, 55, e4604.
[11] Abdelhamid, HN., *Microchim Acta* 2019, 186, 682.
[12] Chiang, C-K., Chen, W-T., Chang, H-T., *Chem. Soc. Rev.* 2011, 40, 1269–1281.
[13] Sekuła, J., Nizioł, J., Rode, W., Ruman, T., *Anal. Chim. Acta* 2015, 875, 61–72.
[14] Herizchi, R., Abbasi, E., Milani, M., Akbarzadeh, A., *Artif Cells Nanomed Biotechnol* 2016, 44, 596–602.
[15] Khan, A., Rashid, R., Murtaza, G., Zahra, A., *Trop. J. Pharm Res* 2014, 13, 1169.
[16] Magro, M., Zaccarin, M., Miotto, G., Da Dalt, L., Baratella, D., Fariselli, P., Gabai, G., Vianello, F., *Anal Bioanal Chem* 2018, 410, 2949–2959.
[17] Xu, L., Wang, Y-Y., Huang, J., Chen, C-Y., Wang, Z-X., Xie, H., *Theranostics* 2020, 10, 8996–9031.
[18] McLean, JA., Stumpo, KA., Russell, DH., *J. Am. Chem. Soc.* 2005, 127, 5304–5305.
[19] Pilolli, R., Palmisano, F., Cioffi, N., *Anal Bioanal Chem* 2012, 402, 601–623.
[20] Amendola, V., Litti, L., Meneghetti, M., *Anal. Chem.* 2013, 85, 11747–11754.
[21] Płaza, A., Kołodziej, A., Nizioł, J., Ruman, T., *ACS Meas. Au* 2022, 2, 1, 14-22.
[22] Płaza-Altamer, A., Kołodziej, A., Nizioł, J., Ruman, T., *J Mass Spectrom* 2022;57 (3): .
[23] Rafique, M., Rafique, MS., Kalsoom, U., Afzal, A., Butt, SH., Usman, A., *Opt Quant Electron* 2019, 51, 179.
[24] Zulfajri, M., Huang, W-J., Huang, G-G., Chen, H-F., *Materials* 2021, 14, 11, 2937.
[25] Amendola, V., Meneghetti, M., *Phys. Chem. Chem. Phys.* 2009, 11, 3805.
[26] Ruman, T., Długopolska, K., Jurkiewicz, A., Rut, D., Frączyk, T., Cieśla, J., Leś, A., Szewczuk, Z., Rode, W., *Bioorg. Chem.* 2010, 38, 74–80.
[27] Arendowski, A., Ossoliński, K., Ossolińska, A., Ossoliński, T., Nizioł, J., Ruman, T., *Adv Med Sci* 2021, 66, 326–335.
[28] Arendowski, A., Ossoliński, K., Nizioł, J., Ruman, T., *Int. J. Mass Spectrom* 2020, 456, 116396.
[29] McLean, JA., Stumpo, KA., Russell, DH., *J. Am. Chem. Soc.* 2005, 127, 5304–5305.
[30] Abdelhamid, HN., Wu, H-F., *Anal Bioanal Chem* 2016, 408, 17, 4485–4502.
[31] Daruich De Souza, C., Ribeiro Nogueira, B., Rostelato, MECM., *J. Alloys Compd* 2019, 798, 714–740.
[32] Slepička, P., Slepičková Kasálková, N., Siegel, J., Kolská, Z., Švorčík, V., *Materials* 2019, 13, 1.
[33] Su, C-L., Tseng, W-L., *Anal. Chem.* 2007, 79, 4, 1626–1633.
[34] Haiss, W., Thanh, NTK., Aveyard, J., Fernig, DG., *Anal. Chem.* 2007, 79, 4215–4221.
[35] Amendola, V., Meneghetti, M., *J. Phys. Chem. C* 2009, 113, 11, 4277–4285.
[36] Dufresne, M., Thomas, A., Breault-Turcot, J., Masson, J-F., Chaurand, P., *Anal. Chem*. 2013, 85, 3318–3324.
[37] Arendowski, A., Nizioł, J., Ruman, T., *J. Mass Spectrom.* 2018, 53, 369–378.
[38] Nitta, S., Kawasaki, H., Suganuma, T., Shigeri, Y., Arakawa, R., *J. Phys. Chem. C* 2013, 117, 238–245.
[39] Arendowski, A., Ruman, T., *Anal. Methods* 2018, 10, 45, 5398–5405.
[40] Okuno, S., Wada, Y., Arakawa, R., *Int. J. Mass Spectrom* 2005, 241, 43–48.

Article received: September 2022
Article accepted: October 2022

scientific reports

Check for updates

OPEN

Untargeted ultra-high-resolution mass spectrometry metabolomic profiling of blood serum in bladder cancer

Joanna Nizioł[1]✉, Krzysztof Ossoliński[2], Aneta Płaza-Altamer[3], Artur Kołodziej[3], Anna Ossolińska[2], Tadeusz Ossoliński[2] & Tomasz Ruman[1]

Bladder cancer (BC) is a common urological cancer of high mortality and recurrence rates. Currently, cystoscopy is performed as standard examination for the diagnosis and subsequent monitoring for recurrence of the patients. Frequent expensive and invasive procedures may deterrent patients from regular follow-up screening, therefore it is important to look for new non-invasive methods to aid in the detection of recurrent and/or primary BC. In this study, ultra-high-performance liquid chromatography coupled with ultra-high-resolution mass spectrometry was employed for non-targeted metabolomic profiling of 200 human serum samples to identify biochemical signatures that differentiate BC from non-cancer controls (NCs). Univariate and multivariate statistical analyses with external validation revealed twenty-seven metabolites that differentiate between BC patients from NCs. Abundances of these metabolites displayed statistically significant differences in two independent training and validation sets. Twenty-three serum metabolites were also found to be distinguishing between low- and high-grade of BC patients and controls. Thirty-seven serum metabolites were found to differentiate between different stages of BC. The results suggest that measurement of serum metabolites may provide more facile and less invasive diagnostic methodology for detection of bladder cancer and recurrent disease management.

Bladder cancer (BC) is the second most frequently diagnosed cancer of the urinary tract after prostate cancer in the world. In 2020, this disease affected over 473,000 individuals worldwide and was responsible for 212 536 deaths[1]. According to TNM Classification of Malignant Tumors system proposed by American Joint Committee on Cancer (AJCC), bladder cancer can be classified according to whether the tumor infiltrates into or out of the muscular tissue as muscle-invasive bladder cancer (MIBC) and non-muscle-invasive bladder cancer (NMIBC) respectively[2]. NMIBC is the most common type of BC and includes noninvasive papillary carcinomas (pathologic stage Ta), submucosal invasive tumors (T1) and carcinoma in situ (CIS). MIBC includes tumor which extends into the muscle (stage T2), into the perivisceral fat layer (stage T3) or nearby organs (stage T4). Statistically, in case of 80% of patients tumor do not spread outside of the bladder wall. BC can also be classified by histology as low-grade (LG) tumor that rarely spread from their primary site, and high-grade ones (HG) that are more aggressive and invasive[3].

Generally, the first treatment for early BC is a trans urethral resection of bladder tumor (TURBT) sometimes followed by intravesical instillation of mitomycin or *Bacillus* Calmette-Guerin (BCG) therapy. On the other hand, standard treatment for MIBC is a radical cystectomy with pelvic lymph-node dissection. This is combined with neoadjuvant or adjuvant cisplatin based chemotherapy[4]. Despite such aggressive type of treatment, the survival rate of bladder cancer patients is low. Thus, it is essential to combine local and systemic therapies to improve outcomes. High-grade tumors are usually detected by cytology with high specificity and selectivity, but in the case of low-grade tumors, their determination is very difficult.

Metabolomic instrumental analysis is powerful family of tools mainly often used for study of biofluids. Small molecules levels in biofluids such as serum reflects the current state of the organism allowing for identification and characterization of potential disease biomarkers. The number of metabolomics studies in the diagnosis and

[1]Faculty of Chemistry, Rzeszów University of Technology, 6 Powstańców Warszawy Ave., 35-959 Rzeszow, Poland. [2]Department of Urology, John Paul II Hospital, Grunwaldzka 4 St., 36-100 Kolbuszowa, Poland. [3]Doctoral School of Engineering and Technical Sciences at the Rzeszów University of Technology, 8 Powstańców Warszawy Ave., 35-959 Rzeszow, Poland. ✉email: jniziol@prz.edu.pl

understanding of many diseases is rapidly growing in recent years[5]. Numerous analytical methods have been used to better understand the metabolic changes occurring in living systems and especially cancer phenotypic changes. However, two analytical platforms including nuclear magnetic resonance (NMR) spectroscopy[6] and mass spectrometry (MS) often coupled with liquid chromatography (LC)[7] allow to achieve the most comprehensive screening of cancer metabolomes. MS in comparison to NMR, allows the detection of much broader range of compounds with much higher sensitivity, resolution, and precision using very small amount of sample[8]. Over the past fifteen years, metabolomic analytical methods have been used extensively to investigate BC and to identify potential biomarkers of this cancer in urine, serum, and tissues[9,10]. Compared to urine, serum metabolomics is less prone to be affected by dilution factor. Serum is also more readily available than tissue and procedure less invasive[11]. Despite the advantages of examining the metabolomes of human sera, there are only a few studies on serum metabolomics focused on BC biomarker discovery. So far, most studies related to the analysis of serum of patients with bladder cancer have been carried out using NMR[12–14] or mass spectrometry coupled with liquid[7,15–19] and gas chromatography (GC) [3,20,21]. The first such study of serum from BC patients with LC–MS is from 2012, when Lin et al.[22] analyzed serum profiles of BC with LC–MS, and revealed five potential biomarkers for diagnosis of different types of genitourinary cancer. Five years later Tan et al. (Tan 2017) analyzed serum metabolites of 120 BC patients and 52 healthy persons using ultrahigh performance liquid chromatography (UHPLC) coupled with quadrupole time-of-flight (Q-TOF) mass spectrometry in conjunction with univariate and multivariate statistical analyses. They selected and validated 3 differential metabolites including inosine, acetyl-*N*-formyl-5-methoxykynurenamine and phosphatidylserine, PS(*O*-18:0/0:0) that could discriminate HG and LG BC patients and also LG BC and healthy controls. In the same year, Sahu et al. applied GC and LC–MS to identify metabolite associated with urothelial carcinoma in 72 patients and 7 patients without urothelial neoplasia[17]. Their research indicated potential metabolic pathways altered in NMIBC and MIBC BC. In 2019, Vantaku et al. presented serum targeted metabolomic analysis based on LC–MS to investigated to investigate the molecular differences in BC patients from different parts of the world. The study included two independent cohorts of 54 European Americans and 18 African Americans patients and corresponding healthy controls[16]. In the same year, Amara et al.[15] applied LC–MS for targeted analysis of serum metabolites of 67 BC smokers and 53 post-operative BC patients and 152 healthy controls. Their research showed that serum analysis before and after tumor resection can reveal progressive and significant changes of concentration of selected metabolites. In 2021, Troisi et al. applied LC–MS to profile serum metabolites of 64 patients with BC, 74 patients with RCC, and 141 healthy controls. They used different ensemble machine learning models in order to identify metabolites that differentiate cancer patients from controls and allow to classify the tumor in terms of its stage and grade (Troisi 2021).

In this work we report the first results of untargeted analysis of human sera with ultra-high-resolution mass spectrometry coupled to ultra-high-performance liquid chromatography. This study employed the large number of patients—100 cancer patients and 100 controls. Untargeted analysis was focused on serum metabolic changes generated by bladder cancer but also stratifying the disease by stage and grade. Our study reveals potential BC biomarkers for early detection, screening and differential diagnosis.

Materials and methods

All chemicals were of analytical reagent grade. Deionized water (18 MΩ cm) was produced locally. LC–MS-grade methanol was bought from Sigma Aldrich (St. Louis, MO, USA).

Instrumentation. Instrumental configuration consisted of a Bruker Elute UHPLC system operated by Hystar 3.3 software and a ultra-high-resolution mass spectrometer Bruker Impact II (60,000+ resolution version; Bruker Daltonik GmbH) ESI QTOF-MS equipped with Data Analysis 4.2 (Bruker Daltonik GmbH), and Metaboscape (2021b). A Waters UPLC column ACQUITY BEH (C18 silica, 1.7 µm particles, 50 × 2.1 mm) with compatible column guard was used for all analyses. Two mobile phases were: A = Water with 0.1% formic acid, B = acetonitrile with 0.1% formic acid (v/v). Samples in autosampler were thermostated at 4 °C temperature. Volume of 5 µL of extract was loaded on the column at a flow rate of 200 µL min^{-1}, using 4% B. B percentage was changed with time as follows: 0 min—1%, 0.56 min—1% B, 4.72 min—99%, 5.56 min—99%, 5.6 min—1%, 9.45 min—1%. Solvent flow was 450 µL min^{-1}. Column was thermostated at 40 °C temperature. Internal calibration on 10 mM sodium formate (water: isopropanol 1:1 v/v) ions was performed automatically in Metaboscape with the use of syringe pump at an infusion flow rate of 0.12 mL h^{-1}, using a high precision calibration (HPC) mode. Analyses in positive autoMSMS mode were carried out using the following parameters: *m/z* 50–1200; capillary voltage: 4.5 kV; nebulizer: 2.7 bar; dry gas: 12 L min^{-1}; drying gas temperature: 220 °C; hexapole voltage: 50 Vpp; funnel 1: 200 Vpp; funnel 2: 200 Vpp; pre-pulse storage time: 5 µs; transfer time: 60 µs. Collision-Induced Dissociation (CID) was used with following settings: absolute threshold (per 100 sum): 200 cts; absolute threshold 88 cts; active exclusion 3 spectra; release after 0.3 min, isolation mass: for *m/z* = 100, width was 3, for 500 width was 4, for 1000 was 6 and for 1300 was 8); collision energy value was 30 eV. MS frequency was 20 Hz and MSMS from 5 to 30. The untargeted annotations were performed in Metaboscape (ver. 2021b) with a criterion of mass deviation ($\Delta m/z$) under 2 ppm and mSigma value under 15 as the maximum acceptable deviation of the mass of the compound and the isotopic pattern respectively. For identification and molecular formula generation, exact mass of parent ions was matched with < 3 ppm error and mSigma value < 50 in most cases. All the molecular formulas were obtained using the Smart Formula tool and the C, H, N, O, P, S, Cl, Br, I and F elements. MSMS spectra was automatically matched against MSMS libraries: Bruker HMDB 2.0 library, MassBank of North America (MoNA)[23] library and NIST ver. 2020 MSMS library[24]. The quality control (QC) sample were prepared from 100 different serum extracts and were measured every ten samples throughout the analytical run

to provide a set of data from which method stability and repeatability can be assessed. All measurements were made in technical triplicates.

Collection of human blood samples. Serum samples were collected from one hundred bladder cancer patients (average age 73, Caucasian race) at John Paul II Hospital in Kolbuszowa (Poland). Control serum samples were collected from healthy volunteers after medical examination focused on detection of urinary cancers. All the patients underwent transurethral resection of bladder tumor (TURBT) following detailed clinical questioning and laboratory testing. The study was approved by local Bioethics Committee at the University of Rzeszow (Poland, permission no. 2018/04/10) and performed in accordance with relevant guidelines and regulations. All patients involved in the study were informed about the purpose of this research and planned procedures, and signed an informed consent form. Just over half of the patients (n = 54) had low-grade bladder cancer and papillary urothelial neoplasm of low malignant potential (PUNLMP) (n = 3), while the remaining patient group exhibited high-grade disease (n = 41). In two cases, both high- and low-grade neoplasms were detected. The majority of these patients (n = 69) displayed noninvasive papillary carcinomas (pathologic stage Ta, pTa) stage disease, nineteen had submucosal invasive tumors (pathologic stage T1, pT1) stage and twelve patients had muscle invasive bladder cancer (pathologic stage T2, pT2). The average age for diagnosed patients with BC was 74 ± 10 years while in NCs group the average age was 64 ± 12. The entire NCs group consists of patients admitted to the urology department for surgical treatment of benign urological conditions (urolithiasis, benign prostate hyperplasia, testicular hydrocele, varicocele, phimosis, ureteropelvic junction stenosis, urinary incontinence, urethral stricture). Each of these patients has had performed at least an abdominal ultrasound to rule out neoplasms (patients with urolithiasis usually also had a computed tomography (CT) scan) and a basic bundle of lab tests required for urological surgery that rule out inflammation. Patients were selected according to a similar age range. After familiarizing patients with the research program, patients from the control group gave written consent to donate residual serum for study (no additional blood was drawn for the purpose of this study, except that taken before urological surgery). The clinical characteristics of the patients are presented in supplementary information 1, table S1. Approximately 2.6 ml of blood was drawn from each participant. Samples were centrifuged at 3000 rpm for 10 min at room temperature. The serum was then separated and kept at − 60 °C until further use.

Sample preparation. Polar metabolites were extracted from serum samples as described in our recent publication (Nizioł, Ossoliński, et al. 2021). In brief, deep frozen blood plasma samples (300 µL) were thawed on ice to 4 °C before use. Samples were then centrifuged at 12,000×*g* for 5 min also at 4 °C temperature. Volume of 300 µL of serum was pipetted into sterile 2.0 mL Eppendorf tubes and room-temperature acetone (900 µL) was added and vial vortexed for 1 min. Resulting suspension was incubated at room temperature for 20 min followed by 30 min at − 20 °C. Tubes was then centrifuged at 6000×*g* for 5 min at 4 °C temperature to sediment serum precipitated proteins and phospholipids and then clarified supernatant A (800 µL) was transferred to a new 2 ml microcentrifuge tube. Volume of 500 µL of a 3:1 acetone/H_2O solution was added to the pellet and vortexed vigorously until the pellet was resuspended, this tube was then centrifuged at 12,000×*g* for 10 min at 4 °C to sediment serum precipitated proteins again. Resulting supernatant B was then combined with supernatant A. Volume of 260 µL of combined supernatants were vacuum dried in speedvac-type concentrator and dissolved in 400 µL of methanol, vortexed and centrifuged (12,000×*g* for 5 min at 4 °C). Supernatant volume of 100 µL was transferred into HPLC vial insert of 130 µL capacity and inserted into Elute autosampler.

Multivariate statistical analysis. All metabolite datasets exported from Metaboscape v.2021b were analyzed using the MetaboAnalyst 5.0 online software[25]. Prior to analysis, data was log-transformed, auto-scaled and normalized by sum. Resulting metabolite profiles were then subjected to unsupervised Principal Component Analysis (PCA). The separation between the BC and control groups observed in the 2D and 3D PCA scores plot was further examined using the supervised multivariate statistical analysis such as Orthogonal Partial Least Squares Discriminant Analysis (OPLS-DA). The quality of the OPLS-DA models was assessed by the goodness of fit (R^2Y) and the predictive ability of the models (Q^2). VIP plots were generated to recognize metabolites most significantly responsible for groups separation. Metabolites with VIP value higher than 1.0 were considered potential biomarker candidates. To test the accuracy of the multivariate statistical models, and to rule out that the observed separation in the OPLS-DA is due to chance ($p < 0.05$), permutation tests were performed with 2000-fold repetition. Statistical significance of metabolite level differences was assessed with paired parametric t-test using Mann–Witney and Bonferroni correction. *P* values and false discovery rates (FDR; q-value) less than 0.05 were considered statistically significant. Receiver operating characteristic curve (ROC) analyses together with random forest modeling were commenced to evaluate the diagnostic value of all selected metabolites. The performance of the metabolites was estimated using the area under the curve (AUC), 95% confidence interval, specificity and selectivity. Only variables with an AUC value higher than 0.75 were considered to be relevant. Multivariate statistical analyses were performed independently for the training and validation datasets. Compounds differentiating between tumor and control serum samples were selected based on external validation, which uses two independent datasets (here called training and validation dataset) to validate the performance of a model[26]. The final set of potential BC biomarkers selected fulfilled all criteria in both testing and validation data sets. Chemometric tools such as 2D PCA, OPLS-DA and ROC analysis were also used to assess metabolic profile similarities and differences between different grades and stages of bladder cancer. To identify metabolic pathways impacted by bladder cancer, a metabolic pathway impact analysis was made in MetaboAnalyst 5.0 and the Kyoto Encyclopedia of Genes and Genomes (KEGG) pathway library for *Homo sapiens*[27]. Quantitative pathway enrichment analysis was conducted based on Small Molecule Pathway Database (SMPD). Each impacted

pathway was classified according to statistical *p* value, Holm p (*p* value adjusted by Holm–Bonferroni method) and FDR (*p* value adjusted using False Discovery Rate), calculated from pathway topology analysis.

Ethics approval. The study protocol was approved by local Bioethics Committee at the University of Rzeszow (Poland) (permission no. 2018/04/10).

Results

In this study, we characterized the metabolic profiles of one-hundred patients suffering from bladder cancer, in an effort to develop serum-specific metabolic signatures for early and specific detection of bladder cancer. For this purpose, we recorded ultra-high-resolution LC–MS spectra of 200 total (100 BC and 100 control = NCs) metabolite extracts from patient and healthy control serum samples in an effort to identify potential discriminant biomarkers of bladder cancer. Datasets from the BC patients and NCs were divided into two groups, a training set, comprising 80% of all samples and a validation set, corresponding to 20% of all samples. Patient samples of a given stage of BC in the training set accounted for 80% of all samples of that stage. Serum metabolic profiling was performed independently on the two datasets. The training set was used to identify serum diagnostic markers for cancer and stage of its malignancy and, in turn, the validation set was used to independently validate the diagnostic performance of serum metabolite biomarkers.

Distinguishing between bladder cancer and control serum samples. In total, 5498 m/*z* features were found in each serum sample in both training and validation set with applied filtration that required that software show only features that were in at least nine samples. Unsupervised 2D PCA score plots of both subsets indicated a good separation between cancer patients and controls based on distinct and characteristic metabolite profiles. The best separation of groups in the training set was obtained along principal components 1 and 2 (i.e. PC1 and PC2) which accounted for 27.8% and 5.5% respectively. Only a few outliers were detected in the central 95% of the field of view (Fig. 1a). In turn, in the validation set, the best separation between cancer and control serum samples was also observed along PC1 (28.2%) and PC2 and (6.6%) (Fig. 1b).

A supervised multivariate analysis using OPLS-DA analysis was carried out to explore the metabolic differences between the BC and NC groups. In the training set, the score plot indicated a clear separation between those two groups (Fig. 1c). Two thousand permutation tests were conducted to validate the OPLS-DA model (Fig. S1 A). Good discrimination was observed between the two groups ($Q^2 = 0.971$, $R^2Y = 0.992$, *p* value < 5E-04 (0/2000)), revealing substantial differences in the metabolic profiles of cancer versus control serum samples. Model overview showing high R^2Y and Q^2 indicating good interpretability and predictability by this OPLS-DA model (Fig. S1 B). A similar tendency to discriminate BC patients and NCs was observed in OPLS-DA model of the validation set (Fig. 1d), which was confirmed by the very good results of the permutation test ($Q^2 = 0.929$, $R^2Y = 0.995$, *p* value < 5E-04 (0/2000)) (Fig. S1C). Potential serum bladder cancer biomarkers were selected on the basis of the VIP plot resulting from the OPLS-DA model. By combining the VIP (> 1.0) with the results from the independent t-test (*p* value and FDR from t-test < 0.05) 1012 variables were selected in training set as differential for BC patients and NCs (Table 1, Supplementary information 2). In turn, in validation set 1052 variables were considered as significant (Table 2, Supplementary information 2). Finally, 864 common *m/z* and rt values were indicated, both in the training and validation sets. Among these features, to 121 m/*z* values were assigned to a specific chemical compound (Table 1). Next, univariate ROC analysis was separately performed on both training and validation sets to evaluate the diagnostic ability of the models. The results indicated that in the serum samples all 85 out of previously selected 121 metabolites exhibit very high area under the curve (AUC) above 0.8. As shown in Fig. 1e,f, the combination of mass features in both subsets was found to be a powerful discriminator of control versus bladder cancer serum samples (AUC > 99%). Finally, set of twenty-seven potential BC biomarkers were selected with cut-off criteria of FC > 2 and < 0.5, $\Delta m/z < 2$ ppm and mSigma < 50 in both testing and validation data sets. The sensitivity and specificity of the selected 27 metabolites were also determined and all metabolites disclosed sensitivity and specificity greater than 77 and 85%, respectively (Table 1 and S1, Supplementary information 2).

Distinguishing between low- and high- grade bladder cancer and control serum samples. To determine whether metabolomics analysis of serum samples could help discriminate between different grades of BC, another series of PCA and OPLS DA analyses were performed on the training (80 NCs, 32 patients with HG and 45 patients with LG,) and validation (20 NCs, 8 patients with HG and 12 patients with LG,) data sets (Tabe S1) excluding three samples from patients with PUNLMP. PCA and OPLS-DA scores plots revealed good discrimination between separately control and cancer groups of varying grades of tumors (LG vs NCs and HG vs NCs) in both training and validation set (Fig. 2, S2). Quality factors for those models amounted to $Q^2 > 0.89$ and $R^2Y > 0.982$, with p values based on permutation tests (n = 2000) smaller than 5E-4 (Fig. S3, S4) indicating a perfect discrimination of metabolites profiles between those groups. However, we did not observe a substantial difference between the LG and HG BC patients in the PCA scores plot (data not shown).

In HG BC vs NCs OPLS-DA model 1500 variables were considered as significant (VIP > 1, *p* value < 0.05) in both training and validation set. Among these features, 138 m/*z* values were assigned to a specific chemical compound. Analysis of LG BC vs NCs in OPLS-DA model in training and validation set revealed common 1600 m/*z* values as significant contributors to the separation between those two groups of which 148 were assigned to specific compound. Univariate ROC curve analyses indicated that these models have a good diagnostic performance (Fig. 2, S2). AUC values for five out of fifteen metabolites were found to be greater than 0.75. Finally, set of twenty-three potential LG and HG BC biomarkers were selected with cut-off criteria of FC > 2 and < 0.5, $\Delta m/z < 2$ ppm and mSigma < 50 in both testing and validation data sets. The sensitivity and specificity of the

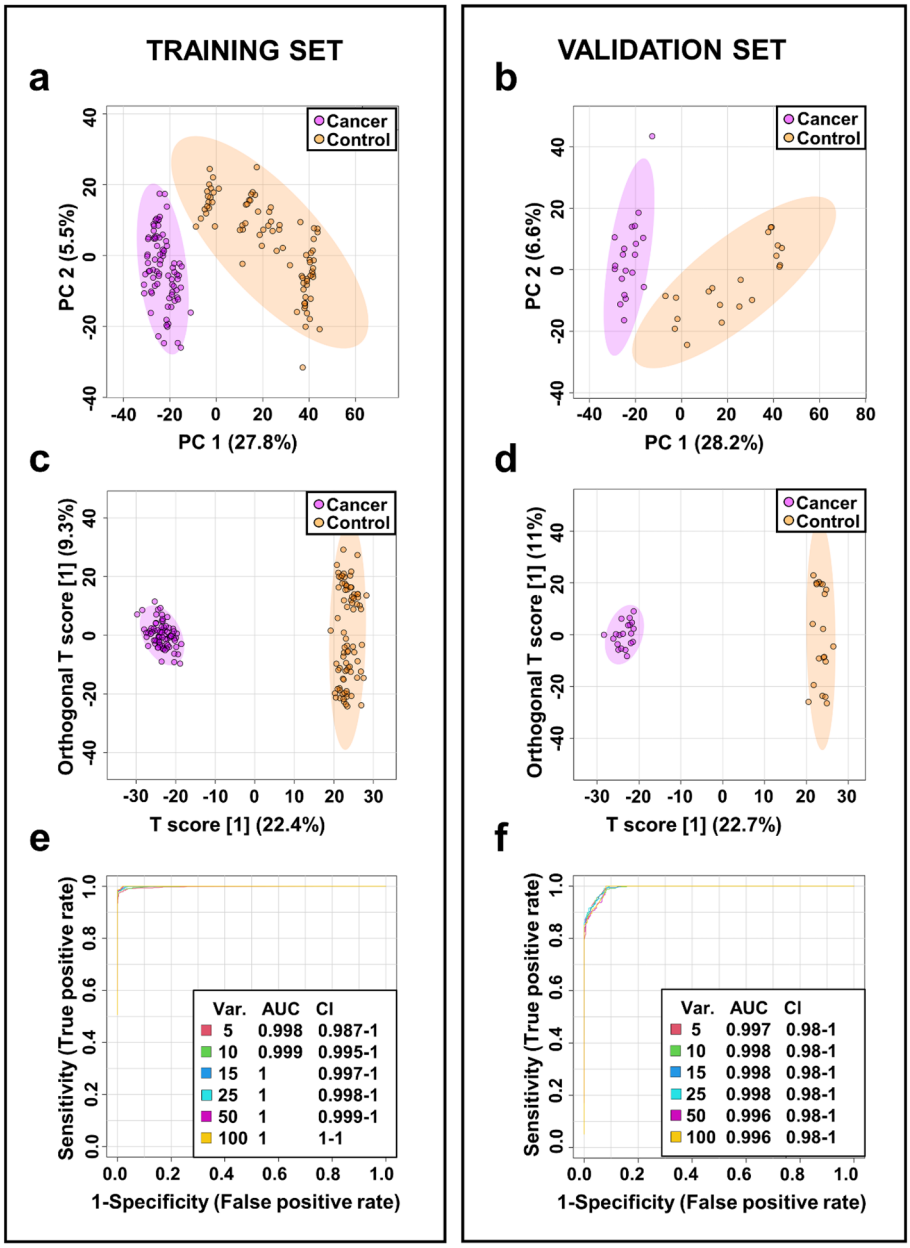

Figure 1. Metabolomic analysis of serum samples from BC and NCs. PCA and OPLS-DA scores plots of the tumor (violet) and control (orange) serum samples in the training set (**a**,**c**) and validation set (**b**,**d**). The receiving operator characteristic (ROC) curves in the training set (**e**) and validation set (**f**).

selected 23 metabolites were also determined and all metabolites disclosed sensitivity and specificity greater than 78% (Table 2 and S2, Supplementary information 2).

Distinguishing between different stages of bladder cancer and control serum samples. Analysis of tumor stages was performed for the entire LC–MS dataset of serum metabolite extracts from patients diagnosed with bladder cancer. Metabolite profiling analysis included 69 serum samples from patients with noninvasive papillary carcinomas (pTa) 19 samples from pT1 stage and 12 from patients with muscle invasive bladder cancer (pT2).

PCA and OPLS-DA scores plot indicated good separation between NCs and different stages of BC (pTa vs NCs, pT1 vs NCs and pT2 vs NCs, Fig. 3). Quality factors for those models were $Q^2 > 0.904$ and $R^2Y > 0.988$, with *p* values based on permutation tests (n = 2000) smaller than 5E-4 (Fig. S5) indicating a very good discrimination of metabolites profiles between those groups. Fold Change and VIP plot analysis of the OPLS-DA model indicated 63, 66 and 69 m/*z* values that appeared to be most relevant for sample differentiation between pTa BC vs NCs, pT1 BC vs NCs and pT2 BC vs NCs respectively out of pool of features assigned to specific chemical compounds. Next, ROC curve analysis was performed to assess the performance of three models in distinguishing

No	Name	Structure	m/z[a]	Δm/z [ppm]	RT [s]	VIP[b]	FC[c]	*p* value	FDR	AUC	Spec. [%][d]	Sens. [%][d]
1	Aureonitol[e,g,h]	$C_{13}H_{18}O_2$	207.1378	−0.7	173.2	1.82	0.20	5.00E−27	3.20E−25	0.993	96	98
2	Norcamphor[e,g,h]	$C_7H_{10}O$	111.0803	−1.0	143.2	1.79	0.29	5.80E−27	3.30E−25	0.992	96	100
3	Perillyl alcohol[e,g]	$C_{10}H_{16}O$	153.1273	−0.8	210.3	1.83	0.25	6.30E−27	3.30E−25	0.992	96	100
4	Thymol[e,f,g]	$C_{10}H_{14}O$	151.1116	−0.8	204.2	1.78	0.39	7.30E−27	3.40E−25	0.991	94	99
5	Methyl 2-octynoate[e,g,h]	$C_9H_{14}O_2$	155.1065	−1.3	177.7	1.72	0.31	8.40E−27	3.40E−25	0.991	95	98
6	3,5,5-Trimethyl-2-cyclohexen-1-one[e,g,h]	$C_9H_{14}O$	139.1116	−0.9	193.2	1.83	0.17	9.80E−27	3.50E−25	0.990	96	99
7	Alantolactone[e,g,h]	$C_{15}H_{20}O_2$	233.1535	−0.3	194.6	1.80	0.23	9.80E−27	3.50E−25	0.990	94	98
8	4-Heptanone[e,f,g]	$C_7H_{14}O$	115.1116	−0.9	206.7	1.79	0.24	1.00E−26	3.50E−25	0.990	94	96
9	7-Epi-Jasmonic acid[e,g,h]	$C_{12}H_{18}O_3$	211.1328	−0.2	160.9	1.80	0.19	1.50E−26	4.10E−25	0.988	96	96
10	Dihydrojasmone[e,g,h]	$C_{11}H_{18}O$	167.1429	−0.8	228.3	1.78	0.41	1.60E−26	4.20E−25	0.988	94	94
11	Valeric acid[e,f,g]	$C_5H_{10}O_2$	103.0753	−0.8	132.2	1.75	0.41	2.30E−26	5.10E−25	0.987	91	96
12	4,4,7a-trimethyl-3a,5,6,7-tetrahydro-3*H*-indene-1-carboxylic acid[e,g,h]	$C_{13}H_{20}O_2$	209.1534	−0.8	197.8	1.75	0.4	5.50E−26	9.20E−25	0.983	94	95
13	1-Acetylindole[e,g,h]	$C_{10}H_9NO$	160.0757	0.1	131.1	1.65	2.13	1.50E−25	2.20E−24	0.978	93	98
14	Linoleic acid[e,g]	$C_{18}H_{32}O_2$	281.2473	−0.8	258.6	1.52	2.55	3.50E−25	4.40E−24	0.975	94	94
15	1-Phenyl-1-pentanone[e,g,h]	$C_{11}H_{14}O$	163.1116	−0.8	200.5	1.73	0.34	7.50E−25	8.30E−24	0.971	94	86
16	Umbelliferone[e,g,h]	$C_9H_6O_3$	163.0389	−0.6	182.1	1.69	0.49	1.10E−24	1.10E−23	0.970	91	90
17	Elaidic acid[e,g]	$C_{18}H_{34}O_2$	283.2629	−0.9	278.4	1.67	3.33	1.20E−24	1.30E−23	0.969	95	94
18	3-Ethylphenol[e,g,h]	$C_8H_{10}O$	123.0803	−0.9	122.9	1.72	0.36	1.30E−24	1.30E−23	0.969	96	95
19	D-Limonene[e,g]	$C_{10}H_{16}$	137.1324	−0.7	143.9	1.72	0.30	2.90E−24	2.60E−23	0.965	91	90
20	6-Hydroxy-4,4,7a-trimethyl-5,6,7,7a-tetrahydrobenzofuran-2(4*H*)-one[e,h]	$C_{11}H_{16}O_3$	197.1171	−0.8	143.2	1.60	0.41	8.60E−23	6.00E−22	0.950	89	90
21	LysoPE(P-18:0/0:0) [e,g,h]	$C_{23}H_{48}NO_6P$	466.3288	−1.0	294.2	1.58	0.38	1.30E−22	8.40E−22	0.948	86	91
22	Palmitoleoyl Ethanolamide[e,g,h]	$C_{18}H_{35}NO_2$	298.2738	−0.9	236.5	1.41	2.08	1.50E−22	1.00E−21	0.947	90	91
23	PE(P-16:0e/0:0) [e,g,h]	$C_{21}H_{44}NO_6P$	438.2977	−0.6	267.5	1.48	0.48	4.70E−20	2.30E−19	0.920	85	88
24	3-Hexanone[e,g,h]	$C_6H_{12}O$	211.1328	−0.2	160.9	1.40	0.50	5.20E−18	2.10E−17	0.896	86	96
25	Epsilon-caprolactam[e,f,g,h]	$C_6H_{11}NO$	114.0914	−0.2	114.5	1.16	2.35	5.70E−18	2.30E−17	0.896	85	81
26	L-Acetylcarnitine[e,f,g]	$C_9H_{17}NO_4$	204.1230	−0.3	22.9	1.37	2.36	1.50E−16	5.40E−16	0.878	85	78
27	LysoPC(18:3)[e,g,h]	$C_{26}H_{48}NO_7P$	518.3236	−1.0	237.9	1.25	0.48	1.30E−15	4.60E−15	0.866	86	78

Table 1. Differential metabolites for discrimination between BC patients and NCs (p value < 0.05; FDR < 0.05; VIP > 1; FC < 0.5 and > 2). [a]Experimental monoisotopic mass; [b]VIP scores derived from OPLS-DA model; [c]fold change between cancer and control serum calculated from the abundance mean values for each group—cancer-to-normal ratio; [d]ROC curve analysis for individual biomarkers; [e]the metabolites identified by high precursor mass accuracy; [f]the metabolites identified by matching retention time; [g]the metabolites identified by matching isotopic pattern; [h]the metabolites identified by matching MS/MS fragment spectra; AUC: area under the curve; CI: confidence interval; FC: fold change; FDR: false discovery rate; *m/z*: mass-to-charge ratio; RT: retention time; Sens.: Sensitivity; Spec.: Specificity; VIP: variable influence on projection.

between pTa; pT1 and pT2 bladder cancer stages and NCs. Finally, set of thirty-seven potential pTa, pT1 and pT2 BC biomarkers were selected with cut-off criteria of FC > 2 and < 0.5, Δm/z < 2 ppm and mSigma < 50 in both testing and validation data sets (Table 3). The sensitivity and specificity of the selected 37 metabolites were also determined and all metabolites disclosed sensitivity and specificity greater than 74 and 62%, respectively S3, Supplementary information 2). Comparison of the three groups of cancer stage (pT1 vs. pTa vs. pT2) did not reveal any statistically significant differences (data not shown).

Pathway analysis of potential biomarkers. A metabolic pathway impact analysis was performed using MetaboAnalyst 5.0 to identify the most relevant pathways involved in the observed changes of serum metabolite levels. Forty-five metabolites identified in the UHPLC-UHRMS analysis were subjected to pathway analysis and quantitative pathway enrichment analysis. Forty-nine compounds were found to be relevant to human metabolism. Five metabolic pathways, including linoleic acid metabolism, glycerophospholipid metabolism, alpha-linolenic acid metabolism, arachidonic acid metabolism and biosynthesis of unsaturated fatty acids were found to be significantly impacted comparing BC to controls. Results from pathway impact analysis is shown in Fig. 4a and Table S2 (supplementary information 1).

To expand the metabolomic analysis of pathways related to bladder cancer, we performed a quantitative enrichment analysis using the MetaboAnalyst 5.0 pathway enrichment module and its associated Small Molecule Pathway Database (SMPDB). Two additional pathways were found to be relevant to bladder cancer: beta oxidation of very long chain fatty acids, phospholipid biosynthesis and oxidation of branched chain fatty acids (Fig. 4b and Table S3.

No	Metabolites	Formula	*m/z*[a]	RT [s]	HG versus control				LG versus control			
					VIP[b]	FC[c]	Spec. [%][d]	Sens. [%][d]	VIP[b]	FC[c]	Spec. [%][d]	Sens. [%][d]
1	Aureonitol [e,g,h]	$C_{13}H_{18}O_2$	207.1378	173.22	1.82	0.20	98	97	1.84	0.20	100	96
2	7-Epi-Jasmonic acid [e,g,h]	$C_{12}H_{18}O_3$	211.1328	160.86	1.80	0.19	96	97	1.83	0.19	96	96
3	3,5,5-Trimethyl-2-cyclohexen-1-one [e,g,h]	$C_9H_{14}O$	139.1116	193.16	1.86	0.17	95	94	1.87	0.17	98	93
4	Alantolactone [e,g,h]	$C_{15}H_{20}O_2$	233.1535	194.63	1.80	0.25	95	94	1.84	0.22	98	93
5	Valeric acid[e,f,g]	$C_5H_{10}O_2$	103.0753	132.22	1.78	0.41	98	94	1.79	0.41	95	93
6	4-Heptanone [e,g,h]	$C_7H_{14}O$	115.1116	206.71	1.78	0.24	96	97	1.81	0.23	96	93
7	Methyl 2-octynoate [e,g,h]	$C_9H_{14}O_2$	155.1065	177.72	1.77	0.30	98	91	1.84	0.32	98	98
8	4,4,7a-trimethyl-3a,5,6,7-tetrahydro-3*H*-indene-1-carboxylic acid [e,g,h]	$C_{13}H_{20}O_2$	209.1534	197.75	1.74	0.40	98	91	1.75	0.40	96	89
9	Thymol [e,g,h]	$C_{10}H_{14}O$	151.1116	204.15	1.74	0.39	99	94	1.76	0.39	99	93
10	Umbelliferone [e,g,h]	$C_9H_6O_3$	163.0389	182.05	–	–	–		1.74	0.49	94	91
11	4,7-Dimethyl-1,3-benzothiazol-2-ylamine [e,g,h]	$C_9H_{10}N_2S$	179.0638	142.04	1.66	2.00	93	88	–	–	–	–
12	D-Limonene[e,g]	$C_{10}H_{16}$	137.1324	143.88	1.66	0.30	89	94	1.70	0.31	86	93
13	LysoPE(P-18:0/0:0) [e,g,h]	$C_{23}H_{48}NO_6P$	466.3288	294.22	1.63	0.36	91	91	1.55	0.39	86	87
14	1-Acetylindole [e,g,h]	$C_{10}H_9NO$	160.0757	131.14	1.58	2.14	93	94	1.61	2.13	98	93
15	6-Hydroxy-4,4,7a-trimethyl-5,6,7,7a-tetrahydrobenzofuran-2(4*H*)-one[e,h]	$C_{11}H_{16}O_3$	197.1171	143.16	1.57	0.43	94	81	1.64	0.40	91	89
16	PE(P-16:0e/0:0) [e,g,h]	$C_{21}H_{44}NO_6P$	438.2977	267.49	1.56	0.44	88	88	–	–	–	–
17	LysoPC(20:3) [e,g,h]	$C_{28}H_{52}NO_7P$	546.3545	259.45	1.48	0.45	84	81	–	–	–	–
18	Linoleic acid[e,g]	$C_{18}H_{32}O_2$	281.2473	258.56	1.43	2.64	94	94	1.39	2.44	93	93
19	LysoPC(18:3)[e,g,h]	$C_{26}H_{48}NO_7P$	518.3236	237.91	1.33	0.45	78	78	–	–	–	–
20	L-Acetylcarnitine[e,f,g]	$C_9H_{17}NO_4$	204.1230	22.91	1.33	2.39	79	84	1.35	2.29	86	80
21	Epsilon-caprolactam[e,f,g,h]	$C_6H_{11}NO$	114.0914	114.47	1.19	2.08	89	94	1.32	2.58	89	82
22	3-Hexanone[e,g,h]	$C_6H_{12}O$	101.0960	152.86	–	–	–	–	1.42	0.49	79	93
23	Elaidic acid[e,g]	$C_{18}H_{34}O_2$	283.2629	278.39	–	–	–	–	1.67	3.36	91	98

Table 2. Differential metabolites for discrimination between LG and HG BC patients and NCs (p value < 0.05; FDR < 0.05; VIP > 1; FC < 0.5 and > 2). [a]Experimental monoisotopic mass; [b]VIP scores derived from OPLS-DA model; [c]fold change between cancer and control serum calculated from the abundance mean values for each group—cancer-to-normal ratio; [d]ROC curve analysis for individual biomarkers; [e]the metabolites identified by high precursor mass accuracy; [f]the metabolites identified by matching retention time; [g]the metabolites identified by matching isotopic pattern; [h]the metabolites identified by matching MS/MS fragment spectra; AUC: area under the curve; CI: confidence interval; FC: fold change; FDR: false discovery rate; HG: high-grade; LG: low-grade; *m/z*: mass-to-charge ratio; RT: retention time; Sens.: Sensitivity; Spec.: Specificity; VIP: variable influence on projection.

Discussion

Over the past decade, metabolomics studies have provided valuable information on the metabolic profile of patients suffering from various diseases, including cancer, and identified potential markers of developing or recurring disease. Cancer cells have the ability to reprogram their metabolism in order to support the increased need for energy caused by rapid proliferation. Monitoring of changes in the levels of various metabolites in cancer cells or body fluids may be a potential source of new cancer biomarkers. To date, many studies have been published indicating the high potential of metabolomic markers in the diagnosis of various cancers and in understanding of the mechanisms of cancer initiation and development[28].

In this study UHPLC-UHRMS and -UHRMS/MS methods were employed to evaluate changes in serum metabolite levels between 100 bladder cancer patients and 100 normal controls. The largest class of compounds differentiating the NCs group from the BC patients were lipids and lipid-like molecules. Lipids are the fundamental building blocks of all cell membranes and serve as a long-term energy storage. Furthermore, lipids have many other important functions within living organisms including transmit nerve impulses, production and regulation of certain hormones, cushion vital organs, intracellular signal transmission and cell transporting systems. Lipid metabolism is involved in various processes associated with cancer cells. Over the past decade, numerous studies have demonstrated that lipids and metabolites associated with lipid metabolism may be potential markers in human cancers including bladder cancer[29]. We found that the plasma content of 10 glycerophospholipids including PE(P-16:0e/0:0), PC(16:1/16:1), PC(16:0/18:3), LPE(P-18:0/0:0), LPC(14:0/0:0), LPC(P-18:0), LPC(18:3), LPC(18:2), LPC(20:3), LPC(22:5) were significantly higher in the serum of NCs than in the BC subjects. This finding is in line with previous metabolomic studies that demonstrated an association of changes in the levels of these lipids in the blood with various cancers[30]. Thus, alterations in these lipids' metabolism may, therefore, play important roles in the development and progression of bladder cancer.

Glycerophospholipids (GPs), also called phospholipids include phosphatidylethanolamines (PE), phosphatidylcholines (PC) and phosphatidylethanolamines (PE), all of which are glycerol-based phospholipids. These compounds are a major component of the membranes of animal cells in which they are asymmetrically distributed

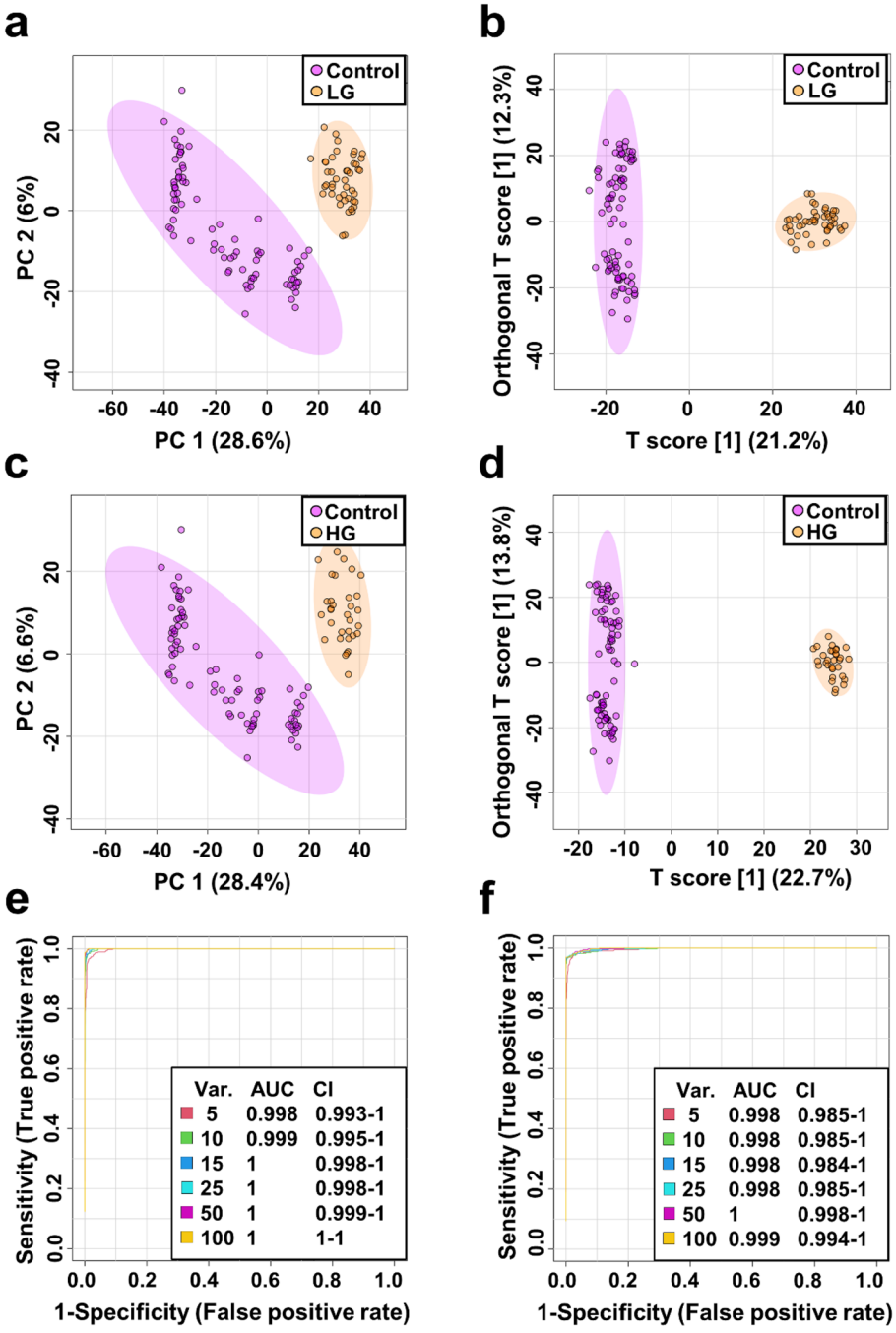

Figure 2. Metabolomic differentiation between different grades of BC and NCs in training set. PCA (**a**) and OPLS-DA (**b**) scores plots of the control (violet) and low-grade (orange). PCA (**c**) and OPLS-DA (**d**) scores plots of the control (violet) and high-grade (orange). ROC curves for LG (**e**) and HG (**f**) BC serum samples vs NCs.

acting as the matrix of different membrane proteins. Many previous studies have found low serum PE levels in various cancers including colon, prostate, lung, and breast cancers indicating these compounds as potential tumor markers[31,32]. Serum levels of PE(P-16:0e/0:0) were found by Lin et. al significantly lower in patients with kidney cancer compared to controls[22]. Some studies have provided evidence that translocation of PE from the inner to the outer leaflet of the plasma membrane indicating a loss of asymmetric distribution of aminophospholipids has been shown as the first sign of impending apoptosis. Thus, lower levels of PE(P-16:0e/0:0) in serum may be an early symptom of apoptotic cell death[33]. Moreover, human phosphatidylethanolamine-binding protein is associated with resistance to apoptosis of tumor cells[34]. It has been reported that exogenous PEs inhibits the growth and indicates an apoptosis of human hepatoma HepG2 cells[35]. Lysophosphatidylethanolamine LPC, LysoPC), LysoPE (P-18:0/0:0) also known as LPE(18:0) was found in lower level in plasma of patients with liver, gastric colorectal, ovarian and lung cancer compared to the control group[32,36,37]. Lysophosphatidylcholines (LPC, lysoPC)

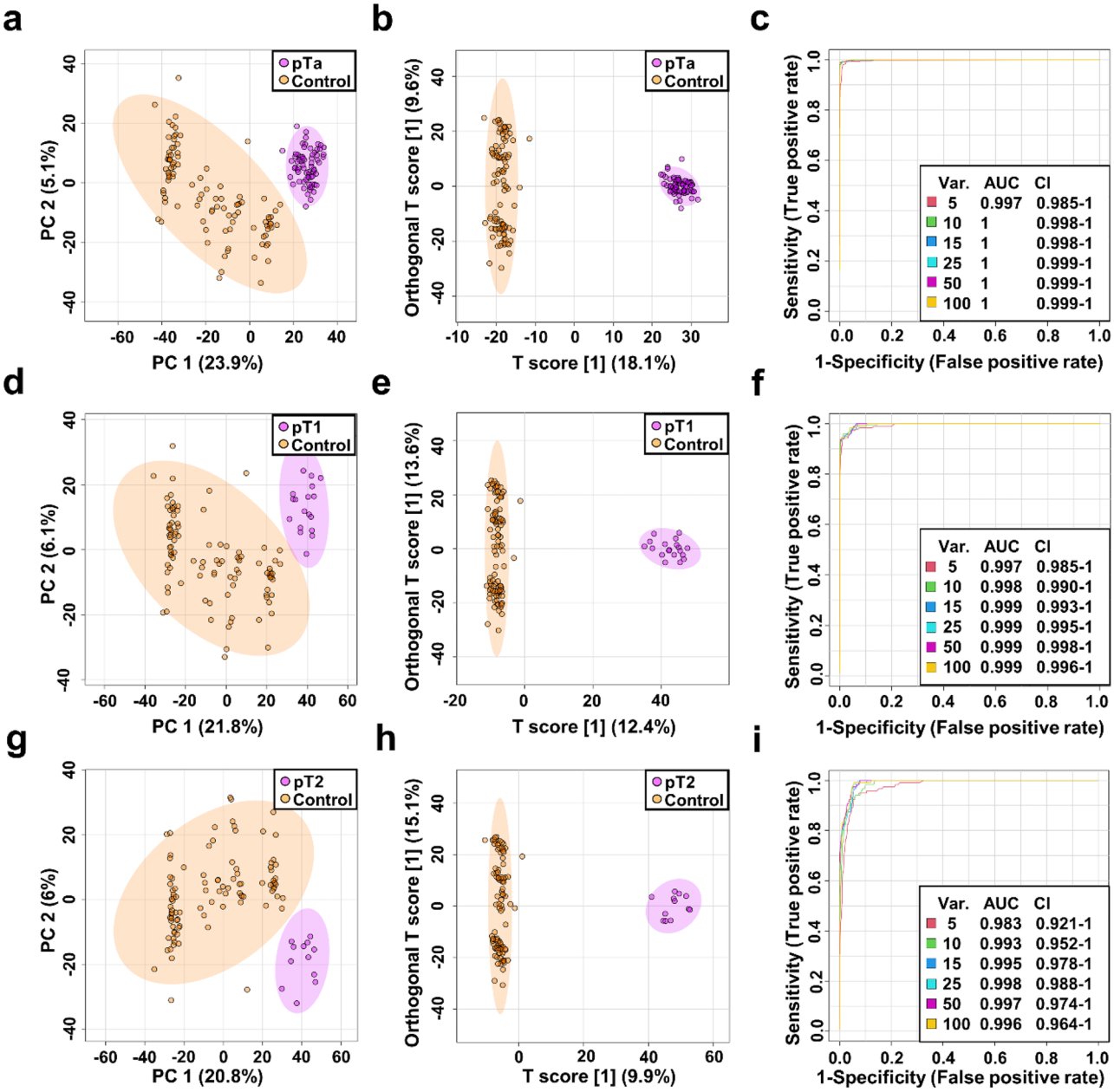

Figure 3. Metabolomic differentiation between different stages of BC and NCs. PCA (**a**), OPLS-DA (**b**) scores plots and ROC curve (**c**) of the pTa (violet) and control (orange). PCA (**d**), OPLS-DA (**e**) scores plots and ROC curve (**f**) of the pT1 (violet) and control (orange). PCA (**g**), OPLS-DA (**h**) scores plots and ROC curve (**i**) of the pT2 (violet) and control (orange).

are an important endogenous signaling phospholipids involved in a variety of important processes, including cell migration, cell proliferation, inflammation and angiogenesis. Decreased LPC plasma level in cancer was also observed in previous study and was associated with body weight loss and increased inflammation. Level of these compounds is inversely correlated with C-reactive protein levels in plasma (CRP)[38]. LPCs were found to be disturbed in several diseases including cancer. Previous metabolomic studies have reported lower level of PC(34:4), LysoPC(20:3) and LPC(P-18:0) in plasma of patients with ovarian cancer (EOC) compared to control[39]. Zhang et al.[40] have reported that LPC(14:0) was down-regulated in patients with recurrent EOC. Lower level of lysophospholipids have been associated with high activity of specific cell-surface G protein-coupled receptors which may cause apoptosis. Tan et al.[41] observed significantly lower of LPC(14:0) in the serum of patients with colorectal cancer compared with healthy controls. LPC(18:1), LPC(18:2) and LPC(18:3) were significantly decreasing in plasma of patients with colorectal cancer compared with healthy controls[42,43]. Lee et al.[32] showed that the levels of LPC(18:2) were lower in plasma samples of patients with colorectal cancer and higher in plasma samples of patients with liver, gastric, lung and thyroid compared to those of healthy control individuals using UHPLC-MS/MS. LPC(18:2) was also found in lower level in plasma of patients with ovarian cancer compared to the control group[36]. Previous metabolomic studies have demonstrated that LysoPC(18:1), LysoPC(20:3) were

No	Metabolites	Formula	*m/z*[a]	RT [s]	pTa versus control		pT1 versus control		pT2 versus control	
					VIP[b]	FC[c]	VIP[b]	FC[c]	VIP[b]	FC[c]
1	Alpha-hydroxyisobutyric acid[d,e]	$C_4H_8O_3$	87.0439	49.21	–	–	1.20	2.66	1.05	3.92
2	Valeric acid[d,e,f]	$C_5H_{10}O_2$	103.0753	132.22	1.90	0.41	1.99	0.41	2.05	0.40
3	Creatinine[d,e,f]	$C_4H_7N_3O$	114.0661	21.28	–	–	–	–	1.48	2.02
4	Epsilon-caprolactam[d,e,f,g]	$C_6H_{11}NO$	114.0914	114.47	1.28	2.30	1.51	2.33	1.34	2.46
5	4-Heptanone[d,e,f]	$C_7H_{14}O$	115.1116	206.71	1.96	0.23	1.99	0.25	2.05	0.23
6	3-Ethylphenol[d,f,g]	$C_8H_{10}O$	123.0803	122.87	1.88	0.36	1.94	0.35	1.95	0.35
7	D-Limonene[d,f]	$C_{10}H_{16}$	137.1324	143.88	1.86	0.30	1.74	0.33	1.87	0.28
8	3,5,5-Trimethyl-2-cyclohexen-1-one[d,f,g]	$C_9H_{14}O$	139.1116	193.16	2.00	0.17	2.11	0.17	2.17	0.17
9	Thymol[d,e,f]	$C_{10}H_{14}O$	151.1116	204.15	1.91	0.39	1.82	0.41	1.84	0.40
10	Perillyl alcohol[d,f]	$C_{10}H_{16}O$	153.1273	210.29	2.03	0.25	2.20	0.26	2.31	0.24
11	Methyl 2-octynoate[d,f,g]	$C_9H_{14}O_2$	155.1065	177.72	1.89	0.31	1.99	0.32	2.23	0.29
12	1-Acetylindole[d,f,g]	$C_{10}H_9NO$	160.0757	131.14	1.78	2.09	1.75	2.19	1.70	2.08
13	Umbelliferone[d,f,g]	$C_9H_6O_3$	163.0389	182.05	1.84	0.49			2.06	0.46
14	1-Phenyl-1-pentanone[d,f,g]	$C_{11}H_{14}O$	163.1116	200.50	1.94	0.33	2.04	0.36	2.04	0.37
15	4,7-Dimethyl-1,3-benzothiazol-2-ylamine[d,f,g]	$C_9H_{10}N_2S$	179.0638	142.04	–	–	1.82	2.02	–	–
16	Benzophenone[d,f,g]	$C_{13}H_{10}O$	183.0809	226.43	1.56	2.00	1.45	2.14	–	–
17	L-Acetylcarnitine[d,e,f]	$C_9H_{17}NO_4$	204.1230	22.91	1.46	2.15	1.48	2.37	1.53	2.81
18	Aureonitol[d,f,g]	$C_{13}H_{18}O_2$	207.1378	173.22	1.97	0.20	2.00	0.22	2.11	0.20
19	4,4,7a-trimethyl-3a,5,6,7-tetrahydro-3*H*-indene-1-carboxylic acid[d,f,g]	$C_{13}H_{20}O_2$	209.1534	197.75	1.89	0.40	1.87	0.42	1.99	0.38
20	7-Epi-Jasmonic acid[d,f,g]	$C_{12}H_{18}O_3$	211.1328	160.86	1.97	0.19	2.03	0.20	1.99	0.21
21	Cys-Pro[d,f,g]	$C_8H_{14}N_2O_3S$	219.0797	91.87	1.03	2.34	–	–	–	–
22	Pro-Leu[d,f,g]	$C_{11}H_{20}N_2O_3$	229.1546	46.53	–	–	–	–	1.14	2.35
23	Alantolactone[d,f,g]	$C_{15}H_{20}O_2$	233.1535	194.63	1.95	0.23	1.99	0.25	1.94	0.27
24	Curcumol[d,f,g]	$C_{15}H_{24}O_2$	237.1848	226.69	1.12	0.23				
25	Isovalerylcarnitine[d,e,f]	$C_{12}H_{23}NO_4$	246.1697	121.55	1.16	2.18	1.11	2.49	1.07	2.45
26	Linoleic acid[d,f]	$C_{18}H_{32}O_2$	281.2473	258.56	1.59	2.35	1.53	2.62	1.49	2.73
27	Elaidic acid[d,f]	$C_{18}H_{34}O_2$	283.2629	278.39	1.87	3.35	2.02	3.86	1.73	2.91
28	PE(P-16:0e/0:0)[d,f,g]	$C_{21}H_{44}NO_6P$	438.2977	267.49	1.59	0.49	1.95	0.39	2.08	0.36
29	Cefazolin[d,f,g]	$C_{14}H_{14}N_8O_4S_3$	455.0371	135.59	–	–	1.02	288.76	1.30	62.93
30	LysoPE(P-18:0/0:0)[d,f,g]	$C_{23}H_{48}NO_6P$	466.3288	294.22	1.72	0.39	1.90	0.34	2.16	0.28
31	LysoPC(14:0/0:0)[d,f,g]	$C_{22}H_{46}NO_7P$	468.3080	236.23	–	–	–	–	1.96	0.33
32	LysoPC(P-18:0)[d,g]	$C_{26}H_{54}NO_6P$	508.3756	294.32	–	–	–	–	1.60	0.48
33	LysoPC(18:2)[d,f,g]	$C_{26}H_{50}NO_7P$	520.3393	246.39	–	–	–	–	1.80	0.44
34	LysoPC(20:3)[d,f,g]	$C_{28}H_{52}NO_7P$	546.3545	259.45	–	–	1.57	0.45	1.76	0.39
35	LysoPC(22:5)[d,f,g]	$C_{30}H_{52}NO_7P$	570.3546	255.47	–	–	–	–	1.48	0.45
36	PC(16:1/16:1)[d,g]	$C_{40}H_{76}NO_8P$	730.5380	312.51	–	–	1.61	0.15	–	–
37	PC(16:0/18:3)[d,g]	$C_{42}H_{78}NO_8P$	756.5535	313.85	–	–	1.19	0.42	–	–

Table 3. Differential metabolites for discrimination between pTa, pT1 and pT2 BC patients and NCs (*p* value < 0.05; FDR < 0.05; VIP > 1; FC < 0.5 and > 2). [a] Experimental monoisotopic mass; [b]VIP scores derived from OPLS-DA model; [c]fold change between cancer and control serum calculated from the abundance mean values for each group—cancer-to-normal ratio; [d]the metabolites identified by high precursor mass accuracy; [e]the metabolites identified by matching retention time; [f]the metabolites identified by matching isotopic pattern; [g]the metabolites identified by matching MS/MS fragment spectra; AUC: area under the curve; FC: fold change; FDR: false discovery rate; *m/z*: mass-to-charge ratio; pT1 and pTa—high risk non-muscle invasive bladder cancer; pT2—muscle invasive bladder cancer; RT: retention time; VIP: variable influence on projection.

down-regulated in patients with ovarian cancer. Four of these compounds including LPC(14:0), LPC(18:3), LPC(20:3), LPC(22:5) were previously related to kidney injury. Metabolic profiling of plasma from patients with cancer cachexia revealed significantly lower levels of LPC(14:0), LPC(P-18:0), LPC(18:2), LPC(20:3), LPC(22:5) and LPE(18:0) compared to healthy controls[44]. Three of these six LPC including LPC(18:1), LPC(18:3), LPC(22:5) we identified previously at lower levels in serum of patients with thyroid carcinoma[45]. To our knowledge, only one lipid out of the ten most differentiating both groups cancer and control we indicated has been previously associated with bladder cancer. Tan et al.[18] indicated slightly higher level of LPC(18:2) in serum of patients with BC compared to controls using UHPLC-Q-ToF MS.

Lower levels of four prenol lipids including perillyl alcohol, D-limonene, thymol, alantolactone were found in serum of BC compared to controls. These monoterpenoids commonly occurring in many plants are known

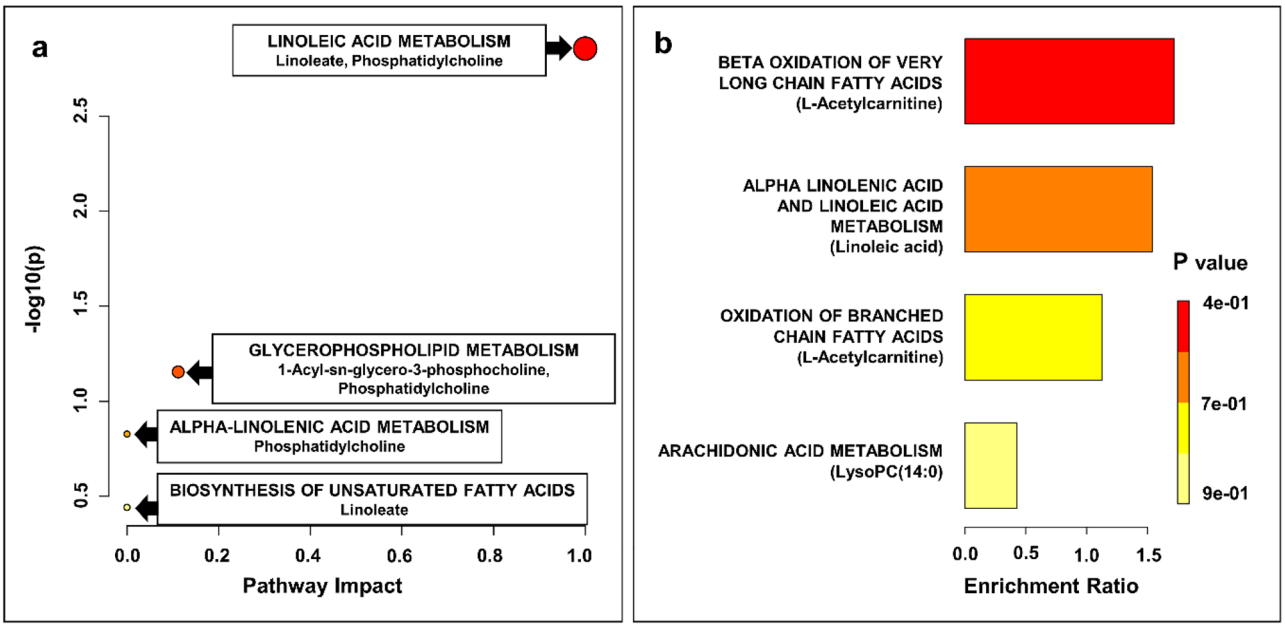

Figure 4. Results of pathway topology analysis of selected statistically significant metabolites in BC. A Pathway analysis based on KEGG (**a**); bubble area donating to the impact of each pathway with color representing the significance from highest in red to lowest in white; (**b**) Quantitative enrichment analysis based on SMPDB.

for their anti-tumor, antioxidant, anti-inflammatory and anti-fungal activity. Thymol and limonene have been shown to inhibit bladder cancer cell proliferation and induces these cells apoptosis[46,47].

We found that serum levels of metabolites: L-acetylcarnitine, linoleic acid and elaidic acid were higher and three others: valeric acid and 7-epi-jasmonic acid lower in BC patients compared to NCs. The levels of linoleic and elaidic acid were also found as significantly higher in patients with colorectal cancer[48]. Increased serum activity of acetylcarnitine have been previously pointed out as a potential tumor biomarkers[49,50]. Acetylcarnitine is a naturally occurring acetic acid ester of carnitine, important in mitochondrial tricarboxylic acid (TCA) cycle activity. Increased urine levels of this compound have previously been reported in patients with BC[51]. Elevation of acetylcarnitine may be an indication of decreased carbon flow into the TCA cycle or excess production of acetyl-CoA[52]. Previous studies revealed elevated urine level of acetylcarnitine and isovalerylcarnitine in BC patients compared to controls[53,54]. However, the association between isovalerylcarnitine and bladder cancer has not yet been explained.

In order to apply the correct treatment regimens for BC patients, in addition to indicating the neoplasm, it is necessary to precisely and accurately indicate the stage and grade of this cancer. In total, 23 differential metabolites were identified as potential marker for discriminating between LG and HG BC patients and NCs. Among these metabolites, 18 metabolites were the common characteristic of both LG and HG BC patients. Three metabolites including lysoPC(20:3), PE(P-16:0e/0:0) and 2(4H)-benzofuranone, 6-Hydroxy-4,4,7a-trimethyl-5,6,7,7a-tetrahydrobenzofuran-2(4*H*)-one were identified in much higher level only in the serum of patients with HG BC, while four metabolites including 3-hexanone, diethylene glycol 2-ethylhexyl ether, elaidic acid, umbelliferone were found in significant higher level only in the serum of patients with LG BC patients.

In total, 38 differential metabolites were identified as potential marker for discriminating between pTa, pT1 and pT2 BC patients and NCs. Among these metabolites, 22 metabolites were the common to all three stages of BC. Two metabolites including Cys-Pro and curcumol were identified in much higher levels only in the serum of patients with pTa BC, while two metabolites including LysoPC(20:3) and alpha-hydroxyisobutyric acid were found in significant higher level only in the serum of patients with pT1 BC patients. Moreover, five metabolites including norcamphor, creatinine, dihydrojasmone, pro-leu, palmitoleoyl ethanolamide were found in significant higher level only in the serum of patients with pT2 BC patients.

We demonstrate that ultra-high-resolution mass spectrometry is a powerful tool for the characterization of the serum metabolome differences in BC. Twenty-seven potentially robust metabolic biomarkers were identified for 100 tumor serum samples from patients with BC patients after comparison against 100 healthy controls owing to the excellent predictive ability of AUC > 0.99. We also identified twenty-three metabolites that might be used as potential biomarkers to distinguish LG and HG and thirty-seven metabolites that may serve to differentiate between the pTa/pT1 and pT2 stages of BC. Our results suggest that differential serum metabolite profiles and can help identify patients with BC compared with NCs, with significant discriminating power between different stages and grades of bladder cancer. Our findings, may potentially provide facile and less invasive diagnostic methodology for detection of different stages and grades of bladder cancer and recurrent disease management. In the future, a new class of biomarkers of BC could contribute to development of non-invasive, highly specific and sensitive diagnostic tests that could be employed to aid the detection of new tumors and also predict recurrences.

Data availability

The data that support the findings of this study is available from the corresponding author upon reasonable request.

Received: 12 June 2022; Accepted: 31 August 2022
Published online: 07 September 2022

References

1. Sung, H. *et al.* Global Cancer Statistics 2020: GLOBOCAN Estimates of Incidence and Mortality Worldwide for 36 Cancers in 185 Countries. *CA. Cancer J. Clin.* **71**, 209–249 (2021).
2. Robins, D. J. *et al.* Mp86-17 the 2017 American joint committee on cancer eighth edition cancer staging manual: changes in staging guidelines for cancers of the kidney, renal pelvis and ureter, bladder, and urethra. *J. Urol.* **197**, e1163 (2017).
3. Troisi, J. *et al.* A serum metabolomic signature for the detection and grading of bladder cancer. *Appl. Sci.* **11**, 2835 (2021).
4. Lee, H. H. & Ham, W. S. Perioperative immunotherapy in muscle-invasive bladder cancer. *Transl. Cancer Res.* **9**, 6546–6553 (2020).
5. Yang, Q. *et al.* Metabolomics biotechnology, applications, and future trends: a systematic review. *RSC Adv.* **9**, 37245–37257 (2019).
6. Raja, G., Jung, Y., Jung, S. H. & Kim, T. J. 1H-NMR-based metabolomics for cancer targeting and metabolic engineering—a review. *Process Biochem.* **99**, 112–122 (2020).
7. Liu, X. *et al.* LC-MS-based plasma metabolomics and lipidomics analyses for differential diagnosis of bladder cancer and renal cell carcinoma. *Front. Oncol.* **10**, 717 (2020).
8. Pan, Z. & Raftery, D. Comparing and combining NMR spectroscopy and mass spectrometry in metabolomics. *Anal. Bioanal. Chem.* **387**, 525–527 (2007).
9. Ng, K., Stenzl, A., Sharma, A. & Vasdev, N. Urinary biomarkers in bladder cancer: A review of the current landscape and future directions. *Urol. Oncol. Semin. Orig. Investig.* **39**, 41–51 (2021).
10. Batista, R. *et al.* Biomarkers for bladder cancer diagnosis and surveillance: A comprehensive review. *Diagnostics* **10**, 39 (2020).
11. Walsh, M. C., Brennan, L., Malthouse, P. G., Roche, H. M. & Gibney, M. J. Effect of acute dietary standardization on the urinary, plasma, and salivary metabolomic profiles of healthy humans 13. *Am. J. Clin. Nutr.* **84**, 531–539 (2006).
12. Gupta, A. *et al.* NMR-derived targeted serum metabolic biomarkers appraisal of bladder cancer: A pre- and post-operative evaluation. *J. Pharm. Biomed. Anal.* **183**, 113134 (2020).
13. Bansal, N. *et al.* Low- and high-grade bladder cancer determination via human serum-based metabolomics approach. *J. Proteome Res.* **12**, 5839–5850 (2013).
14. Cao, M., Zhao, L., Chen, H., Xue, W. & Lin, D. NMR-based metabolomic analysis of human bladder cancer. *Anal. Sci.* **28**, 451–456 (2012).
15. Amara, C. S. *et al.* Serum metabolic profiling identified a distinct metabolic signature in bladder cancer smokers: A key metabolic enzyme associated with patient survival. *Cancer Epidemiol. Biomarkers Prev.* **28**, 770–781 (2019).
16. Vantaku, V. *et al.* Large-scale profiling of serum metabolites in African American and European American patients with bladder cancer reveals metabolic pathways associated with patient survival. *Cancer* **125**, 921–932 (2019).
17. Sahu, D., Lotan, Y., Wittmann, B., Neri, B. & Hansel, D. E. Metabolomics analysis reveals distinct profiles of nonmuscle-invasive and muscle-invasive bladder cancer. *Cancer Med.* **6**, 2106–2120 (2017).
18. Tan, G. *et al.* Three serum metabolite signatures for diagnosing low-grade and high-grade bladder cancer. *Sci. Rep.* **7**, 1–11 (2017).
19. Lin, L. *et al.* LC-MS based serum metabonomic analysis for renal cell carcinoma diagnosis, staging, and biomarker discovery. *J. Proteome Res.* **10**, 1396–1405 (2011).
20. Zhou, Y. *et al.* The development of plasma pseudotargeted GC-MS metabolic profiling and its application in bladder cancer. *Anal. Bioanal. Chem.* **408**, 6741–6749 (2016).
21. Lepara, Z. *et al.* Serum malondialdehyde (MDA) level as a potential biomarker of cancer progression for patients with bladder cancer. *Rom. J. Intern. Med.* **58**, 146–152 (2020).
22. Lin, L. *et al.* LC-MS-based serum metabolic profiling for genitourinary cancer classification and cancer type-specific biomarker discovery. *Proteomics* **12**, 2238–2246 (2012).
23. MassBank of North America. Available at: https://mona.fiehnlab.ucdavis.edu/. Accessed: 8th June 2022
24. Mass Spectrometry Data Center, NIST. *ass Spectral Library* Available at: https://chemdata.nist.gov/. Accessed 1st April 2022.
25. Pang, Z. *et al.* MetaboAnalyst 50: Narrowing the gap between raw spectra and functional insights. *Nucleic Acids Res.* **49**, W388–W396 (2021).
26. Ho, S. Y., Phua, K., Wong, L. & Bin Goh, W. W. Extensions of the external validation for checking learned model interpretability and generalizability. *Patterns* **1**, 100129 (2020).
27. Okuda, S. *et al.* KEGG Atlas mapping for global analysis of metabolic pathways. *Nucleic Acids Res.* **36**, W423–W426 (2008).
28. Han, J., Li, Q., Chen, Y. & Yang, Y. Recent metabolomics analysis in tumor metabolism reprogramming. *Front. Mol. Biosci.* **8**, 763902 (2021).
29. Besiroglu, H. Lipid metabolism profiling and bladder cancer. *Metabolomics Open Access* **5**, 1–4 (2015).
30. Wolrab, D., Jirásko, R., Chocholoušková, M., Peterka, O. & Holčapek, M. Oncolipidomics: Mass spectrometric quantitation of lipids in cancer research. *TrAC Trends Anal. Chem.* **120**, 10 (2019).
31. Lu, Y. *et al.* Comparison of hepatic and serum lipid signatures in hepatocellular carcinoma patients leads to the discovery of diagnostic and prognostic biomarkers. *Oncotarget* **9**, 5032 (2018).
32. Lee, G. B., Lee, J. C. & Moon, H. Plasma lipid profile comparison of five different cancers by nanoflow ultrahigh performance liquid chromatography-tandem mass spectrometry. *Anal Chim Acta* https://doi.org/10.1016/j.aca.2019.02.021 (2019).
33. Wang, X. *et al.* A novel human phosphatidylethanolamine-binding protein resists tumor necrosis factor α-induced apoptosis by inhibiting mitogen-activated protein kinase pathway activation and phosphatidylethanolamine externalization*. *J. Biol. Chem.* **279**, 45855–45864 (2004).
34. Wang, X. *et al.* Silencing of human phosphatidylethanolamine-binding protein 4 sensitizes breast cancer cells to tumor necrosis factor-alpha-induced apoptosis and cell growth arrest. *Clin. Cancer Res.* **11**, 7545–7553 (2005).
35. Yao, Y. *et al.* Exogenous phosphatidylethanolamine induces apoptosis of human hepatoma HepG2 cells via the bcl-2/bax pathway. *World J. Gastroenterol.* **15**, 1751 (2009).
36. Yagi, T. *et al.* Challenges and inconsistencies in using lysophosphatidic acid as a biomarker for ovarian cancer. *Cancers* **11**, 520 (2019).
37. Ravipati, S., Baldwin, D. R., Barr, H. L., Fogarty, A. W. & Barrett, D. A. Plasma lipid biomarker signatures in squamous carcinoma and adenocarcinoma lung cancer patients. *Metabolomics* **11**, 1600–1611 (2015).
38. Taylor, L. A., Arends, J., Hodina, A. K., Unger, C. & Massing, U. Plasma lyso-phosphatidylcholine concentration is decreased in cancer patients with weight loss and activated inflammatory status. *Lipids Health Dis.* **6**, 1–8 (2007).
39. Li, J. *et al.* Distinct plasma lipids profiles of recurrent ovarian cancer by liquid chromatography-mass spectrometry. *Oncotarget* **8**, 46834 (2017).

40. Zhang, F. *et al.* The predictive and prognostic values of serum amino acid levels for clear cell renal cell carcinoma. *Urol. Oncol. Semin. Orig. Investig.* **35**, 392–400 (2017).
41. Tan, B. *et al.* Metabonomics identifies serum metabolite markers of colorectal cancer. *J. Proteome Res.* https://doi.org/10.1021/pr400337b (2013).
42. Shen, S. *et al.* A plasma lipidomics strategy reveals perturbed lipid metabolic pathways and potential lipid biomarkers of human colorectal cancer. *J. Chromatogr. B* **1068–1069**, 41–48 (2017).
43. Zhao, Z. *et al.* Plasma lysophosphatidylcholine levels: potential biomarkers for colorectal cancer. *J Clin Oncol* **25**, 2696–2701 (2007).
44. Cala, M. P. *et al.* Multiplatform plasma fingerprinting in cancer cachexia: a pilot observational and translational study. *J. Cachexia. Sarcopenia Muscle* **9**, 348–357 (2018).
45. Yao, Z. *et al.* Serum metabolic profiling and features of papillary thyroid carcinoma and nodular goiter. *Mol. Biosyst.* **7**, 2608–2614 (2011).
46. Li, Y. *et al.* Thymol inhibits bladder cancer cell proliferation via inducing cell cycle arrest and apoptosis. *Biochem. Biophys. Res. Commun.* **491**, 530–536 (2017).
47. Ye, Z., Liang, Z., Mi, Q. & Guo, Y. Limonene terpenoid obstructs human bladder cancer cell (T24 cell line) growth by inducing cellular apoptosis, caspase activation, G2/M phase cell cycle arrest and stops cancer metastasis. *JBUON* **25**, 280–285 (2020).
48. Wang, X., Wang, J., Rao, B. & Deng, L. I. Gut flora profiling and fecal metabolite composition of colorectal cancer patients and healthy individuals. *Exp. Ther. Med.* **13**, 2848–2854 (2017).
49. Nizioł, J. *et al.* Metabolomic study of human tissue and urine in clear cell renal carcinoma by LC-HRMS and PLS-DA. *Anal. Bioanal. Chem.* **410**, 3859–3869 (2018).
50. Ganti, S. *et al.* Urinary acylcarnitines are altered in human kidney cancer. *Int. J. Cancer* **130**, 2791–2800 (2012).
51. Wittmann, B. M. *et al.* Bladder cancer biomarker discovery using global metabolomic profiling of urine. *PLoS ONE* **9**, e115870 (2014).
52. Schroeder, M. A. *et al.* The cycling of acetyl-coenzyme A through acetylcarnitine buffers cardiac substrate supply: A hyperpolarized 13C magnetic resonance study. *Circ. Cardiovasc. Imaging* **5**, 201–209 (2012).
53. Jin, X. *et al.* Diagnosis of bladder cancer and prediction of survival by urinary metabolomics. *Oncotarget* **5**, 1635–1645 (2014).
54. Rodrigues, D. *et al.* Biomarkers in bladder cancer: A metabolomic approach using in vitro and ex vivo model systems. *Int. J. Cancer* **139**, 256–268 (2016).

Acknowledgements

Research was supported mainly by National Science Centre (Poland), research project SONATA Number UMO-2018/31/D/ST4/00109.

Author contributions

J.N.: Conceptualization, Methodology, Formal analysis, Investigation, Resources, Data Curation, Writing—Original draft, Writing—Review & Editing, Visualization, Supervision, Project administration, Funding acquisition, K.O: Investigation, Resources; Writing—Original draft; A.P.: Investigation; Data Curation; A.K.: Investigation, Data Curation; A.O.: Resources; T.O.: Resources; T.R.: Methodology, Resources, Data Curation, Writing—Review & Editing, Supervision.

Competing interests

The authors declare no competing interests.

Additional information

Supplementary Information The online version contains supplementary material available at https://doi.org/10.1038/s41598-022-19576-9.

Correspondence and requests for materials should be addressed to J.N.

Reprints and permissions information is available at www.nature.com/reprints.

Publisher's note Springer Nature remains neutral with regard to jurisdictional claims in published maps and institutional affiliations.

Journal of Pharmaceutical Analysis 12 (2022) 889–900

Contents lists available at ScienceDirect

Journal of Pharmaceutical Analysis

journal homepage: www.elsevier.com/locate/jpa

Original article

Metabolomic and elemental profiling of blood serum in bladder cancer

Krzysztof Ossoliński [a], Tomasz Ruman [b], Valérie Copié [c], Brian P. Tripet [c], Leonardo B. Nogueira [d], Katiane O.P.C. Nogueira [e], Artur Kołodziej [f], Aneta Płaza-Altamer [f], Anna Ossolińska [a], Tadeusz Ossoliński [a], Joanna Nizioł [b, *]

[a] Department of Urology, John Paul II Hospital, 36-100, Kolbuszowa, Poland
[b] Rzeszów University of Technology, Faculty of Chemistry, 35-959, Rzeszów, Poland
[c] The Department of Chemistry and Biochemistry, Montana State University, Bozeman, MT, 59717, USA
[d] Department of Geology, Federal University of Ouro Preto, 35400-000, Ouro Preto, Brazil
[e] Department of Biological Sciences, Federal University of Ouro Preto, 35400-000, Ouro Preto, Brazil
[f] Doctoral School of Engineering and Technical Sciences at the Rzeszów University of Technology, 35-959, Rzeszów, Poland

ARTICLE INFO

Article history:
Received 22 March 2022
Received in revised form
19 August 2022
Accepted 27 August 2022
Available online 2 September 2022

Keywords:
Bladder cancer
Biomarkers
Human serum
Metallomics
Metabolomics

ABSTRACT

Bladder cancer (BC) is one of the most frequently diagnosed types of urinary cancer. Despite advances in treatment methods, no specific biomarkers are currently in use. Targeted and untargeted profiling of metabolites and elements of human blood serum from 100 BC patients and the same number of normal controls (NCs), with external validation, was attempted using three analytical methods, i.e., nuclear magnetic resonance, gold and silver-109 nanoparticle-based laser desorption/ionization mass spectrometry (LDI-MS), and inductively coupled plasma optical emission spectrometry (ICP-OES). All results were subjected to multivariate statistical analysis. Four potential serum biomarkers of BC, namely, isobutyrate, pyroglutamate, choline, and acetate, were quantified with proton nuclear magnetic resonance, which had excellent predictive ability as judged by the area under the curve (AUC) value of 0.999. Two elements, Li and Fe, were also found to distinguish between cancer and control samples, as judged from ICP-OES data and AUC of 0.807 (in validation set). Twenty-five putatively identified compounds, mostly related to glycans and lipids, differentiated BC from NCs, as detected using LDI-MS. Five serum metabolites were found to discriminate between tumor grades and nine metabolites between tumor stages. The results from three different analytical platforms demonstrate that the identified distinct serum metabolites and metal elements have potential to be used for noninvasive detection, staging, and grading of BC.

1. Introduction

Bladder cancer (BC) is the tenth most commonly diagnosed cancer in the world with approximately 570,000 new cases diagnosed each year. The incidence rate per 100,000 person per year varies from 2.4 for women to 9.5 for men, and the mortality rate varies from 0.86 for women to 3.3 for men [1]. Globally, urothelial carcinoma (UC) identified histopathologically constitutes more than 90% of all the cases of BC. In endemic regions such as Egypt with a high prevalence of schistosomiasis infection, squamous cell carcinoma (SCC) accounts for the majority of BC. However, control over the *Schistosoma haematobium* infection has led to a shift from SCC to UC being the most prevalent type of BC [2]. The remaining 10% includes exposure to aromatic amines, hydrocarbons, dyes, some solvents, and coal tar [3]. The most common symptoms of BC include macroscopic and microscopic hematuria. The mainstay for BC diagnosis includes cystoscopy and urine cytology, and may include ultrasound and computed tomography urography. Unfortunately, cystoscopy is considered as an invasive procedure and the sensitivity of urine cytology is low. Therefore, to reduce the number of procedures, urinary markers have been proposed to track BC recurrence [4,5]. These urinary markers are associated with higher sensitivity, although at the expense of lower specificity, compared

Peer review under responsibility of Xi'an Jiaotong University.
* Corresponding author.
E-mail address: jniziol@prz.edu.pl (J. Nizioł).

https://doi.org/10.1016/j.jpha.2022.08.004

with the accuracy of urine cytology. However, these markers have not been incorporated into clinical guidelines regarding the diagnosis and surveillance of BC. Therefore, there is a significant need for noninvasive methods for the early detection of BC with high sensitivity, specificity, and low cost.

Instrumental analyses of small molecules in biofluids, such as blood, serum, and urine, are very powerful approaches to identify and characterize diagnostic metabolic biomarkers. Metabolite concentrations are reflective of the state of the organism and may be the indicators of disease states including cancer states [6]. In the past decade, numerous sensitive analytical methods have been developed to allow the study of the metabolic state of living system. The most frequently used analytical platforms for study of metabolites are nuclear magnetic resonance (NMR) [7] and mass spectrometry (MS), the latter usually coupled with liquid chromatography (LC) or gas chromatography (GC) [8–10].

Metabolomic methods have been used for study of BC with the aim of identifying potential biomarkers in urine, serum, and tissues [11,12]. The advantage of serum analysis is that it is much less susceptible to the dilution factor compared to urine [13]. Although from an application point of view, serum analysis is the best option, the published data are very limited. A majority of reports of BC serum metabolomics describe MS results. The first such study [14] was focused on human serum profiling of BC with LC-MS, and the authors proposed five potential biomarkers. Later, Zhou et al. [15] applied GC-MS to perform plasma metabolomics analyses of 92 patients and 48 controls. The results identified increased levels of metabolites associated with the pentose phosphate pathway, fatty acid synthesis, and nucleotide metabolism in BC samples compared with the controls. The authors focused on three metabolites that could discriminate between the BC and control groups. In the following years, several publications appeared that focused on identifying potential biomarkers of BC using LC-MS [16–20] and GC-MS [21,22]. To date, only three reports have reported metabolic differences in serum within BC with NMR. The first NMR serum metabolomics study of BC was published by Cao et al. [23] in 2012, and involved 67 BC patients and 25 healthy controls, and revealed a few metabolites for which concentrations differed significantly between these two groups. The metabolite changes were linked to impacted pathways of lipogenesis, aromatic amino acid metabolism, glycolysis, and the citrate cycle. In 2013, Bansal et al. [24] applied proton nuclear magnetic resonance (^{1}H NMR) spectroscopy to compare 36 low-grade (LG) and 31 high-grade (HG) BC samples with those of 32 healthy control patients. The study identified six metabolites that could, together, serve as differentiating biomarkers of LG versus HG BC. This same research team recently reported the use of NMR to identify variations in the concentration of previously selected potential serum BC biomarkers in 55 preoperative and 53 post-operative BC patients, and 152 controls [25].

Various studies have established the connection between levels of metals, including trace-level metals and other trace elements, with an increased risk of developing cancer in humans [26]. Toxic elements are known risk factors for genetic and epigenetic effects, which enhance the risk of developing different cancers [27]. Inductively coupled plasma optical emission spectrometry (ICP-OES) has emerged as one of the most frequently used methods for assessing the concentrations of metals in samples of biological origin [28] including BC serum [29]. Studies recruited 27 BC patients, 29 non-tumor patients with acute and chronic inflammation, and 30 healthy control patients, who were divided into validation and discovery cohorts. ICP-OES methods have also been used in the search for biomarkers of other cancers, including kidney cancer [30,31].

Herein, we report the results of the largest investigation to date, comprising the targeted and non-targeted, elemental- and metabolomics-based profiling of 200 serum samples obtained from 100 patients with BC and 100 healthy controls. This study has enabled the elucidation of the detailed metabolic and elemental changes resulting from BC, with a specific focus on the stage and grade of BC. The analytical platforms used were high-resolution ^{1}H NMR, ICP-OES, and high-resolution laser desorption/ionization MS (LDI-MS), and the associated data were subjected to robust validation by multivariate and univariate statistical analyses.

2. Materials and methods

2.1. Materials and instruments

High-resolution LDI-MSI experiments were performed on Autoflex Speed time-of-flight mass spectrometer (Bruker, Bremen, Germany) with a declared resolution of >20,000 for *m/z* values of >1,000 in positive-ion reflectron mode. The samples were placed on a stainless-steel target with automatic pipette and then covered by nebulization with a silver-109 nanoparticle (^{109}AgNP) suspension generated by pulsed fiber laser (PFL) two-dimensional (2D) galvoscanner (GS) laser synthesis in solution/suspension (LASiS) and nebulization of ^{109}AgNPs (^{109}AgNPs LDI-MS) as described in our recent publication [32]. Gold nanoparticle (AuNP)-based LDI-MS (AuNPs LDI-MS) was prepared analogically as described above with the exception for PFL-2D GS LASiS material/substrate, which was gold foil of 1 mm thickness. All solvents were of minimum LC-MS grade and were acquired from Sigma Aldrich (St. Louis, MO, USA). Deuterium oxide (D_2O) and 4,4-dimethyl-4-silapentane-1-sulfonic acid were purchased from Sigma Inc. (Boston, MA, USA). Nitric acid EMSURE ISO-grade 65% and hydrogen peroxide EMSURE ACS ISO-grade 30% were purchased from Merck KGaA (Darmstadt, Germany).

2.2. Collection of human serum samples

Serum samples were collected at John Paul II Hospital (Kolbuszowa, Poland). Control serum samples were collected from healthy volunteers after a medical examination focused on the detection of urinary cancers. Both types of serum samples from the original NMR, MS, and ICP-OES datasets were randomly divided every time into two groups, a training set, comprising 80% of all samples, and a validation set, corresponding to 20% of all samples. All the patients underwent transurethral resection of bladder tumor following detailed clinical questioning and laboratory testing. The local bioethics committee approved the study (Permission No.: 2018/04/10). Just over half of the patients ($n = 54$) had LG BC and papillary urothelial neoplasm of low malignant potential (PUNLMP) ($n = 3$), whereas the remaining patient group exhibited HG disease ($n = 41$). In two cases, both HG and LG neoplasms were detected. Most of these patients ($n = 69$) displayed noninvasive papillary carcinomas (pathologic stage Ta, pTa) stage disease, 19 had submucosal invasive tumors (pathologic stage T1 (pT1)) stage, and 12 patients had muscle invasive BC (pathologic stage T2 (pT2)). The average age of patients diagnosed with BC and in the NC group was 74 ± 10 and 64 ± 12 years, respectively. The clinical characteristics of the patients are presented in Table S1. A 2.6 mL of blood sample was drawn from each participant and centrifuged (3,000 *g*, 10 min, room temperature), then separated and kept at −60 °C.

2.3. Preparation of serum metabolite extracts for ^{1}H NMR metabolomics

Medium-to-high polarity metabolites were extracted from serum samples as stated in our recent publication [33] and detailed in Section S1 in the Supplementary data.

2.4. Preparation of serum samples for LDI-MS studies

Serum samples were thawed at room temperature and diluted 500 times with methanol. Then, 0.3 μL of serum sample was placed directly on target plates (^{109}Ag and Au PFL-2D GS LASiS [32]). After the solvent was evaporated in air, the plates with the samples were measured with Autoflex Speed apparatus.

2.5. Data processing and spectral acquisition

NMR and MS spectral acquisition and processing are shown in the Supplementary data (Sections S2–S4).

2.6. ICP-OES analysis

Determination of the concentrations of Ca, Fe, K, Na, Mg, as well as minor elements (Mn, P, and S) and trace elements (Cu and Zn) in serum, was performed for 116 samples (65 BC and 51 NC) as stated in our recent publication [31] and detailed in Section S5 in the Supplementary data and Table S2.

2.7. Multivariate statistical analysis

All metabolite datasets were analyzed using the MetaboAnalyst 5.0 [34]. The statistical analysis approach presented in this publication is similar to one we previously presented [31] and another unrelated study [35]; details are presented in the Supplementary data (Section S6).

3. Results

In this work, we studied the metabolic profiles of BC in an effort to propose serum-specific metabolic and/or elemental markers for the specific detection of BC. Two hundred (100 BC and 100 normal control (NC)) ^{1}H NMR spectra were recorded of metabolite extracts from patients and healthy control serum samples. Four hundred LDI mass spectra were recorded with the use of ^{109}Ag and Au PFL-2D GS LASiS targets. Additionally, 116 ICP-OES spectra of samples from 65 patients with BC and 51 NCs were studied.

3.1. Differences between BC and control serum by ^{1}H NMR

Two hundred extracts from sera (100 cancer and 100 control) were analyzed with ^{1}H NMR spectroscopy. Overall, 39 compounds were identified in each serum sample following standard protocols [36,37]. An overlay of control and cancer NMR spectra, presented as blue and red traces, respectively, in Figs. 1B and C, shows a relatively high degree of similarity in the raw NMR data. These spectral regions depict NMR signals observed from 3-hydroxybutyrate and acetate metabolites, respectively. The intensity-normalized spectral overlays shown in Figs. 1B and C clearly indicate that 3-hydroxybutyrate levels (Fig. 1B) are higher and acetate levels (Fig. 1C) are lower in the serum profiles of patients with BC (red) compared with healthy controls (blue). Detailed analysis of the spectra indicated significant differences in metabolite levels between serum samples from patients with BC and healthy controls.

Metabolite concentration datasets obtained by NMR metabolomics were randomly divided into two subsets: a training dataset to train the model (n = 80 BC and n = 80 NCs), and a validation dataset to assess the validity and robustness of the trained model (n = 20 BC and n = 20 NCs). Metabolite concentrations from both datasets were subjected to statistical analyses to assess differences in metabolite levels. The results of these analyses are summarized in Tables S3 and S4. The 2D principal components analysis (PCA) score plots of both subsets indicated good separation between the cancer and the controls (Fig. 2A). In the validation set, separation between cancer and control serum samples was also observed along principal components 1 and 2 (Fig. 2B). The three-dimensional (3D) PCA plots for training and validation sets are provided in Figs. S1A and B.

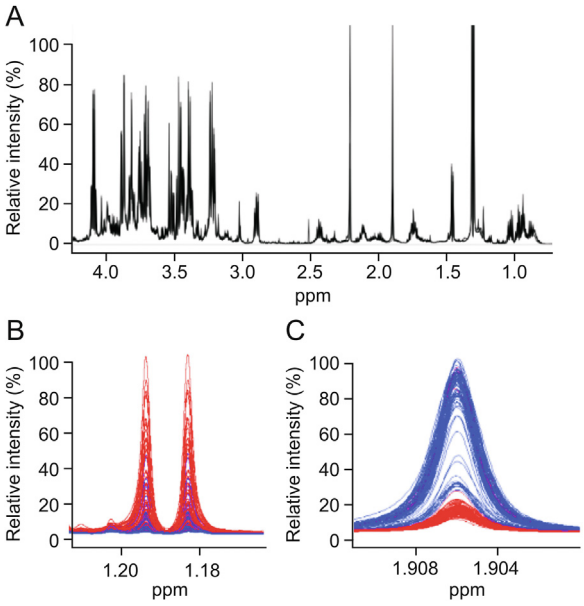

Fig. 1. (A) Characteristic proton nuclear magnetic resonance (^{1}H NMR) spectrum fragment (0.5–4.2 ppm) of a protein-free metabolite extract mixture obtained from serum sample from a patient with BC, recorded on a 600 MHz (14 T) solution NMR spectrometer. Expanded NMR spectral regions, corresponding to ^{1}H chemical shift ranges of (B) 1.16–1.21 ppm for 3-hydroxybutyrate and (C) 1.900–1.911 ppm for acetate, with a spectral overlay of 80 serum metabolic profiles obtained from healthy control patients depicted in blue (blue spectral traces) and BC patients in red (red spectral traces).

A supervised multivariate analysis of the training set with the aid of orthogonal partial least-squares discriminant analysis (OPLS-DA) indicated the strong separation of the BC and NC groups (Fig. 2C). Two thousand permutation tests were conducted to evaluate the statistical robustness of the OPLS-DA model (Figs. S2A and B). Good discrimination was observed between the two groups (Q^2 = 0.880, R^2Y = 0.914, P < 0.0005 (0/2000)), revealing significant differences in the metabolic profiles of cancer versus control serum samples. Group separations were observed with OPLS-DA in the validation set (Fig. 2D) and were confirmed by the good results of the permutation test (Q^2 = 0.780, R^2Y = 0.932, P < 0.0005 (0/2000)) (Figs. S2C and D). Potential serum BC biomarkers were selected on the basis of the S-plot resulting from the OPLS-DA model. Variables with $|P(\text{corr})| > 0.5$ were considered significant. Four variables (acetate, propionate, pyroglutamate, and choline) were positively correlated with the group separation, as determined by a $P(\text{corr})[1]$ score of >0.5, while one metabolite (isobutyrate) negatively correlated with the group separation, as assessed by $-P(\text{corr})[1] < -0.5$ (Fig. S1C). The S-plot of the OPLS-DA model in the validation set confirmed almost all of the selected metabolites (except for propionate) as the most significant for the differentiation of the BC and NC groups (Fig. S1D). Finally, four metabolites were identified as significant discriminators: acetate, pyroglutamate, and choline, which all exhibited higher concentrations in the sera of NCs, and isobutyrate, which was significantly elevated in the sera of BC patients. The P-value of each variable was calculated using independent t-tests and only variables with P-values and false discovery rate < 0.05 were considered significant. Metabolite concentration information for a set of 39 significant metabolites is presented in

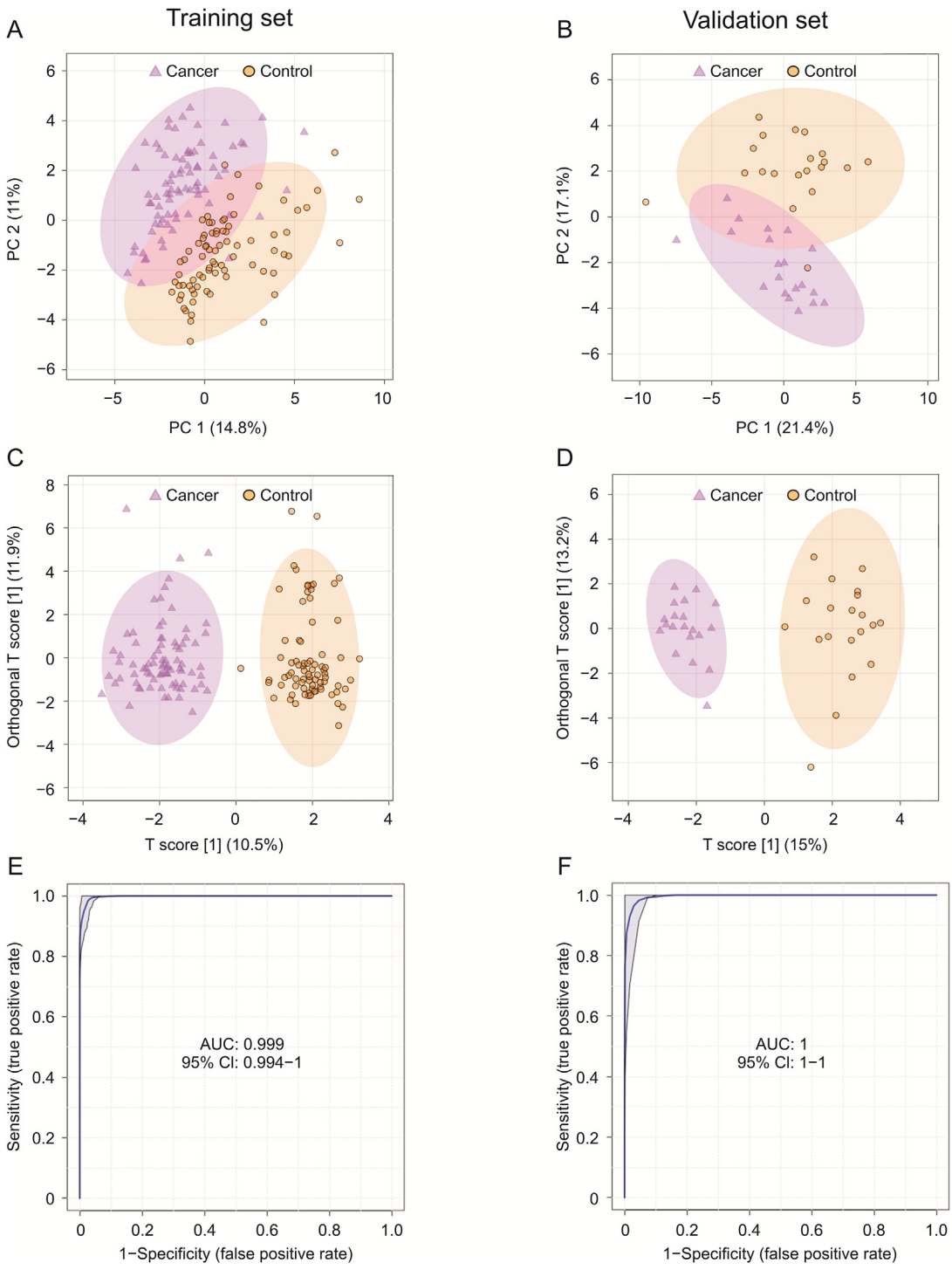

Fig. 2. Two-dimensional principal component analysis (PCA) and orthogonal partial least-squares discriminant analysis (OPLS-DA) score plots of the tumor (violet) and control (orange) serum samples in the (A and C) training set and (B and D) validation set for ^{1}H NMR data. The receiving operator characteristic (ROC) curves of the combination of four differential metabolites, namely, isobutyrate, pyroglutamate, choline, and acetate, in the (E) training set and (F) validation set. AUC: area under the ROC curve; CI: confidence interval; PC: principal component.

Tables S3 and S4. Next, univariate receiver operating characteristic (ROC) curve analysis was separately performed on both the training and validation sets to evaluate the diagnostic ability of the models. The quality of the ranking represents the area under the curve (AUC) above 0.7. The results indicated that in the serum samples, all four previously selected metabolites (acetate, choline, pyroglutamate, and isobutyrate) exhibited very high AUC (above 0.82). The best ROC analyses with the highest significance were obtained for isobutyrate (AUC = 0.953, specificity = 0.9, and sensitivity = 0.9), followed by pyroglutamate (AUC = 0.894, specificity = 0.8, and sensitivity = 0.9), propionate (AUC = 0.859, specificity = 1.0, and sensitivity = 0.7), choline (AUC = 0.828, specificity = 0.8, and sensitivity = 0.8), and

acetate (AUC = 0.824, specificity = 0.8, and sensitivity = 1.0). The range of concentrations compared to all these metabolites in the serum samples of cancer patients compared to NCs is reported in Fig. S3. The most significant results from our statistical analyses of compounds identified as potential biomarkers of BC are presented in Table 1.

The classification ROC model was built with the use of MetaboAnalyst 5.0 online service and was based on a random forest algorithm. As shown in Figs. 2E and F, the combination of levels of these metabolites was a better discriminator (AUC > 0.999) than each metabolite separately in both data sets. An excellent discriminating classification was found for four metabolites, i.e., acetate, propionate, choline, and isobutyrate, with an AUC of 0.999. For this model, the confidence interval ranged from 0.994 to 1.000 (Fig. 2E). The validation of the ROC model is shown in Fig. S4 and a permutation test with 1000 permutations yielded a *P*-value < 0.001, supporting the validity of the ROC analysis. The average of the predicted class probabilities of each sample and the average accuracy of the ROC curve demonstrated good classification discriminatory power, with most of the samples classified accurately in their respective groups. The results suggested that four specific metabolites, namely, acetate, propionate, choline, and isobutyrate, could significantly increase diagnostic potential and serve as useful discriminators of cancerous versus healthy phenotypes in patients diagnosed with BC.

3.2. Differences between grades of BC with ^{1}H NMR

To determine whether metabolomics analysis of serum samples by ^{1}H NMR could help discriminate between different grades of BCs, PCA and OPLS-DA analyses were performed on the entire metabolite dataset. The analysis of BC included 95 serum samples from patients with a uniquely defined grade of cancer; three samples from patients with PUNLMP and two samples from patients with tumor only partially classified as HG were excluded. Finally, 41 serum extracts from patients with HG cancer and 54 samples from patients with LG cancer were used for analysis. The 2D and 3D PCA score plots, which revealed relatively low discrimination between LG and HG cases with a few outliers, are shown in Figs. S5A and B. Likewise, the OPLS-DA score plots highlighted little separation between the HG and LG cancer groups (Fig. S5C), yet yielded an acceptable *P*-value ($P = 0.002$). The statistical significance of the model was examined using Q^2 (0.192) and permutation tests ($n = 2000$), which yielded a *P*-value lower than 0.05. Detailed assessments of the quality of the OPLS-DA model are shown in Fig. S6. The S-plot analysis of the OPLS-DA model indicated that 15 metabolites were significant contributors to the small separation observed between LG vs. HG samples in the 2D and 3D OPLS-DA score plot (Fig. S7). Of these 15 metabolites, leucine, histidine, alanine, 3-methyl-2-oxovalerate, tyrosine, phenylalanine, choline, tryptophan, hypoxanthine, asparagine, valine, proline, threonine, 2-hydroxybutyrate, and glutamine were found to be positively correlated with group separation with a *P*(corr)[1] score > 0.5. These biomarker candidates were subjected to a *t*-test to assess the significance of altered levels in LG versus HG. All 15 metabolites were found to exhibit statistically significant differences in concentration ($P < 0.05$; $q < 0.05$ and $|P(corr)| > 0.5$), suggesting that examining the different levels of these metabolites in human sera may be an effective way to identify LG and discriminate LG from HG in patients with BC. AUC values for five of the 15 metabolites were found to be greater than 0.74 (Fig. S8). Additionally, ROC curve analysis of these five metabolites (i.e., leucine, histidine, alanine, 3-methyl-2-oxovalerate, and tyrosine) only yielded a satisfactory AUC value of 0.775 (Fig. S9A), and a valid permutation test with a *P*-value < 0.001. The average accuracy based on 100 cross validations amounted to a value of 0.693 (Fig. S9D). These analyses support that leucine, histidine, alanine, 3-methyl-2-oxovalerate, and tyrosine may be good indicators discriminating bladder tumor grades.

3.3. Differences between stages of BC identified by ^{1}H NMR

Analysis of tumor stages was also performed for the entire ^{1}H NMR dataset of serum metabolite extracts. Metabolite profiling analysis included 88 serum samples from patients with non-muscle

Table 1
Summary of targeted quantitative analysis of potential biomarkers of BC from proton nuclear magnetic resonance (^{1}H NMR) and inductively coupled plasma optical emission spectrometry (ICP-OES) spectral analyses of serum samples (*P*-value < 0.05; |*P*(corr)[1]| > 0.5; area under the curve (AUC) > 0.75).

Comparison mode	Data set	Metabolite/element	AUC	VIP [t]	*P*(corr)[1]	*P*-value [a]	Fold change [b]
Cancer vs. control	^{1}H NMR	Isobutyrate	0.95	2.2	−0.718	4.3×10^{-23}	1.9
		Pyroglutamate	0.89	1.9	0.626	7.8×10^{-18}	0.5
		Propionate	0.86	2.0	0.638	4.2×10^{-15}	0.8
		Choline	0.83	1.7	0.536	7.6×10^{-13}	0.7
		Acetate	0.82	2.3	0.729	1.6×10^{-12}	0.4
	ICP-OES	Li	0.71	1.4	0.512	5.8×10^{-4}	0.1
		Fe	0.85	2.0	−0.740	1.1×10^{-8}	1.9
Low-grade vs. high-grade	^{1}H NMR	Leucine	0.80	1.5	0.711	1.3×10^{-6}	0.8
		Histidine	0.79	1.7	0.830	2.2×10^{-6}	0.7
		Alanine	0.77	1.5	0.718	1.4×10^{-5}	0.8
		3-methyl-2-oxovalerate	0.77	1.4	0.690	2.2×10^{-5}	0.6
		Tyrosine	0.75	1.2	0.568	6.3×10^{-5}	0.8
pTa/pT1 vs. pT2	^{1}H NMR	Histidine	0.80	1.9	−0.832	0.0001	1.9
		Alanine	0.79	1.7	−0.732	0.0002	1.6
		Tryptophan	0.77	1.7	−0.718	0.0002	1.6
		Glutamine	0.77	1.5	−0.645	0.0017	1.4
		Glycine	0.75	1.4	−0.593	0.0069	1.4
		Methylhistidine	0.88	1.3	−0.580	0.0094	2.1
		Choline	0.88	1.3	−0.566	0.0015	1.5
		Isobutyrate	0.82	1.2	−0.537	0.0021	1.4
		Threonine	0.78	1.2	−0.531	0.0009	1.3

[a] *P*-value determined from Student's *t*-test.
[b] Fold change between cancer and control serum calculated from the concentration mean values for each group; pTa: noninvasive papillary carcinomas; pT1: submucosal invasive tumors; pT2: muscle invasive bladder cancer; VIP: variable influence on projection.

invasive BC (pTa/pT1) and 12 serum samples from patients with muscle invasive BC (pT2). Preliminary PCA analysis was performed using the entire dataset of metabolite concentrations. PCA and OPLS-DA score plots indicated relatively low separation between the pTa/pT1 and pT2 stage of BC, with a few outliers that were removed prior to the further OPLS-DA analysis. Figs. S5D–F contain the 2D, 3D-PCA, and OPLS-DA scores plots of the two groups that were classified by BC grades. The quality factors for the OPLS-DA model included Q^2 of 0.141 and R^2Y of 0.347 and permutation test *P*-value lower than 0.05 (Figs. S6C and D). The S-plot analysis of the OPLS-DA model revealed the 12 serum metabolites that appeared to be most relevant for sample differentiation between pTa/pT1 and pT2 cancer grade: histidine, alanine, tryptophan, glutamine, glycine, methylhistidine, choline, isobutyrate, threonine, phenylalanine, leucine, and 3-methyl-2-oxovalerate (Fig. S7C). All those compounds corresponded to $|P(\mathrm{corr})| > 0.05$ and variable influence on projection (VIP) > 1.2 and were found to be at a higher concentration in the sera of patients with noninvasive pTa/pT1 BC stage (Fig. S7D). However, the ROC analysis narrowed this group down to nine metabolites with an AUC greater than 0.75: histidine, alanine, tryptophan, glutamine, glycine, methylhistidine, choline, isobutyrate, and threonine. The ROC curve analysis of nine potential biomarkers is shown in Fig. S10. For those nine selected metabolites, a ROC curve analysis was performed to assess the performance of this model in distinguishing between pTa/pT1 and pT2 BC stages, and yielded an AUC value of 0.844, which indicated the good discriminatory ability of the model (Fig. S9E). The permutation test based on the measured area under the ROC curve (AUC) for that model yielded a *P*-value < 0.01 (Fig. S9F). The average of the predicted class probabilities of each sample across 100 cross validations and the associated permutation tests are shown in Figs. S9G and H. Analysis of the changes in metabolite concentration for a given stage of BC, i.e., pTa/pT1 versus pT2, reveals higher levels of histidine, alanine, tryptophan, glutamine, glycine, methylhistidine, choline, isobutyrate, and threonine in the serum samples of BC patients with a pTa/pT1 stage of tumor compared to the sera of BC patients with a pT2 stage tumor. The comparison of the three groups of cancer stage (pT1 vs. pTa vs. pT2) did not reveal any statistically significant differences.

3.4. Elemental profile of serum in BC determined by ICP-OES

The concentrations of chemical elements obtained from ICP-OES analysis of 116 extracts of serum samples (65 BC and 51 NCs) were subjected to statistical data analysis. A total of 12 elements were identified and quantified. The mean concentration of each of these elements is summarized in Tables S5 and S6. Prior to statistical analysis, the data were randomly divided into two subsets: a training set (control, $n = 42$ and cancer, $n = 52$) and a validation set (control, $n = 10$ and cancer, $n = 13$). As shown in Fig. 3A, the PCA score plot revealed a trend for separation between the two groups in the training set. Results from the OPLS-DA analysis, shown in Fig. 3B, provided a slightly clearer separation (compared to the PCA analysis) between cancer and controls, and the validation parameters for the model were R^2X and Q^2 values of 0.334 and 0.476, respectively (Fig. S11). The analysis of the VIP scores of the OPLS-DA model in the training set is presented at Fig. 3C.

Three elements (Cu, Fe, and Li) could be used to distinguish between the two groups of study participants; however, only two of them (Cu and Fe) were confirmed to be the most significant

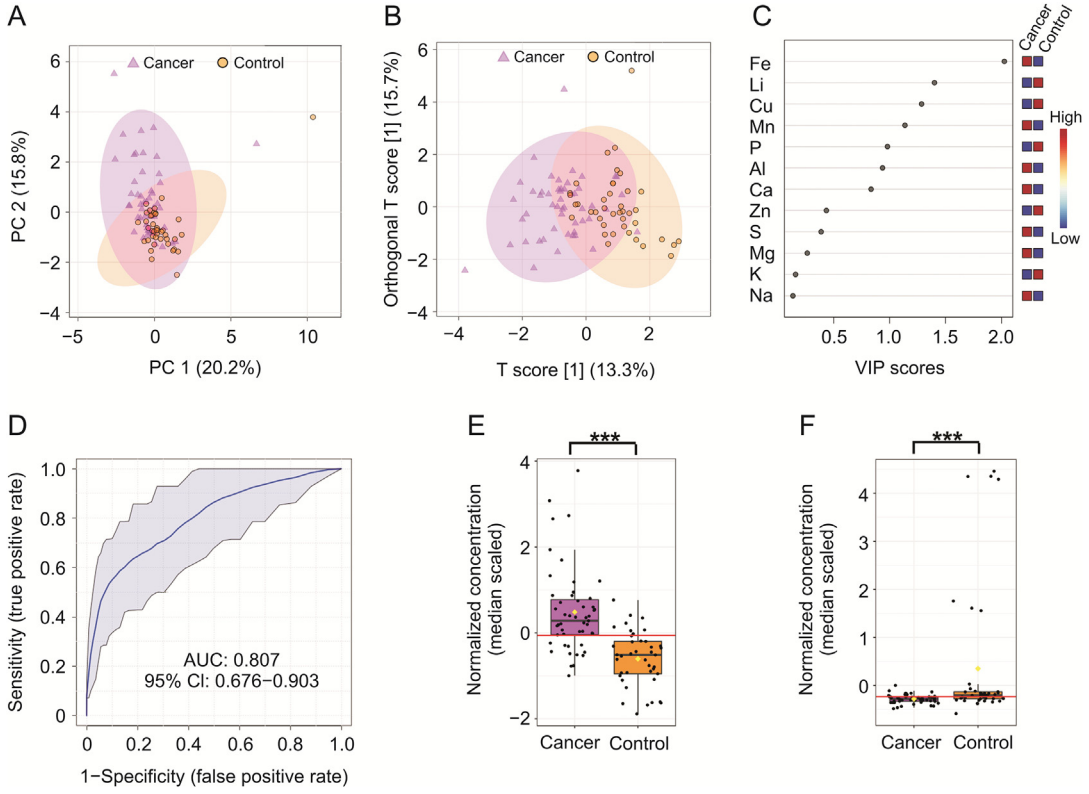

Fig. 3. Statistical analysis of serum metabolite profiles created from inductively coupled plasma optical emission spectrometry (ICP-OES) data. Two-dimensional (A) principal component analysis and (B) orthogonal partial least-squares discriminant analysis (OPLS-DA) score plots of the tumor (violet) and control (orange) serum samples for ICP-OES data in the training set. (C) The potential discriminatory elements identified from the variable importance in projection (VIP) scores derived from the OPLS-DA model in the training set. (D) The receiving operator characteristic (ROC) curves of the combination of two differential elements, Fe and Li. (E and F) The box-and-whisker plots of Fe and Li level values observed in the control and BC serum samples. *** $P < 0.001$. PC: principal component; AUC: area under the curve; CI: confidence interval.

discriminators following model validation assessments (Fig. S12). The loading S-plot of OPLS-DA of the training set revealed that Fe was negatively correlated with group separation, with $-P(\mathrm{corr})[1] < -0.5$, and indicated that a significantly higher level of this element was found in the serum of patients diagnosed with BC compared with the control group. Subsequently, Li was found to be positively correlated with the group separation, with $P(\mathrm{corr})[1] > 0.5$, indicating that it was found in higher levels in the serum samples of NCs. ROC analysis revealed that Fe was the most significant, with an associated AUC value of 0.850, sensitivity of 0.8, and specificity of 0.8, whereas for Li, the AUC value was 0.710, sensitivity was 0.8, and specificity was 0.6. In addition, ROC curve analysis assessing the performance of the ICP-OES model in distinguishing between cancer and control samples was performed using only two selected elements (Fe and Li). This analysis yielded an AUC value of 0.807 for the training set, which indicated good discriminatory power to separate the two (BC and NC) groups (Fig. 3D). The permutation test yielded a significant *P*-value of <0.001. The average accuracy amounted to a value of 0.728 (Fig. S13D).

These statistical analyses demonstrated that differential levels of Fe and Li are potentially good indicators of BC in human serum. The results from the statistical analyses of these two selected elements are summarized in Table 1.

3.5. Untargeted metabolic profiling by PFL-2D GS LASiS AuNPs and ^{109}AgNPs LDI-MS

In total, 335 and 650 features were detected in the serum samples of 200 participants analyzed with PFL-2D GS LASiS AuNPs and ^{109}AgNPs LDI-MS. Statistical analysis was performed using data randomly divided into two subsets: a training set ($n = 80$ BC and $n = 80$ NCs) and a validation dataset ($n = 20$ BC and $n = 20$ NCs).

2D-PCA and OPLS-DA score plots of mass spectral features created for PFL-2D GS LASiS ^{109}AgNPs LDI-MS data revealed clear discrimination between cancer and control serum samples in both subsets (Fig. S14). The analysis of both subsets (training and validation set) indicated 216 common features with |p[1]| and |*P*(corr)| above 0.5, of which 96 *m/z* values were more abundant in serum from patients with BC compared with the control group, and 119 features displayed the opposite trend. The validation of the OPLS-DA model using 2000 permutations resulted in R^2Y and Q^2 values of 0.986 ($P < 0.0005$) and 0.982 ($P < 0.0005$) (Fig. S15). All 11 previously selected *m/z* mass spectral features were found to exhibit AUC values of >0.73. Figs. S16A and D indicate the combination of *m/z* values, which is a better discriminator (AUC >99% in the training and validation set) than independent evaluation of each feature, which reinforces the improved capacity of biomarker patterns to accurately distinguish between the BC and NC groups. In the next step, putative identification of mass spectral features was performed by searching various metabolite databases, i.e., Human Metabolome Database [38], MetaCyc Metabolic Pathway Database [39], LIPID MAPS® Lipidomics Gateway [40], and Metlin [41]. Seventeen mass spectral features were putatively identified as naturally occurring metabolites in the human body. Important mass spectral features and annotated metabolite IDs resulting from the PFL-2D GS LASiS ^{109}AgNPs LDI-MS analyses are reported in Table S7. All statistical data with mean feature abundance for control versus cancer serum samples based on PFL-2D GS LASiS ^{109}AgNPs LDI-MS in the training and validation datasets are presented in Tables S8 and S9.

The acquired data from untargeted PFL-2D GS LASiS AuNPs LDI-MS analysis were also analyzed using PCA and OPLS-DA to identify novel metabolites. In both cases, score plots showed clear separation in both subsets, suggesting that the PFL-2D GS LASiS AuNPs LDI-MS-based serum metabolomics model could be used to identify BC (Fig. S17). The S-plots derived from the OPLS-DA model using the training set ($R^2Y = 0.962$, $Q^2 = 0.955$) and the validation set ($R^2Y = 0.982$, $Q^2 = 0.964$) generated a list of mass spectral features (*m/z*) of interest that were found to be important for group discrimination (Fig. S18). All relevant mass spectral features are reported in Tables S10 and S11. The analysis of both subsets (training and validation sets) identified 172 common features with |p[1]| and |*P*(corr)| above 0.5, of which 44 *m/z* values were more abundant in the sera of BC patients compared to the control group, and 128 features exhibited the opposite trend. This analysis was followed by a multivariate ROC analysis. As shown in Fig. S19, the combination of mass spectral features in both subsets was found to be a more powerful discriminator between control and BC serum samples (AUC > 99%), compared with that of any individual mass spectral feature.

The results presented above suggest that selected mass spectral features can significantly increase the performance of the diagnostic model and can be used to distinguish cancer serum samples from controls. Putative identifications of selected features allowed for the identification of eight compounds that are often present in the human body (Table S7).

3.6. Pathway analysis of potential cancer biomarkers

Metabolic pathway impact analysis suggested that 14 out of 25 metabolites identified in the NMR and LDI-MS analyses were relevant to human metabolism. Seven pathways (glycine, serine and threonine metabolism, glycerophospholipid metabolism, propanoate metabolism, glutathione metabolism, pyruvate metabolism, glyoxylate and dicarboxylate metabolism, and glycolysis/gluconeogenesis) were significantly impacted in BC compared with the controls. The results from this pathway impact analysis are shown in Fig. 4A and Table S12. The bubble area (Fig. 4A) reveals the degree of impact on the pathway and the color represents the significance (highest in red and lowest in white). Quantitative enrichment analysis found 10 additional pathways relevant to BC, i.e., amino sugar metabolism, aspartate metabolism, betaine metabolism, ethanol degradation, fatty acid biosynthesis, methionine metabolism, phosphatidylcholine biosynthesis, phosphatidylethanolamine biosynthesis, phospholipid biosynthesis, and vitamin K (K1 and K2) metabolism (Fig. 4B and Table S13).

4. Discussion

In this study, NMR, ICP-OES, and LDI-MS with both ^{109}AgNPs and AuNPs-based targets were employed to evaluate changes in serum metabolite and element levels between patients with BC and controls. BC is characterized by several metabolic changes that promote cancer cell proliferation and thus tumor growth [42]. These changes in metabolism provide an essential source of energy for intracellular metabolism and building blocks for rapidly dividing tumor cells. The Warburg effect, a hallmark of cancer cell metabolic activity, involves aerobic glycolysis in the presence of an aerobic environment and fully functioning mitochondria, and relies on increased glucose uptake and the conversion of glucose to lactate. This type of energy gain for cancer cells is much less energy efficient than mitochondrial respiration (2 adenosine triphosphate (ATP) vs. 36 ATP respectively) [43]. However, studies have shown that the rate of glucose-to-lactate conversion is 10–100 faster compared with that of the complete mitochondrial oxidation of glucose [44]. Moreover, the decoupling of glycolysis from oxidative phosphorylation offers a biosynthetic advantage for cancer cells by enabling the increased production of diverse biosynthetic precursors [45].

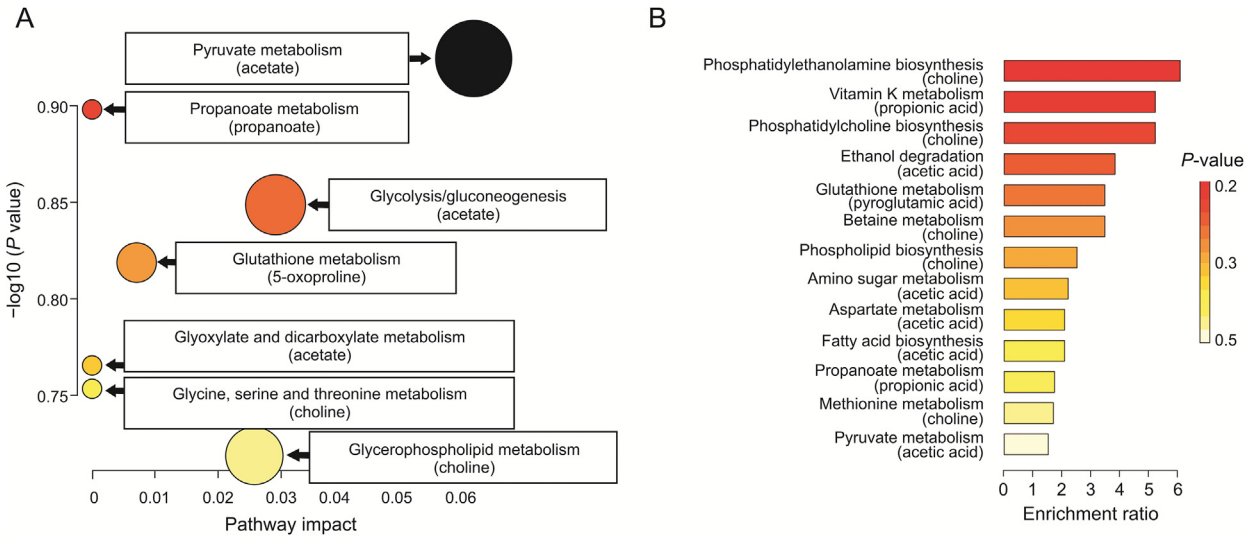

Fig. 4. Pathway topology analysis of statistically significant metabolites in bladder cancer (BC) that were found in the nuclear magnetic resonance and mass spectrometry (MS) datasets. (A) Kyoto Encyclopedia of Genes and Genomes pathway analysis. (B) Quantitative enrichment analysis based on Small Molecule Pathway Database.

In this study, we investigated the serum metabolic profiles among LG BC, HG BC, non-muscle invasive bladder cancer (pTa/pT1), muscle invasive BC (MIBC, pT2), and healthy subjects. The OPLS-DA modeling of the ^{1}H NMR metabolomics data revealed a clear separation between the BC and control serum sample groups. Metabolites with the highest AUC values (>0.82) included isobutyrate, pyroglutamate, propionate, choline, and acetate. The differences in the concentration of pyroglutamate, acetate, propionate, and choline were statistically significantly and higher in the sera of healthy individuals, whereas isobutyrate concentrations were much higher in the sera of BC patients.

Negative charges of short-chain fatty acids are considered to be crucial metabolic and immune cell regulators [46]. Acetate plays a key role in the metabolism of acetyl coenzyme A (acetyl-CoA), bioenergetics, cell proliferation, and regulation [47]. In cells, acetate is mainly used to generate acetyl-CoA through an ATP-dependent reaction by acetyl-CoA synthetase. Tumor cells use acetate in the form of acetyl-CoA, primarily for fuel or as a carbon source for lipid synthesis [48]. Acetyl-CoA synthetase 2 (ACSS2), one of the enzymes capable of using acetate as a substrate, contributes to cancer cell growth and is highly upregulated in multiple cancer types [49]. Based on these studies, we surmise that the lower levels of acetate in the serum samples of patients with BC may be due to its significant uptake and utilization by ACSS2 in cancer cells. Recently, Lee et al. [50] reported that acetate in urine, along with four urine metabolites, may contribute to the discrimination of different urological cancers. Their research showed that acetate levels in urine were slightly elevated in kidney cancer patients compared to patients with bladder and prostate cancer. Unfortunately, these results were not directly compared to those of a healthy control group [50].

Other metabolites present at lower concentration in the sera of BC cancer patients compared with healthy controls include choline and propionate. Studies have shown that the consumption of choline may protect against cancer [51]. Propionate, a metabolite produced by the intestinal microbiota, reduces the proliferation of cancer cells in the liver and the lungs [52,53]. Acetate and propionate are the end-products of the indigestible carbohydrate fermentation in the human colon, and are distributed systemically via blood circulation. These compounds have been shown to exhibit anti-inflammatory properties in immune cells, inhibit colon cancer cell growth, and induce cancer cell death by apoptosis [53,54]. The levels of serum propionate are also associated with circulating immune cells in patients with multiple sclerosis, and lower serum propionate levels were found in patients with multiple sclerosis compared with the healthy controls [55]. In our study, the increased absorption of propionate by cancer cells is reflected by the lower propionate concentration in the sera of the patients with BC. However, no study to date has focused on the role of propionate in the progression of BC.

Choline is a water-soluble quaternary amine that is often grouped with vitamin B owing to its chemical similarities, and is a key nutrient for humans. This compound has various key functions in the human body, especially with respect to neurochemical processes [56]. Choline is involved in phospholipid production and triglyceride metabolism, and is therefore necessary for the proper structure and function of cell membranes. In this study, patients with BC had lower serum levels of choline compared with the controls, which could be a consequence of increased choline absorption by cancer cells. Our results are consistent with those of other studies that have shown that cancer cells often increase the synthesis of fatty acids; in turn, these can act as substrates for phosphatidylcholine synthesis, which is increased in tumor cells [57,58]. Furthermore, the increase in serum choline levels in cancer patients is consistent with our previous study results, where choline levels were found to be decreased in the sera of patients with renal cell carcinoma compared with controls [59]. The opposite situation was observed in urine, where urine choline levels were increased in patients with BC [60,61].

Ohara et al. [62] revealed that isobutyrate exerted an anticancer effect by suppressing the growth/metabolic networks supporting colorectal cancer. Previously, Wang et al. [63] showed that the levels of isobutyrate were lower in fecal samples of patients with colorectal cancer compared to those of healthy control individuals. To date, there is no report that isobutyrate is a potential biomarker of BC. In our research, isobutyrate levels were found to be significantly altered, as shown by the cancer-to-control mean concentration (fold change) ratio of 1.9.

Pyroglutamate is a cyclized derivative of L-glutamate and is related to the gamma-glutamyl cycle, which is the main pathway for glutathione synthesis [64]. Glutathione is a major antioxidant produced in the human body, the levels of which can drop

significantly as a result of oxidative stress or chemical exposure. In the case of low glutathione levels, the level of pyroglutamate from which it is reconstituted is also decreased [65]. Pyroglutamate was found to be a promising biomarker for the diagnosis of nonalcoholic liver disease [64]. Several studies have observed elevated levels of pyroglutamate in the biofluids of patients with several genetic disorders and an acetaminophen-induced metabolic disorder [66]. Most of the research devoted to urinary or serum metabolomics of BC has suggested a higher level of pyroglutamate in patients with BC compared with healthy controls [22,67]. However, both of these cited publications are based on GC-MS results with derivatization, which can be considered inferior in terms of quantitation compared to the measurement of unmodified extracts with NMR.

Fe is a crucial trace element in which the deficiency or excess is associated with numerous disease states [68]. ICP-OES analysis indicated an increase in serum Fe in patients with BC, which is surprising, given that these patients often have micro/macrohematuria, so Fe deficiency would be expected [69]. However, the higher level of Fe in serum of patients with BC may be explained by the activation of mechanisms stimulating Fe absorption from the gastrointestinal tract, which provides a possible compensation for the level of Fe in the blood. Moreover, previous studies have suggested that excess Fe in the sera of patients with cancer may be associated with malignant transformation and cancer progression [70]. In tumor tissues, rapid cell proliferation and increased DNA synthesis are often observed, which require high Fe bioavailability. In the human body, the main source of Fe in the blood is heme, which is released following the breakdown of red blood cells [70]. Further, our results are consistent with earlier studies that reported elevated serum Fe levels in various types of diseases, such as hepatocellular carcinoma, lung cancer, and colorectal cancer [71].

Li is an alkali metal used to treat psychiatric disorders, and has potential benefits for the treatment of leukemia or thyroid disorders [72]. It inhibits several enzymes, including inositol monophosphatase and glycogen synthase kinase-3 [73]. However, the ingestion of Li causes many side effects, including hypercalcemia, cardiovascular, and gastrointestinal and parathyroid disorders [74]. Recent studies demonstrated that Li uptake is associated with reduced tumor incidence, probably through inhibited cell proliferation, which may be linked to reduced DNA replication and S-phase cell cycle arrest [75]. Wach et al. [29] detected significantly increased concentration of Li in the sera of patients with BC compared with healthy controls using ICP-OES.

Lower concentration of the serum amino acids histidine, alanine, tryptophan, glutamine, glycine, and threonine in patients with muscle invasive BC (pT2) in comparison to non-muscle invasive BC (pTa/pT1) may suggest the higher uptake of these amino acids and their potential role in protein synthesis underlying muscle cancer invasion. This inference is supported by proteomic studies that reported significant differences in tissue protein expression, which were correlated with BC ability to invade into muscle tissue [76]. Another possibility as to why these amino acids are present at lower concentrations may be due to general state of cachexia and malnutrition observed in patients with MIBC, which is usually a systemic disease and often manifests at a stage when metastases are present. Interestingly, lower concentrations of serum amino acids (leucine, histidine, alanine, and tyrosine) can be also observed in LG BC when compared to HG BC. In healthy organisms, de novo lipogenesis is limited to hepatocytes and adipocytes. Cancer cells may reactivate this anabolic pathway, which relies on glucose, glutamine, and acetate to synthesize citrate. Both acetate and citrate are substrates for extramitochondrial acetyl-CoA production, which is essential for fatty acid and cholesterol biosynthesis [57].

To date, several papers have focused on metabolite analyses in urine and blood from BC patients in an effort to potentially differentiate the different grades of this cancer. However, to our knowledge, only two studies have explored the relationships between changes in metabolite levels in urine and different tumor stages (Ta/Tis, T1, and >T2) [61,77]. At present, there are no reports of serum profiling in patients with different types of BC, probably owing to the fact that this type of analysis would require quite a large group of patients and healthy controls.

A pilot urine analysis conducted by Kim et al. [67] in 2010 studied a relatively small group of patients and revealed slightly elevated levels of alanine, glutamine, leucine, tyrosine, and glycine and slightly decreased levels of threonine and tryptophan in patients with BC compared with controls. Subsequent studies also using GC-MS confirmed higher levels of alanine in the serum of the healthy controls compared to patients with BC, but the levels of alanine were not found to be potentially diagnostic of BC stages [22]. In our study, a slightly lower concentration of alanine in the serum of patients with BC was found compared to the control group; however, this trend was not found to be statistically significant in differentiating between the two groups. However, we measured significantly lower levels of alanine in the sera of patients with LG and pTa/pT1 BC, which has not been previously reported in the literature.

Troisi et al. [22] obtained comparable results to Kim et al. [67] study with respect to glutamine level changes, but also found higher levels of threonine in the sera samples from the LG group compared with the HG group, and a higher level of glycine in the HG group compared with the LG group. The results from our study indicated that differential concentrations of glycine, glutamine, and threonine in human sera may be used as diagnostic markers and may help distinguish between different stages of BC, as we have found that these metabolites were present at higher concentrations in the sera of patients with pTa/pT1 stage disease compared to those with pT2 stage. Bansal et al. [24] undertook an NMR-based study of serum metabolite profiles and identified glutamine as one of three metabolites that can differentiate between LG and HG BC, as it was reported to be slightly elevated in the sera of patients with HG BC [24]. Our results on serum glutamine levels are consistent with published studies, and suggest that elevated levels of glutamine in the pTa/pT1 stage of BC may be the result of increased glutaminolysis, which is observed in some types of tumors as an important mechanism to provide an additional source of cellular energy [78].

Bansal et al. [24] also reported histidine as one of the six metabolites that can distinguish patients with LG and HG BC from healthy controls, and was reported to be in higher concentrations in the sera of LG BC patients compared to HG BC patients and healthy controls. The authors' finding about serum histidine levels was consistent with that of our study, which found higher serum levels of histidine in LG and pTa/pT1 BC cancer [24,79]. The link between differential levels of serum histidine and BC progression, as well as concentration changes in methylhistidine, tyrosine, leucine, and tryptophan, has also been reported by Alberice et al. [80]. The authors' study reported elevated levels of these metabolites in the sera of patients with bladder tumors compared to those of patients with early stages of BC [80]. In contrast, an LC-MS-based study reported lower levels of histidine in the urine of patients with BC compared to healthy controls [56,81]. Moreover, Li et al. [60] indicated an increased level of L-methylhistidine in the urine of patients with BC. Histidine is a precursor for histamine synthesis in a reaction catalyzed by histidine decarboxylase (HDC). The overexpression of HDC has been observed in various cancers. Histidine via histamine is associated with inflammation in the urinary bladder, which is commonly associated with cancer development in this organ [82].

Our research has shown a significant difference in serum leucine levels in BC patients with LG compared to HG. In addition to the research of Kim et al. [67] and Alberice et al. [80], the level of leucine in patients with BC was also examined by Cao et al. [23], who reported, using NMR, lower levels of leucine/isoleucine as well as tyrosine and glycine in the sera of patients with HG BC compared to LG BC, which was consistent with our findings. Another study, conducted by Loras et al. [83], reported increased levels of tyrosine and tryptophan in the urine of patients with BC compared to healthy controls. Our research results are also consistent with those of Yumba Mpanga et al. [84], which indicated significantly higher levels of tryptophan in the urine of patients with HG BC compared to LG BC group.

The use of the gold and silver-109-modified targets in LDI-MS experiments allowed for direct measurement of serum samples without analyte separation and extraction. Using this technique, serum analysis allowed the identification of 13 compounds that were found in greater concentrations in control serum samples compared to those of patients with BC, and 12 compounds that displayed the opposite trend; these included three compounds found independently using both silver-109- and gold-based MS methods. Most of these compounds were lipids, 12 of which belonged to the class of sphingolipids, and the remaining contained fatty acyls, saccharolipids, polyketides, nucleosides or nucleotides, and others.

Lipid metabolism plays a key role in various processes associated with cancer cells. Fatty acids are the building blocks of complex lipids, which are used for energy storage or as building blocks of cell membranes [85]. As reported by many authors, BC initiation and progression are associated with changes in lipid metabolism [86]. Sphingolipids are a group of lipids comprising sphingoid bases (i.e., set of aliphatic amino alcohols that include sphingosine) that play an important role in regulation of diverse cellular processes including cellular apoptosis, proliferation, angiogenesis, senescence, and transformation [87]. The importance of sphingolipids in the regulation of cancer growth and pathogenesis has been well described in the literature [88]. The sphingolipid metabolism may be responsible for the invasion and mobility of cancer cells in muscle-infiltrating BC [89]. Human BC cells have also been shown to upregulate the cannabinoid receptors 2, which induces cell apoptosis by stimulating de novo ceramide synthesis [90].

Lastly, the gold- and silver-109-based LDI-MS spectral analyses shown in this work have indicated a higher concentration of serum cyanidin in healthy individuals. Cyanidin is classified as a natural antioxidant present in both fruits and vegetables, and has confirmed with anticancer properties. It has been reported to induce apoptosis and differentiation in prostate and renal cancer cells [91,92].

5. Conclusion

We demonstrate that high-resolution NMR, ICP-OES, and gold- and silver-109-based LDI-MS, together with multivariate statistics, are powerful sets of tools for the characterization of the serum metabolome and elemental differences in BC. With regard to biomarker discovery using ^{1}H NMR spectroscopy, four potentially robust metabolic biomarkers were identified for 100 tumor serum samples from patients with BC patients after comparison against 100 healthy controls owing to the excellent predictive ability of AUC > 0.999. Two elements (Fe and Li) exhibited significant concentration differences in the serum of NCs compared to that of patients with BC, suggesting that they may serve as useful biomarkers of BC. Additionally, 22 compounds (mainly lipids) were observed to differentiate between cancer and control samples, as judged from laser MS results. We also identified five metabolites that might be used as potential biomarkers to distinguish LG and HG and nine metabolites that may serve to differentiate between the pTa/pT1 and pT2 stages of BC. Our results suggest that differential serum metabolite profiles and elements can help identify patients with BC compared with NCs, with significant discriminating power between different stages and grades of BC. Moreover, our findings demonstrate that combining serum metabolite profiles and elements has a stronger predictive value than either compound/element alone to assess disease severity and progression in BC.

CRediT author statement

Krzysztof Ossoliński: Investigation, Resources, Writing - Original draft preparation; **Tomasz Ruman:** Methodology, Resources, Data curation, Writing - Reviewing and Editing, Supervision; **Valérie Copié:** Resources, Data curation, Writing - Reviewing and Editing, Funding acquisition; **Brian P. Tripet:** Resources, Data curation, Writing - Reviewing and Editing, Visualization, Funding acquisition; **Leonardo B. Nogueira:** Resources, Investigation, Data curation; Writing - Original draft preparation; **Katiane O.P.C. Nogueira:** Data curation, Writing - Original draft preparation; **Artur Kołodziej:** Investigation, Data curation; **Aneta Płaza-Altamer:** Investigation; **Anna Ossolińska:** Resources; **Tadeusz Ossoliński:** Resources; **Joanna Nizioł:** Conceptualization, Methodology, Formal analysis, Investigation, Data curation, Writing - Original draft preparation, Reviewing and Editing, Visualization, Supervision, Project administration, Funding acquisition.

Declaration of competing interest

The authors declare that there are no conflicts of interest.

Acknowledgments

Research was supported mainly by the National Science Center (Poland) (Project SONATA No.: UMO-2018/31/D/ST4/00109). ^{1}H NMR spectra were recorded at Montana State University (MSU), Bozeman, USA, on a cryoprobe-equipped 600 MHz (14 T) AVANCE III solution NMR spectrometer housed in MSU's NMR Center. Funding for MSU NMR Center's NMR instruments has been provided in part by the National Institutes of Health Shared Instrumentation Grant program (Grant Nos.: 1S10RR13878 and 1S10RR026659), the National Science Foundation (Grant Nos: NSF-MRI:DBI-1532078 and NSF-MRI CHE 2018388), the Murdock Charitable Trust Foundation (Grant No.: 2015066:MNL), and support from the office of the Vice President for Research, Economic Development, and Graduate Education at MSU.

Appendix A. Supplementary data

Supplementary data to this article can be found online at https://doi.org/10.1016/j.jpha.2022.08.004.

References

[1] H. Sung, J. Ferlay, R.L. Siegel, et al., Global cancer statistics 2020: GLOBOCAN estimates of incidence and mortality worldwide for 36 cancers in 185 countries, CA Cancer J. Clin. 71 (2021) 209–249.
[2] H.A.A. Amin, M.H. Kobaisi, R.M. Samir, Schistosomiasis and bladder cancer in Egypt: Truths and myths, open access maced, Open Access Maced. J. 7 (2019) 4023–4029.
[3] M. Burger, J.W. Catto, G. Dalbagni, et al., Epidemiology and risk factors of urothelial bladder cancer, Eur. Urol. 63 (2013) 234–241.
[4] F.A. Yafi, F. Brimo, J. Steinberg, et al., Prospective analysis of sensitivity and specificity of urinary cytology and other urinary biomarkers for bladder cancer, Urol. Oncol. 33 (2015) 66.e25–66.e31.
[5] F. Soria, M.J. Droller, Y. Lotan, et al., An up-to-date catalog of available urinary biomarkers for the surveillance of non-muscle invasive bladder cancer, World J. Urol. 36 (2018) 1981–1995.

[6] Q. Yang, A.-H. Zhang, J.-H. Miao, et al., Metabolomics biotechnology, applications, and future trends: A systematic review, RSC Adv. 9 (2019) 37245–37257.
[7] G. Raja, Y. Jung, S.H. Jung, et al., ^{1}H-NMR-based metabolomics for cancer targeting and metabolic engineering – A review, Process Biochem. 99 (2020) 112–122.
[8] X.-W. Zhang, Q.-H. Li, Z.-D. Xu, et al., Mass spectrometry-based metabolomics in health and medical science: A systematic review, RSC Adv. 10 (2020) 3092–3104.
[9] P.K. Cheung, M.H. Ma, H.F. Tse, et al., The applications of metabolomics in the molecular diagnostics of cancer, Expert Rev. Mol. Diagn. 19 (2019) 785–793.
[10] Z. Pan, D. Raftery, Comparing and combining NMR spectroscopy and mass spectrometry in metabolomics, Anal. Bioanal. Chem. 387 (2007) 525–527.
[11] K. Ng, A. Stenzl, A. Sharma, et al., Urinary biomarkers in bladder cancer: A review of the current landscape and future directions, Urol. Oncol. 39 (2021) 41–51.
[12] R. Batista, N. Vinagre, S. Meireles, et al., Biomarkers for bladder cancer diagnosis and surveillance: A comprehensive review, Diagnostics (Basel) 10 (2020), 39.
[13] M.C. Walsh, L. Brennan, J.P. Malthouse, et al., Effect of acute dietary standardization on the urinary, plasma, and salivary metabolomic profiles of healthy humans, Am. J. Clin. Nutr. 84 (2006) 531–539.
[14] L. Lin, Z. Huang, Y. Gao, et al., LC-MS-based serum metabolic profiling for genitourinary cancer classification and cancer type-specific biomarker discovery, Proteomics 12 (2012) 2238–2246.
[15] Y. Zhou, R. Song, Z. Zhang, et al., The development of plasma pseudotargeted GC-MS metabolic profiling and its application in bladder cancer, Anal. Bioanal. Chem. 408 (2016) 6741–6749.
[16] G. Tan, H. Wang, J. Yuan, et al., Three serum metabolite signatures for diagnosing low-grade and high-grade bladder cancer, Sci. Rep. 7 (2017), 46176.
[17] D. Sahu, Y. Lotan, B. Wittmann, et al., Metabolomics analysis reveals distinct profiles of nonmuscle-invasive and muscle-invasive bladder cancer, Cancer Med. 6 (2017) 2106–2120.
[18] V. Vantaku, S.R. Donepudi, D.W.B. Piyarathna, et al., Large-scale profiling of serum metabolites in African American and European American patients with bladder cancer reveals metabolic pathways associated with patient survival, Cancer 125 (2019) 921–932.
[19] C.S. Amara, C.R. Ambati, V. Vantaku, et al., Serum metabolic profiling identified a distinct metabolic signature in bladder cancer smokers: A key metabolic enzyme associated with patient survival, Cancer Epidemiol. Biomarkers Prev. 28 (2019) 770–781.
[20] X. Liu, M. Zhang, X. Cheng, et al., LC-MS-based plasma metabolomics and lipidomics analyses for differential diagnosis of bladder cancer and renal cell carcinoma, Front. Oncol. 10 (2020), 717.
[21] Z. Lepara, O. Lepara, A. Fajkić, et al., Serum malondialdehyde (MDA) level as a potential biomarker of cancer progression for patients with bladder cancer, Rom. J. Intern. Med. 58 (2020) 146–152.
[22] J. Troisi, A. Colucci, P. Cavallo, et al., A serum metabolomic signature for the detection and grading of bladder cancer, Appl. Sci. 11 (2021), 2835.
[23] M. Cao, L. Zhao, H. Chen, et al., NMR-based metabolomic analysis of human bladder cancer, Anal. Sci. 28 (2012) 451–456.
[24] N. Bansal, A. Gupta, N. Mitash, et al., Low- and high-grade bladder cancer determination via human serum-based metabolomics approach, J. Proteome Res. 12 (2013) 5839–5850.
[25] A. Gupta, K. Nath, N. Bansal, et al., Role of metabolomics-derived biomarkers to identify renal cell carcinoma: A comprehensive perspective of the past ten years and advancements, Expert Rev. Mol. Diagn. 20 (2020) 5–18.
[26] S.J. Mulware, Trace elements and carcinogenicity: A subject in review, 3 Biotech 3 (2013) 85–96.
[27] S. Mishra, S.P. Dwivedi, R.B. Singh, A review on epigenetic effect of heavy metal carcinogens on human health, Open Nutraceuticals J. 3 (2010) 188–193.
[28] R.S. Amais, G.L. Donati, M.A. Zezzi Arruda, ICP-MS and trace element analysis as tools for better understanding medical conditions, Trends Analyt. Chem. 133 (2020), 116094.
[29] S. Wach, K. Weigelt, B. Michalke, et al., Diagnostic potential of major and trace elements in the serum of bladder cancer patients, J. Trace Elem. Med. Biol. 46 (2018) 150–155.
[30] M. Abdel-Gawad, E. Elsobky, M. Abdel-Hameed, et al., Quantitative and qualitative evaluation of toxic metals and trace elements in the tissues of renal cell carcinoma compared with the adjacent non-cancerous and control kidney tissues, Environ. Sci. Pollut. Res. Int. 27 (2020) 30460–30467.
[31] J. Nizioł, V. Copié, B.P. Tripet, et al., Metabolomic and elemental profiling of human tissue in kidney cancer, Metabolomics 17 (2021), 30.
[32] A. Płaza, A. Kołodziej, J. Nizioł, et al., Laser ablation synthesis in solution and nebulization of silver-109 nanoparticles for mass spectrometry and mass spectrometry imaging, ACS Meas. Sci. Au 2 (2022) 14–22.
[33] J. Nizioł, K. Ossoliński, B.P. Tripet, et al., Nuclear magnetic resonance and surface-assisted laser desorption/ionization mass spectrometry-based metabolome profiling of urine samples from kidney cancer patients, J. Pharm. Biomed. Anal. 193 (2021), 113752.
[34] Z. Pang, J. Chong, G. Zhou, et al., MetaboAnalyst 5.0: Narrowing the gap between raw spectra and functional insights, Nucleic Acids Res. 49 (2021) W388–W396.
[35] S.Y. Ho, K. Phua, L. Wong, et al., Extensions of the external validation for checking learned model interpretability and generalizability, Patterns (N Y) 1 (2020), 100129.
[36] A.H. Emwas, E. Saccenti, X. Gao, et al., Recommended strategies for spectral processing and post-processing of 1D ^{1}H-NMR data of biofluids with a particular focus on urine, Metabolomics 14 (2018), 31.
[37] L. Yu, I.W. Liou, S.W. Biggins, et al., Copper deficiency in liver diseases: A case series and pathophysiological considerations, Hepatol. Commun. 3 (2019) 1159–1165.
[38] D.S. Wishart, D. Tzur, C. Knox, et al., HMDB: The human metabolome database, Nucleic Acids Res. 35 (2007) D521–D526.
[39] R. Caspi, R. Billington, C.A. Fulcher, et al., The MetaCyc database of metabolic pathways and enzymes, Nucleic Acids Res. 46 (2017) D633–D639.
[40] M. Sud, E. Fahy, D. Cotter, et al., LIPID MAPS-nature lipidomics Gateway: An online resource for students and educators interested in lipids, J Chem. Educ. 89 (2012) 291–292.
[41] C.A. Smith, G. O'Maille, E.J. Want, et al., METLIN A metabolite mass spectral database, Ther. Drug Monit. 27 (2005) 747–751.
[42] F. Massari, C. Ciccarese, M. Santoni, et al., Metabolic phenotype of bladder cancer, Cancer Treat. Rev. 45 (2016) 46–57.
[43] W. Jones, K. Bianchi, Aerobic glycolysis: Beyond proliferation, Front. Immunol. 6 (2015), 227.
[44] M.V. Liberti, J.W. Locasale, The Warburg effect: How does it benefit cancer cells? Trends Biochem. Sci. 41 (2016) 211–218.
[45] M.G. Vander Heiden, L.C. Cantley, C.B. Thompson, Understanding the Warburg effect: The metabolic requirements of cell proliferation, Science 324 (2009) 1029–1033.
[46] J. Frampton, K.G. Murphy, G. Frost, et al., Short-chain fatty acids as potential regulators of skeletal muscle metabolism and function, Nat. Metab. 2 (2020) 840–848.
[47] S.A. Comerford, Z. Huang, X. Du, et al., Acetate dependence of tumors, Cell 159 (2014) 1591–1602.
[48] A.M. Hosios, M.G. Vander Heiden, Acetate metabolism in cancer cells, Cancer Metabol. 2 (2014), 27.
[49] Z.T. Schug, J. Vande Voorde, E. Gottlieb, The metabolic fate of acetate in cancer, Nat. Rev. Cancer 16 (2016) 708–717.
[50] S. Lee, J.Y. Ku, B.J. Kang, et al., A unique urinary metabolic feature for the determination of bladder cancer, prostate cancer, and renal cell carcinoma, Metabolites 11 (2021), 591.
[51] S. Sun, X. Li, A. Ren, et al., Choline and betaine consumption lowers cancer risk: A meta-analysis of epidemiologic studies, Sci. Rep. 6 (2016), 35547.
[52] L.B. Bindels, P. Porporato, E.M. Dewulf, et al., Gut microbiota-derived propionate reduces cancer cell proliferation in the liver, Br. J. Cancer 107 (2012) 1337–1344.
[53] K. Kim, O. Kwon, T.Y. Ryu, et al., Propionate of a microbiota metabolite induces cell apoptosis and cell cycle arrest in lung cancer, Mol. Med. Rep. 20 (2019) 1569–1574.
[54] K.M. Maslowski, A.T. Vieira, A. Ng, et al., Regulation of inflammatory responses by gut microbiota and chemoattractant receptor GPR43, Nature 461 (2009) 1282–1286.
[55] S. Trend, J. Leffler, A.P. Jones, et al., Associations of serum short-chain fatty acids with circulating immune cells and serum biomarkers in patients with multiple sclerosis, Sci. Rep. 11 (2021), 5244.
[56] S.K. Tayebati, I. Martinelli, M. Moruzzi, et al., Choline and choline alphoscerate do not modulate inflammatory processes in the rat brain, Nutrients 9 (2017), 1084.
[57] N. Koundouros, G. Poulogiannis, Reprogramming of fatty acid metabolism in cancer, Br. J. Cancer 122 (2020) 4–22.
[58] R.F. Saito, L.N.S. Andrade, S.O. Bustos, et al., Phosphatidylcholine-derived lipid mediators: The crosstalk between cancer cells and immune cells, Front. Immunol. 13 (2022), 768606.
[59] J. Nizioł, K. Ossoliński, B.P. Tripet, et al., Nuclear magnetic resonance and surface-assisted laser desorption/ionization mass spectrometry-based serum metabolomics of kidney cancer, Anal. Bioanal. Chem. 412 (2020) 5827–5841.
[60] J. Li, B. Cheng, H. Xie, et al., Bladder cancer biomarker screening based on non-targeted urine metabolomics, Int. Urol. Nephrol. 54 (2022) 23–29.
[61] A. Loras, C. Suárez-Cabrera, M.C. Martínez-Bisbal, et al., Integrative metabolomic and transcriptomic analysis for the study of bladder cancer, Cancers 11 (2019), 686.
[62] T. Ohara, T. Mori, Antiproliferative effects of short-chain fatty acids on human colorectal cancer cells via gene expression inhibition, Anticancer Res. 39 (2019) 4659–4666.
[63] X. Wang, J. Wang, B. Rao, et al., Gut flora profiling and fecal metabolite composition of colorectal cancer patients and healthy individuals, Exp. Ther. Med. 23 (2022), 250.
[64] S. Qi, D. Xu, Q. Li, et al., Metabonomics screening of serum identifies pyroglutamate as a diagnostic biomarker for nonalcoholic steatohepatitis, Clin. Chim. Acta 473 (2017) 89–95.
[65] T.W. Sedlak, B.D. Paul, G.M. Parker, et al., The glutathione cycle shapes synaptic glutamate activity, Proc. Natl. Acad. Sci. U S A 116 (2019) 2701–2706.
[66] J.A. Eckstein, G.M. Ammerman, J.M. Reveles, et al., Analysis of glutamine, glutamate, pyroglutamate, and GABA in cerebrospinal fluid using ion pairing HPLC with positive electrospray LC/MS/MS, J. Neurosci. Methods 171 (2008) 190–196.
[67] J.W. Kim, G. Lee, S.M. Moon, et al., Metabolomic screening and star pattern recognition by urinary amino acid profile analysis from bladder cancer patients, Metabolomics 6 (2010) 202–206.

[68] A. Yiannikourides, G.O. Latunde-Dada, A short review of iron metabolism and pathophysiology of iron disorders, Medicines (Basel) 6 (2019), 85.
[69] H. Mazdak, F. Yazdekhasti, A. Movahedian, et al., The comparative study of serum iron, copper, and zinc levels between bladder cancer patients and a control group, Int. Urol. Nephrol. 42 (2010) 89–93.
[70] R.A.M. Brown, K.L. Richardson, T.D. Kabir, et al., Altered iron metabolism and impact in cancer biology, metastasis, and immunology, Front. Oncol. 10 (2020), 476.
[71] S.V. Torti, D.H. Manz, B.T. Paul, et al., Iron and cancer, Annu. Rev. Nutr. 38 (2018) 97–125.
[72] W. Young, Review of lithium effects on brain and blood, Cell Transplant. 18 (2009) 951–975.
[73] S.Y. Aghdam, S. Barger, Glycogen synthase kinase-3 in neurodegeneration and neuroprotection: Lessons from lithium, Curr. Alzheimer Res. 4 (2007) 21–31.
[74] M. Kiełczykowska, M. Polz-Dacewicz, E. Kopciał, et al., Selenium prevents lithium accumulation and does not disturb basic microelement homeostasis in liver and kidney of rats exposed to lithium, Ann. Agric. Environ. Med. 27 (2020) 129–133.
[75] A. Sun, I. Shanmugam, J. Song, et al., Lithium suppresses cell proliferation by interrupting E2F-DNA interaction and subsequently reducing S-phase gene expression in prostate cancer, Prostate 67 (2007) 976–988.
[76] A. Latosinska, M. Mokou, M. Makridakis, et al., Proteomics analysis of bladder cancer invasion: Targeting EIF3D for therapeutic intervention, Oncotarget 8 (2017) 69435–69455.
[77] J. Pinto, Â. Carapito, F. Amaro, et al., Discovery of volatile biomarkers for bladder cancer detection and staging through urine metabolomics, Metabolites 11 (2021), 199.
[78] M. Meng, S. Chen, T. Lao, et al., Nitrogen anabolism underlies the importance of glutaminolysis in proliferating cells, Cell Cycle 9 (2010) 3921–3932.
[79] A. Gupta, N. Bansal, N. Mitash, et al., NMR-derived targeted serum metabolic biomarkers appraisal of bladder cancer: A pre- and post-operative evaluation, J. Pharm. Biomed. Anal. 183 (2020), 113134.
[80] J.V. Alberice, A.F. Amaral, E.G. Armitage, et al., Searching for urine biomarkers of bladder cancer recurrence using a liquid chromatography-mass spectrometry and capillary electrophoresis-mass spectrometry metabolomics approach, J. Chromatogr. A 1318 (2013) 163–170.
[81] K. Łuczykowski, N. Warmuzińska, S. Operacz, et al., Metabolic evaluation of urine from patients diagnosed with high grade (HG) bladder cancer by SPME-LC-MS method, Molecules 26 (2021), 2194.
[82] L. Graff, M. Frungieri, R. Zanner, et al., Expression of histidine decarboxylase and synthesis of histamine by human small cell lung carcinoma, Am. J. Pathol. 160 (2002) 1561–1565.
[83] A. Loras, M. Trassierra, D. Sanjuan-Herráez, et al., Bladder cancer recurrence surveillance by urine metabolomics analysis, Sci. Rep. 8 (2018), 9172.
[84] A. Yumba Mpanga, D. Siluk, J. Jacyna, et al., Targeted metabolomics in bladder cancer: From analytical methods development and validation towards application to clinical samples, Anal. Chim. Acta 1037 (2018) 188–199.
[85] C.R. Santos, A. Schulze, Lipid metabolism in cancer, FEBS J. 279 (2012) 2610–2623.
[86] M.Y. Lee, A. Yeon, M. Shahid, et al., Reprogrammed lipid metabolism in bladder cancer with cisplatin resistance, Oncotarget 9 (2018) 13231–13243.
[87] H. Furuya, Y. Shimizu, T. Kawamori, Sphingolipids in cancer, Cancer Metastasis Rev. 30 (2011) 567–576.
[88] B. Ogretmen, Sphingolipids in cancer: Regulation of pathogenesis and therapy, FEBS Lett. 580 (2006) 5467–5476.
[89] S. Kawamura, C. Ohyama, R. Watanabe, et al., Glycolipid composition in bladder tumor: A crucial role of GM3 ganglioside in tumor invasion, Int. J. Cancer 94 (2001) 343–347.
[90] A. Bettiga, M. Aureli, G. Colciago, et al., Bladder cancer cell growth and motility implicate cannabinoid 2 receptor-mediated modifications of sphingolipids metabolism, Sci. Rep. 7 (2017), 42157.
[91] V. Sorrenti, L. Vanella, R. Acquaviva, et al., Cyanidin induces apoptosis and differentiation in prostate cancer cells, Int. J. Oncol. 47 (2015) 1303–1310.
[92] X. Liu, D. Zhang, Y. Hao, et al., Cyanidin curtails renal cell carcinoma tumorigenesis, Cell. Physiol. Biochem. 46 (2018) 2517–2531.

Received: 29 June 2022 | Revised: 26 July 2022 | Accepted: 5 August 2022

DOI: 10.1002/rcm.9375

RESEARCH ARTICLE

Rapid Communications in Mass Spectrometry WILEY

Infrared pulsed fiber laser-produced silver-109 nanoparticles for laser desorption/ionization mass spectrometry of 3-hydroxycarboxylic acids

Artur Kołodziej[1,2] | Aneta Płaza-Altamer[1,2] | Joanna Nizioł[2] | Tomasz Ruman[2]

[1]Doctoral School of Engineering and Technical Sciences at the Rzeszów University of Technology, Rzeszów, Poland

[2]Faculty of Chemistry, Rzeszów University of Technology, Rzeszów, Poland

Correspondence
A. Kołodziej, Doctoral School of Engineering and Technical Sciences at the Rzeszów University of Technology, 8 Powstańców Warszawy Ave., 35-959 Rzeszów, Poland.
Email: a.kolodziej@prz.edu.pl

Funding information
Narodowe Centrum Nauki, Grant/Award Number: UMO-2018/31/D/ST4/00109

Rationale: 3-Hydroxycarboxylic acids are one of the major components of bacterial lipopolysaccharides (LPS), also known as endotoxins. Endotoxins pose a serious health risk and can seriously damage the internal organs of humans and animals. 3-Hydroxycarboxylic acids can be used as environmental markers to determine endotoxin levels. At the time of preparation of this manuscript no studies on laser mass spectrometry (MS) and analysis with silver nanoparticles (NP) for 3-hydroxycarboxylic acids have been published in literature.

Methods: Six acids, 3-hydroxyoctanoic (3-OH-C8:0), 3-hydroxydecanoic (3-OH-C10:0), 3-hydroxydodecanoic (3-OH-C12:0), 3-hydroxytetradecanoic (3-OH-C14:0), 3-hydroxyhexadecanoic (3-OH-C16:0), and 3-hydroxyoctadecanoic (3-OH-C18:0) acids, were used as test compounds on the target containing silver-109 NPs for quantification using matrix-assisted laser desorption/ionization (MALDI)–type mass spectrometer. Methods were also tested on spiked human blood serum samples to quantify 3-hydroxycarboxylic acids and verify the influence of the biological matrix on the measurement.

Results: Analyzed acids were directly tested in 1 000 000-fold concentration change conditions ranging from 1 mg/mL to 1 ng/mL. The semi-automatic MSI (MS imaging) method allowed us to obtain two to five times lower limit of detection (LOD) and lower limit of quantitation (LLOQ) values than common LDI (Bruker Daltonics, Bremen, Germany) method for analyzed acids. For almost all results of 3-hydroxycarboxylic acids, the trendline fit was better for the semi-automatic MSI method than the manual LDI method.

Conclusion: For the first time, the use of laser MS for the quantification of 3-hydroxycarboxylic acids has been demonstrated, and it has been proven that it can be used in the quantitative analysis of such compounds over a wide range of concentrations. In addition, a comparison of two methods—manual LDI-MS and semi-automatic MSI—is presented.

1 | INTRODUCTION

Matrix-assisted laser desorption/ionization-mass spectrometry (MALDI-MS) is one of the most popular soft ionization methods in modern MS. Since 1988 when this method was presented by Tanaka et al for the first time,[1] many various modifications were developed. The MALDI method is still very popular despite the development of liquid and gas chromatography coupled with MS. This method is widely used for protein analysis in proteomics, for the identification of microorganisms in microbiology, and for the analysis of drugs

distribution in pharmacy.[2–4] Although it has many advantages such as high sensitivity and efficiency, the MALDI method is rarely used for the detection and quantification of low-molecular-weight (LMW) compounds. Analysis of these compounds is difficult because of the need for organic matrices, which are usually LMW organic acids, and during analysis the matrix produces various types of ions that interfere with the signals of the analyzed sample in the low mass range. This problem can be avoided by modifying the MALDI method with nanostructures (SALDI method). In the SALDI method, traditional acid matrix is replaced by metallic nanoparticles (NPs), which allow one to obtain mass spectra without the interfering signals of the organic acid matrix. The NPs have additional advantages: allows easy sample preparation, low chemical background, easier data analysis, and fast data collection.[5] Moreover, monoisotopic silver NPs have some additional properties like the simplest possible peak pattern, a much higher intensity of analyte peaks, and simplified calculations of isotopic distribution.[6] Laser ablation methods have an advantage over chemical synthesis because they allow for very quick synthesis of NPs (several seconds vs. hours in chemical synthesis), and the synthesized NPs are stabilizer- and reducing-agent-free.[7] The literature provides many examples of the use of NPs in LMW analysis.

3-Hydroxycarboxylic acids are one of the major components of lipid A, which is the lipid part of the endotoxins that are responsible for the toxicity of gram-negative bacteria. It has also been reported in the literature that lipid A is important in the immune system response during infection with gram-negative bacteria.[8] Bacterial lipopolysaccharide is an inflammatory stimulator that may trigger septic shock, which is a severe pathophysiological syndrome in response to an infection that in many cases is fatal as it can lead to organ failure.[9] Considering this fact, detection and quantification of 3-hydroxycarboxylic acids can be used to determine the endotoxins level in various samples.[10]

As high risk is involved, the concentration of endotoxins should be strictly controlled. For this purpose, various methods, including gas chromatography (GC) and liquid chromatography (LC) or biosensors, are used for their quantification. GC is a popular method in the quantification of endotoxins, but its limitation is the need for chemical derivatization such as transesterification or acetylation of the compounds in tested samples to obtain volatile derivatives or analogues.[11,12] LC, especially when coupled with MS, allows the measurement of very low levels of endotoxins without the need to modify the samples; however, the analysis itself takes quite a long time and requires the consumption of large amounts of reagents.[9] Using biosensors is a novel approach for quantification and detection of endotoxin. These devices are even more sensitive in detecting endotoxins; in the case of aptasensor by Zamani et al the detection limit is approximately 0.2 fg/mL.[13] A common element of all biosensors is the use of metal NPs, which enables the extremely sensitive detection of endotoxins.[13–15]

This work describes a new method for the detection of 3-hydroxyacids that are markers of bacterial lipopolysaccharides (endotoxin). In this publication we also present the quantification result of 3-hydroxycarboxylic acids with a chemically pure silver-109 NPs produced by 1064 nm pulsed fiber laser with 2D galvanometer scanner. In addition, we compare manual LDI-MS with semi-automatic MS imaging (MSI) in the quantification of 3-hydroxycarboxylic acids along with discussion of results and comparison with various SALDI and MALDI methods previously used in acid analysis. It is worth noting that this is the first study that reports the possibility of using laser MS and NP-coated targets for the detection of 3-hydroxycarboxylic acids.

2 | MATERIALS AND METHODS

2.1 | Materials

All 3-hydroxyacids standards were purchased from Sigma-Aldrich. Steel targets were machined from H17 stainless steel polished to the mirror finish. Before the LDI-MS and MS imaging experiments, steel targets were cleaned by dipping them in boiling solvents: toluene, chloroform, acetonitrile, and deionized water. After washing, plates were dried in high vacuum overnight. All solvents were of HPLC grade, except for water (18 MΩ·cm water produced locally).

2.2 | Sample preparation and handling

All 3-hydroxyacids standards (3-hydroxyoctanoic, 3-hydroxydecanoic, 3-hydroxydodecanoic, 3-hydroxytetradecanoic, 3-hydroxyhexadecanoic, and 3-hydroxyoctadecanoic acids) were dissolved in water to obtain a final concentration of 1 mg/mL. Lower concentrations of the standards were prepared by diluting higher concentration ones 10 times. An amount of 1 μL of plasma was dissolved in 249 μL of ultrapure water, then 250 μL of 100 μg/mL acid solution was added. About 0.3 μL of 3-hydroxyacid standards and blood plasma spiked with acid solutions were placed directly on the target plate and air-dried, and then the target was coated with ^{109}AgNPs suspension.

2.3 | Silver-109 NP synthesis and nebulization on target

Silver-109 foil was put into the beaker, and then acetonitrile was added. Laser ablation was then performed using a pulsed fiber laser (Raycus, Wuhan, China) with a wavelength of 1064 nm. The obtained suspension of monoisotopic silver NPs was sprayed on the surface of a steel plate with acid samples applied. Argon was used as an inert gas. A detailed protocol for the synthesis using laser ablation and nebulization of NPs is available in our previous publication on the preparation of silver-109 NPs using the pulsed fiber laser.[7] After the NPs were sputtered, the target was moved to the LDI-ToF-MS apparatus.

2.4 | Laser desorption/ionization-mass spectrometry

LDI-ToF-MS experiments were performed in reflectron mode using a Bruker Autoflex Speed time-of-flight mass spectrometer equipped with a SmartBeam II laser (355 nm). Laser impulse energy was approximately 90–140 μJ, and laser repetition rate was 1000 Hz. The total number of laser shots was 4000 for each spot divided in packs of 1000 shots per one measurement point. At each point, 1000 laser shots were made with default random walk applied (random points with 50 laser shots). The measurement range was *m/z* 80–1500. Suppression was turned on typically for ions of *m/z* lower than 80. Reflector voltages used were 21 kV (the first) and 9.55 kV (the second). The data were calibrated and analyzed with FlexAnalysis (version 3.3) using centroid calibration model. Mass calibration (enhanced cubic calibration based on 8–10 calibration points) was performed using internal standards (IS, silver-109 ions and clusters from $^{109}Ag^+$ to $^{109}Ag_9^+$).

2.5 | LDI-MS imaging

Measurements were performed using a Bruker Autoflex Speed time-of-flight mass spectrometer in reflectron positive mode. The apparatus was equipped with a SmartBeam II 1000 Hz 355 nm laser. Laser impulse energy was approximately 100–120 μJ, the laser repetition rate was 1000 Hz, and deflection was set on *m/z* lower than 80 Da. The *m/z* range was 80–1500, and the spatial resolution was 600 × 600 μm. The imaging experiments were made with 2000 laser shots per individual spot with a default random walk applied (FlexImaging 4.0). All spectra were pre-calibrated (cubic calibration function) with the use of silver-109 ions ($^{109}Ag^+$ to $^{109}Ag_9^+$) as an IS. The first accelerating voltage was held at 19 kV, and the second ion source voltage was held at 16.7 kV. Reflector voltages used were 21 kV (the first) and 9.55 kV (the second). All of the shown imaging pictures are for ± 0.05% *m/z* window. MSI experiments were performed on all spots of 3-hydroxyacid standards and blood plasma solution.

3 | RESULTS AND DISCUSSION

The method of synthesis of laser-generated nanomaterial (LGN) with PFL 2D GS laser, properties of silver-109 NPs, and their application are available in our recent publication.[7] This work presents the use of laser-generated ^{109}AgNPs for qualitative and quantitative analysis of 3-hydroxycarboxylic acids. A large number of results have been reported in the literature indicating that silver NPs are effective for ionization and rapid detection of various pure low-molecular-weight compounds (especially olefin-containing compounds) or complex biological mixtures such as urine, blood serum, or plant extracts.[16–21]

3.1 | Quantification results

Standards of all listed acids were directly measured in concentrations ranging from 1 mg/mL to 1 ng/mL, which equates to 1 000 000-fold concentration change. Limit of detection (LOD) values were calculated with the use of signal/noise (S/N) ratio value of 3 for lowest concentration samples. Each sample was placed on target plate in 0.3 μL volume equating to 0.3 μg to 0.3 pg of acid per measurement spot, which is approximately 1.87 nmol to 1.87 fmol, respectively, calculated, for example, for 3-hydroxyoctanoic acid molar mass. Examples of obtained mass spectra are presented in supporting information. LOD and lower limits of quantification (LLOQ) values were calculated based on S/N ratio value for manual LDI experiment and semi-automatic MSI (Table 1).

For analyzed hydroxycarboxylic acids, MSI method allowed to obtain lower LLOD value than manual LDI-MS except 3-hydroxyoctadecanoic acid. For this acid, due to the high values of the standard deviation, it is difficult to clearly show which method produces better results. It is worth noting that the application of semi-automatic MSI method allowed us to obtain two to five times lower LOD and LLOQ values for these acids.

Figure 1 presents results of LDI-MS and MSI analyses for 3-hydroxyoctanoic acid with ^{109}AgNPs PFL 2D GS laser-generated nanomaterial. Manual measurements were performed at four random

TABLE 1 Limits of detection and lower limit of quantification for studied 3-hydroxyacids

	Manual LDI-MS		Semi-automatic MSI	
	LOD±SD[a] (ng/mL)	LLOQ±SD[b] (ng/mL)	LOD±SD[a] (ng/mL)	LLOQ±SD[b] (ng/mL)
3-Hydroxyoctanoic acid	2563 ± 1770	4272 ± 2449	1549 ± 1173	2582 ± 1956
3-Hydroxydecanoic acid	1120 ± 896	1866 ± 1494	253 ± 195	422 ± 326
3-Hydroxydodecanoic acid	1915 ± 1292	3191 ± 2153	420 ± 410	700 ± 683
3-Hydroxytetradecanoic acid	1573 ± 782	2622 ± 1304	562 ± 385	937 ± 641
3-Hydroxyhexadecanoic acid	1482 ± 782	2470 ± 1303	366 ± 80	610 ± 150
3-Hydroxyoctadecanoic acid	1351 ± 268	2252 ± 447	1721 ± 233	2868 ± 389

Note: LLOQ, lower limit of quantitation; LOD, limit of detection; LDI-MS, laser desorption/ionization-mass spectrometry; MSI, mass spectrometry imaging; SD, standard deviation.

[a]Based on S/N ratio of 3.

[b]Based on S/N ratio of 5.

locations inside the sample spot for each analyzed acid; the measurement scheme is presented in Figure 1A. The acid was found in spectra mainly as silver-109 adduct of $[M + {}^{109}Ag]^+$ formula in amounts of ca. 300 ng to 3 pg per sample spot. All these data were presented in the form of intensity vs. concentration bar chart, and both axes are presented on a logarithmic scale (Figure 1B). Regression analysis of these data provided trendline with R^2 value 0.846. After manual LDI-MS measurement of the sample the same spots with carboxylic acids were analyzed using the semi-automatic MSI method. Figure 1C presents the scheme of semi-automatic MSI method, which was used in the measurement of all 3-hydroxycarboxylic acids. Figure 1D shows results of this analysis. During this measurement the whole sample spot was covered with a grid of measurement points with a defined resolution. The regression analysis of the MSI results clearly shows a much better fit of the trendline with an R^2 value of 0.969. Figure 4D also shows ion images of $[C_8H_{16}O_3 + {}^{109}Ag]^+$ adduct for all concentrations, proving that the sample is distributed non-homogeneously on the plate.

LOD based on S/N ratio of 3 was found to be 769 pg (4.80 pmol) of 3-hydroxyoctanoic acid per measured spot for LDI-MS. In contrast, LOD for MSI and LDI-MS was found to be 456 pg (2.90 pmol) per measured spot.

Quantitative analysis of 3-hydroxycarboxylic acids is presented only for LC- and GC–MS results in the literature, but no information is available for LDI-MS methods.[9,22] The publication by Uhlig et al shows that the LOD value for 3-hydroxyoctanoic acid was 0.7 ng/mL and the LLOQ value was 1.7 ng/mL.[9]

The next analyzed acid was 3-hydroxydecanoic acid. Figures 2A and 2C present results of LDI-MS and MSI analyses for this acid with PFL 2D GS LGN ^{109}AgNPs. The acid was found in spectra mainly as silver-109 adduct of $[M + {}^{109}Ag]^+$ ion formula in 0.1 mg/mL to 0.1 μg/mL concentration samples. Similar to 3-hydroxyoctanoic analysis, bar chart with trendlines is shown in Figure 2A. R^2 value for linear trendline for manual LDI-MS was 0.974, but for the MSI experiment a higher value was obtained for linear trendline of 0.978 (Figures 2A and 2C).

The LOD value for 3-hydroxydecanoic acid was found to be 336 pg (1.79 pmol) per spot for LDI-MS and 76 pg (0.40 pmol) per measurement spot for MSI. In the LC–MS method, the LOD value for this acid was 0.9 ng/mL.[9]

The next acid was 3-hydroxydodecanoic acid. Figures 2B and 2D present results of LDI-MS and MSI analyses. This acid was measured as it was presented in Figures 1A and 1C. The acid was found in spectra mainly as silver-109 adduct of $[M + {}^{109}Ag]^+$ ion formula in 1 mg/mL to 1 ng/mL concentration samples. Adduct *m/z* value was of 325.0768. Bar chart of intensity vs. concentration (Figure 2B) presents the trendline fit with R^2 value 0.987 for a very wide concentration range. However, the application of MSI allowed slightly better fit of R^2 value being equal to 0.988 for 10^6-fold concentration range. The LOD was found to be 575 pg (2.66 pmol) for LDI-MS and 126 pg (0.58 pmol) for MSI of 3-hydroxydodecanoic acid per measured spot. In the LC–MS method the LOD value for this acid was 2.2 ng/mL.[9]

Figures 3A and 3C show the results of analysis of 3-hydroxytetradecanoic acid. Similar to previous analysis, acid was

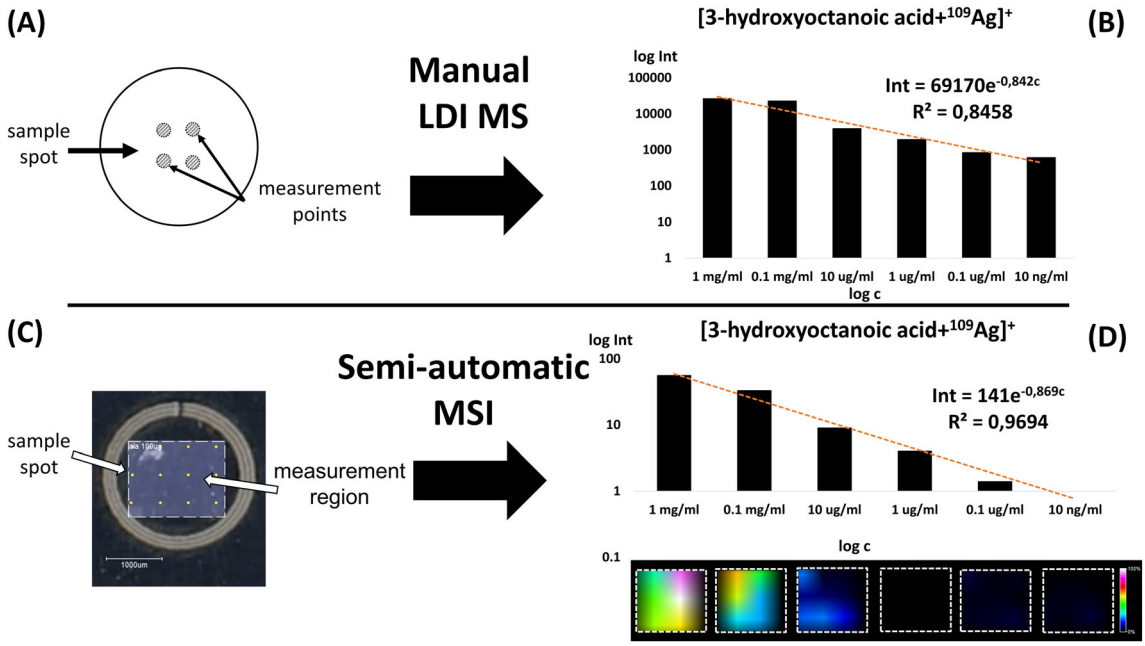

FIGURE 1 Panel A shows the scheme of manual laser desorption/ionization-mass spectrometry (LDI-MS) measurement with four random measure points. Panel C presents the scheme of semi-automatic mass spectrometry imaging (MSI) measurement. Column charts B and D present results of quantification based on silver-109 adduct of 3-hydroxyoctanoic acid signal for different concentrations obtained in LDI-MS and MSI experiments. Both panels (B, D) contain exponential trendline with its equation and R^2 value. Panel D also contains ion images for adduct [C8H16O3 + 109Ag] + images for each concentration [Color figure can be viewed at wileyonlinelibrary.com]

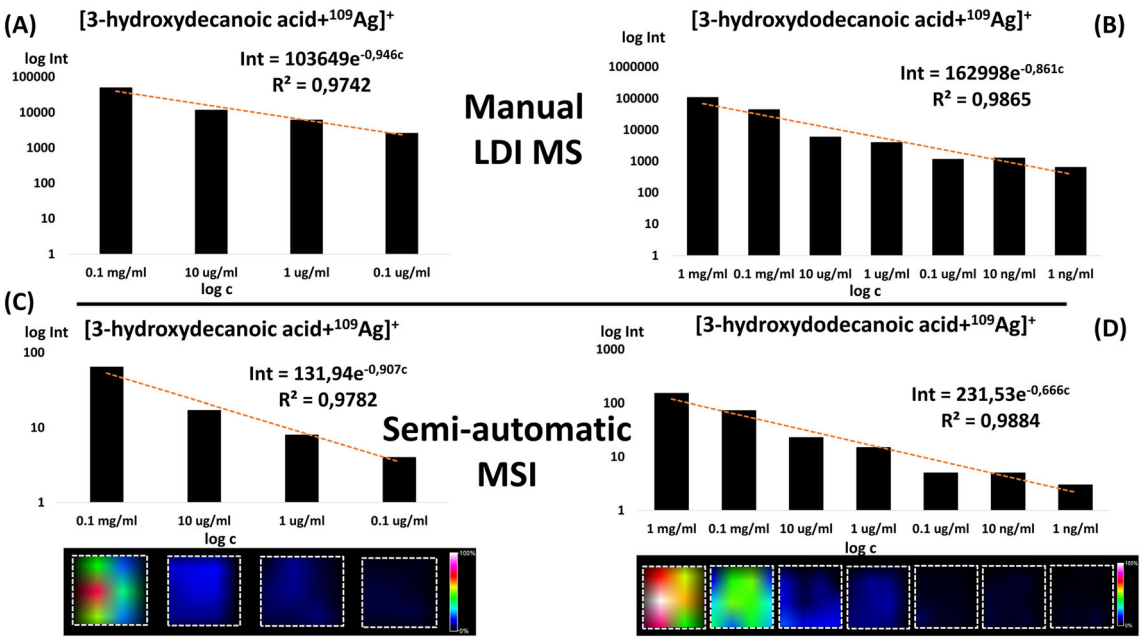

FIGURE 2 Column charts A and C present results of quantification based on silver-109 adduct of 3-hydroxydecanoic acid signal for different concentrations obtained in laser desorption/ionization-mass spectrometry (LDI-MS) and mass spectrometry imaging (MSI) experiments. Column charts B and D present the same results for 3-hydroxydodecanoic acid. All panels contain the equations and the R^2 values of exponential trendline. Panels C and D also contain ions [C10H20O3 + 109Ag] + and [C12H24O3 + 109Ag] + images for each concentration [Color figure can be viewed at wileyonlinelibrary.com]

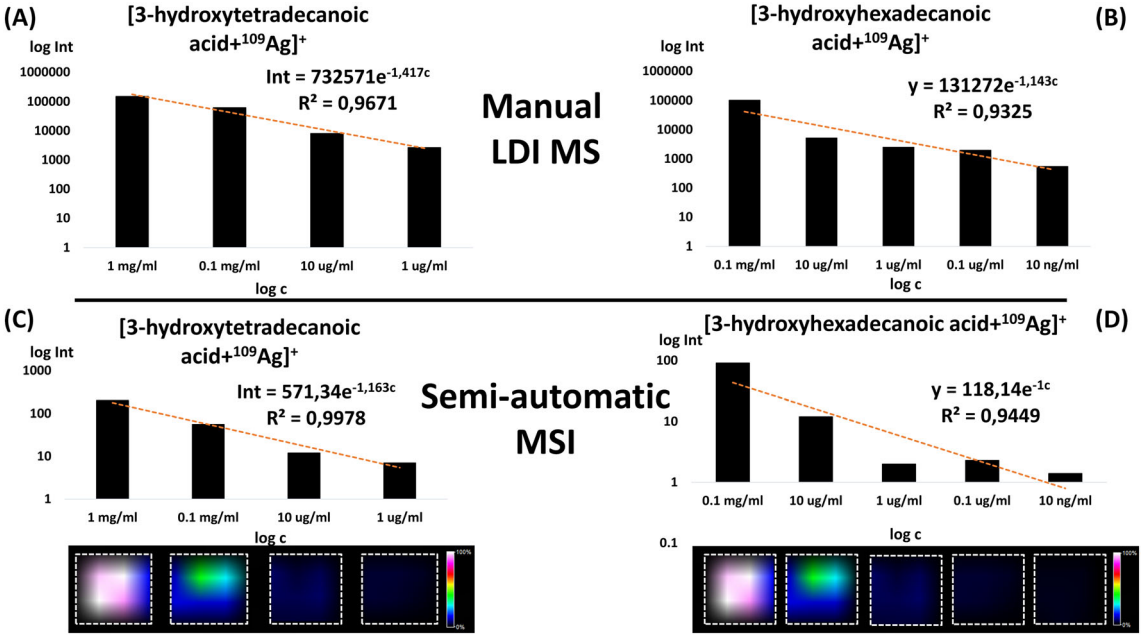

FIGURE 3 Column charts A and C present results of quantification based on silver-109 adduct of 3-hydroxytetradecanoic acid signal for different concentrations obtained in laser desorption/ionization-mass spectrometry (LDI-MS) and mass spectrometry imaging (MSI) experiments. Column charts B and D present the same results for 3-hydroxyhexadecanoic acid. All panels contain the equations and the R^2 values of exponential trendline. Panels C and D also contain ions [C14H28O3 + 109Ag] + and [C16H32O3 + 109Ag] + images for each concentration [Color figure can be viewed at wileyonlinelibrary.com]

analyzed in two measurement modes: manual LDI-MS and semi-automatic MSI. 3-Hydroxytetradecanoic acid was found in spectra mainly as silver-109 adduct of $[M + {}^{109}Ag]^+$ at the *m/z* value of 353.1081. The results of manual measurements for this acid are shown in Figure 3A for 1 mg/mL to 1 μg/mL concentration of sample. Figure 3C presents results of semi-automatic MSI method. On both

charts trendline fitted to obtained during experiment result are presented. The R^2 value of exponential trendline for the manual LDI method was 0.967. For the MSI method trendline fit was better with R^2 value 0.998. The LOD was found to be 472 (1.93 pmol) for LDI-MS and 169 pg (0.69 pmol) for MSI of 3-hydroxytetradecanoic acid per measured spot. In Uhlig et al's work the LOD value 1.7 ng/mL.[9]

3-Hydroxyhexadecanoic acid was analyzed next, and the results are presented in Figures 3B and 3D. The acid was found in spectra mainly as silver-109 adduct of $[M + {}^{109}Ag]^+$ at the *m/z* value of 381.1394. The results of manual measurements are shown in Figure 4B as a bar chart of intensity vs. concentration. This acid was found in 0.1 mg/mL to 10 ng/mL concentration sample. R^2 value of trendline fit for the manual LDI method was 0.933 and that for MSI was 0.945. In all presented cases quantification results of MSI experiment resulted in better fit than manual LDI-MS. The LOD value was found to be 445 pg (1.63 pmol) for LDI-MS and 110 pg (0.40 pmol) of 3-hydroxyhexadecanoic acid per measurement spot. In the LC–MS method, the LOD value was 0.6 ng/mL.[9]

Figure 4 presents results of analysis of 3-hydroxyoctadecanoic acid. This acid was found in spectra mainly as silver-109 adduct of $[M + {}^{109}Ag]^+$ at the *m/z* value of 409.1707. The results of the manual measurements for 3-hydroxyoctadecanoic acid are shown in Figure 4A. Figure 4B present results of the semi-automatic MSI method. R^2 value of exponential trendline for manual LDI method was 0.993, and that for automated MSI was 0.988. This is the only case where the trendline fit was better for the LDI-MS method. On the contrary, the R^2 value for the MSI was almost 0.99 at a 1000-fold dilution of the sample. The LOD was found to be 405 pg (1.35 pmol) for LDI-MS and 516 pg (1.72 pmol) of 3-hydroxyoctadecanoic acid per measured spot. During the LC–MS analysis, the LOD value was 0.7 ng/mL for this acid.[9]

The use of MSI for the quantification of 3-hydroxycarboxylic acids enabled us to obtain a better fit of the experiment results than manual LDI-MS method with R^2 ca. 0.98 for five analyzed acids, and only for 3-hydroxyoctadecanoic acid the trendline fit was lower for MSI than for LDI-MS and still was above 0.98. These analyses clearly indicate the usefulness of MSI for quantitative analysis of these acids. It should be noted that the regressions were performed over a very wide concentration range, from 1000 for 3-hydroxydecanoic, 3-hydroxytetradecanoic and 3-hydroxyoctadecanoic acids to 1 000 000 fold concentration change for 3-hydroxydodecanoic acid.

The analyses presented in this publication lead to the conclusion that MSI allows for quantitative analyses. During the measurement, the entire sample spot was covered with a grid or raster of measurement points with a defined resolution. The MSI analysis can be applied to mainly detect signals of 3-hydroxycarboxylic acid-silver-109 adducts at various concentrations. The mass spectra also presented sodium and potassium adducts of the tested acids, but the sum of the intensities of these signals did not exceed 10% of the signal intensity of the silver-109 adduct. In most cases the results obtained using MSI had a better trendline fit compared to manual measurements and yielded an R^2 value 0.98 for most of the analyzed acids. As can be seen on Figures 1D, 2C, 2D, 3C, 3D, and 4B ion images prove that studied sample was deposited nonuniformly in all studied sample spots. By covering the entire surface of the spot with the sample, it is possible to better match the trendline to the obtained results. In the case of manual measurements, there is a high probability of selecting a point where the concentration of the sample

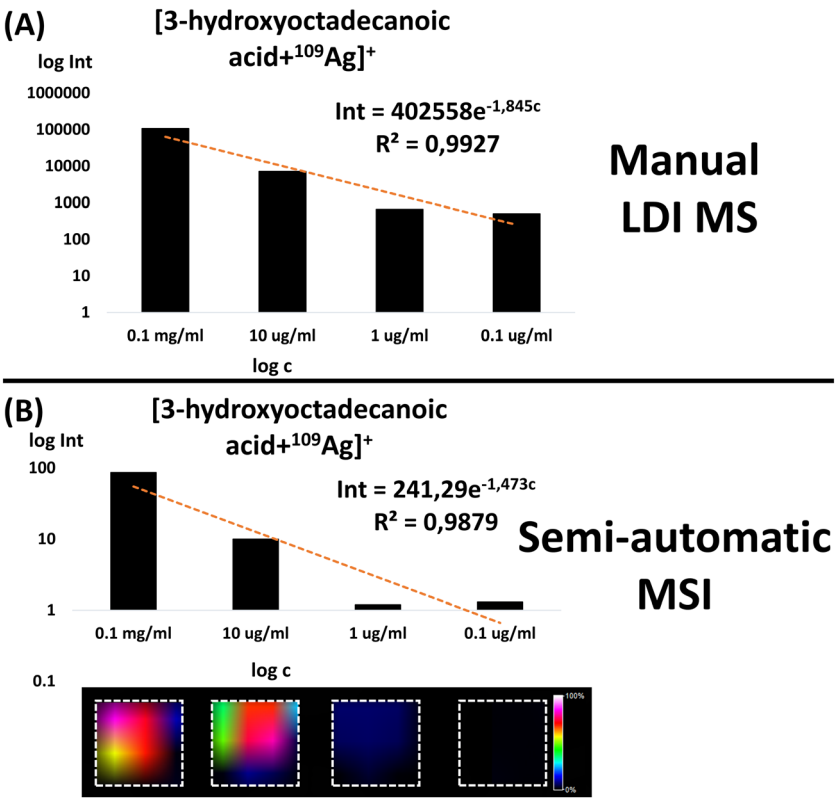

FIGURE 4 Column charts A and B present results of quantification based on silver-109 adduct signal of 3-hydroxyoctadecanoic acid for different concentrations obtained in laser desorption/ionization-mass spectrometry (LDI-MS) and mass spectrometry imaging (MSI) experiments. Both panels (A, B) contain the equations and the R^2 values for exponential trendline. Panel B also contains ion [C18H36O3 + 109Ag] + images for each concentration [Color figure can be viewed at wileyonlinelibrary.com]

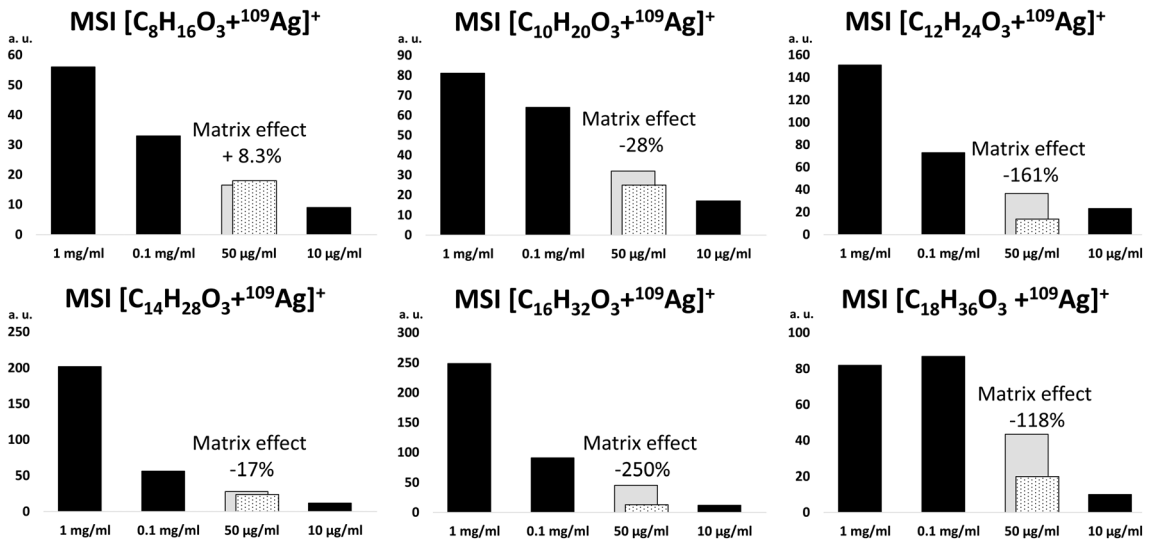

FIGURE 5 Results of quantitative analysis of selected 3-hydroxycarboxylic acids in human blood serum by semi-automatic mass spectrometry imaging (MSI) with monoisotopic silver-109 NPs PFL 2D GS LGN. For concentration 50 µg/mL theoretical intensity of signal was calculated (gray bar) and compared with the experimental intensity of signal of analyzed acid in human blood serum spiked with carboxylic acid (white bar with dots). Intensity of signals for water solutions of carboxylic acid standards 1 mg/mL, 0.1 mg/mL, and 10 µg/mL was also presented (black bars)

is higher or lower than the average concentration of the sample over the entire surface, and this is a common problem in MALDI-MS method. LOD values obtained in manual LDI-MS and semi-automatic MSI methods were worse than the values obtained during LC–MS analysis; however, the advantages of these methods are (a) the possibility of obtaining ion images (which is impossible with normal HPLC-MS analysis), (b) very easy sample preparation (usually it involves only diluting the sample in a suitable solvent and applying the solution to the steel plate), and (c) short analysis time (for manual measurement it is about seconds, and for semi-automatic MSI one sample measurement takes from a few seconds to several minutes). All the advantages presented above also apply to the GC–MS method, and additionally there is no need to perform derivatization, which allows unmodified samples to be tested.

3.2 | Detection of 3-hydroxycarboxylic acids in human blood serum

The results presented in the previous section were used to analyze the effects of suppression of the biological matrix. For this purpose, a spiked human blood serum sample was prepared. A 500-fold dilution of blood serum in distilled water was prepared, then the same volume of 100 µg/mL of carboxylic acid solution was added. The final concentration of the analyzed acids in spiked blood serum suspension was ca. 50 µg/mL. The highest intensity signals found in the spectra belonged to the 3-hydroxycarboxylic acid silver-109 adducts.

Figure 5 summarizes the results of this analysis. Theoretical intensity for 50 µg/mL of carboxylic acid solution was calculated based on intensity value of 0.1 mg/mL sample. Theoretical intensity values were compared with experimental data obtained for diluted human blood serum spiked with carboxylic acids. For 3-hydroxyoctanoic, 3-hydroxydecanoic, and 3-hydroxytetradecanoic acids matrix effect was +8.3%, −28%, and −17%, respectively. In the case of these three acids, no significant matrix effect on the measurement result was noticed. However, for 3-hydroxydodecanoic, 3-hydroxyhexadecanoic and 3-hydroxyoctadecanoic acids the matrix effect was −161%, −250%, and −118%, respectively. The results presented in this study show that the biological matrix (in this example, human blood serum) for these three acids causes a significant reduction in signal intensity compared to the predicted value, clearly indicating the presence of a matrix suppression effect. Due to the high content of lipid compounds in the blood serum, the matrix suppression effect may arise, which in turn causes a significant reduction in the intensity of the signals of the tested 3-hydroxycarboxylic acids.

4 | CONCLUSION

The application of stainless steel plates coated with silver-109 NPs synthesized by the new PFL 2D GS LGN method for the analysis of 3-hydroxycarboxylic acids was presented. ^{109}AgNPs ionize and allow for analysis using laser MS of 3-hydroxycarboxylic acids in a very wide range of concentrations, even up to 10 ng/mL (for 3-hydroxydodecanoic acid). Two measurement methods were compared: manual LDI-MS and semi-automatic MSI; the presented results of regression analyses prove the possibility of using MSI for quantitative analyses. The use of laser MS for the quantification of 3-hydroxycarboxylic acids was demonstrated for the first time. The results obtained during the experiments show that laser MS can be used to determine the concentration of endotoxins in the samples. Ion images obtained in MSI experiments proved highly nonuniform analyte deposition that makes semi-automatic, multi-pixel MSI a

modern requirement rather than improvement. The biological matrix has a significant effect on the intensity value of some of the analyzed 3-hydroxycarboxylic acids in MSI.

ACKNOWLEDGMENTS

This work was supported by the Narodowe Centrum Nauki (NCN), SONATA grant no. UMO-2018/31/D/ST4/00109.

PEER REVIEW

The peer review history for this article is available at https://publons.com/publon/10.1002/rcm.9375.

DATA AVAILABILITY STATEMENT

The data that support the findings of this study are available from the corresponding author upon reasonable request.

ORCID

Artur Kołodziej https://orcid.org/0000-0002-9222-0937

REFERENCES

1. Tanaka K, Waki H, Ido Y, et al. Protein and polymer analyses up to m/z 100 000 by laser ionization time-of-flight mass spectrometry. *Rapid Commun Mass Spectrom*. 1988;2(8):151-153. doi:10.1002/rcm.1290020802
2. Greco V, Piras C, Pieroni L, et al. Applications of MALDI-TOF mass spectrometry in clinical proteomics. *Expert Rev Proteomics*. 2018;15(8):683-696. doi:10.1080/14789450.2018.1505510
3. Topić Popović N, Kazazić SP, Bojanić K, Strunjak-Perović I, Čož-Rakovac R. Sample preparation and culture condition effects on MALDI-TOF MS identification of bacteria: A review. *Mass Spectrom Rev*. Published online October 13. 2021;mas.21739. doi:10.1002/mas.21739
4. Guo S, Li K, Chen Y, Li B. Unraveling the drug distribution in brain enabled by MALDI MS imaging with laser-assisted chemical transfer. *Acta Pharm Sin B* Published Online November 16. 2021. doi:10.1016/j.apsb.2021.11.007
5. Sekuła J, Nizioł J, Rode W, Ruman T. Gold nanoparticle-enhanced target (AuNPET) as universal solution for laser desorption/ionization mass spectrometry analysis and imaging of low molecular weight compounds. *Anal Chim Acta*. 2015;875:61-72. doi:10.1016/j.aca.2015.01.046
6. Nizioł J, Rode W, Laskowska B, Ruman T. Novel monoisotopic ^{109}AgNPET for laser desorption/ionization mass spectrometry. *Anal Chem*. 2013;85(3):1926-1931. doi:10.1021/ac303770y
7. Płaza A, Kołodziej A, Nizioł J, Ruman T. Laser ablation synthesis in solution and nebulization of Silver-109 nanoparticles for mass spectrometry and mass spectrometry imaging. *ACS Meas Au* Published Online August 25. 2021. doi:10.1021/acsmeasuresciau.1c00020
8. Steimle A, Autenrieth IB, Frick JS. Structure and function: Lipid a modifications in commensals and pathogens. *Int J Med Microbiol*. 2016;306(5):290-301. doi:10.1016/j.ijmm.2016.03.001
9. Uhlig S, Negård M, Heldal KK, et al. Profiling of 3-hydroxy fatty acids as environmental markers of endotoxin using liquid chromatography coupled to tandem mass spectrometry. *J Chromatogr A*. 2016;1434:119-126. doi:10.1016/j.chroma.2016.01.038
10. Reynolds SJ, Milton DK, Heederik D, et al. Interlaboratory evaluation of endotoxin analyses in agricultural dusts—Comparison of LAL assay and mass spectrometry. *J Environ Monit*. 2005;7(12):1371-1377. doi:10.1039/B509256F
11. Mielniczuk Z, Mielniczuk E, Larsson L. Gas chromatography-mass spectrometry methods for analysis of 2- and 3-hydroxylated fatty acids: Application for endotoxin measurement. *J Microbiol Methods*. 1993;17(2):91-102. doi:10.1016/0167-7012(93)90002-Y
12. Shende N, Karale A, Marne K, et al. Quantitation of endotoxin by gas chromatography-mass spectrometry in Neisseria meningitidis serogroups a, C, W, Y and X during polysaccharide purification used in conjugate vaccine. *J Pharm Biomed Anal*. 2022;209:114536. doi:10.1016/j.jpba.2021.114536
13. Zamani M, Pourmadadi M, Seyyed Ebrahimi SA, Yazdian F, Shabani SJ. A novel labeled and label-free dual electrochemical detection of endotoxin based on aptamer-conjugated magnetic reduced graphene oxide-gold nanocomposite. *J Electroanal Chem*. 2022;908:116116. doi:10.1016/j.jelechem.2022.116116
14. Mu Z, Tian J, Wang J, Zhou J, Bai L. A new electrochemical aptasensor for ultrasensitive detection of endotoxin using Fe-MOF and AgNPs decorated P-N-CNTs as signal enhanced indicator. *Appl Surf Sci*. 2022;573:151601. doi:10.1016/j.apsusc.2021.151601
15. Zandieh M, Hosseini SN, Vossoughi M, Khatami M, Abbasian S, Moshaii A. Label-free and simple detection of endotoxins using a sensitive LSPR biosensor based on silver nanocolumns. *Anal Biochem*. 2018;548:96-101. doi:10.1016/j.ab.2018.02.023
16. Kołodziej A, Ruman T, Nizioł J. Gold and silver nanoparticles-based laser desorption/ionization mass spectrometry method for detection and quantification of carboxylic acids. *J Mass Spectrom*. 2020;55(10):e4604. doi:10.1002/jms.4604
17. Arendowski A, Nizioł J, Ruman T. Silver-109-based laser desorption/ionization mass spectrometry method for detection and quantification of amino acids. *J Mass Spectrom*. 2018;53(4):369-378. doi:10.1002/jms.4068
18. Szulc J, Kołodziej A, Ruman T. Silver-109/silver/gold nanoparticle-enhanced target surface-assisted laser desorption/ionisation mass spectrometry—The new methods for an assessment of mycotoxin concentration on building materials. *Toxins*. 2021;13(1):45. doi:10.3390/toxins13010045
19. Nizioł J, Rode W, Zieliński Z, Ruman T. Matrix-free laser desorption–ionization with silver nanoparticle-enhanced steel targets. *Int J Mass Spectrom*. 2013;335:22-32. doi:10.1016/j.ijms.2012.10.009
20. Arendowski A, Nizioł J, Ossoliński K, et al. Laser desorption/ionization MS imaging of cancer kidney tissue on silver nanoparticle-enhanced target. *Bioanalysis*. 2018;10(2):83-94. doi:10.4155/bio-2017-0195
21. Sherrod SD, Diaz AJ, Russell WK, Cremer PS, Russell DH. Silver nanoparticles as selective ionization probes for analysis of olefins by mass spectrometry. *Anal Chem*. 2008;80(17):6796-6799. doi:10.1021/ac800904g
22. Jones PM, Quinn R, Fennessey PV, et al. Improved stable isotope dilution-gas chromatography-mass spectrometry method for serum or plasma free 3-Hydroxy-fatty acids and its utility for the study of disorders of mitochondrial fatty acid β-oxidation. *Clin Chem*. 2000;46(2):149-155. doi:10.1093/clinchem/46.2.149

SUPPORTING INFORMATION

Additional supporting information can be found online in the Supporting Information section at the end of this article.

How to cite this article: Kołodziej A, Płaza-Altamer A, Nizioł J, Ruman T. Infrared pulsed fiber laser-produced silver-109 nanoparticles for laser desorption/ionization mass spectrometry of 3-hydroxycarboxylic acids. *Rapid Commun Mass Spectrom*. 2022;36(21):e9375. doi:10.1002/rcm.9375

Advances in Medical Sciences 68 (2023) 38–45

Contents lists available at ScienceDirect

Advances in Medical Sciences

journal homepage: www.elsevier.com/locate/advms

Monoisotopic silver nanoparticles-based mass spectrometry imaging of human bladder cancer tissue: Biomarker discovery

Krzysztof Ossoliński [a], Tomasz Ruman [b], Tadeusz Ossoliński [a], Anna Ossolińska [a], Adrian Arendowski [b], Artur Kołodziej [b,c], Aneta Płaza-Altamer [b,c], Joanna Nizioł [b,*]

[a] Department of Urology, John Paul II Hospital, Kolbuszowa, Poland
[b] Rzeszów University of Technology, Faculty of Chemistry, Rzeszów, Poland
[c] Doctoral School of Engineering and Technical Sciences at the Rzeszów University of Technology, Rzeszów, Poland

ARTICLE INFO

Keywords:
Silver nanoparticles
LDI-MS
Biomarkers
Bladder cancer
Human tumor tissue

ABSTRACT

Purpose: Bladder cancer (BC) is the 10th most common form of cancer worldwide and the 2nd most common cancer of the urinary tract after prostate cancer, taking into account both incidence and prevalence.
Materials/methods: Tissues from patients with BC and also tissue extracts were analyzed by laser desorption/ionization mass spectrometry imaging (LDI-MSI) with monoisotopic silver-109 nanoparticles-enhanced target (^{109}AgNPET).
Results: Univariate and multivariate statistical analyses revealed 10 metabolites that differentiated between tumor and normal tissues from six patients with diagnosed BC. Selected metabolites are discussed in detail in relation to their mass spectrometry (MS) imaging results. The pathway analysis enabled us to link these compounds with 17 metabolic pathways.
Conclusions: According to receiver operating characteristic (ROC) analysis of biomarkers, 10 known metabolites were identified as the new potential biomarkers with areas under the curve (AUC) higher than >0.99. In both univariate and multivariate analysis, it was predicted that these compounds could serve as useful discriminators of cancerous versus normal tissue in patients diagnosed with BC.

1. Introduction

Bladder cancer (BC) is the 12th most common form of cancer worldwide and the 2nd most common cancer of the urinary tract after prostate cancer, taking into account both incidence and prevalence [1]. Globally, 573,278 new cases of BC were diagnosed in 2020. In terms of incidence, it is the 6th most common cancer in men, the 17th in women and the 10th most frequent cancer in both sexes [1]. Cystoscopic examination of bladder remains the gold standard for BC diagnosis, but it is invasive, associated with discomfort, sometimes painful and costly. It is estimated that 4–27% of tumors are omitted during the examination. This value increases to 32–77% in the case of carcinoma *in situ* (CIS) [2].

In recent years, numerous urine-based BC biomarkers have been evaluated but currently there is no reliable diagnostic and prognostic BC biomarker that has been accepted for diagnosis and follow-up in routine practice or clinical guidelines and which could be an alternative to cystoscopy. Over the past decade, due to the molecular specificity and sensitivity mass spectrometry (MS) has been used as a main technique in biomarker discovery field [3]. Two-dimensional variety of MS – mass spectrometry imaging (MSI) plays an increasingly important role in the field of molecular imaging because it allows direct mapping of the distribution of a variety of endogenous and exogenous compounds within biological tissues with high specificity and without the need for radioactive or fluorescent radioactive labelling normally used in histochemical protocols [4]. BC tissues were studied previously with MSI techniques such as matrix-assisted laser desorption ionization (MALDI) [5] and desorption electrospray ionization (DESI) [6]. It should be noted that there are no BC MS and MSI results made with the use of nanoparticle-based methods published to date. It is important to state that nanoparticle-based methods have many advantages with regard to other methods including very efficient cationization of low molecular weight compounds, relatively high sensitivity of analyte detection, very low chemical background and high mass accuracy due to internal calibration, unlike commonly used one - MALDI. They allow for higher lateral resolutions and higher sensitivity when compared to DESI. In our recent publications we presented new methods such as gold nanoparticle-enhanced target (AuNPET) [7], silver

* Corresponding author. University of Technology, Faculty of Chemistry, 6 Powstańców Warszawy Ave., 35-959, Rzeszów, Poland.
E-mail address: jniziol@prz.edu.pl (J. Nizioł).

https://doi.org/10.1016/j.advms.2022.12.002
Received 21 May 2022; Received in revised form 5 September 2022; Accepted 8 December 2022

nanoparticle-enhanced target (AgNPET) [8] and monoisotopic silver-109 nanoparticles-enhanced target (^{109}AgNPET) [9] with results of their application for imaging of plant, animal and human tissues [10–12].

2. Materials and methods

2.1. Participants

Cancer and normal tissue samples were collected from 6 patients (Caucasian race, average age 65 years, 2 females and 4 males) with diagnosed BC at John Paul II Hospital in Kolbuszowa (Poland). All patients underwent transurethral resection of bladder tumor (TURBT) following a detailed clinical history and laboratory examination. Each of these patients had at least an abdominal ultrasound to exclude other tumors (patients with urolithiasis usually also had a CT scan) and a basic package of laboratory tests required for urological surgery to exclude inflammation. Whole tumor and a small fragment of adjacent healthy uroephitelium were resected (cancer and control tissue). The histopathological analysis of resected tumors from all patients, confirmed non-invasive (pTa) low-grade (LG) urothelial papillary carcinoma, according to 2004 WHO grading system [13,14]. Control tissues were free of cancer cells. The clinical characteristics of the patients are presented in Supplementary Table S1.

2.2. Materials and equipment

Silver-109 (min. 99.75% of ^{109}Ag) isotope was purchased from BuyIsotope (Neonest AB, Stockholm, Sweden) and transformed to trifluoroacetate salt by commonly known methods (involving dissolving in HNO_3, precipitation of ^{109}AgOH and reaction with trifluoroacetic acid) and recrystallized from tetrahydrofurane/hexane system. 2,5-Dihydroxybenzoic acid (DHB) was purchased from Sigma-Aldrich (St. Louis, USA). Steel targets were locally machined from H17 stainless steel. All solvents were of high-performance liquid chromatography (HPLC) quality, except for water (18 MΩ water was produced locally) and methanol (liquid chromatography-mass spectrometry - LC MS - grade, Fluka™, (Seelze, Germany). The silver-109 nanoparticles were synthesized on the surface of steel targets as described in our recent publication [9]. Optical photographs of tissue samples were made with the use of an Olympus SZ10 microscope equipped with an 8 MPix Olympus digital camera (Hamburg, Germany).

2.3. Preparation of monoisotopic silver suspension

Four miligrams of silver-109 trifluoroacetate (^{109}AgTFA) and 14 mg of DHB were quantitatively transferred to a glass tube by dissolving in 2 ml of isopropanol and 2 ml of acetonitrile. The prepared solution was placed in an ultrasonic bath set at 50 °C for about 30 min. After this time, the suspension was ready to use.

2.4. Imaging sample preparation

Tissues from 6 patients with the same tumor stage and grade were selected for LDI-MSI analysis. Three independent imaging experiments were performed to exclude possible random results, one for tissues from patient no. 1, another for patients no. 2–4 and the last for patients no. 5 and 6. The material examined was six pairs of BC and normal tissue fragments of average 3 × 3 mm size. MS imaging for patient no. 1 was carried out within about an hour after the material was collected after surgery. Until then, the tissue samples were stored at a temperature of approx. 2–4 °C. Tissues from patients no. 2–6 were stored at −60 °C and thawed to 4 °C before the MSI measurements. To remove excess liquid material, samples were touched to cellulose filter paper (3 times). Next, with the use of sterile needles and tweezers, a few imprints of the examined tissues were made on the previously prepared ^{109}AgNPET plate. The material was transferred from the BC patients to the ^{109}AgNPET substrate by briefly touching (3 s) the tissue samples to steel surface with light pressure. Steel target with imprints was placed on a computer-controlled 3D positioning table and sprayed with nanoparticles using an electrospray ionization mass spectrometry (ESI-MS) nebulizer with nitrogen as nebulizing gas (2 bar). Target was placed in a MALDI time-of-flight MS (MALDI-ToF/ToF MS) (Autoflex Speed ToF/ToF, Bruker, Bremen, Germany) and selected imprints were then directly analyzed.

2.5. LDI-MS imaging experiments

LDI-MSI experiments were performed using a Bruker Autoflex Speed ToF/ToF mass spectrometer (MALDI ToF/ToF, Bruker, Bremen, Germany) in positive-ion reflectron mode. FlexImaging 4.0 software was used for data processing and analysis. The apparatus was equipped with a SmartBeam II 1000 Hz 355 nm laser. Laser impulse energy was approximately 100–190 μJ, laser repetition rate was 1000 Hz, and deflection was set on *m/z* lower than 80 Da. The *m/z* range was 80−2000 Da, spatial resolution 250 × 250 μm. The experiments were made with 20,000 laser shots per individual spot with a default random walk applied (random points with 50 laser shots). All spectra were calibrated with the use of silver ions ($^{109}Ag^+$ to $^{109}Ag_{10}^+$). The first accelerating voltage was held at 19 kV, and the second ion source voltage was held at 16.7 kV. Reflector voltages used were 21 kV (the first) and 9.55 kV (the second). All of the ion images were within ±0.05% of *m/z*. Total ion current (TIC) normalization was used for all results shown.

2.6. Preparation of tissue extracts

Small portions of frozen neoplastic bladder tissue (n = 6) and normal control tissues (n = 6) of approximately 2 mg each were transferred to Eppendorf tubes and then homogenized by three cycles of freezing and thawing. Next to the homogenates 500 μl of 2:1 (v/v) chloroform/methanol were added and then extracted for 30 min in ultrasonic bath (at 2–4 °C.) The tubes were centrifuged for 5 min at an acceleration of 6000×*g* and the phases were allowed to separate. The water-methanol and methanol-chloroform phases were transferred to separate tubes and then methanol-chloroform phases were diluted 100x whereas the water-methanol phases were measured without dilution. Volume of 0.3 μl of each sample was placed on ^{109}AgNPET and allowed to dry at room temperature and target placed in a MALDI ToF/ToF MS. Tissue extracts were made to confirm the structure of the identified compounds by MS/MS measurements.

2.7. LDI-MS and MS/MS of tissue extracts

LDI-MSI experiments were performed using a Bruker Autoflex Speed MALDI ToF/ToF MS (Autoflex Speed ToF/ToF, Bruker, Bremen, Germany) in positive-ion reflectron mode. The apparatus was equipped with a SmartBeam II 1000 Hz 355 nm laser. Laser impulse energy was approximately 100–190 μJ, laser repetition rate was 1000 Hz, and deflection was set on *m/z* lower than 80 Da. The *m/z* range was 80−2000 Da. Spectrum for each extract contained data from 20k laser shots with a default random walk applied (random points with 50 laser shots). All spectra were calibrated with the use of silver ions ($^{109}Ag^+$ to $^{109}Ag_{10}^+$). The first accelerating voltage was held at 19 kV, and the second ion source voltage was held at 16.7 kV. Reflector voltages used were 21 kV (the first) and 9.55 kV (the second). MS/MS measurements were performed using the LIFT (low mass) method [15]. The mass window for precursor ion selection used was ±0 Da. FlexAnalysis (version 4.0, Bruker, Bremen, Germany) was used for data analysis.

2.8. Data processing

The average spectra of the imprint area of cancerous and normal tissue from patient no. 1 were generated and then compared in the using

the SCiLS Lab software version 2016b (SCiLS, Bremen, Germany) and FlexAnalysis (version 4.0, Bruker, Bremen, Germany). Statistical analysis was performed using the Cardinal MSI (R package) [16] with hotspot suppression and Gaussian smoothing applied and MetaboAnalyst 5.0 platform [17]. Database search of chemical compounds were carried out using a custom-made program. Theoretical *m/z* values were calculated using ChemCalc program available online [18].

Data of peak mean abundance from the entire area of the examined cancer (n = 6) and control (n = 6) tissue were formatted as comma separated values (.csv) files and uploaded to the MetaboAnalyst 5.0 server [17]. Metabolite data was checked for data integrity and normalized using MetaboAnalyst's normalization protocols (normalization by sum, log transformation and auto-scaling), both for biomarker and pathway analyses. Univariate analysis (*t*-test), fold-change analysis and orthogonal partial least squares discriminant analysis (OPLS-DA) were applied to calculate the statistical significance of the metabolites between the two groups (cancer over control). To identify the potential biomarkers associated with BC, the Receiver Operating Characteristic (ROC) curve was applied using biomarker analysis module of MetaboAnalyst v 5.0. The ROC curves were generated using an algorithm based on Monte-Carlo cross validation (MCCV) through balanced subsampling coupled with linear support vector machine (SVM) for the classification method and SVM built-in for the feature ranking method. To identify the most relevant metabolic pathways involved in BC, metabolic pathway analysis was performed using MetaboAnalyst with *Homo sapiens* pathway libraries.

3. Ethical issues

The study protocol was approved by local Bioethics Committee at the University of Rzeszow, Poland (permission no. 2018/04/10) and performed in accordance with relevant guidelines and regulations, including the 1964 Helsinki declaration and its later amendments. Specimens and clinical data from patients involved in the study were collected with written consent.

4. Results and discussion

^{109}AgNPET method was used previously for LDI-MS analysis of low molecular weight (LMW) compounds and biological material and was shown to be a promising alternative to traditional MALDI method [9,19]. LDI-MSI experiments were performed by measuring series of high-resolution MS spectra with 250 × 250 μm resolution of bladder tissue imprints of *ca.* 3 × 3 mm size made on ^{109}AgNPET target plate. In order to estimate whether there is a sample-related differentiation between cancer and normal tissue imprints, a statistical analysis was performed for patient no. 1 tissue pair. Data derived from MSI experiment were analyzed by comparison of average spectra of cancer and normal areas by spatial shrunken centroids with adaptive weights (SSCA). The mentioned method allows estimation of the probability that a location of interest belongs to a particular segment and was previously used among others for segmentation of data for whole-body MALDI MSI experiment [20]. Images of the major regions of the BC tissue from patient no. 1 were outlined by SSCA segmentation as shown in Supplementary Fig. S1. What is interesting, images generated with the aid of Cardinal MSI with SSCA method are very similar to the ion images obtained in MSI experiment and suggest that: (i) areas of imprints are clearly different from target area with no fuzzy boundaries and (ii) cancerous area is clearly different from the normal one.

4.1. Identification of metabolite biomarkers

The analysis of MSI data revealed a list of 28 compounds for which the highest abundance differences between the normal and cancerous areas. Only those ion images were selected for which the trend for a given *m/z* value was similar in all 6 experiments. As judged from generated ion images 2 adducts have higher average intensities in cancer tissue, and the next 26 ions are of higher intensity in normal tissue. The list of identified compounds is presented in Supplementary Table S2. The identity of some of compounds was confirmed with LIFT® MS/MS experiments (Supplementary Table S3). Metabolite mean abundance data from both cancer and normal tissue regions of 28 identified compounds were further subjected to supervised and unsupervised multivariate statistical analysis using the MetaboAnalyst 5.0 online software. The 2D principal components analysis (PCA) score plots of both subsets indicated good separation between the cancer and the normal tissue regions (Fig. 1A).

The best separation of groups was obtained along principal components 1 and 2 (i.e. PC1 and PC2) which accounted for 61.2% and 18.8%, respectively. The separation between the BC and normal tissue samples was further examined using the supervised multivariate statistical analysis - Orthogonal Partial Least Squares Discriminant Analysis (OPLS-DA) (Fig. 1B). We conducted 2000 permutation tests to evaluate the statistical robustness of the OPLS-DA model (Supplementary Fig. S2). Good discrimination was observed between cancer and normal groups (Q^2 = 0.774, R^2Y = 0.998, *P*-value <0.03 (0/2000)). Potential BC biomarkers were selected on the basis of the variable influence on projection (VIP) value resulting from the OPLS-DA model (Fig. 1C). By combining the VIP (>1.0) with the results from the independent *t*-test (P-value from *t*-test <0.05) and fold change analysis (0.5 < FC > 1.2) 10 metabolites were selected as differential for BC tissue and normal samples (Table 1). All data for identified compounds analyzed within this work are presented in Supplementary Table S2.

Next, univariate ROC curve analysis was separately performed to evaluate the diagnostic ability of the models. ROC curves analyses were used to estimate the accuracy of combined signatures model of imaging data. The areas under curves (AUC) of ROC curves were used to determine the diagnostic effectiveness of important metabolites. Applying a ROC approach to biomarker analysis allowed characterization of diagnostic accuracy, and evaluation of the predictive accuracy. The results indicated that all previously selected metabolites have AUC above 0.81 (Table 1). The best ROC analyses with the highest statistical significance were obtained for hypotaurine and 3-methylbutanal (AUC = 0.944, specificity = 1.0 and sensitivity = 0.8). The classification ROC model was based on a random forest algorithm. As shown in Fig. 1D, the combination of levels of 10 selected metabolites was a better discriminator (AUC = 0.993) than each metabolite separately. The results suggest that 10 specific metabolites: glycine, hypotaurine, 3-methylbutanal, ethylphosphate, glutamine, myosmine, PI(22:0/0:0), aminopentanal, proline betaine and methylguanidine coul, significantly increase the diagnostic potential and serve as useful discriminators of cancer tissues from normal tissues in patients diagnosed with BC. Ion images of all these compounds that differentiate the neoplastic and normal area to the greatest extent are presented in Figs. 2 and 3.

Ion images of 2 amino acids that play essential roles in human tissues were generated and the structure of one of them was confirmed with LIFT MS/MS method. One of the ion images of *m/z* 98.021 (Fig. 2 A) shows spatial distribution of the $[C_2H_5NO_2+Na]^+$ adduct (sodiated glycine). This ion was found to be present at a higher intensity in the normal tissue compared with the cancer tissue. The decreased levels of glycine were observed in lung cancer patients [21] and in serum of BC patients [22]. Similarly, ion assigned to potassium adduct of glutamine (*m/z* 185.032, Fig. 2 E) was found at a higher intensity in the normal tissue compared to the cancer tissue. NMR-based metabolomics studies have shown the decreased blood levels of glutamine in plasma samples from pancreatic cancer patients [23]. The decrease in the levels of the amino acids discussed above indicates an increased demand for these metabolites for tumor growth. This observation suggests that tumor's biochemistry may be associated with an increased glycolytic flux that has been found to be a major source of respiratory energy for tumor cells, and with the need for increased protein synthesis in tumor cells [24]. It has also been suggested that glycolysis is required to maintain lipogenesis and cholesterogenesis, that are essential for the growth and proliferation of tumor cells [25].

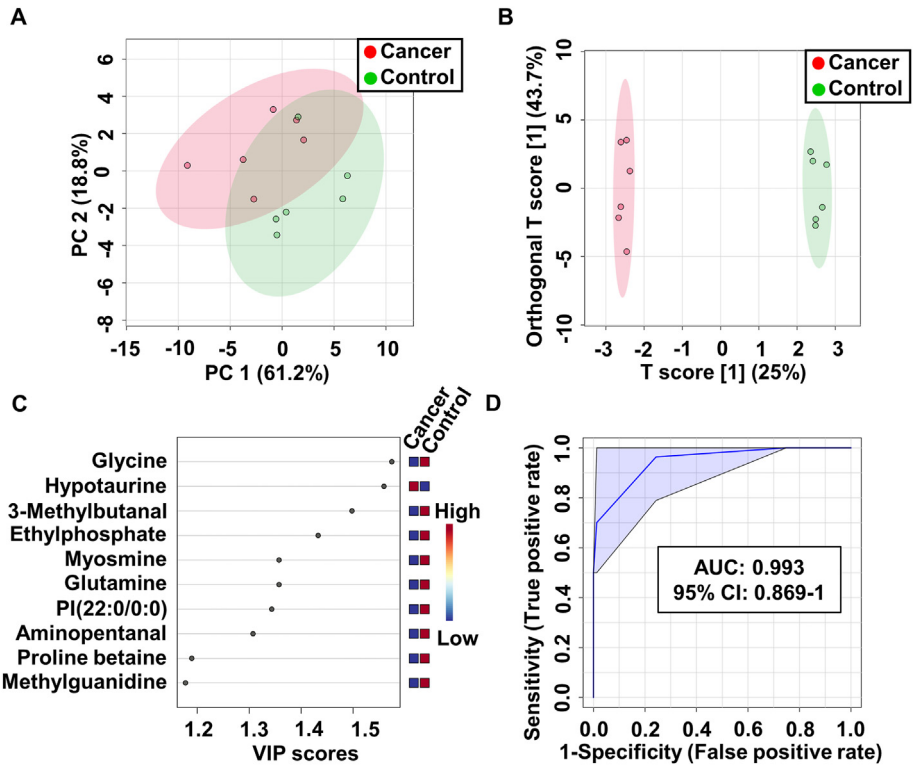

Fig. 1. Metabolomic analysis of tissue samples from bladder cancer (BC) patients. **(A)** PCA and **(B)** OPLS-DA scores plots of the cancer (red) and control (green) tissue samples. **(C)** VIP plot from OPLS-DA analysis. **(D)** The receiving operator characteristic (ROC) curves for the 10 selected metabolites.

Table 1
Mean metabolite abundance for controls vs. bladder cancer tissues. Bolded metabolites are considered statistically significantly different (P-value <0.05; VIP >1; FC < 0.5 and >1.2) between controls and cancer tissues.

No.	Compound name	Addut type	*m/z*[c]	*P*-value[d]	Fold Change[e]	VIP[f]	AUC	Power of the test	
								Sensitivity [%]	Specificity [%]
1	Glycine[a]	$[C_2H_5NO_2+Na]+$	98.021	0.0025	0.30	1.56	0.92	100	83
2	Hypotaurine[a]	$[C_2H_7NO_2S+^{109}Ag]^+$	217.924	0.0035	1.39	1.54	0.94	83	100
3	3-Methylbutanal[a]	$[C_5H_{10}O + H]^+$	87.080	0.0053	0.19	1.47	0.94	83	100
4	Ethylphosphate[a]	$[C_2H_7O_4P + K]^+$	164.971	0.0088	0.30	1.41	0.92	83	83
5	Glutamine[b]	$[C_5H_{10}N_2O_3+K]^+$	185.032	0.0147	0.29	1.35	0.92	83	83
6	Myosmine[b]	$[C_9H_{10}N_2+H]^+$	147.092	0.0147	0.29	1.35	0.92	83	83
7	PI(22:0/0:0)[a]	$[C_{31}H_{61}O_{12}P+^{109}Ag]^+$	765.294	0.0171	0.19	1.32	0.92	100	83
8	Aminopentanal[b]	$[C_5H_{11}NO + H]^+$	102.091	0.0214	0.39	1.29	0.83	100	67
9	Proline betaine[a]	$[C_7H_{13}NO_2+Na]^+$	166.084	0.0417	0.44	1.17	0.83	100	67
10	Methylguanidine[a]	$[C_2H_7N_3+Na]^+$	96.053	0.0451	0.45	1.16	0.81	67	83

Abbreviations: AUC - area under the curve; FC - fold change; PI - phosphatydylinositol; PS – phosphatidylserine; VIP - variable influence on projection.
[a] Putative identification.
[b] Identity confirmed with LIFT MS/MS method.
[c] Calculated *m/z* values.
[d] P-value determined from Student's t-test.
[e] Fold change between cancer and control tissue samples.
[f] VIP scores derived from OPLS-DA model.

Moreover, it was found that glycine metabolism is necessary and sufficient for cell transformation and malignancy [26].

In the present study, 11 lipids that play essential roles in the human body showed a large differentiation between neoplastic and normal tissue, and their structures were in some cases successfully confirmed with LIFT MS/MS method (Supplementary Tables S2 and S3). We found, that 5 ions of ^{109}Ag isotope adducts of phosphoglycerol PG(32:1) (*m/z* 829.398), phosphoinositol PI(22:0/0:0) (*m/z* 765.294), phosphoserines PS(*O*-30:1) (*m/z* 800.383), PS(30:1) (*m/z* 814.362), phosphoethanolamine PE(34:4) (*m/z* 820.388), 4 sodium adducts of diacylglyceride DG(44:1) (*m/z* 757.668), phosphocholine PC(40:10) (*m/z* 848.520), phosphoglycerolphosphate PGP(32:1) (*m/z* 801.471), phosphoethanolamine PE(26:1) (*m/z* 628.395), and 2 potassium adducts of phosphoserine PS(36:4) (*m/z* 822.468), sphingomyeline SM(d18:0/12:0) (*m/z* 689.499), dominated in the cancer tissue MSI region compared to normal tissue. However, only 1 lipid - PI(22:0/0:0) showed statistically significant differentiation between normal and neoplastic tissues (Fig. 3A). Lipids are the building blocks of cell membranes and play important roles in various biological processes, such as cellular signaling, chemical-energy storage, homeostasis, apoptosis, metabolism, cell adhesion and migration, neurotransmission, signal transduction, vesicular trafficking, post-translational modifications and cell–cell interactions in tissues. These cellular processes are associated with cellular transformations, cancer progression and metastasis. Lipids are linked to cancer at the metabolic level and are expected to be present in

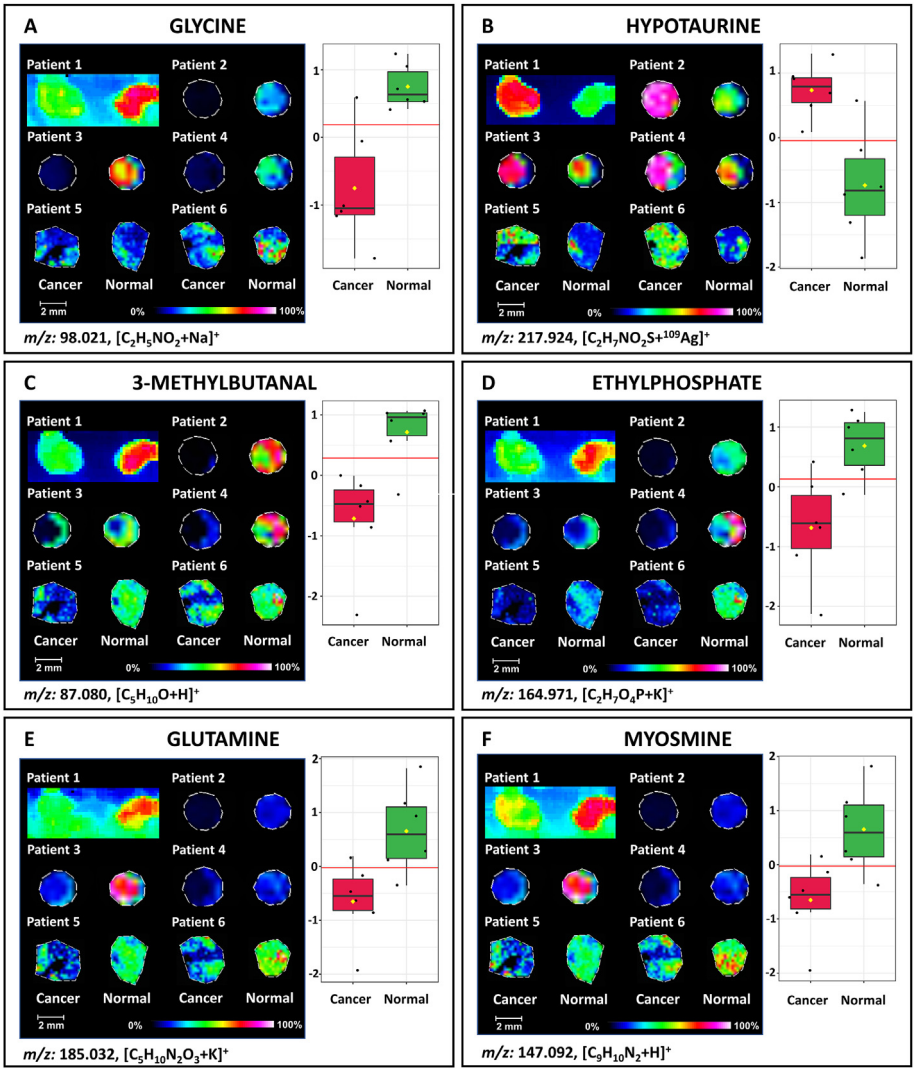

Fig. 2. Results of LDI-MSI analysis of the surface of the bladder cancer (BC) specimens on ^{109}AgNPET. The left sides of the individual metabolite panel **(A–F)** present ion images (TIC normalization) for ions of *m/z* as stated below each image. The right sides contain plots of distribution of abundance values of metabolite in control and cancer samples with optimal cut-off as a horizontal dashed line. All ion images are within ±0.05 *m/z*.

cancer cells, tissues and biofluids. Multiple studies have demonstrated altered lipid profiles in biological samples that have been screened to identify biomarkers in cancer research [27,28]. Several reports have shown the spatial distributions of many potential lipid-based biomarkers in various malignant tumors such as lung [29], breast [30], ovarian [31], colorectal [32], prostate [33], kidney [34], renal [35], bladder [36] and thyroid cancers [37]. Dill et al. [38] demonstrated distributions of the multiple lipids and free fatty acids species between cancerous and noncancerous dog bladder tissue samples with desorption electrospray ionization MS (DESI-MS). The same group of researchers in another study used human BC tissue samples to visualize of glycerophospholipid (GP) distribution in cancerous and normal tissue. They found that tumor tissue shows increased intensities for different GPs such as phosphatidylserine (PS) and phosphatidylinositol (PI) when compared to the normal tissue [36]. Wittman et al. [39], measured multiple distinct compounds in human urine samples, that differentiate BC from non-cancer controls. They selected 25 potential biomarkers related to lipid metabolism.

Ion assigned to proton adduct of 3-methylbutanal (*m/z* 87.080; Fig. 2C) was found in higher intensity in normal tissue compared to cancer tissue. 3-Methylbutanal also known as isovaleraldehyde is an aldehyde that occurs naturally in all eukaryotes. In humans, this compound has been found to be associated with several diseases. Previous research revealed significantly reduced level of 3-methylbutanal in urine samples from patients with clear cell renal cell carcinoma which may be associated with higher level of aldehyde dehydrogenase that converts aldehydes to their respective carboxylic acids and is often upregulated in cancer [40]. Furthermore, in the human lung cancer cell line, 3-methylbutanal was found at decreased concentrations [41].

One of the ion images of *m/z* 166.084 (Fig. 2C) shows spatial distribution of the sodium adduct of proline betaine. This secondary metabolite has been described previously as a highly effective osmoprotectant in many plants. In humans, proline betaine was at reduced levels in plasma samples from patients with esophageal squamous cell carcinoma compared to healthy controls which is also in line with our results [42]. Similar results were obtained in metabolomic analysis of serum samples from patients with preeclampsia [43]. Proline betaine was found to be up-regulated in urine samples from patients with uterine cervix cancer and renal cell carcinoma [44,45].

The MSI results of the bladder tissue imprint suggest, that the ion of *m/z* 96.053 (Fig. 3 D) corresponds to sodiated adduct of methylguanidine which was found in higher abundance in normal tissue. Methylguanidine is an organic compound containing a guanidine moiety in which one of the amino hydrogens is substituted by a methyl group. Endogenous methylguanidine is produced by conversion from creatinine and some

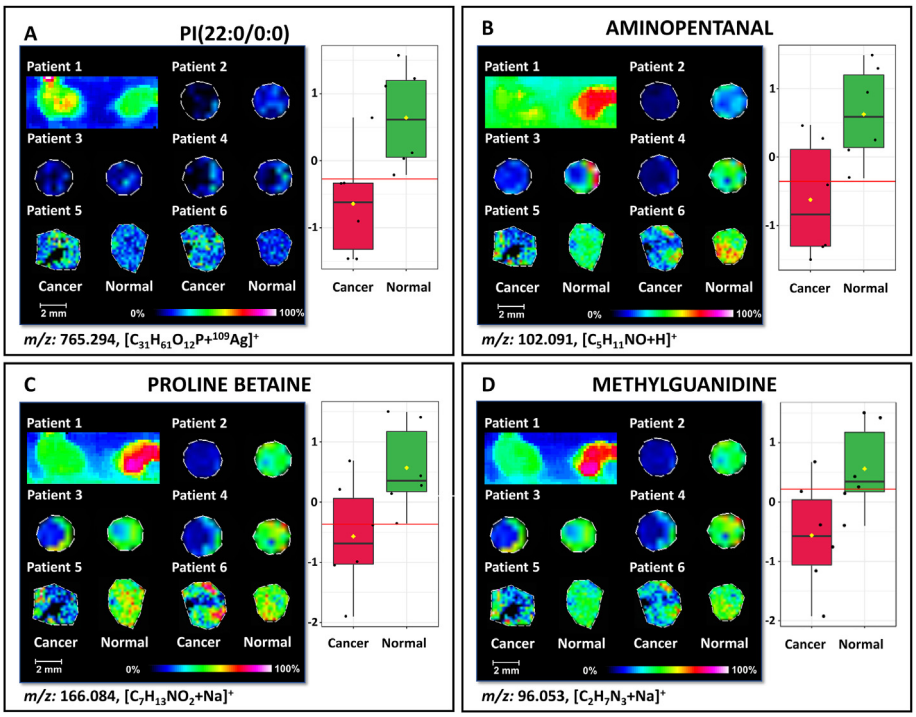

Fig. 3. Results of LDI-MSI analysis of the surface of the bladder cancer (BC) specimens on ^{109}AgNPET. **(A–D)** The left sides of the individual metabolite panel **(A–D)** present ion images (TIC normalization) for ions of *m/z* as stated below each image. The right sides contain plots of distribution of abundance values of metabolite in control and cancer samples with optimal cut-off as a horizontal dashed line. All ion images are within ±0.05 *m/z*.

amino acids [46]. Previous studies reported the potential toxicity of methylguanidine [47]. Methylguanidine was proposed as a serum potential biomarker of pancreatic cancer based on LC/GC–MS analyses which revealed a higher abundance of this compound in serum of patients with this tumor compared to controls [48]. Higher level of methylguanidine was also observed in serum of patients with cholangiocarcinoma [49]. This metabolite was identified in higher concentration in urine samples from patients with chronic pancreatitis by NMR-based metabolomics [50]. Significantly increased level of methylguanidine was identified in urine samples from dogs with BC compared to controls in an NMR-based metabolomics study [51].

Ion images presenting higher average intensity in the area of normal tissue were recorded for proton adduct of myosmine (*m/z* 147.092; Fig. 2F). Myosmine is a derivative of pyridines which can be found in tobacco and in various foods. It is suspected that this compound may be related to esophageal cancer [52]. Ion assigned to potassium adduct of ethylphosphate (*m/z* 164.971; Fig. 2 D) was found in higher intensity in normal tissue compared to cancer tissue. Ethylphosphate is an organic compound that belongs to the class of monoalkyl phosphates. This compound was identified in human saliva by LC-MS [53]. Also, the ion of *m/z* 102.091 (Fig. 3 B) was found in higher abundance in normal tissue and was assigned to $[M+H]^+$ adduct of aminopentanal.

Ion image that shows higher intensity in the area of cancer tissue has been created for the *m/z* 217.924 which corresponds to the ^{109}Ag adduct of hypotaurine (Fig. 2B). Hypotaurine is a sulfinic acid that is an intermediate in the biosynthesis of taurine from cysteine sulphinic acid. Previous research has established that hypotaurine has antioxidant properties *in vivo* [54] and also acts as a neurotransmitter [55]. Previously, using ^{1}H NMR, hypotaurine was found in increased level in serum samples of BC patients resistant to neoadjuvant chemotherapy [56]. Elevated level of hypotaurine was found in saliva of patients with medication-related osteonecrosis of the jaw [57]. In addition, hypotaurine was found to be upregulated in tissue of patients with colorectal cancer and related to the progression of this tumor [58].

4.2. Pathway analysis

A metabolic pathway impact analysis was performed to identify the most relevant pathways involved in the observed changes of tissue metabolite levels. Ten most significant metabolites were subjected to pathway analysis and quantitative pathway enrichment analysis. Three of them were found to be relevant to human metabolism (Table 2). Seventeen metabolic pathways i.e., glyoxylate and dicarboxylate metabolism, aminoacyl-tRNA biosynthesis, D-glutamine and D-glutamate metabolism, nitrogen metabolism, taurine and hypotaurine metabolism, arginine biosynthesis, glutathione metabolism, alanine, aspartate and glutamate metabolism, porphyrin and chlorophyll metabolism, glycine, serine and threonine metabolism, pyrimidine metabolism, primary bile acid biosynthesis, purine metabolism, mercaptopurine action pathway, thioguanine action pathway, azathioprine action pathway and mercaptopurine metabolism pathway, were found to be significantly impacted when comparing BC to normal tissue. Results from pathway impact analysis are shown in Supplementary Tables S3 and S4. Glycine,

Table 2
Selected metabolites and their involvement in different pathways.

Compound name	Pathway involved
Glycine	Glyoxylate and dicarboxylate metabolism, aminoacyl-tRNA biosynthesis, glutathione metabolism, porphyrin and chlorophyll metabolism, glycine, serine and threonine metabolism, primary bile acid biosynthesis, mercaptopurine action pathway, thioguanine action pathway, azathioprine action pathway
Glutamine	Glyoxylate and dicarboxylate metabolism, aminoacyl-tRNA biosynthesis, D-glutamine and D-glutamate metabolism, nitrogen metabolism, arginine biosynthesis, alanine, aspartate and glutamate mercaptopurine action pathway metabolism, pyrimidine metabolism, purine metabolism, thioguanine action pathway, azathioprine action pathway, mercaptopurine metabolism pathway
Hypotaurine	Taurine and hypotaurine metabolism

glutamine and hypotaurine were found to be involved in these metabolic pathways (Table 2). These pathways are well known to be related to cancer, e.g. taurine and hypotaurine metabolism have been shown to be related to BC [59,60] and renal cell carcinoma [61], sulfur metabolism has been shown to be related to breast cancer [62], and aminoacyl-tRNA biosynthesis pathway has been shown to be related to prostate cancer [63].

4.3. Diagnostic value of nanoparticles for MSI of cancer tissues

The diagnosis of most cancers is based on a molecular pathology that is currently most often performed by immunohistochemical analysis (IHC) or fluorescence *in situ* hybridization (FISH) which most often uses macromolecules such as proteins or nucleic acids of varying lengths [64,65]. These methods are complex, time-consuming, and require specialized and expensive antibodies or labeling. Surgical excision of the bladder tumor is currently a method of choice for treating patients suffering from BC, therefore it is important to quickly and precisely define the neoplastic tissue border during surgery in order to completely remove the tumor without damaging normal tissue. Numerous previous studies have shown that metabolites enable a more precise determination of pathology and may serve as potential diagnostic biomarkers in a variety of malignancies [66]. The use of MSI allows not only to identify potential tumor biomarkers but also to determine their location on the surface of the examined tissue. Nowadays almost all of MSI is made with the use of MALDI with many of its drawbacks including (i) abundant and numerous chemical background peaks in the low-mass region ($m/z < \approx 1000$) due to the presence of the applied matrix; (ii) the frequent need for external mass calibration; (iii) low mass resolution and accuracy due to the thickness of the tissue samples; (iv) low ionization efficiency for many organic compounds present in the samples in their non-charged states; (v) inhomogeneous matrix crystallization; and (vi) commonly observed acid-catalyzed hydrolysis of various biomolecules, and thus it is not suitable for metabolites. On the other hand, some nanoparticles such as silver and gold-based lacks most of above mentioned MALDI drawbacks and are one of the most interesting choices for studying of differentiation between cancer and normal tissues.

5. Conclusion

In this study, LDI-MSI technique with the use of nanoparticle-enhanced SALDI-type ^{109}AgNPET target was used for MSI of human bladder tissue. Ion images produced for few dozens of compounds of interest presented attention-grabbing differentiation of intensities. Univariate and multivariate statistical analyses revealed 10 metabolites that differentiated cancer from normal tissues. Among these metabolites, glycine, 3-methylbutanal, ethylphosphate, glutamine, myosmine, PI(22:0/0:0), aminopentanal, proline betaine and methylguanidine were found in higher abundance in normal tissue samples and hypotaurine was found at a higher level in cancer tissue samples. These compounds may significantly increase diagnostic potential and serve as useful discriminators of cancerous versus normal tissues in patients diagnosed with BC. Published results demonstrate that nanoparticle-based LDI-MSI must be considered as a powerful tool for analysis of biological objects and especially for biomarker discovery.

Financial disclosure

This work was supported by the National Science Centre (NCN), SONATA grant no. UMO-2018/31/D/ST4/00109.

The author contributions

Study design: Krzysztof Ossoliński Tomasz Ruman, Joanna Nizioł.

Data collection: Joanna Nizioł, Adrian Arendowski, Aneta Płaza-Altamer, Krzysztof Ossoliński, Anna Ossolińska, Tadeusz Ossoliński.

Statistical Analysis: Joanna Nizioł.

Data interpretation: Joanna Nizioł, Tomasz Ruman.

Manuscript preparation: Joanna Nizioł, Krzysztof Ossoliński, Artur Kołodziej, Tomasz Ruman.

Literature Search: Joanna Nizioł, Krzysztof Ossoliński.

Funds Collection: Joanna Nizioł.

Declaration of competing interest

The authors declare no conflict of interests.

Acknowledgements

Mr Dominik Ruman is acknowledged for creating MS search engine of chemical compounds.

Appendix A. Supplementary data

Supplementary data to this article can be found online at https://doi.org/10.1016/j.advms.2022.12.002.

References

[1] Sung H, Ferlay J, Siegel RL, Laversanne M, Soerjomataram I, Jemal A, et al. Global cancer statistics 2020: GLOBOCAN estimates of incidence and mortality worldwide for 36 cancers in 185 countries. CA A Cancer J Clin 2021;71:209–49. https://doi.org/10.3322/CAAC.21660.

[2] Kamat AM, Hegarty PK, Gee JR, Clark PE, Svatek RS, Hegarty N, et al. ICUD-EAU international consultation on bladder cancer 2012: screening, diagnosis, and molecular markers. Eur Urol 2013;63:4–15. https://doi.org/10.1016/J.EURURO.2012.09.057.

[3] González de Vega R, Clases D, Fernández-Sánchez ML, Eiró N, González LO, Vizoso FJ, et al. MMP-11 as a biomarker for metastatic breast cancer by immunohistochemical-assisted imaging mass spectrometry. Anal Bioanal Chem 2019;411:639–46. https://doi.org/10.1007/s00216-018-1365-3.

[4] Paine MRL, Kooijman PC, Fisher GL, Heeren RMA, Fernández FM, Ellis SR. Visualizing molecular distributions for biomaterials applications with mass spectrometry imaging: a review. J Mater Chem B 2017;5:7444–60. https://doi.org/10.1039/C7TB01100H.

[5] Steurer S, Singer JM, Rink M, Chun F, Dahlem R, Simon R, et al. MALDI imaging–based identification of prognostically relevant signals in bladder cancer using large-scale tissue microarrays. Urol Oncol Semin Orig Investig 2014;32:1225–33. https://doi.org/10.1016/J.UROLONC.2014.06.007.

[6] Ifa DR, Wiseman JM, Song Q, Cooks RG. Development of capabilities for imaging mass spectrometry under ambient conditions with desorption electrospray ionization (DESI). Int J Mass Spectrom 2007;259:8–15. https://doi.org/10.1016/J.IJMS.2006.08.003.

[7] Sekuła J, Nizioł J, Rode W, Ruman T. Gold nanoparticle-enhanced target (AuNPET) as universal solution for laser desorption/ionization mass spectrometry analysis and imaging of low molecular weight compounds. Anal Chim Acta 2015;875:61–72. https://doi.org/10.1016/J.ACA.2015.01.046.

[8] Nizioł J, Rode W, Zieliński Z, Ruman T. Matrix-free laser desorption–ionization with silver nanoparticle-enhanced steel targets. Int J Mass Spectrom 2013;335:22–32. https://doi.org/10.1016/J.IJMS.2012.10.009.

[9] Nizioł J, Rode W, Laskowska B, Ruman T. Novel monoisotopic 109AgNPET for laser desorption/ionization mass spectrometry. Anal Chem 2013;85:1926–31. https://doi.org/10.1021/ac303770y.

[10] Nizioł J, Ruman T. Surface-transfer mass spectrometry imaging on a monoisotopic silver nanoparticle enhanced target. Anal Chem 2013;85. https://doi.org/10.1021/ac4031658.

[11] Nizioł J, Ossoliński K, Ossoliński T, Ossolińska A, Bonifay V, Sekuła J, et al. Surface-Transfer mass spectrometry imaging of renal tissue on gold nanoparticle enhanced target. Anal Chem 2016;88. https://doi.org/10.1021/acs.analchem.6b01859.

[12] Arendowski A, Nizioł J, Ossoliński K, Ossolińska A, Ossoliński T, Dobrowolski Z, et al. Laser desorption/ionization MS imaging of cancer kidney tissue on silver nanoparticle-enhanced target. Bioanalysis 2018;10:83–94. https://doi.org/10.4155/bio-2017-0195.

[13] Moch H, Cubilla AL, Humphrey PA, Reuter VE, Ulbright TM. The 2016 WHO classification of tumours of the urinary system and male genital organs—Part A: renal, penile, and testicular tumours. Eur Urol 2016;70:93–105. https://doi.org/10.1016/J.EURURO.2016.02.029.

[14] Sauter G, Algaba F, Amin MB, Busch C, Cheville J, Gasser T, et al. Tumours of the urinary system: non-invasive urothelial neoplasias. In: WHO classification of classification of tumours of the urinary system and male genital organs. IARCC Press Lyon; 2004. p. 89–157.

[15] Suckau D, Resemann A, Schuerenberg M, Hufnagel P, Franzen J, Holle A. A novel MALDI LIFT-TOF/TOF mass spectrometer for proteomics. Anal Bioanal Chem 2003;376:952–65. https://doi.org/10.1007/s00216-003-2057-0.

[16] Bemis KD, Harry A, Eberlin LS, Ferreira C, van de Ven SM, Mallick P, et al. Cardinal : an R package for statistical analysis of mass spectrometry-based imaging experiments. Bioinformatics 2015;31:2418–20. https://doi.org/10.1093/bioinformatics/btv146.
[17] Pang Z, Chong J, Zhou G, De Lima Morais DA, Chang L, Barrette M, et al. MetaboAnalyst 5.0: narrowing the gap between raw spectra and functional insights. Nucleic Acids Res 2021;49:W388–96. https://doi.org/10.1093/NAR/GKAB382.
[18] Patiny L, Borel A. ChemCalc: a building block for tomorrow's chemical infrastructure. J Chem Inf Model 2013;53:1223–8. https://doi.org/10.1021/ci300563h.
[19] Arendowski A, Nizioł J, Ruman T. Silver-109-based laser desorption/ionization mass spectrometry method for detection and quantification of amino acids. J Mass Spectrom 2018;53:369–78. https://doi.org/10.1002/jms.4068.
[20] Luehr TC, Koide EM, Wang X, Han J, Borchers CH, Helbing CC. Metabolomic insights into the effects of thyroid hormone on Rana [Lithobates] catesbeiana metamorphosis using whole-body Matrix Assisted Laser Desorption/Ionization-Mass Spectrometry Imaging (MALDI-MSI). Gen Comp Endocrinol 2018;265:237–45. https://doi.org/10.1016/J.YGCEN.2018.02.012.
[21] Duarte IF, Rocha CM, Barros AS, Gil AM, Goodfellow BJ, Carreira IM, et al. Can nuclear magnetic resonance (NMR) spectroscopy reveal different metabolic signatures for lung tumours? Virchows Arch 2010;457:715–25. https://doi.org/10.1007/s00428-010-0993-6.
[22] Cao M, Zhao L, Chen H, Xue W, Lin D. NMR-Based metabolomic analysis of human bladder cancer. Anal Sci 2012;28:451–6. https://doi.org/10.2116/ANALSCI.28.451.
[23] Owusu-Sarfo K M. Asiago V, Deng L, Gu H, Wei S, Shanaiah N, et al. NMR-Based metabolite profiling of pancreatic cancer n.d.
[24] Moreadith RW, Lehninger AL. The pathways of glutamate and glutamine oxidation by tumor cell mitochondria. In: Role of mitochondrial NAD(P)+-dependent malic enzyme, 259; 1984. p. 6215–21.
[25] Costello LC, Franklin RB. 'Why do tumour cells glycolyse?': from glycolysis through citrate to lipogenesis. Mol Cell Biochem 2005;280:1–8. https://doi.org/10.1007/s11010-005-8841-8.
[26] Possemato R, Marks KM, Shaul YD, Pacold ME, Kim D, Birsoy K, et al. Functional genomics reveal that the serine synthesis pathway is essential in breast cancer. Nature 2011;476:346–50. https://doi.org/10.1038/nature10350.
[27] Yoshioka Y, Tsutsumi T, Adachi M, Tokumura A. Altered phospholipid profile in urine of rats with unilateral ureteral obstruction. Metabolomics 2009;5:429–33. https://doi.org/10.1007/s11306-009-0167-1.
[28] Lee GK, Lee HS, Park YS, Lee JH, Lee SC, Lee JH, et al. Lipid MALDI profile classifies non-small cell lung cancers according to the histologic type. Lung Cancer 2012;76:197–203. https://doi.org/10.1016/J.LUNGCAN.2011.10.016.
[29] Marien E, Meister M, Muley T, Fieuws S, Bordel S, Derua R, et al. Non-small cell lung cancer is characterized by dramatic changes in phospholipid profiles. Int J Cancer 2015;137:1539–48. https://doi.org/10.1002/ijc.29517.
[30] Guo S, Wang Y, Zhou D, Li Z. Significantly increased monounsaturated lipids relative to polyunsaturated lipids in six types of cancer microenvironment are observed by mass spectrometry imaging. Sci Rep 2015;4:5959. https://doi.org/10.1038/srep05959.
[31] Kang S, Lee A, Park YS, Lee SC, Park SY, Han SY, et al. Alteration in lipid and protein profiles of ovarian cancer. Int J Gynecol Cancer 2011;21:1566–72. https://doi.org/10.1097/IGC.0b013e318226c5f5.
[32] Mirnezami R, Spagou K, Vorkas PA, Lewis MR, Kinross J, Want E, et al. Chemical mapping of the colorectal cancer microenvironment via MALDI imaging mass spectrometry (MALDI-MSI) reveals novel cancer-associated field effects. Mol Oncol 2014;8:39–49. https://doi.org/10.1016/j.molonc.2013.08.010.
[33] Goto T, Terada N, Inoue T, Kobayashi T, Nakayama K, Okada Y, et al. Decreased expression of lysophosphatidylcholine (16:0/OH) in high resolution imaging mass spectrometry independently predicts biochemical recurrence after surgical treatment for prostate cancer. Prostate 2015;75:1821–30. https://doi.org/10.1002/pros.23088.
[34] Lin L, Huang Z, Gao Y, Chen Y, Hang W, Xing J, et al. LC-MS-based serum metabolic profiling for genitourinary cancer classification and cancer type-specific biomarker discovery. Proteomics 2012;12:2238–46. https://doi.org/10.1002/pmic.201200016.
[35] Dill AL, Eberlin LS, Zheng C, Costa AB, Ifa DR, Cheng L, et al. Multivariate statistical differentiation of renal cell carcinomas based on lipidomic analysis by ambient ionization imaging mass spectrometry. Anal Bioanal Chem 2010;398:2969–78. https://doi.org/10.1007/s00216-010-4259-6.
[36] Dill AL, Eberlin LS, Costa AB, Zheng C, Ifa DR, Cheng L, et al. Multivariate statistical identification of human bladder carcinomas using ambient ionization imaging mass spectrometry. Chem Eur J 2011;17:2897–902. https://doi.org/10.1002/chem.201001692.
[37] Bandu R, Mok HJ, Kim KP. Phospholipids as cancer biomarkers: mass spectrometry-based analysis. Mass Spectrom Rev 2018;37:107–38. https://doi.org/10.1002/mas.21510.
[38] Dill AL, Ifa DR, Manicke NE, Costa AB, Ramos-Vara JA, Knapp DW, et al. Lipid profiles of canine invasive transitional cell carcinoma of the urinary bladder and adjacent normal tissue by desorption electrospray ionization imaging mass spectrometry. Anal Chem 2009;81:8758–64. https://doi.org/10.1021/ac901028b.
[39] Wittmann BM, Stirdivant SM, Mitchell MW, Wulff JE, McDunn JE, Li Z, et al. Bladder cancer biomarker discovery using global metabolomic profiling of urine. PLoS One 2014;9:e115870. https://doi.org/10.1371/journal.pone.0115870.
[40] Pinto J, Amaro F, Lima AR, Carvalho-Maia C, Jerónimo C, Henrique R, et al. Urinary volatilomics unveils a candidate biomarker panel for noninvasive detection of clear cell renal cell carcinoma. J Proteome Res 2021;20:3068–77. https://doi.org/10.1021/ACS.JPROTEOME.0C00936/ASSET/IMAGES/LARGE/PR0C00936_0004.JPEG.
[41] Hanai Y, Shimono K, Oka H, Baba Y, Yamazaki K, Beauchamp GK. Analysis of volatile organic compounds released from human lung cancer cells and from the urine of tumor-bearing mice. https://doi.org/10.1186/1475-2867-12-7; 2012.
[42] Zhu ZJ, Qi Z, Zhang J, Xue WH, Li LF, Shen ZB, et al. Untargeted metabolomics analysis of esophageal squamous cell carcinoma discovers dysregulated metabolic pathways and potential diagnostic biomarkers. J Cancer 2020;11:3944. https://doi.org/10.7150/JCA.41733.
[43] Chen T, He P, Tan Y, Xu D. Biomarker identification and pathway analysis of preeclampsia based on serum metabolomics. Biochem Biophys Res Commun 2017;485:119–25. https://doi.org/10.1016/J.BBRC.2017.02.032.
[44] Chen Y, Xu J, Zhang R, Shen G, Song Y, Sun J, et al. Assessment of data pre-processing methods for LC-MS/MS-based metabolomics of uterine cervix cancer. Analyst 2013;138:2669–77. https://doi.org/10.1039/C3AN36818A.
[45] Oto J, Fernández-Pardo Á, Roca M, Plana E, Solmoirago MJ, Sánchez-González JV, et al. Urine metabolomic analysis in clear cell and papillary renal cell carcinoma: a pilot study. J Proteonomics 2020;218:103723. https://doi.org/10.1016/J.JPROT.2020.103723.
[46] Perez G, Faluotico R. Creatinine: a precursor of methylguanidine. Export 1973 2912 1973;29:1473–4. https://doi.org/10.1007/BF01943863.
[47] Wang F, Yang B, Ling GH, Yao C, Jiang YS. Methylguanidine cytotoxicity on HK-2 cells and protective effect of antioxidants against MG-induced apoptosis in renal proximal tubular cells in vitro, vol. 32; 2010. p. 85. https://doi.org/10.3109/0886022X.2010.501935. Https://DoiOrg/103109/0886022X2010501935, 978.
[48] Xie G, Lu L, Qiu Y, Ni Q, Zhang W, Gao YT, et al. Plasma metabolite biomarkers for the detection of pancreatic cancer. J Proteome Res 2015;14:1195–202. https://doi.org/10.1021/PR501135F/SUPPL_FILE/PR501135F_SI_001.PDF.
[49] Suksawat M, Phetcharaburanin J, Klanrit P, Namwat N, Khuntikeo N, Titapun A, et al. Metabolic phenotyping predicts gemcitabine and cisplatin chemosensitivity in patients with cholangiocarcinoma. Front Public Health 2022;10:766023. https://doi.org/10.3389/FPUBH.2022.766023/FULL.
[50] Lusczek ER, Paulo JA, Saltzman JR, Kadiyala V, Banks PA, Beilman G, et al. Urinary 1H-NMR metabolomics can distinguish pancreatitis patients from healthy controls. JOP 2013;14:161.
[51] Zhang J, Wei S, Liu L, Nagana Gowda GA, Bonney P, Stewart J, et al. NMR-based metabolomics study of canine bladder cancer. Biochim Biophys Acta, Mol Basis Dis 2012;1822:1807–14. https://doi.org/10.1016/j.bbadis.2012.08.001.
[52] Wilp J, Zwickenpflug W, Richter E. Nitrosation of dietary myosmine as risk factor of human cancer. Food Chem Toxicol 2002;40:1223–8. https://doi.org/10.1016/S0278-6915(02)00039-X.
[53] Álvarez-Sánchez B, Priego-Capote F, Luque de Castro MD. Study of sample preparation for metabolomic profiling of human saliva by liquid chromatography–time of flight/mass spectrometry. J Chromatogr A 2012;1248:178–81. https://doi.org/10.1016/J.CHROMA.2012.05.029.
[54] Aruoma OI, Halliwell B, Hoey BM, Butler J. The antioxidant action of taurine, hypotaurine and their metabolic precursors. Biochem J 1988;256:251. https://doi.org/10.1042/BJ2560251.
[55] Kalir A, Kalir HH. Biological activity of sulfinic acid derivatives. Sulphinic Acids, Esters Deriv 2010:665–76. https://doi.org/10.1002/9780470772270.CH23.
[56] Cicero DO, Zhuang J, Yang X, Zheng Q, Li K, Cai L, et al. Metabolic profiling of bladder cancer patients' serum reveals their sensitivity to neoadjuvant chemotherapy. Metabolism 2022;12:558. https://doi.org/10.3390/METABO12060558.
[57] Yatsuoka W, Ueno T, Miyano K, Uezono Y, Enomoto A, Kaneko M, et al. Metabolomic profiling reveals salivary hypotaurine as a potential early detection marker for medication-related osteonecrosis of the jaw. PLoS One 2019;14:e0220712. https://doi.org/10.1371/JOURNAL.PONE.0220712.
[58] Hou X, Hu J, Zhao X, Wei Q, Zhao R, Li M, et al. Taurine attenuates the hypotaurine-induced progression of CRC via ERK/RSK signaling. Front Cell Dev Biol 2021;9:954. https://doi.org/10.3389/FCELL.2021.631163/BIBTEX.
[59] Loras A, Suárez-Cabrera C, Martínez-Bisbal MC, Quintás G, Paramio JM, Martínez-Máñez R, et al. Integrative metabolomic and transcriptomic analysis for the study of bladder cancer. Cancers 2019;11:1–36. https://doi.org/10.3390/cancers11050686.
[60] Loras A, Martínez-Bisbal MC, Quintás G, Gil S, Martínez-Máñez R, Ruiz-Cerdá JL. Urinary metabolic signatures detect recurrences in non-muscle invasive bladder cancer. Cancers 2019;11:914. https://doi.org/10.3390/CANCERS11070914. 2019;11:914.
[61] Yang W, Yoshigoe K, Qin X, Liu JS, Yang JY, Niemierko A, et al. Identification of genes and pathways involved in kidney renal clear cell carcinoma. BMC Bioinf 2014;15:S2. https://doi.org/10.1186/1471-2105-15-S17-S2.
[62] Ryu CS, Kwak HC, Lee KS, Kang KW, Oh SJ, Lee KH, et al. Sulfur amino acid metabolism in doxorubicin-resistant breast cancer cells. Toxicol Appl Pharmacol 2011;255:94–102. https://doi.org/10.1016/J.TAAP.2011.06.004.
[63] Vellaichamy A, Sreekumar A, Strahler JR, Rajendiran T, Yu J, Varambally S, et al. Proteomic interrogation of androgen action in prostate cancer cells reveals roles of aminoacyl tRNA synthetases. PLoS One 2009;4:e7075. https://doi.org/10.1371/journal.pone.0007075.
[64] Naumova AV, Modo M, Moore A, Murry CE, Frank JA. Clinical imaging in regenerative medicine. Nat Biotechnol 2014 328 2014;32:804–18. https://doi.org/10.1038/nbt.2993.
[65] Harris TJR, McCormick F. The molecular pathology of cancer. Nat Rev Clin Oncol 2010;7:251–65. https://doi.org/10.1038/NRCLINONC.2010.41.
[66] Baker M. Metabolomics: from small molecules to big ideas. Nat Methods 2011 82 2011;8:117–21. https://doi.org/10.1038/nmeth0211-117.